

COMPUTATIONAL STUDIES OF DEFORMATION IN HCP METALS AND DEFECTS  
IN A LEAD-FREE FERROELECTRIC CERAMIC

By

DONG-HYUN KIM

A DISSERTATION PRESENTED TO THE GRADUATE SCHOOL  
OF THE UNIVERSITY OF FLORIDA IN PARTIAL FULFILLMENT  
OF THE REQUIREMENTS FOR THE DEGREE OF  
DOCTOR OF PHILOSOPHY

UNIVERSITY OF FLORIDA

2011

© 2011 DONG-HYUN KIM

To my family with love

## ACKNOWLEDGMENTS

First, I would like to thank Prof. Simon Phillpot for his support and guidance throughout my Ph. D course. I am really fortunate and happy to have been one of his students. I would also like to thank Prof. Susan Sinnott. Her passion and management for work and research are impressive to me. Although Dr. Ebrahimi has passed away, her legacy will be left in my research. I also appreciate Prof. Michele Manuel for serving on my committee and for their helpful suggestions for my research. Prof. Kwangho Kim, my master course advisor, made me first realize what research is and how to do it. He should be also appreciated here.

Many people have helped to make my time at the University of Florida enjoyable, and particularly I will never forget 'SINPOT (Sinnott +Phillpot)' group members. I must also thank my family for their constant support, even with a thousand miles between us. Without them, none of this would have been possible. Finally, I offer my deepest gratitude to my wife, Hyunjung, to whom this dissertation is dedicated. Her unconditional love and encouragement have been instrumental in my success.

## TABLE OF CONTENTS

	<u>page</u>
ACKNOWLEDGMENTS .....	4
LIST OF TABLES .....	8
LIST OF FIGURES .....	9
ABSTRACT .....	15
CHAPTER	
1 INTRODUCTION .....	17
1-1. Motivation .....	17
1-2. Part I: Nanocrystalline Hexagonal Close Packed (HCP) Metal .....	18
1-3. Part II: $\text{Na}_{0.5}\text{Bi}_{0.5}\text{TiO}_3$ .....	19
2 BACKGROUND: MD SIMULATIONS OF NANOCRYSTALLINE-HCP METALS....	21
2-1. Slip in HCP Metals .....	23
2-2. Twinning in HCP Metals .....	25
2-3. Nanocrystalline Metals and Molecular Dynamics Simulation .....	29
2-4. Molecular Dynamics Simulation .....	31
2-4-1. Pressure Control .....	32
2-4-2. Temperature Control .....	32
2-5. Interatomic Potentials .....	33
2-5-1. Embedded-Atom Method (EAM) Potential .....	35
2-5-2. Modified Embedded-Atom Method (MEAM) Potential .....	35
2-6. Computational Details .....	38
2-6-1. Generation of Structure .....	38
2-6-2. Simulation of Mechanical Test .....	42
2-6-3. Analysis Method .....	43
2-7. Summary .....	43
3 OVERALL MECHANICAL RESPONSE OF TEXTURED NANOCRYSTALLINE MG .....	44
3-1. Stress-Dependence of Mechanical Response .....	44
3-2. Signatures of Dislocations and Twins .....	45
3-3. Microstructure Evolution .....	50
3-4. Stress Analysis of Dislocation Activation .....	59
3-5. Transitions in Dislocation Mode .....	60
3-6. Competition between Slip and Twinning .....	61
3-7. Summary .....	62

4	OVERALL MECHANICAL RESPONSE OF 2D NANOCRYSTALLINE-TI METALS .....	64
	4-1. Potentials and Mechanical Response.....	65
	4-2. Stress-dependence of Mechanical Response in Ti.....	69
	4-3. Comparison of Mg and Ti .....	70
	4-4. Summary .....	75
5	PYRAMIDAL <C+A> SLIP IN COLUMNAR NC-MG .....	76
	5-1. Occurrence of <c+a> Slip .....	78
	5-2. Structures of <c+a> Dislocations .....	80
	5-3. Activation Process of <c+a> Dislocations.....	91
	5-4. Comparison of Different Potentials .....	95
	5-5. Role of Pyramidal <c+a> Dislocations in Plastic Deformation .....	96
	5-6. Summary .....	99
6	TWINNING IN 2D NANOCRYSTALLINE-MG .....	101
	6-1. Nucleation of Twins .....	101
	6-2. Nucleation Mechanism of Compressive Twinning from Grain Boundaries ....	106
	6-3. Nucleation Mechanism of Tensile Twinning from GB .....	107
	6-3-1. Nucleation Process in a Large Grain.....	107
	6-3-2. Nucleation process in Small Grains .....	117
	6-4. Summary .....	118
7	OVERALL MECHANICAL RESPONSE OF RANDOMLY ORIENTED HCP METALS .....	120
	7-1. Strain-Stress Response.....	120
	7-2. Hall-Petch Relation .....	121
	7-3. Microstructure Evolution .....	124
	7-4. Individual Defect Process .....	129
	7-4-1. <a> Slip.....	129
	7-4-2. <c+a> and <c> Slip .....	130
	7-4-3. Twinning.....	142
	7-5. Grain Size Effect on Plasticity.....	144
	7-6. Summary .....	149
8	CATION ORDERING IN SODIUM BISMUTH TITANATE .....	151
	8-1. Background .....	155
	8-1-1. First Principles Calculations .....	155
	8-1-2. Density Functional Theory (DFT) .....	156
	8-1-3. Exchange-Correlation Functional.....	158
	8-2. Computational Details.....	159
	8-3. Analysis of Structure Change .....	162
	8-4. Analysis of Layered NBT .....	164

8-5. Distortion of Octahedra.....	169
8-6. Summary .....	173
REFERENCE LIST.....	175
BIOGRAPHICAL SKETCH.....	185

## LIST OF TABLES

<u>Table</u>	<u>page</u>
1-1 Classification of defects found in materials [4]. .....	18
2-1 Physical properties of Mg [24, 25] and Ti[20, 26]. Add density and specific strength .....	25
2-2 Twinning planes, directions, and shears in pure zirconium [28]. .....	27
2-3 Slip and twinning modes in Mg and Ti [8, 20, 31].....	29
2-4 Models of plane strain and stress for two dimensional system.....	32
4-1 c/a ratio and slip modes of various HCP metals [8].....	64
4-2 Lattice constants and stacking fault energies of various HCP metals obtained by First principle calculation.[107].....	65
4-3 Lattice constants of strained 18nm [0001]-textured Ti at 0.1K.....	66
5-1 Stacking fault energies in magnesium.....	94
6-1 Nucleation conditions for for $\{10\bar{1}1\} < 10\bar{1}2 >$ , $\{10\bar{1}2\} < 10\bar{1}1 >$ , and $\{10\bar{1}3\} < 30\bar{3}2 >$ primary twinning. ....	105
7-1 Hall-Petch slopes of pure Cu and Mg from MD simulations and experiments...	123
7-2 $\epsilon_{TS} - \epsilon_{0.1\% \text{ SF atom ratio}}$ , $\sigma_{TS}$ and $\sigma_{0.1\% \text{ SF atom ratio}}$ of nc-Mg at grain sizes of 9, 18, and 36nm .....	147
8-1 Three different phases and crystallographic data of NBT[175] .....	153
8-2 Comparison of ferroelectric properties of PZT[9] and NBT[179].....	155
8-3 Arrangements of Na and Bi in 2 X 2 X 2 super cell. ....	160
8-4 Structural parameters and energies of each ordering type. ....	162
8-5 Structural information of the layered structure, T5. ....	166
8-6 Radius and electronic structures of Bi and La [198-200].....	171

## LIST OF FIGURES

<u>Figure</u>	<u>page</u>
2-1	Comparison of FCC (right) and HCP (left) lattices..... 22
2-2	Simulation methods at different time and length scales. QM, DFT, and MD denotes quantum mechanics, density functional theory, and molecular dynamics, respectively.. ..... 22
2-3	Slip planes and directions of (a) HCP [20]and (b) FCC [21] ..... 24
2-4	Schematics of original and twinned textures. $K_1$ and $K_2$ denote the planes of twinning and the conjugate (or reciprocal) twinning. $\eta_1$ and $\eta$ indicate the directions of twinning and conjugate twinning, respectively [27]..... 26
2-5	Twinning shears as a function of the c/a ration in HCP metals. Filled circles indicate active twin modes..... 28
2-6	Schematics of $\{10\bar{1}2\}$ $\{10\bar{1}1\}$ tensile twinning [30] ..... 29
2-7	Schematic representation of the variation of flw stress as a function of grain size in metals and alloys [53]..... 31
2-8	Schematic representation of three major atomic bonding types. .... 34
2-9	Schematic of 3d-periodic simulation cell with four hexagonal grains. In each grain, the angle $\theta$ is measured between the c-axis of HCP unit cell and the x-axis of the simulation cell..... 40
2-10	Schematic of 3D fully dense structure of nc-HCP metals. Each color indicates a different grain..... 41
3-1	Strain vs. time plots for nanocrystalline structures with 18nm grain size at various external stresses..... 45
3-2	Snapshot of 3.5% strained structure with grain size of 18nm. Here, and in subsequent figures, gray, black and brown denote normal (HCP), disordered (non- HCP or FCC), and stacking fault (FCC), respectively.. ..... 46
3-3	Burgers vectors and circuits of SF/RH type for the dislocations and stacking faults (SF) found in Fig.3-2. .... 48
3-4	Snapshot and schematic of an atomic structure for the extended $\langle a \rangle$ dislocation, as observed for grain size of 40nm under 1.3GPa..... 49
3-5	Snapshots of tensile test for 18n $[11\bar{2}0]$ -textured structure at 1.18 GPa for four times and strains, increasing from 9(a) to (d).. ..... 53

3-6	Activity of $\{10\bar{1}2\} < 10\bar{1}1 >$ tensile twinning in each grain of 18nm $[11\bar{2}0]$ -textured structure at 1.18 GPa.....	54
3.7	Snapshots of strained $[11\bar{2}0]$ -textured structures with grain size of 60nm at 1.3GPa. (a) and (b): total strains are 4.73 and 7.25% at 1.3GPa, including elastic strain of ~3%..	55
3-8	Snapshots of strained $[11\bar{2}0]$ -textured structures with grain sizes from 6 to 40nm at 1.0 or 1.18GPa..	56
3-9	Snapshots of strained $[11\bar{2}0]$ -textured structures with 40nm grain size under various external stresses from 1.25 to 1.5GPa.....	59
3-10	CNA image and shear stress map of strained $[11\bar{2}0]$ -textured structures with 18nm grain size under 1.1GPa.....	60
4-1	Strain-Time curves of 18nm $[0001]$ -textured Ti as a function of external stress.....	67
4-2	PE and CN image of strained $[11\bar{2}0]$ -textured structures with 18nm grain size under 3.0GPa. Kim et. al.'s MEAM potential was used..	68
4-3	Snapshots of strained $[11\bar{2}0]$ -textured structures with 18nm grain size under 2.75GPa. There is no change in CN. Two textures have the same phase. ....	69
4-4	Creep curves of $[11\bar{2}0]$ -textured Ti having a grain size of 18nm. ....	70
4-5	Snapshots of nano-structured Ti (left) and Mg (right) plastically deformed at 3.25 and 1.2GPa, respectively.....	71
4-6	Formation of $\{10\bar{1}2\} < 10\bar{1}1 >$ tensile twins during cooling th $[10\bar{1}0]$ -textured Ti from 700 to 100K.....	73
4-7	Snapshots of shear strain and central symmetry of the 6%-strained 1010-textured Ti at 3GPa..	74
5-1	Snapshots of pyramidal $<c+a>$ slip activated in $[11\bar{2}0]$ -and $[10\bar{1}0]$ - textured structures. Gray, black and brown denote normal (HCP), disordered (non-HCP or FCC), and stacking fault (FCC) atoms respectively. ....	79
5-2	Common neighbor analysis (CNA) and potential energy (PE) map of the partial pyramidal dislocation in the $[11\bar{2}0]$ -textured structure. The white '⊥' denote the cores of the edge dislocations in (b). ....	81
5-3	CNA and PE map of the extended pyramidal dislocation observed in the $[11\bar{2}0]$ -textured structure.....	82

5-4	Atomic structures of a (a) leading and (b) trailing of the extended $\langle \mathbf{c+a} \rangle$ dislocation including CNA. (c) and (d): corresponding atomic displacement on the 1 <sup>st</sup> order pyramidal slip plane, $(10\bar{1}1)$ .	83
5-5	Burgers vectors of the 1 <sup>st</sup> order pyramidal extended dislocation shown in the HCP unit cell.	84
5-6	(a) CNA and (b) PE map of the pyramidal $\langle \mathbf{c+a} \rangle$ dislocation activated in the $[10\bar{1}0]$ -textured structure.	85
5-7	CNA visualization and PE mapping of the extended $\langle \mathbf{c+a} \rangle$ pyramidal dislocation projected onto the $(10\bar{1}0)$ and $(0001)$ planes.	88
5-8	Layer structures of the extended pyramidal $\langle \mathbf{c+a} \rangle$ dislocation in the $[10\bar{1}0]$ -texture by CNA.	89
5-9	Potential energy distributions (snapshots) and strain energy curves within cylinders of radius R having a center of an edge pyramidal $\langle \mathbf{c+a} \rangle$ dislocation line.	93
5-10	Pyramidal $\langle \mathbf{c+a} \rangle$ dislocations simulated by Sun potential. (a ) CNA iamge of $[1\bar{1}20]$ texture at 1.45 GPa.	96
5-11	Creep curves and snapshots of strained columnar Mg with 18nm grain size. Cyan, brown and black in (b) and (c) mean a twinned region, stacking fault (FCC), disordered (non- HCP or FCC), respectively.	98
6-1	Three types of twins found during creep, from a simulation of a grain size of 40nm under 1.25GPa.	103
6-2	Snapshots of nucleation process of $\{10\bar{1}1\} \langle 10\bar{1}2 \rangle$ primary twinning at the grain 1 of $[1\bar{1}20]$ -textured structure with 40nm grain size deformed under 1.25GPa.	104
6-3	twinning activated in the 18nm $[10\bar{1}0]$ -textured Mg. <b>a</b> and <b>c</b> indicate lattice constants of Mg in (e) and (f).	106
6-4	Nucleation process of $\{10\bar{1}2\} \langle 10\bar{1}1 \rangle$ twinning from GB at 293K.	108
6-5	Potential Well Overlap (PWO) model of twin nucleation at GB. (a) Simplified 2D GB structure having a twin nucleation site from Fig. 6-2.	112
6-6	Difference between $E_{PWO}$ and $E_{Thermal}$ at scales of temperature (T) and length (R) from Mg potentials. RT, $T_m$ , and $R_a$ denote room temperature (=293K), melting temperature and normal atomic distance at 0K.	113

6-7	c/a ratios and melting temperatures as functions of cohesive energies of various HCP metals.....	116
6-8	Nucleation of $\{10\bar{1}2\} < 10\bar{1}1 >$ twin in 18nm $[11\bar{2}0]$ -textured Mg. (a) An initial GB structure..	119
7-1	Strain-stress curves of nanocrystalline Mg with fully dense 3D structure. Each simulation of tensile test was conducted at 293K under uniaxial stress. A strain rate was $1.5 \times 10^9 \text{s}^{-1}$ during tensile test.....	121
7-2	The Hall-Petch graph in nc-Mg. The flow stress is calculated by averaging strain values between 8 and 11% in strain-stress curves of Fig. 7-1.....	123
7-3	Snapshot of 11%-strained structure of 18nm grain size at 293K with constant strain rate of $1.5 \times 10^9 \text{s}^{-1}$ . a and b represent structures before and after straining, respectively.....	125
7-4	Shear strain map of nc-Mg with 36nm grain size. Normal HCP atoms are not shown. ....	127
7-5	Shear strain map of nc-Mg with 36nm grain size. Normal HCP atoms are not shown. ....	128
7-6	$\langle a \rangle$ slip process in a 3D Mg structure with 24nm grain size. (a) Various $\langle a \rangle$ slip vectors and planes in a HCP unit cell.....	130
7-7	Prismatic $\langle a \rangle$ slip process in a 3D Mg structure with 36nm grain size. I, II and V denote prismatic $\langle a \rangle$ dislocations. III and IV denote $\{10\bar{1}1\} < 10\bar{1}2 >$ compressive twins..	132
7-8	Dislocation processes which occur from prismatic $\langle a \rangle$ slip. (a) $\langle a \rangle$ dislocations shown in Fig. 7-7c are gliding. $\alpha$ and $\beta$ denote slip planes of basal and prismatic $\langle a \rangle$ ..	133
7-9	Evolution of the dislocation source in a $\langle c+a \rangle$ pyramidal slip [23]. (a) cross slip of a dislocation (b) formation of junction for $\langle c+a \rangle$ dislocation, and (c) cross slip of $\langle c+a \rangle$ dislocation. ....	135
7-10	Activation process of pyramidal $\langle c+a \rangle$ slip from a single prismatic $\langle a \rangle$ dislocation.....	136
7-11	Activation process of $\langle c \rangle$ dislocation between two approaching prismatic $\langle a \rangle$ dislocations. Green dot line denote a part of the prismatic $\langle a \rangle$ dislocation gliding on a different plane. ....	136
7-12	Bowing of a prismatic $\langle a \rangle$ dislocation and activating of second-order pyramidal $\langle c+a \rangle$ slip. ....	137

7-13	Energy difference ( $W_{\text{screw}} - \text{Wedge}/L$ ) as a function of bending angle. $L$ denotes bending length of a straight dislocation.....	138
7-14	Relation between misorientation angle and dislocation energy per unit length ( $E/L$ ) of screw $\langle \mathbf{a} \rangle$ and pyramidal $\langle \mathbf{c}+\mathbf{a} \rangle$ dislocations at dislocation density ( $\rho$ ) of $10^8 \text{cm}^{-2}$ .....	140
7-15	Relation between misorientation angle and dislocation energy per unit length ( $E/L$ ) of screw $\langle \mathbf{a} \rangle$ and pyramidal $\langle \mathbf{c}+\mathbf{a} \rangle$ dislocations at dislocation density ( $\rho$ ) of $10^{12} \text{cm}^{-2}$ .....	141
7-15	Twin nucleation process of the compressive $\{1011 \langle 1012 \rangle$ mode (a ~ d) and tensile $\{10\bar{1}2\} \langle 1011 \rangle$ mode (e ~ h).....	143
7-16	Potential energy map of SFs in 11.1%-strained Mg with 36nm grain size. Normal HCP and disordered atoms like GB are not shown here.....	145
7-17	Strain and evolution of SFs with increasing strain at different grain sizes (9, 18, and 36nm). . . . .	146
7-18	Stress and evolution of SFs with increasing strain at different grain sizes. (a) 36nm, (b) 18nm, and (c) 9nm .....	148
7-19	SF evolutions of 11.1%-strained samples with three different grain sizes. a. 9nm, b. 18nm, and c. 36nm.....	149
8-1	R3c structure of 2 X 2 X 1 unit cell sizes. White, green, and red indicate titanium, Na or Bi, and oxygen, respectively.....	152
8-2	Pseudo-cubic cells of perovskite. (a) The projection of the rhombohedral cell down [001]. open circles denotes Na/Bi sites [175]. (b) The ideal cubic perovskite of $\text{ABX}_3$ (A,B =cation, X= anion) [180].....	154
8-3	Cation arrangements adopted in the present work.....	161
8-4	Cation ordering in T4 with 5 X 4 X 4 psuedo-cubic size. ....	162
8-5	Energy and correlation between structural parameters. (a) 2a-2b. (b) Energy. (c) $\alpha$ - $\beta$ .....	164
8-6	Final optimized structures of T2 (left) and T5 (right) in the perovskite axis ( $a_p$ , $b_p$ , and $c_p$ ).....	165
8-7	Change of force and energy in T2 and T5 as a function of an ionic iteration step. E and F denote energy and force. ....	166
8-8	A unit cell of optimized T5 (a and b) and projections of simplified $\text{Pr}_{0.5}\text{Sr}_{0.5}\text{MnO}_3$ perovskite structure with symmetry of F4/mmc [188] (c).....	167

8-9	Charge density images of P1 phase. a. blue, orange, red, and green denote bismuth, oxygen, titanium, and sodium, respectively.....	168
8-10	Optimized unit cell of $\text{Na}_{0.5}\text{La}_{0.5}\text{TiO}_3$ . Compare with Fig. 8-8(a) and (b) for NBT. ....	172
8-11	Contour map of charge density of $\text{Na}_{0.5}\text{Bi}_{0.5}\text{TiO}_3$ and $\text{Na}_{0.5}\text{La}_{0.5}\text{TiO}_3$ on different planes of pseudo cubic type cell.....	173

Abstract of Dissertation Presented to the Graduate School  
of the University of Florida in Partial Fulfillment of the  
Requirements for the Degree of Doctor of Philosophy

COMPUTATIONAL STUDIES OF DEFORMATION IN HCP METALS AND DEFECTS  
IN A LEAD-FREE FERROELECTRIC CERAMIC

By

Dong-Hyun Kim

August 2011

Chair: Simon R. Phillpot  
Major: Materials Science and Engineering

Plastic deformation of nanocrystalline Mg and Ti is examined using molecular dynamics (MD) simulation. Slip, twinning, and GB processes are observed in textured (2D) columnar and random (3D) microstructures. The deformation simulations of Mg reproduce various twinning modes: tensile  $\{10\bar{1}2\} < 10\bar{1}1 >$  twins, and compressive  $\{10\bar{1}1\} < 10\bar{1}2 >$ ,  $\{11\bar{2}2\} < 11\bar{2}3 >$  and  $\{10\bar{1}3\} < 30\bar{3}2 >$  twins. Two pyramidal  $< \mathbf{c+a} >$  slip modes are manifested in strained structures: first-order  $\{10\bar{1}1\} < \bar{1}\bar{1}23 >$  and second-order  $\{11\bar{2}2\} < \bar{1}\bar{1}23 >$ . Nucleation processes and mechanisms of dislocations and twins are identified (e.g. slip-assisted twin nucleation mechanism of  $\{11\bar{2}2\} < 11\bar{2}3 >$  twin, initiation of  $\{10\bar{1}2\} < 10\bar{1}1 >$  twins by migration at GB). The crossover of initiation process between slip and twinning are found in 2D textures. The strongest grain size in 3D fully dense Mg occurs at 24nm. Single prismatic  $< \mathbf{a} >$  dislocations and their interactions directly result in formation of  $< \mathbf{c+a} >$  and  $< \mathbf{c} >$  dislocations. Among the empirical potentials for Ti, the Henning MEAM potential displays slip and twinning processes most consistent with experiments.

The cation arrangements of Na and Bi in  $\text{Na}_{0.5}\text{Bi}_{0.5}\text{TiO}_3$  are investigated using density functional theory (DFT). The structure with alternative stacking of Na and Bi layers in the perovskite axis has the lowest energy of the cation arrangements. The R3c structure, known to be the room temperature phase of  $\text{Na}_{0.5}\text{Bi}_{0.5}\text{TiO}_3$  has a higher energies than structures with random cation arrangements. The cation-layered structure is revealed to have a P1 phase by distortion of octahedra in its perovskite. To analyze the structure distortion, elements (Ti-Bi and Ti-La) causing the second-order Jahn–Teller effect are chosen and, compared in structure and charge density. The combination of lone pairs and the  $d^0$  transition metal can deform octahedra of a perovskite cell more severely than that of  $d^0$  transition metals. The cation-layered structure of  $\text{Na}_{0.5}\text{Bi}_{0.5}\text{TiO}_3$  may be influenced by the Jahn-Teller effect, thereby having the lowest energy.

# CHAPTER 1 INTRODUCTION

## 1-1. Motivation

A wide variety of materials are used as a component of devices and machines. Both natural materials and engineered materials usually contain defects. We control the properties of the materials by removing, multiplying or manipulating these defects. For example, the numbers of vacancies or dislocations should be minimized in a silicon wafer to be used as a substrate of a high quality for electron devices [1]. A transistor is typically designed with an n- or p-type semiconductor producing excess electrons or holes. Dopants are essential to make semiconductors perform consistently, and can be considered as defects in the base materials, e.g. Si or Ge [2]. In metals, a high density of dislocations or impurities can enhance their strength by preventing slip process [3]. It is a classic and still significant issue in materials science and engineering to control various defects and use their interactions properly.

Defects appear with various shapes inside materials, from point defects such as vacancies, interstitial or substitutional atoms to one-dimensional defects like dislocations and stacking faults, and higher-dimensional defects including GBs, voids and cracks [4] (see Table 1-1). Microscopic defects are big enough to be experimentally examined without any significant difficulty. However, the atomistic defects and their mechanisms of creation and interaction are still hard to probe in spite of the development of analytic instruments. In the present dissertation, a computational study is thus carried out to reveal such defect process in two representative materials: one a metal, the other a ceramic.

Table 1-1. Classification of defects found in materials [4].

Dimension	Names
Point (0D)	vacancy, interstitial, Schottky, Frenkel, antisite
Line (1D)	Dislocation, stacking fault
Interfacial (2D)	Grain boundary, interphase boundary, free surface
Bulk (3D)	cavity, gas bubble, crack,

## 1-2. Part I: Nanocrystalline HCP Metal

Among HCP (hexagonal close-packed) metals, the importance of magnesium and titanium alloys in the automotive and aerospace (jet engines, missiles, and spacecraft) industry has greatly increased in recent years due to their high specific strengths and light weight [5, 6]. Titanium is strong, lustrous, and is corrosion resistant. Titanium can be used in its elemental form or can be alloyed with iron, aluminum, vanadium and molybdenum. However, in case of Mg, its alloys are favored over pure element due to its susceptibility to oxidation and corrosion. The most widely used magnesium alloys adopt the Mg-Al system[6]. Their applications are normally limited to temperatures of up to 120°C due to decreasing of strength [6]. Further improvement in the high-temperature mechanical properties of magnesium alloys will greatly expand their industrial applications.

As engineering materials, the mechanical properties of Mg alloys need to be fully understood. Plasticity in the metals is normally achieved by a number of deformation events, most particularly slip arising from dislocations and twinning. The mechanical response can be changed significantly by promoting or preventing these deformation processes.

Reducing grain size is one simple method to enhance strength. Although nanocrystalline metals exhibit higher strength than coarse-grained ones [7], softening

(or inverse Hall-Petch behavior) is also found in ultra-small grain size of  $< \sim 20\text{nm}$  (see Fig. 2.5). Not only is the collective response of nanocrystalline samples analyzed in this dissertation, but also the defect unit processes .

The mechanical responses of Mg and Ti are explored using molecular dynamics (MD) simulations. The  $c/a$  ratio largely determines the nature of the deformation slip modes that the metal manifests [8]. The anisotropy in HCP metals is revisited with regard to slip and twinning in Chapter 2.

In Chapters 3 through 7, the deformation behavior of polycrystals with columnar texture (“2D structure”) is investigated. Such samples are selected to understand fundamental properties of plastic deformation. The basic phenomena found in columnar nc-Mg are verified in fully dense polycrystals of Mg with randomly oriented grains (“3D structure”) in Chapter 8. The MD simulations of 3D Mg elucidate the relationship among deformation mechanisms, grain size, and strength. The fully dense 3D Mg polycrystals more closely represent typical experimental samples, and thus should more accurately reproduce experimental observations.

### **1-3. Part II: $\text{Na}_{0.5}\text{Bi}_{0.5}\text{TiO}_3$**

With applications in electronic devices, PZT( $\text{Pb}[\text{Zr}_x\text{Ti}_{1-x}]\text{O}_3$ ) shows excellent ferroelectric and piezoelectric properties [9-12]. There are strong environmental drives to replace lead-containing PZT with a lead-free alternative. NBT( $\text{Na}_{0.5}\text{Bi}_{0.5}\text{TiO}_3$ ) is one of the promising substitutes for PZT[13-15]. The ferroelectric and piezoelectric properties of ferroelectrics depend strongly on the on crystallography and defects, e.g., impurities, and vacancies. Na and Bi, which occupy the A site in a perovskite structure of ABO, are known to usually be randomly distributed in NBT having R3C symmetry. The fundamental issues are defined in Chapter 9.

In Chapter 10, the energies of various orderings of Na and Bi are determined using Density Functional Theory (DFT) calculation. Different arrangements of Na<sup>1+</sup> and Bi<sup>3+</sup> may cause different local distortions in bond lengths and electron distributions in the NBT structure due to their very different charges. The defect structure determined from the DFT calculations are compared with those determined from experiment.

## CHAPTER 2

### BACKGROUND: MD SIMULATIONS OF NANOCRYSTALLINE-HCP METALS

Before beginning MD simulations of nc-HCP metals, the fundamental background is reviewed in this chapter. To help understanding plastic deformation in nc-HCP metals, crystal structures, deformation modes, and the basics of nanocrystalline metals are discussed. In addition, the theory and practice of molecular dynamics simulations are discussed.

The crystal structure of a metals largely determined the deformation mechanisms that control plasticity. Metals normally shows FCC (face-centered cubic), BCC (body-centered cubic), or HCP (hexagonal close-packed) lattice structure. FCC and HCP are similar structures, as shown in Fig. 2-1. This similarity means that that a stacking fault in FCC corresponds to a region of HCP, and vice versa. The FCC lattice has a stacking order of ABCABC, while the HCP lattice has a stacking order of ABABAB, as shown in Fig. 2.1. In HCP crystals, the atomic distance and unit length in the stacking direction are noted as  $a$  and  $c$ , respectively. The  $c/a$  ratio, known as the anisotropy, is different in different HCP systems and is determined by details of the electronic structure. As discussed in Sections 2-1 and 2, this anisotropy is related with determining the deformation modes in HCP metals.

Metals, compared to ceramic, have good plasticity at even room temperature because of the occurrence of deformation mechanisms such as slip and twinning. Normal engineering metals have polycrystalline structures, and their grain boundaries (GBs) increase strength and decrease plasticity by preventing conventional deformation process of slip and twinning. However, the GBs activate another mechanism in

nanocrystalline metals. As discussed in Section 2-3, these GB processes can increase the plasticity and decrease the strength.

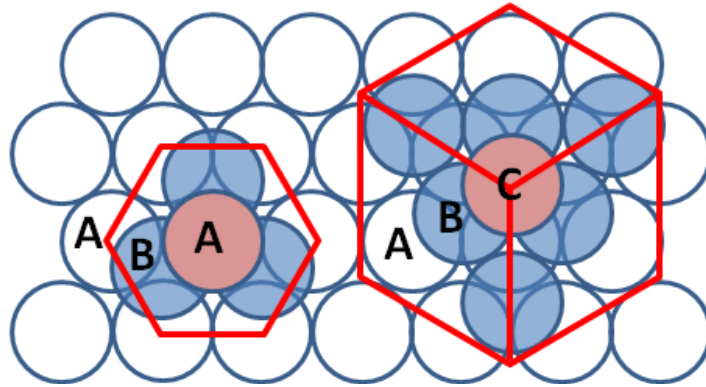


Figure 2-1. Comparison of FCC (right) and HCP (left) lattices. The circles and red lines indicate atoms and the Bravais lattices, respectively. The letters denote which equivalent layers.

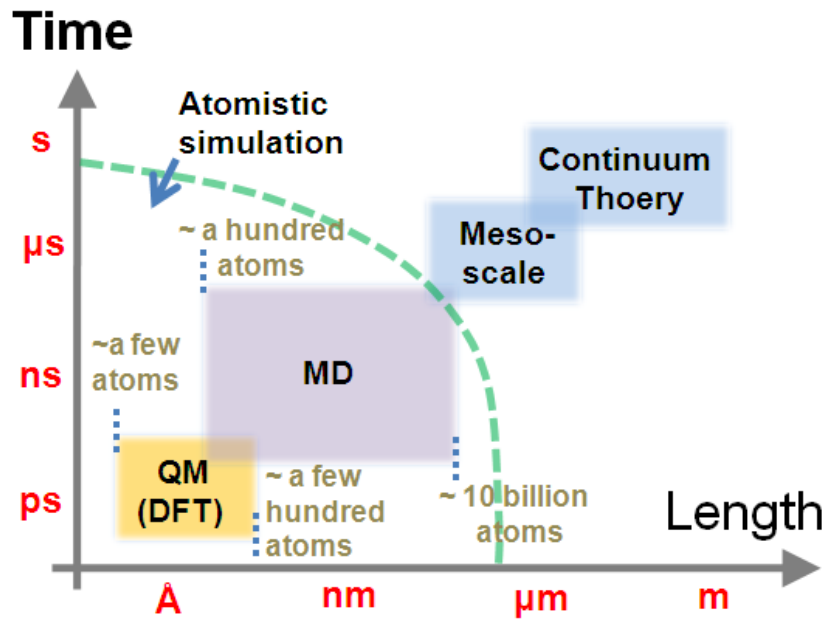


Figure 2-2. Simulation methods at different time and length scales. QM, DFT, and MD denotes quantum mechanics, density functional theory, and molecular dynamics, respectively. MD and QM are atomistic simulations. Numbers of atoms indicate minimum and maximum numbers of atoms normally calculated at simulation of QM and MD.

A computational method effective for nanocrystalline HCP metals is also explained in the Section 2-3. Computational methods can be categorized in terms of the scales of length and time, as show in in Fig. 2-2. MD simulation operates at the appropriate length scale for nanocrystalline materials. The MD simulation method is discussed in Section 2-4. A number of deformation studies of increasing complexity are described in this dissertation.

### **2-1. Slip in HCP Metals**

The plane on which slip takes place is different in different HCP systems. However, the three dominant planes are the (0001) basal plane, the three  $\{10\bar{1}0\}$  prismatic planes and the six  $\{10\bar{1}0\}$  pyramidal planes, as shown in Fig. 2-3(a). In all cases, however, the slip direction is one of the three  $\langle 11\bar{2}0 \rangle$  or  $\langle \mathbf{a} \rangle$ , close-packed directions [16, 17]. While prismatic  $\langle \mathbf{a} \rangle$  and basal  $\langle \mathbf{a} \rangle$  slip is quite common, the activation of the pyramidal  $\langle \mathbf{a} \rangle$  slip system is less common. However it can take place in polycrystalline aggregates, and has been shown to occur primarily due to the large stresses generated in the grain-boundary regions arising from the incompatibility of textures between neighboring grains [16]. If atoms were ideal hard spheres, the  $c/a$  lattice parameter ratio of all HCP metals would be 1.633 [17]. The  $c/a$  ratio of Mg (1.623) is almost ideal, and slip in Mg takes place dominantly on the basal plane. The preference of an HCP metal for basal or prismatic slip depends on its  $c/a$  ratio and on the electronic structure associated with its d-electrons [18]. The primary slip mode is prismatic in Ti, Zr, and Hf, which all have 2 d-electrons; Co, which has 7 d-electrons, shows predominately basal slip [19].

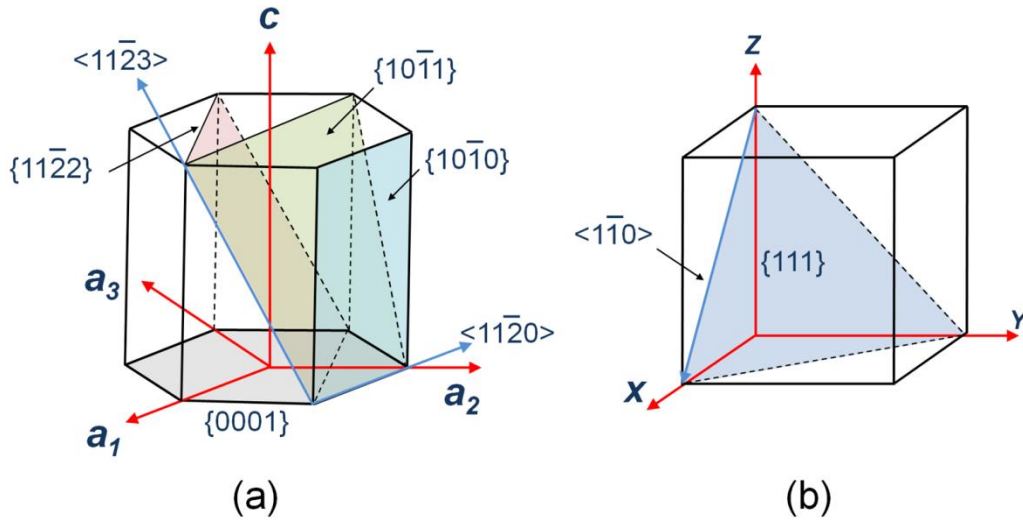


Figure 2-3. Slip planes and directions of (a) HCP [20] and (b) FCC [21]

The  $\langle 11\bar{2}0 \rangle$  slip directions on the basal plane, known to be activated most easily, are perpendicular to the  $\langle 0001 \rangle$   $c$ -axis. Such slip does not produce any elongation or contraction parallel to the  $c$ -axis [16]. This indicates that  $\langle a \rangle$  type dislocations alone cannot produce homogeneous plastic deformation. There are four independent glide systems: two basal ( $a_1$ ,  $a_2$ ) and two prismatic ( $a_1$ ,  $a_2$ ) components in Fig. 2-3 [20, 21]. The third basal component ( $a_3$ ), the third prismatic component ( $a_3$ ), and the pyramidal- $\langle a \rangle$  can all be constructed as linear combinations of the four independent glide systems. Given von Mises criterion that five independent slip systems are necessary for a polycrystalline material to undergo general homogeneous deformation, slip or twin systems with  $\langle c+a \rangle$  slip/twin directions must also be operative [20] for homogeneous deformation to take place. Nevertheless, particularly in pure Mg, because the prismatic  $\langle a \rangle$  type dislocations can generally only be activated at elevated temperature [22], fewer slip systems are typically operative during plastic deformation [20, 23].

This insufficiency in the range of dislocation processes for homogeneous plastic deformation is partially compensated by twinning [17, 19, 20, 23]. Twinning modes in HCP structures are particularly significant for plastic deformation and ductility at low temperatures if the stress axis is parallel to the c-axis and if the dislocations with basal-plane Burgers vectors cannot move [20]. As for the slip processes, the operative twinning systems are strongly correlated with the c/a ratio [18, 19].

As shown in Table. 2-1, the c/a ratios of Mg and Ti are quite different from each other and are on opposite ends of the range manifested by HCP metals.

Table 2-1. Physical properties of Mg [24, 25] and Ti[20, 26]. Add density and specific strength

Properties		Mg	Ti
Lattice constant	a	3.209	2.951
	c	5.210	4.679
	c/a	1.624	1.586
Melting point/K		923	1943
Bulk modulus/GPa		35.2	109.7
Shear modulus/GPa		16.5	42
	C <sub>11</sub>	63.5	176.1
Elastic constants	C <sub>12</sub>	26.0	86.9
	C <sub>13</sub>	21.7	68.3
	C <sub>33</sub>	66.5	190.5
	C <sub>44</sub>	18.4	50.8

## 2-2. Twinning in HCP Metals

Deformation twinning is classically defined as re-orientation of the original lattice by atom displacements corresponding to a simple shear of the lattice points. The invariant plane and direction of this shear is called  $K_1$  and  $\eta_1$ , respectively. Similarly, the second undistorted plane ( $K_2$ ) and its shear direction ( $\eta_2$ ) can be defined. The shear plane normal to  $K_1$  and  $K_2$  is denoted by P in Fig. 2-4.

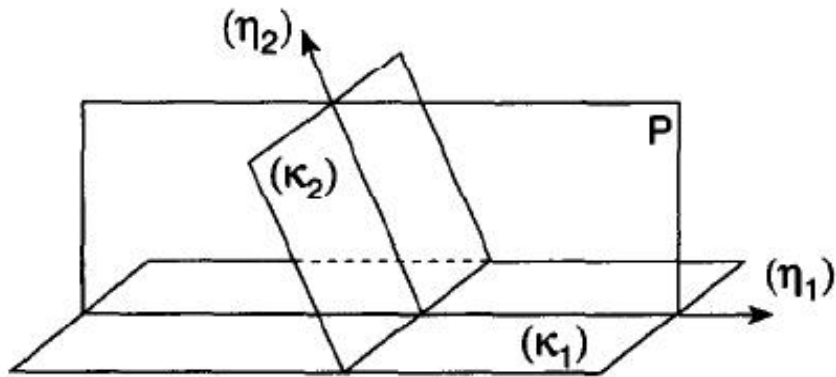


Figure 2-4. Schematics of original and twinned textures.  $\mathbf{K}_1$  and  $\mathbf{K}_2$  denote the planes of twinning and the conjugate (or reciprocal) twinning.  $\boldsymbol{\eta}_1$  and  $\boldsymbol{\eta}_2$  indicate the directions of twinning and conjugate twinning, respectively [27].

The reorientation of original lattice essentially results in stress by a lattice mismatch between the original and twinned textures. The lattice mismatch is normally defined by twinning shear. Figure 2-5 shows how the twinning shear appears at real twin modes. Twinning shear is the difference of  $\mathbf{K}_2$  before and after twinning. Calculated magnitudes of shear and the other twinning elements are shown in Table 2-2.

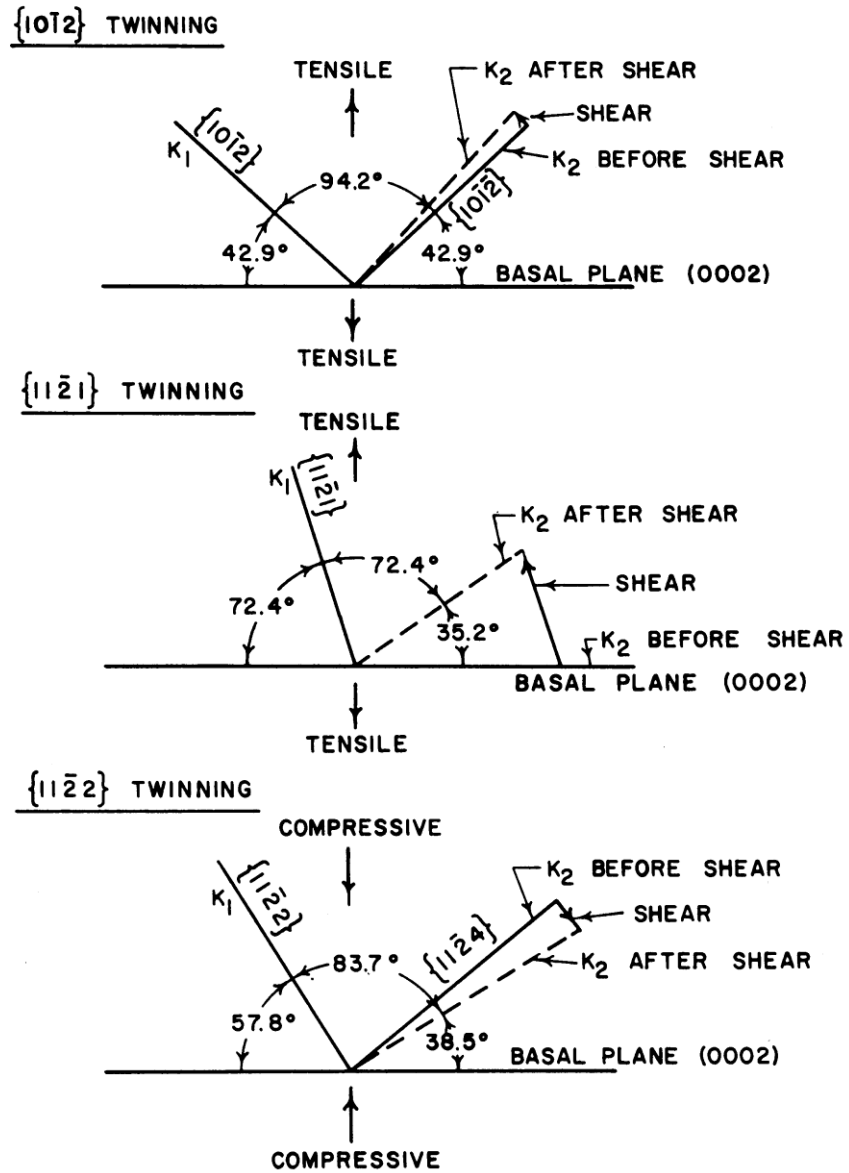


Figure 2-5. Twinning shears at three important twin modes of zirconium [28].

Table 2-2. Twinning planes, directions, and shears in pure zirconium [28].

Twinning or First undistorted plane, $K_1$	Twinning shear direction, $\eta_1$	Second undistorted plane, $K_2$	Twinning shear direction, $\eta_2$	Magnitude of shear
{10 $\bar{1}2$ }	$\langle 10\bar{1}1 \rangle$	{10 $\bar{1}2$ }	$\langle 10\bar{1}1 \rangle$	0.167
{11 $\bar{2}1$ }	$\langle 11\bar{2}6 \rangle$	(0002)	$\langle 11\bar{2}0 \rangle$	0.63
{11 $\bar{2}2$ }	$\langle 11\bar{2}3 \rangle$	{11 $\bar{2}4$ }	$\langle 2243 \rangle$	0.225
{11 $\bar{2}3$ }	-	-	-	-

Twinning shear mentioned above is for zirconium having  $c/a$  ratio of 1.598. Since each HCP metal has a different  $c/a$  ratio, the twinning shear depends on the  $c/a$  ratio. However, each twin shear can be described by the same mathematical expression by the  $c/a$  ratio ( $=\gamma$ ). For instance, the  $\{10\bar{1}2\}$  twin has common shear equation of  $s = (\gamma^2 - 3)/3^{0.5}\gamma$  in all HCP metals [27]. Yoo [29] has reported a relationship between the dominant shear mode and the  $c/a$  ratio of HCP metals, as shown in Fig. 2-5.

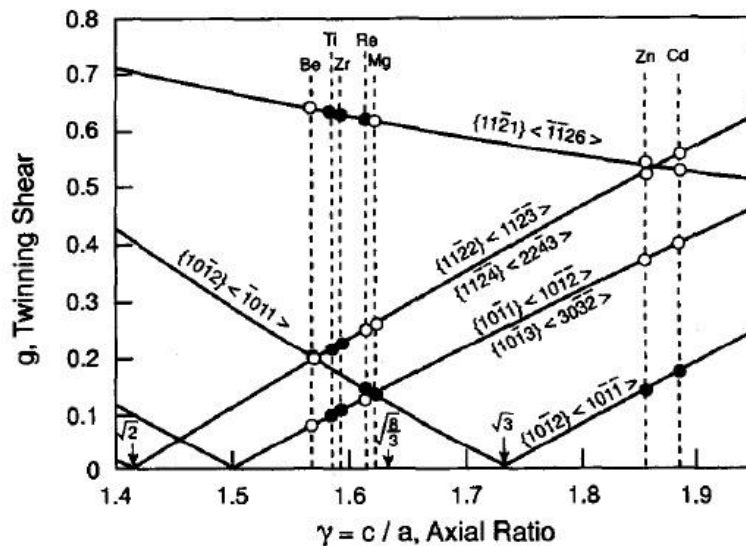


Figure 2-5. Twinning shears as a function of the  $c/a$  ratio in HCP metals. Filled circles indicate active twin modes.

There are two common twinning modes in Mg: the  $\{10\bar{1}2\} \langle 10\bar{1}1 \rangle$  tensile twin and the  $\{10\bar{1}1\} \langle 10\bar{1}2 \rangle$  compressive twin [19]. Figure 2-6 depicts the structure and loading conditions of the more common  $\{10\bar{1}2\} \langle 10\bar{1}1 \rangle$  tensile twinning [30], with the orientations of the crystals on the two sides of the twin differing by  $86.3^\circ$ . This twinning is favored by tensile stress along  $[0001]$  and compressive stress along  $\langle 11\bar{2}0 \rangle$  as shown in Fig. 2-6 (b). Fundamental slip and twinning properties of Mg and Ti are also compared in Table 2-3.

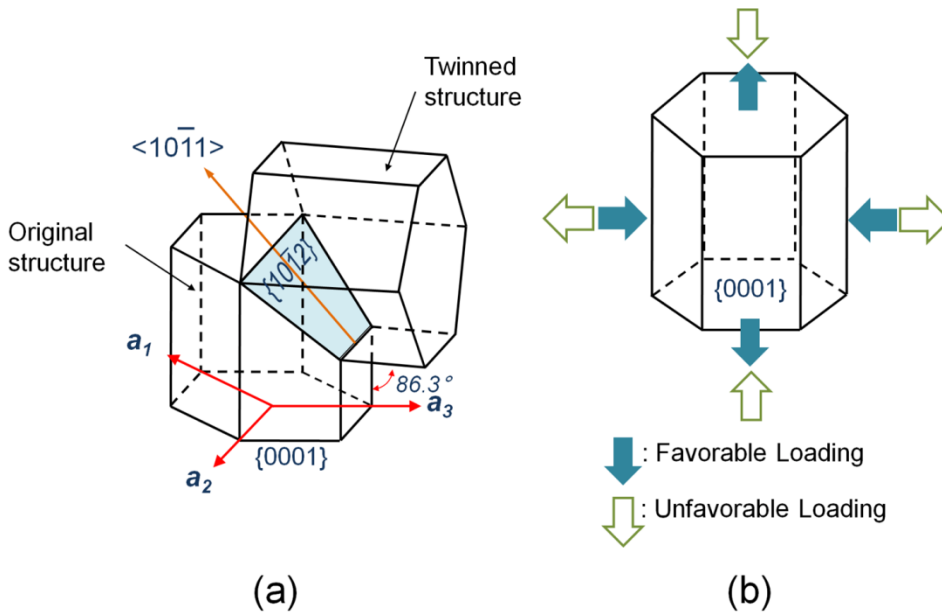


Figure 2-6. Schematics of  $\{10\bar{1}2\} \langle 10\bar{1}1 \rangle$  tensile twinning [30]: (a) The twinned structure has mirror symmetry at an angle of  $86.3^\circ$  in Mg; (b) applied loading in the favorable direction (solid arrow) can most easily cause the  $\{10\bar{1}2\} \langle 10\bar{1}1 \rangle$  tensile twinning.

Table 2-3. Slip and twinning modes in Mg and Ti [8, 20, 31]

Deformation modes		Mg	Ti
<a> slip	Predominant	Basal, $[0002]$	Prismatic, $\langle 10\bar{1}0 \rangle$
	Secondary	Prismatic, $\langle 10\bar{1}0 \rangle$	Basal, $[0002]$
<c+a> slip	Predominant	2 <sup>nd</sup> order, $1/3 \{10\bar{1}1\} \langle \bar{1}123 \rangle$	1 <sup>st</sup> order, $\{1\bar{1}22\} \langle \bar{1}123 \rangle$
	Secondary	1 <sup>st</sup> order, $\{1\bar{1}22\} \langle \bar{1}123 \rangle$	2 <sup>nd</sup> order, $1/3 \{10\bar{1}1\} \langle \bar{1}123 \rangle$
Twinning	Predominant	$\{10\bar{1}2\} \langle 10\bar{1}1 \rangle$	$\{1\bar{1}22\} \langle 112\bar{3} \rangle$ $\{10\bar{1}2\} \langle 10\bar{1}1 \rangle$
	Secondary	$\{10\bar{1}1\} \langle 10\bar{1}2 \rangle$ $\{10\bar{1}3\} \langle 30\bar{3}2 \rangle$	$\{1\bar{1}21\} \langle 112\bar{6} \rangle$ $\{10\bar{1}1\} \langle 10\bar{1}2 \rangle$ $\{10\bar{1}3\} \langle 30\bar{3}2 \rangle$

### 2-3. Nanocrystalline Metals and Molecular Dynamics Simulation

The mechanical response and the deformation processes of conventional coarse-grained polycrystalline metals, such as Fe, Ni, Al, Ti and Mg, have been elucidated in some detail [32, 33]. The study of ultrafine grained (250~1000nm) and nanocrystalline

(< 100nm) metals, which have been produced since the 1980s, has provided fundamental understanding of the physical and chemical phenomena associated with small length scales [34-37]. In comparison to conventional polycrystalline metals, nanocrystalline metals have more interesting properties, such as increased strength and hardness, reduced elastic moduli and ductility, and enhanced diffusivity [37].

Computational methods, in particular molecular dynamics (MD) simulation, have provided important insights into the structure and properties of nanocrystalline metals [38-50]. Dislocation processes [40, 49, 50] and grain boundary (GB) phenomena [41, 44-48] have been characterized in nano-grains of various FCC metals. In particular, the existence of twinning in nanocrystalline Al was identified by simulation [36, 38] before it was observed in experiment [51]. In addition, considerable attention has been paid to the question of the existence of a strongest grain size (maximum yield point) at the crossover from normal (dislocation process dominated) to inverse (grain-boundary process dominated) Hall-Petch behavior. [36, 37, 42, 43]. The typical Hall-Petch graph of ultra-fine and nanocrystalline metals and their alloys is shown in Fig. 2-7.

Previous MD studies have mainly focused on FCC metals such as Al [49, 50], Cu [42, 43], and Ni [41, 44]. Relatively little attention has been paid to nanocrystalline HCP metals such as Mg, Ti, Co and Zr despite their industrial importance. One MD study of 3D nanocrystalline HCP Co identified both an extended and a partial dislocation.[52] In addition, it was found that mechanical twinning seldom took place during deformation, even at high stress levels. This was somewhat surprising because twinning is known to be a significant deformation mechanism in coarse-grained HCP metals. These findings

indicate that plastic behavior of nanocrystalline HCP metals may be substantially different from nanocrystalline FCC metals or coarse-grained HCP metals.

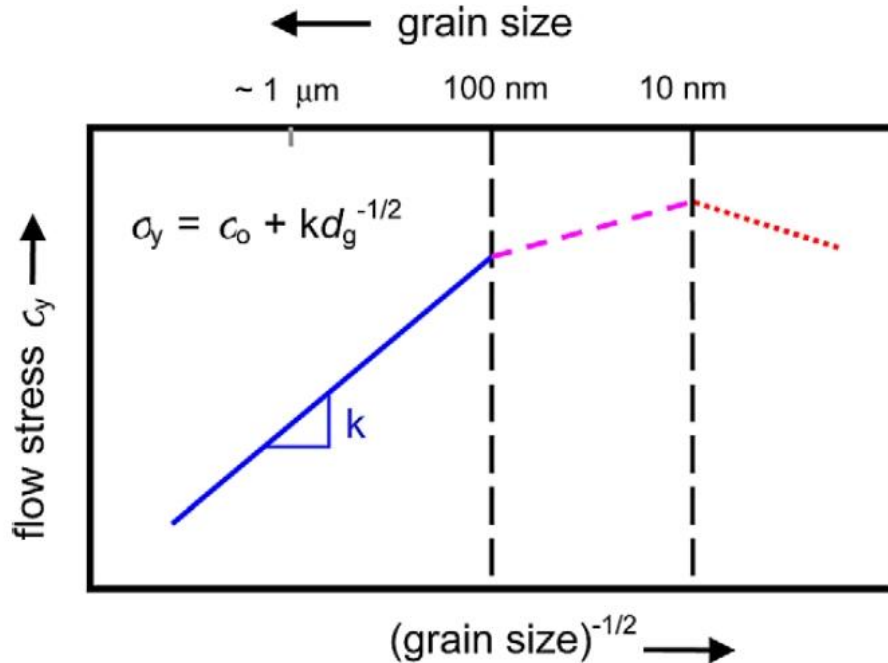


Figure 2-7. Schematic representation of the variation of flow stress as a function of grain size in metals and alloys [53]. The flow stress is adopted instead of yield stress in the Hall-Petch analysis.

#### 2-4. Molecular Dynamics Simulation

Molecular dynamics (MD) simulation [54] is a deterministic approach, in which the motion of atoms in a system is predicted by solving Newton's Equation of motion.

According to Newton's second law

$$\mathbf{F}_i = m_i \mathbf{a}_i \quad (2-1)$$

Where,  $\mathbf{F}_i$  is the force on an atom  $i$ ;  $m_i$  and  $\mathbf{a}_i$  are its mass and acceleration. The force on each atom can be expressed in terms of the gradient of the potential energy with respect to position.

$$\mathbf{F}_i = -\nabla_i V \quad (2-2)$$

Where,  $V$  is the potential energy. This is calculated through the interatomic potential that describes the interaction of the atoms in the simulation system.

### 2-4-1. Pressure Control

There are various algorithms developed to maintain an average pressure in the system. The Andersen scheme uses hydrostatic approach to maintain the pressure [54, 55]. This method allows the simulation system to expand or contract the same amount in each direction. For a more complex scheme, which can allow different expansions or contractions in different directions, Parrinello and Rahman [56, 57] extended the Andersen scheme to allow change in both shape and size of the simulation system.

Stress analysis can be simplified when the physical dimensions and the distribution of loads allow the structure to be treated as one- or two-dimensional. For a two-dimensional analysis, a plane stress or a plane strain condition is typically assumed [58]. A plain stress condition is said to exist when stress in the  $z$  direction is zero, but strain in the  $z$  direction is not zero. Also plain strain condition exists when the strain in  $z$  direction is zero. Properties of plane strain and stress models are explained in Table 2-4.

Table 2-4. Models of plane strain and stress for two dimensional system.

Plane Stress Models	Plane Strain Models
No loading or stresses normal to the plane $\sigma_z = 0, \tau_{xz} = 0, \tau_{yz} = 0$ $\epsilon_z \neq 0$	Strain occurs only in the $xy$ -plane $\epsilon_z = 0, \gamma_{xz} = \gamma_{yz} = 0$ $\sigma_z \neq 0$

### 2-4-2. Temperature Control

In order to maintain the temperature during simulation, thermostats can be implemented. Similar to the constant pressure scheme, the instantaneous temperature of the system is calculated during simulation.

$$\langle K \rangle = \left\langle \sum_{i=1}^N \frac{1}{2} m v_i^2 \right\rangle = \frac{1}{2} k_B N_{df} T \quad (2-3)$$

Where  $N$  is the total number of atoms in the system,  $m$  is the mass of each atom,  $v$  is the velocity,  $k_B$  is the Boltzmann's constant, and  $N_{df}$  is the number of internal degrees of freedom of the system. Therefore, the average instantaneous temperature  $\langle T_{ins} \rangle$  at any time can be expressed as

$$\langle T_{ins} \rangle = \frac{2}{k_B N_{df}} \left\langle \sum_{i=1}^N \frac{1}{2} m v_i^2 \right\rangle \quad (2-4)$$

The instantaneous temperature is compared with the target temperature ( $T_0$ ) to adjust the temperature. There are various constant temperature schemes available, including velocity rescaling and Berendsen [59], Langevin [60-62], and Nosé-Hoover [63, 64] methods.

The simplest approach to maintain the temperature is simple velocity rescaling. Since the temperature of the system is related to the velocity of each atom present in the system, the velocity of the atoms can be adjusted in order to control the system temperature. This is given by

$$v_{new} = v_{old} \sqrt{\frac{T_0}{\langle T_{ins} \rangle}} \quad (2-5)$$

Where  $v_{new}$  is the rescaled velocity and  $v_{old}$  is the velocity prior to rescaling. Most of the MD simulations discussed in this dissertation are performed with velocity rescaling to maintain the temperature of the system.

## 2-5. Interatomic Potentials

Interatomic potentials form the basis for all classical molecular dynamics (MD) simulations. They determine the forces that the atoms experience in a simulation, and it

is through them that material properties are specified. There are various potentials describing interactions between atoms with different mathematical expression. It is important that the expression strongly depends on property of interatomic bonding. Pure Al having metallic bonding is usually simulated with an EAM (Embedded-Atom Method) potential. However, if the Al forms ionic bonding with other element, the Al EAM potential cannot produce realistic results. Nowadays potentials for multifunctional materials are being developed, and used in many simulation fields. Figure 2-8 shows many of the most challenging and important applications of materials involve interfaces between disparate bonding environments [65]. In this study, EAM and MEAM (Modified Embedded-Atom Method) potentials effectively describing metallic bonding are chosen for mechanical properties simulation.

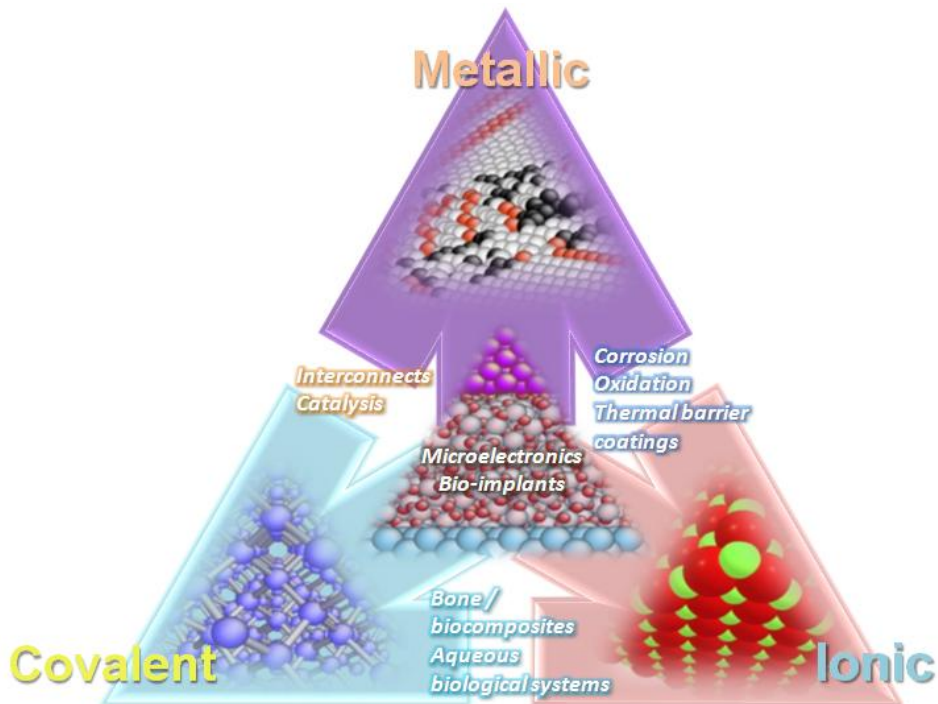


Figure 2-8. Schematic representation of three major atomic bonding types. For metallic, covalent, and ionic bonding, Mg EAM [24], Si COMB [66], and MgO Buckingham-type potential [67] with long range electrostatic interaction were used in this figure [65].

### 2-5-1. Embedded-Atom Method (EAM) Potential

The original Embedded-Atom Method (EAM) potential is an empirical, many-atom description of the total energy of a metallic system. The EAM potential has been extensively applied to various systems of interest and has proved to that compare well with experimental findings. The EAM potentials, first proposed by Daw and Baskes[68], has been applied to a wide range of properties of metals, including point defects, dislocations and surfaces. In the embedded atom formalism, the total energy of a system is expressed as

$$E_{tot} = \frac{1}{2} \sum_{i,j} \Phi(r_{ij}) + \sum_i F(n_i) \quad (2-6)$$

Here  $\Phi_{ij}$  is the pair-interaction energy between atoms  $i$  and  $j$  at positions  $r_i$  and  $r_j$ , and  $F_i$  is the embedding energy of atom  $i$ .  $n_i$  in Eq. 2-6 is the host electron density at site  $i$  induced by all other atoms in the system.

$$n_i = \sum_{j \neq i} \rho_j(r_{ij}) \quad (2-7)$$

$\rho_j(r_{ij})$  is the spherically-averaged atomic electron density of atom  $j$ .

### 2-5-2. Modified Embedded-Atom Method (MEAM) Potential

The Modified Embedded-Atom Method (MEAM) is an extension to the EAM [68]. The extension lies in the fact that angular forces and therefore the effects of directional bonding are included. The total potential energy ( $E_{tot}$ ) in MEAM potential has the same form as in the EAM potential. The essential difference between the EAM and the MEAM is in the way in which the electron density  $n_i$  is calculated, In MEAM it is written as:

$$n_i = n_i^{(0)} \frac{2}{1 + e^{-r_i}} \quad (2-8)$$

$$F_i = \sum_{k=1}^3 w^{(k)} \left( \frac{n_i^{(k)}}{n_i^{(0)}} \right)^2 \quad (2-9)$$

where the  $n_i^{(k)}$  are corrections to  $n_i$  that include angular dependence and the  $w^{(k)}$  are weighting factors. Although other forms for  $n_i$  have been proposed [69], the form shown in Eq. 2-8 and 9 is widely used due to its high accuracy. The  $n_i^{(k)}$  are written as:

$$n_i^{(0)} = \sum_{j(\neq i)} \rho^{(0)}(r_{ij}) \quad (2-10)$$

$$\left( n_i^{(1)} \right)^2 = \sum_{\mu} \left[ \sum_{j(\neq i)} \rho^{(1)}(r_{ij}) \frac{r_{ij\mu}}{r_{ij}} \right]^2 \quad (2-11)$$

$$\left( n_i^{(2)} \right)^2 = \sum_{\mu, \nu} \left[ \sum_{j(\neq i)} \rho^{(2)}(r_{ij}) \frac{r_{ij\mu} r_{ij\nu}}{r_{ij}^2} \right]^2 - \frac{1}{3} \left[ \sum_{j(\neq i)} \rho^{(2)}(r_{ij}) \right]^2 \quad (2-12)$$

$$\left( n_i^{(3)} \right)^2 = \sum_{\mu, \nu, \tau} \left[ \sum_{j(\neq i)} \rho^{(3)}(r_{ij}) \frac{r_{ij\mu} r_{ij\nu} r_{ij\tau}}{r_{ij}^3} \right]^2 - \frac{3}{5} \left[ \sum_{j(\neq i)} \rho^{(3)}(r_{ij}) \frac{r_{ij\mu}}{r_{ij}} \right]^2 \quad (2-13)$$

where  $\mu$ ,  $\nu$ , and  $\tau$  denote the components of the vector between atoms  $i$  and  $j$ . The  $n_i^{(0)}$  has spherical symmetry. Setting  $F_i$  to zero would retrieve the EAM expression for  $n_i$ , with  $\rho^{(0)}$  being the spherically averaged atomic electron density of Eq. 2-10.

The partial atomic electron densities are assumed to be given by a simple exponential form:

$$\rho^{(k)}(r) = \exp \left[ -\beta^{(k)} \left( \frac{r}{r_0} - 1 \right) \right] \quad (2-14)$$

where  $\beta^{(k)}$ ,  $k = 0 - 3$ , are parameters to be determined, and where  $r_0$  denotes the equilibrium nearest-neighbor separation in a reference structure.

The embedding function ( $F$ ) is given by

$$F(n) = AE_0 \frac{n}{N_0} \ln \left( \frac{n}{N_0} \right) \quad (2-15)$$

where  $A$  is a scaling parameter to be determined,  $E_0$  is the sublimation energy (the negative of the cohesive energy  $E_{\text{coh}}$ ), and  $N_0$  is the number of nearest neighbors in the reference structure ( $N_0 = 12$  for HCP metals).

Using Eq. 2-6 and 7, the equation for the energy per atom in the reference structure ( $E_u$ ) as proposed by Rose et al. [70],  $\phi$  can be written as:

$$\phi(r) = \frac{\Phi}{N_0} = \frac{2}{N_0} [E_u(r) - F(n_0(r))] \quad (2-16)$$

where  $n_0 = N_0 \rho^{(0)}$  denotes the effective coordination number of an atom.

The universal energy function [70] ( $E_u$ ) is given by:

$$E_u(r) = -E_0 [1 + a(r) + da(r)^3] e^{-a(r)} \quad (2-17)$$

with

$$a(r) = \alpha \left( \frac{r}{r_0} - 1 \right) \quad (2-18)$$

where  $d$  is an adjustable parameter.

The exponential decay factor ( $\alpha$ ) is related to the bulk modulus and the atomic volume by:

$$\alpha = \sqrt{9B\Omega/E_0} \quad (2-19)$$

Now we can write the energy per atom for any configuration of single type atoms at  $r = r_0$  as

$$E_i = -\frac{N}{N_0} E_0 + F(n_i(r_0)) \quad (2-20)$$

where  $N$  denotes the number of nearest-neighbors for a specific configuration.

## 2-6. Computational Details

In this section, a methodology for MD simulations of nc-HCP metals is presented. 2D and 3D structures of nc-metals are prepared in Section 2-6-1. For the 2D columnar textures, the specific crystallographic direction is chosen so as to activate the dominant slip and twinning in a given HCP metal. Two different tests (creep and tensile tests) are carried out in Section 2-6-2. Analysis methods of strained samples are also discussed in Section 3-3.

### 2-6-1. Generation of Structure

A 2D textured structure is prepared for the simulation of the mechanical properties of nanocrystalline HCP metals. Since nanocrystalline metals can be easily grown using thin film processes, the columnar structure has been a popular choice for basic experimental studies and comparisons to simulation results [37, 71, 72]. Compared to a 3D structure with a random orientation in each grain, a columnar structure allows the simulation of a larger grain size for the same number of atoms. It also makes visualization of deformation processes easier. The simulated polycrystalline structure contains four grains and has a columnar texture. Thus, each grain in the structure has the same crystallographic orientation along the z-axis and the grains are separated from each other by tilt grain boundaries. As noted in previous studies of FCC metals [73], it is necessary to carefully select the crystallographic orientation of the columnar structure so as to allow dislocation processes. In addition, for plastic deformation of HCP metals, twinning has to be taken into account in determining the optimal crystallographic orientation. In the simulation cell shown in Fig. 2-9, the  $[1\bar{1}20]$ -directions is normal to the

texture direction (the z-axis), thus promoting both basal slip parallel to the x-y plane and allowing  $\{10\bar{1}2\} \langle 10\bar{1}1 \rangle$  twinning (see Fig. 2-3).

The HCP structure has two-fold rotational symmetry about the  $[1\bar{1}20]$  tilt axis; thus it would be natural to choose misorientation angles of  $0^\circ$ ,  $30^\circ$ ,  $60^\circ$ , and  $90^\circ$ , as in the work for  $[011]$  Al [38, 49, 50, 73]. However to avoid twinning in the original structure at an angle of  $86.3^\circ$ , misorientation angles of  $11.25^\circ$ ,  $33.75^\circ$ ,  $56.25^\circ$ , and  $78.75^\circ$  were used, as illustrated in Fig. 2-3. Each grain has the  $[1\bar{1}20]$  direction as the z-axis in Fig. 2-9. To compare deformation properties to the  $[1\bar{1}20]$  texture, the  $[10\bar{1}0]$  texture is also tested.

The resulting boundaries are high-angle tilt GBs, with highly disordered atomic structures. The thickness of the simulation cell in the z direction (parallel to the texture) is  $\sim 5.0a_0$  ( $a_0 = 0.3206$  nm), determined by the cutoff radius of the interatomic potential used for the simulations[24]. For a tensile load along the x-direction in Fig. 2-9, two of the three  $1/3[1\bar{1}20]$  slip directions (**a1** and **a3**) on the basal plane can be activated; the third slip plane, (**a2**) lies normal to the load axis. The x-y dimensions range from  $13 \times 11$  nm (for  $d = 6$  nm, giving a total of 9,595 atoms) up to  $112 \times 97$  nm (for  $d = 60$  nm, and a total of 743,705 atoms). The Schmid factors for basal  $\langle \mathbf{a} \rangle$  slip for grains 1, 2, 3, and 4 are 0.46, 0.19, 0.19 and 0.46, respectively

The plasticity behaviors obtained from 2D textures are investigated in fully dense 3D structures. As seen in Fig. 2-10, cube-type simulation cells containing 16 randomly oriented Voronoi grains. The grain size varies from 6 to 36 nm. The largest number of atoms, for a grain size of 36nm, is 16.1 million.

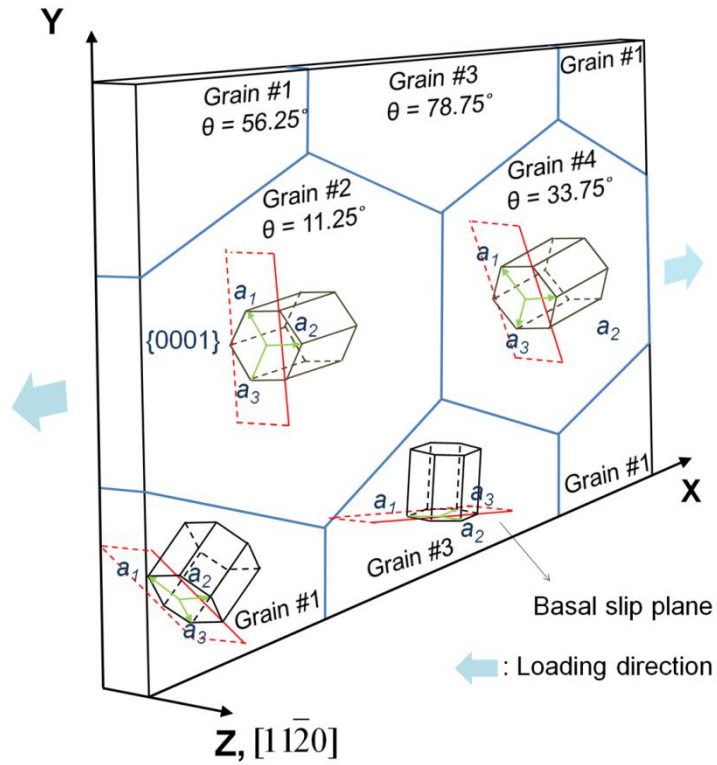


Figure 2-9. Schematic of 3d-periodic simulation cell with four hexagonal grains. In each grain, the angle  $\theta$  is measured between the c-axis of HCP unit cell and the x-axis of the simulation cell.

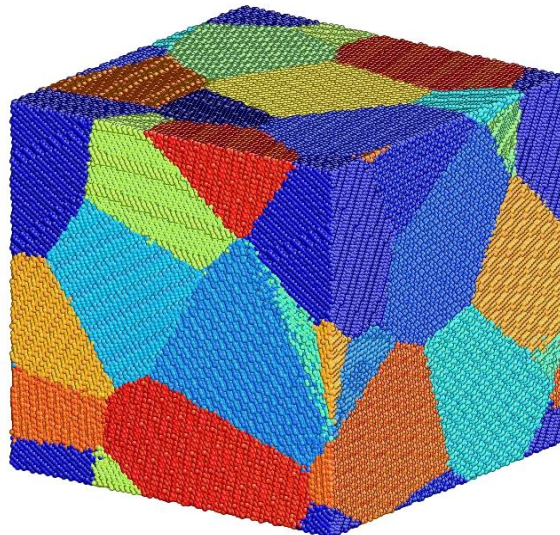


Figure 2-10. Schematic of 3D fully dense structure of nc-HCP metals. Each color indicates a different grain.

Due to their anisotropy, the interatomic interactions in HCP metals are typically described by a modified embedded atom method (MEAM) potential [74, 75]. However, because the anisotropy in Mg is weak (the  $c/a$  ratio is close to ideal), it is possible to apply the simpler EAM formalism [24]. The Mg potential used here [24] has been employed in simulations of mechanical behavior (e.g., twinning [76] and dislocation [77] processes) and crystal-melting [78] for both single component systems and alloys. The stacking-fault energy (SFEs), as determined for this potential, of the intrinsic I1- (ABABACAC) and intrinsic I2- (ABABCACA) type SFs are 27 and 54mJ/m<sup>2</sup>, respectively. The latter is consistent with experimental values for the I2-type stacking-fault energy (SFE), variously reported as <50 [79], 60 [80] and 78mJ/m<sup>2</sup> [81]. Due to its high anisotropy, a MEAM potential is chosen to describe Ti instead of an EAM potential. In the present study three different MEAM potentials are examined for mechanical simulation of nc-Ti metals [26, 75, 82-85].

Nanocrystalline structures were constructed in a manner similar to that previously used for FCC structures [73, 86]. In particular, after removing the small number of atoms at the GBs that have unphysically high energies, the structures were successively annealed at high, low and room temperatures. Such high-temperature (400K) annealing enabled a significant amount of atomic rearrangement and diffusion at the GB; the low temperature (200K) and room-temperature (293K) anneals equilibrated the structure for the room-temperature deformation simulations.

## 2-6-2. Simulation of Mechanical Test

Mechanical simulations were conducted at 293K and with 3d-periodic boundary conditions applied to the simulation cell. The time step was  $\Delta t \approx 0.4\text{fs}$ . Both creep tests and tensile tests were performed.

For a creep test a uniaxial tensile load was applied along the x-direction with magnitudes ranging from 0.6 to 1.8 GPa for Mg and from 2.0 to 3.5 GPa for Ti. Such creep tests allow the determination of the correlation between deformation mechanisms (GB process, dislocation, and twinning) and the magnitude of the applied stress [50, 73]. The activation of specific dislocations at specific values of applied stress can also be determined from creep tests. Plasticity of nc-metals is also examined by tensile test at strain rate of  $1.5 \times 10^9 \text{ s}^{-1}$ . Flow stress obtained by the tensile test shows Hall-Petch behaviors between grain size and strength [42, 43].

As previously seen in Fig. 2-2, MD simulations addresses atomistic phenomena at scale of the short time ( $\sim \text{nsec}$ ), considering maximum physical time of one MD step and normal total MD time of less than a few months. Such a short time scale requires a high strain rate ( $> 10^7 \text{ s}^{-1}$ ) [36]. In nc-materials simulated with a strain rate range of  $1 \times 10^7 \sim 1 \times 10^{10} \text{ s}^{-1}$ , their deformation processes have been consistent with experiments [49, 51]. Schiøtz [87] suggested the speed of sound (4940 m/s for Mg, 5090 m/s for Ti) is considered for a maximum strain rate. The ends of simulation structure have to move below the speed of sound. For example, if a sample with length of 70 nm is strained with a strain rate of  $1 \times 10^9 \text{ s}^{-1}$ , the strain speed is 70 m/s. Strain rates are controlled to be  $1 \times 10^7 \sim 1.5 \times 10^9 \text{ s}^{-1}$  in both creep and tensile tests of this work.

### 2-6-3. Analysis Method

For the visualization of defects, strained structures are rapidly cooled down to 0.01K to minimize thermal energy, followed by common neighbor analysis (CNA) [88, 89]. The common neighboring analysis (CNA) [88, 89] was used to distinguish atoms in (f.c.c. like) stacking faults from h.c.p. coordinated atoms.

The 'AtomEye' software package was used for visualization of the MD results [90]. Images of coordination number (CN), potential energy (PE), common neighboring analysis (CNA), and shear strain are displayed using the AtomEye in this dissertation.

### 2-7. Summary

For MD simulations of nc-HCP metals, the fundamental background was reviewed in this chapter. Slip and twinning of HCP metals are influenced by the  $c/a$  ratio, known as the anisotropy. The  $c/a$  ratios of Mg and Ti are 1.624 and 1.586. The dominant slip modes of Mg and Ti are basal and prismatic  $\langle a \rangle$ , respectively. The most common twin modes in both Ti and Mg is  $\{10\bar{1}2\} \langle 10\bar{1}1 \rangle$ . Computational methods, in particular molecular dynamics (MD) simulation, have provided important insights into the structure and properties of nanocrystalline metals. In this study, EAM and MEAM (Modified Embedded-Atom Method) potentials effectively describing metallic bonding are chosen for mechanical simulation. The  $[1\bar{1}20]$ - and  $[10\bar{1}0]$  textures as well as fully dense 3D structures are chosen for the mechanical properties simulations. Both creep and tensile tests are carried out, and strain rates are controlled to be  $1 \times 10^7 \sim 1.5 \times 10^9 \text{ s}^{-1}$  in this work.

## CHAPTER 3 OVERALL MECHANICAL RESPONSE OF TEXTURED NANOCRYSTALLINE MG

MD simulation of nc-metals is first carried out using 2D textured microstructures. The response of nc-Mg to external stress is investigated, followed by analysis of individual defects in the strained structures in Section 3-1 and 2. The microstructure evolution and interaction between slip and twinning are also analyzed in this chapter.

This chapter focuses on verifying that results from MD simulation of this work are consistent with those of experiments. The stress response of nc-Mg is also compared to that of nc-FCC metals. Slip and twinning in coarse-grained Mg are referred to understand defect process in the deformed Mg samples. Twinning and  $\langle c+a \rangle$  slip, typical and important deformation processes in HCP metals, will be analyzed in detail later.

### **3-1. Stress-Dependence of Mechanical Response**

A creep test of coarse grained material is conventionally carried out at elevated temperatures. Nanocrystalline metals can, however, exhibit similar creep behavior at room temperature and low external stress because of the enhanced contribution of GB-mediated processes [73]. The time evolution of the mechanical responses of  $[1\bar{1}20]$ -textured nanocrystalline Mg structures of various grain sizes were determined under a range of tensile stress at 293K. Figure 3-1 shows strain vs. time curves for an 18nm grain size for stresses ranging from 0.9 to 1.2GPa. As will be discussed below, GB-mediated processes such as grain boundary diffusion and sliding were dominant in plastic deformation below 0.9GPa, for which the strain rate was  $\sim 1.0 \times 10^7 \text{ s}^{-1}$  (slope A). An increase in strain rate is observed at 1.0GPa by an initiation of slip process as denoted as 'S' in Fig.3-1. These large plastic strains for stresses in excess of 1.0GPa

arose from slip and twinning. Consequently, 1.0GPa is considered to be the flow stress ( $\sigma_f$ ) for this particular system and grain size. With increasing applied stress, the strain rates (slopes B-D) increased gradually and slip process are initiated at shorter and shorter times.

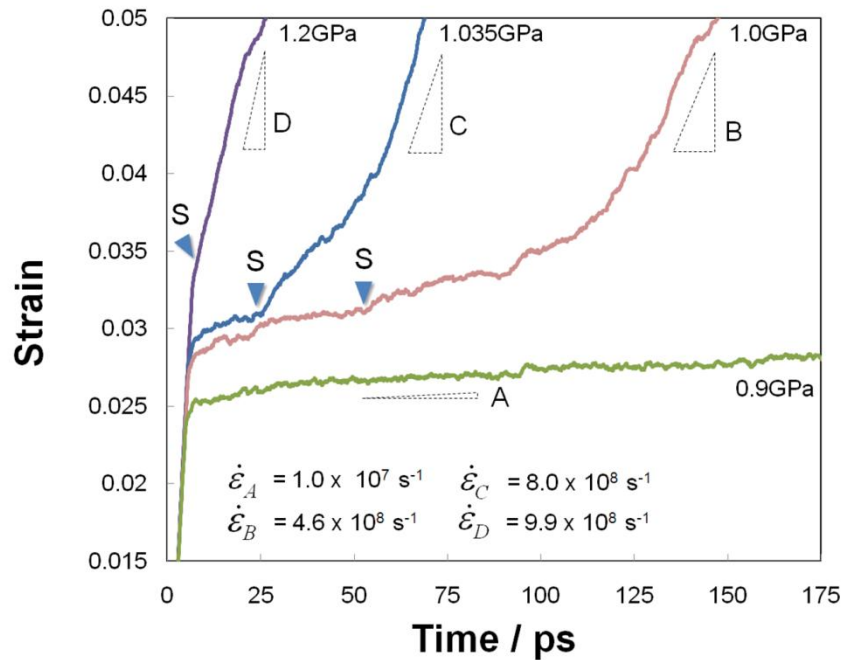


Figure 3-1. Strain vs. time plots for nanocrystalline structures with 18nm grain size at various external stresses. A to D, and the associated triangles, denote increasing strain rates (A: steady state creep by GB process, and B-D: tertiary creep by twinning and slip process). S indicates the initiation point of slip.

### 3-2. Signatures of Dislocations and Twins

Before turning to a detailed analysis of the sequence of plastic deformation processes, it is useful to identify the characteristic signatures of the various kinds of defects that are observed in the simulated mechanical tests. Figure 3-2 displays a number of dislocations and stacking faults that have been produced in a particular deformation simulation. To generate this image the atomic positions at a single instant

of time during an MD system were recorded. The strained structure was then quenched to 0.1K. Atoms with non-twelve fold coordination (i.e., neither HCP nor FCC) were identified and are shown in black in Fig. 3-2. Common neighboring analysis (CNA) [88, 89] was performed to distinguish FCC from HCP environments: FCC atoms are shown in brown, HCP atoms are shown in grey.

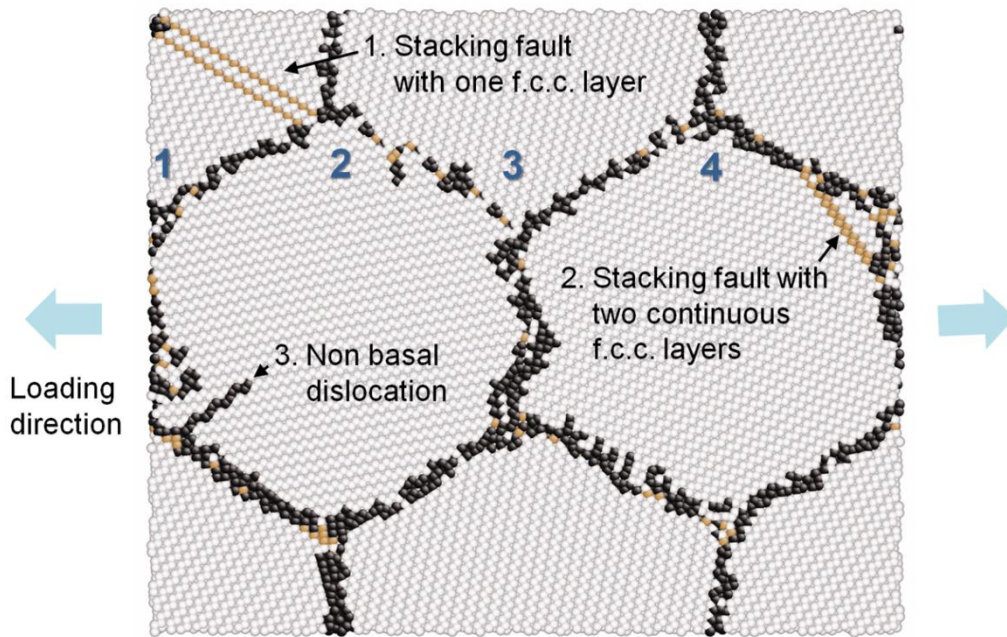


Figure 3-2. Snapshot of 3.5% strained structure with grain size of 18nm. Here, and in subsequent figures, gray, black and brown denote normal (HCP), disordered (non- HCP or FCC), and stacking fault (FCC), respectively. The grains are labeled 1, 2, 3, and 4.

Figure 3-3 (a) shows that the single brown lines (labeled 1 in Fig. 3-2) are intrinsic I1-type SF (ABABACACA) stacking faults, while Fig. 4-3(b) shows that the double brown lines (labeled 2 in Fig. 3-2) are intrinsic I2-type SFs (ABABCACA). (All dislocations and stacking faults are characterized in the conventional manner with a right-handed Burgers circuits in Fig. 3-3 [21].) The two single SF lines in Fig. 3-3(a)

propagate with their cores connected, essentially acting as a single dislocation. The two SFs are formed by  $\langle \mathbf{a} \rangle$  partial slip of  $1/3[\bar{1}100]$  or  $2/3[\bar{1}100]$ ,  $A\alpha$  or  $D\alpha$  on the basal plane, as shown in Fig. 3-3(d). The  $\langle \mathbf{a} \rangle$  partial edge dislocations given in Figs. 3-3(a) and (b) have a direction and magnitude of  $2/3[\bar{1}100]$ . The non-basal dislocation (labeled 3) in Fig. 3-2 is a  $\langle \mathbf{c}+\mathbf{a} \rangle$  partial edge dislocation, whose Burgers circuit is  $1/6[\bar{2}023]$  with a slip vector of  $BA_0$ , see Fig. 3-3(d). In contrast with  $\langle \mathbf{a} \rangle$  partial slip, no SF is produced by the  $\langle \mathbf{c}+\mathbf{a} \rangle$  partial dislocation of  $1/6[\bar{2}203]$ ; instead, just an extra half plane of atoms is produced - the layer of red 'A' in Fig. 3-3(c). All of the dislocations are edge type. Thus the dislocation lines are parallel to the z-axis of  $[1\bar{1}20]$ .

In addition to the partial dislocations,  $\langle \mathbf{a} \rangle$  and  $\langle \mathbf{c}+\mathbf{a} \rangle$  extended dislocations are also observed. A snapshot and a schematic of the atomic structure of the extended  $\langle \mathbf{a} \rangle$  dislocation are shown in Figs. 3-4(a) and (b), taken from the same simulation. Layers A, B and C at or near the extended  $\langle \mathbf{a} \rangle$  dislocation are parallel to basal plane in Fig. 3-4(a). The C layer has slipped in a manner similar to the basal  $\langle \mathbf{a} \rangle$  partial dislocation under the shear, thereby forming the extended  $\langle \mathbf{a} \rangle$  dislocation. Consistent with previous studies [21, 91], it can be seen from Fig. 3-4(b) that the extended  $\langle \mathbf{a} \rangle$  dislocation consists of two partial dislocations,  $1/3[\bar{1}100]$  and  $1/3[10\bar{1}0]$  joined by a stacking fault. As previously noted, dislocation lines are normally parallel to  $[1\bar{1}20]$  (z-direction). The  $1/3[\bar{1}100]$  partial slip is at an angle of  $90^\circ$  to the dislocation line, and is thus pure-edge type. By contrast, the  $1/3[10\bar{1}0]$  partial lies at an angle of  $60^\circ$  to the dislocation line. In Fig. 3-3(d), the two partial dislocations of  $1/3[\bar{1}100]$  and  $1/3[10\bar{1}0]$ ,  $A\alpha$  and  $\alpha B$ , can be expressed as a complete  $1/3[2\bar{1}10]$  dislocation, AB.

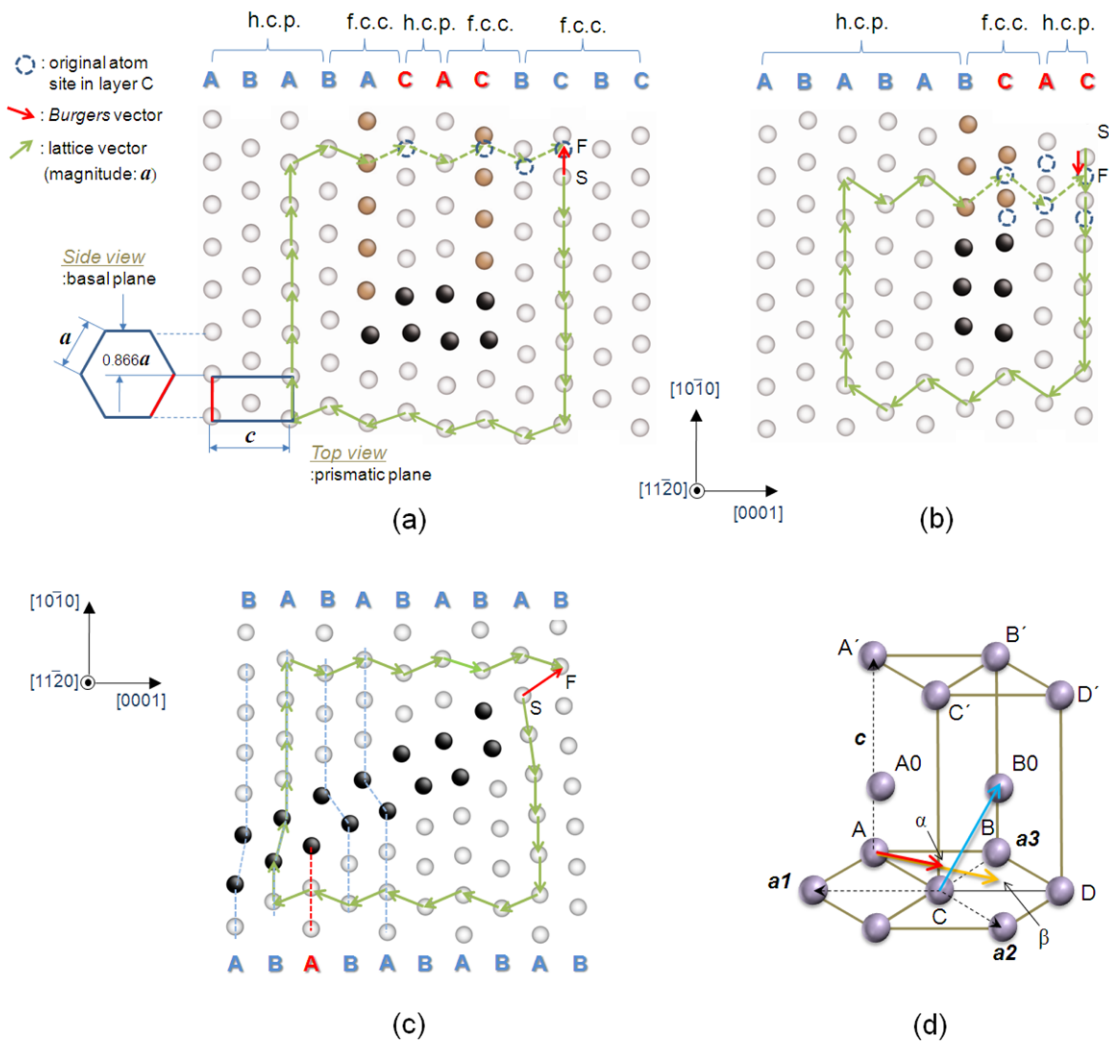


Figure 3-3. Burgers vectors and circuits of SF/RH type for the dislocations and stacking faults (SF) found in Fig.3-2: (a) I1-type SF with  $\langle a \rangle$  partial dislocation of  $2/3 [1100]$ , (b) I2-type SF with  $\langle a \rangle$  partial dislocation of  $2/3 [1100]$ , (c)  $\langle c+a \rangle$  partial dislocation of  $1/6 [2\bar{2}03]$ , and (d) Burgers vectors in HCP unit cell:  $A\alpha$ ,  $D\alpha$ , and  $BA_0$  are  $1/3 [1100]$ ,  $2/3 [1100]$ , and  $1/6 [2023]$  partial dislocations, respectively [21].

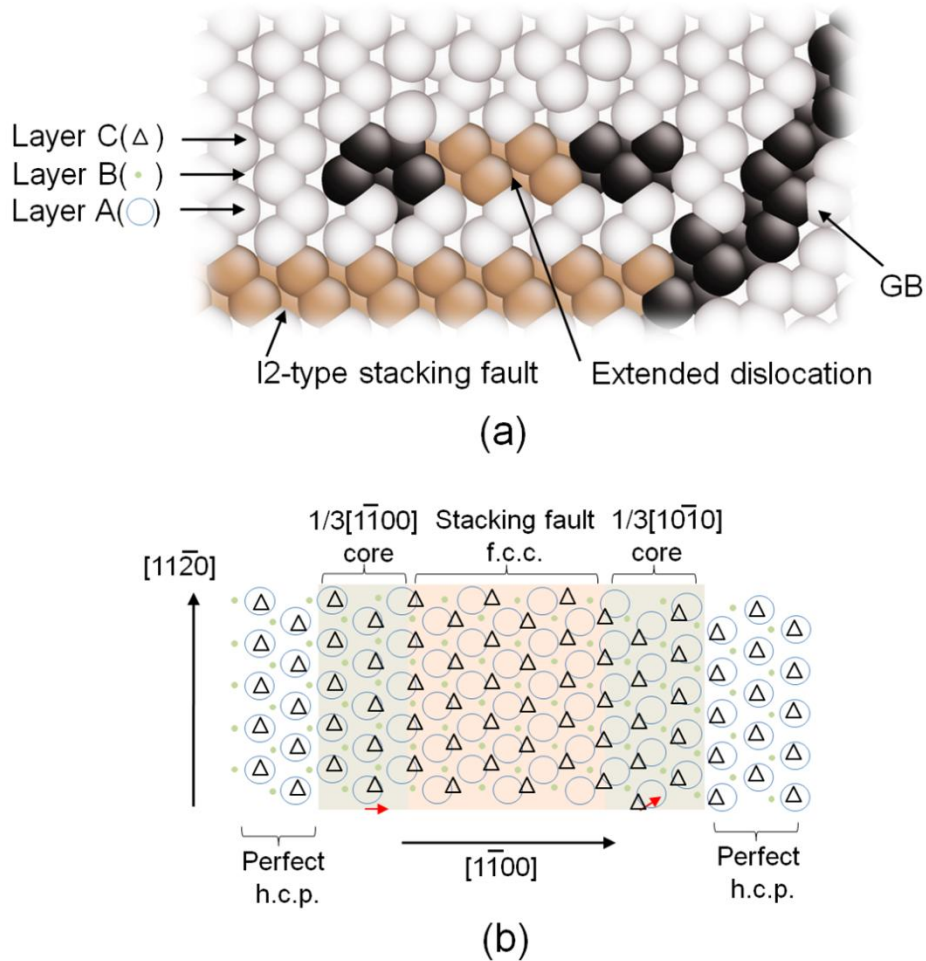


Figure 3-4. Snapshot and schematic of an atomic structure for the extended  $\langle \mathbf{a} \rangle$  dislocation, as observed for grain size of 40nm under 1.3GPa. (a) Atomic arrangement on  $(1\bar{1}\bar{2}0)$ . (b) Three pertinent atomic layers (A: circle, B: dot, and C: triangle) in (a) on  $(0001)$ . The extended  $\langle \mathbf{a} \rangle$  dislocation with two partial cores,  $1/3[\bar{1}\bar{1}00]$  and  $1/3[10\bar{1}0]$ , moves from right to left. The dislocation lines are parallel to  $[1\bar{1}\bar{2}0]$  (z-direction), red arrows indicates the slip vector of each partial dislocation.

In some simulations  $\langle \mathbf{c}+\mathbf{a} \rangle$  extended dislocations were produced. They sometimes developed from the  $1/6[\bar{2}\bar{2}03]$  partial dislocation, previously seen in Fig. 3-3(c), showing a complete pyramidal  $1/3[\bar{1}\bar{1}23]$  dislocation. It is known from a previous

MD study of HCP metals that the pyramidal dislocation of  $1/3[\bar{1}\bar{1}23]$  can be split into two [92, 93] or three [94] partials.

### 3-3. Microstructure Evolution

In this section, the nucleation and development of slip and twinning are characterized. As noted in Fig. 3-1, an accelerated deformation process for the  $[11\bar{2}0]$ -textured structure with grain size of 18nm was found at 1.0GPa; thus, to observe all of the salient deformation processes, a sample was strained at 1.18GPa. Figure 3-5 illustrates the evolution of the defects, with HCP coordinated atoms not being shown; twinned regions are solid color. The  $\{10\bar{1}2\} < 10\bar{1}1 >$  twins, indicated as 'A' in Fig. 3-5(a), are nucleated at grain boundaries. In particular, the twinning is initiated at the right side of grain 2, growing continuously with time in Figs. 3-5(b) and (c). This is consistent with the experimental observation that the  $\{10\bar{1}2\} < 10\bar{1}1 >$  twins typically appear in the early stage of deformation [95]. Grain 2 displays much more twinning activity than the other grains because its crystallographic orientation is comparatively close to the favored stress direction for twinning (parallel to c-axis, see Figs. 2-6 and 2-9): the angle between them being only  $11^\circ$ . In Fig. 4-5(d), compressive twins,  $\{10\bar{1}1\} < 10\bar{1}2 >$  and  $\{10\bar{1}3\} < 30\bar{3}2 >$ , are found, having sizes of a few nanometers.

In contrast to small elastic strains ( $\sim 0.2\%$ ) of coarse-grained metals, the elastic strain in MD is typically large (2~3 % of total strain) due to the high strain rate, small grain size, and the absence of pre-existing dislocations. If an elastic strain of 3% is excluded from the total strain of 10% shown in Fig. 3-5(d), then the purely plastic strain at saturation of twinning process is about 6%, consistent with earlier simulation [96] and experimental [97, 98] results that twinning occurs dominantly for 6 ~ 8% strain for Mg and its alloys.

Normalized twinned areas, obtained by dividing total number of atoms by numbers of twinned atoms in each grain, are shown as a function of strain in Fig. 3-6. The  $\{10\bar{1}2\} <10\bar{1}1 >$ -twinned area in grain 2 of Fig. 3-6 increases monotonically from initial step of plastic deformation. This is a typical process of tensile twin nucleated from GB in this simulation. The total twinned area decreases slightly from 6% plastic deformation after saturation. This implies that twins have a limited role in the whole deformation process because they have a mechanism of growing, not gliding.

Analyzing the situation from the point of view of a basal slip process, the  $<a>$  partial dislocations in grains 2 and 4 of Fig. 3-5(b) were mostly activated from twinned sites. This is consistent with experimental reports that the dislocation emission relieves the long-range stress field from an incoherent tip of an advancing twin [21]. The  $<a>$  partial slip is also observed inside the twinned region. With twinning progressing in grain 2, the  $<a>$  partial slip produced by the growth of the twin is an I1-type stacking fault having no dislocation core. It has been experimentally noted that dislocations in twinned regions can aid the propagation of twinning in HCP metals due to a local deformation of twin boundary by slip [99-102]. This is also agreed with the present simulation results. Grain 2, after being completely twinned, can support  $<a>$  slip processes more easily due to a change of crystallographic orientation from low Schmid factor (0.19) to a higher Schmid factor (0.26). Indeed, after the twinning process is completed,  $<a>$  partial slip cores are found to be ubiquitous in the twinned region of Fig. 3-5(d). In addition to the initiation of intra-grain slip process after twinning, the density of dislocations increased substantially in grains 1 and 4, which both have Schmid factor of 0.46 for basal  $<a>$  partial slip, Fig. 3-5(d). I1-type SFs also begin to be formed in grain 4 out of a twinned

area by interaction between  $\langle \mathbf{a} \rangle$  partial slips. Thus, activation of  $\langle \mathbf{a} \rangle$  slip process in our simulation structures is promoted at both twinned and neighboring grains for plastic strains greater than 5~7%. The majority of  $\langle \mathbf{a} \rangle$  dislocations are partial at early and middle stage of deformation; very few extended  $\langle \mathbf{a} \rangle$  dislocations were observed in Fig. 3-5(d).

A pyramidal  $\langle \mathbf{c}+\mathbf{a} \rangle$  partial dislocation of  $1/6 [\bar{2}023]$ , noted as 'C' in grain 4 of Fig. 3-5(a), was formed from the GB and has a length of a few nanometers; however, it did not propagate through the grain. Given its high Schmid factor, 0.46, basal  $\langle \mathbf{a} \rangle$  partial dislocations should be able to propagate through grain 4. Considering Mg or its alloys, the pyramidal  $\langle \mathbf{c}+\mathbf{a} \rangle$  partial slip process, having a high critical resolved shear stress (CRSS) value in the grain 4, is thus limited by activation of a basal  $\langle \mathbf{a} \rangle$  partial slip having a low CRSS value [17, 96]. As previously seen in Fig. 3-2, the  $\langle \mathbf{c}+\mathbf{a} \rangle$  dislocation in grain 2 does propagate. The suppression of the basal  $\langle \mathbf{a} \rangle$  partial slip in grain 2 allows the pyramidal  $\langle \mathbf{c}+\mathbf{a} \rangle$  partial be activated.

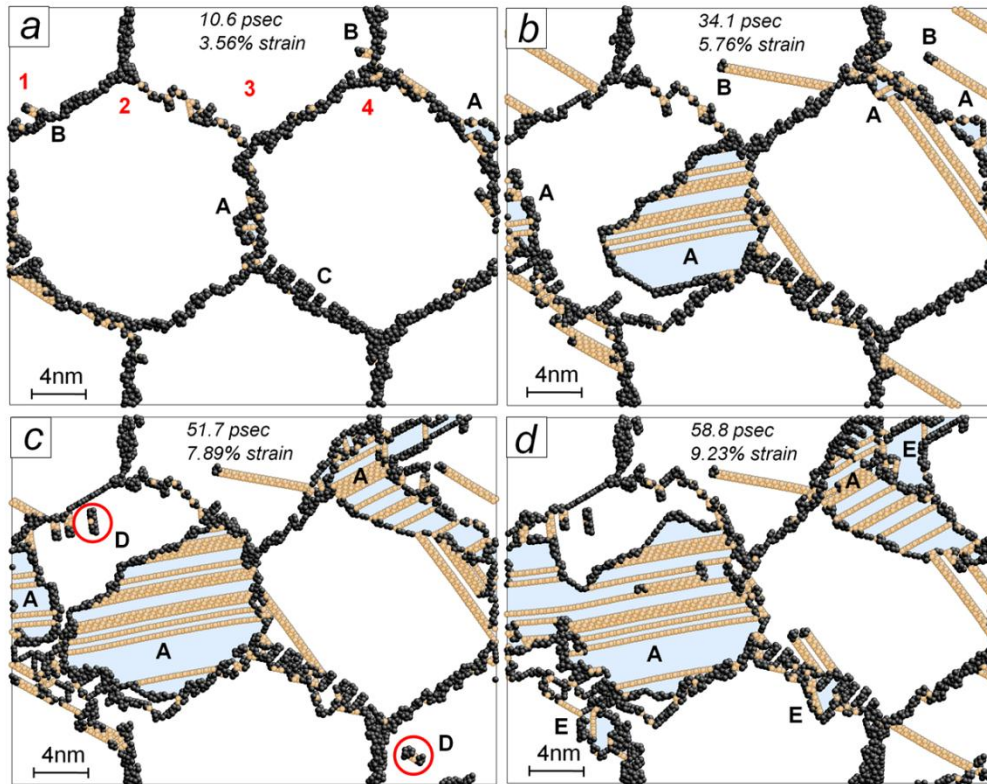


Figure 3-5. Snapshots of tensile test for 18nm  $[11\bar{2}0]$ -textured structure at 1.18 GPa for four times and strains, increasing from 9(a) to (d). Note microstructural figures: A -  $\{10\bar{1}2\} \langle 10\bar{1}1 \rangle$  tensile twin; B - basal  $\langle a \rangle$  partial dislocations of  $1/3[\bar{1}100]$  or  $2/3[\bar{1}100]$ ; C - pyramidal  $\langle c+a \rangle$  partial dislocations of  $1/6[\bar{2}023]$ ; D - the extended dislocation with basal slip; and E:  $\{10\bar{1}1\} \langle 10\bar{1}2 \rangle$  and  $\{10\bar{1}3\} \langle 30\bar{3}2 \rangle$  compressive.

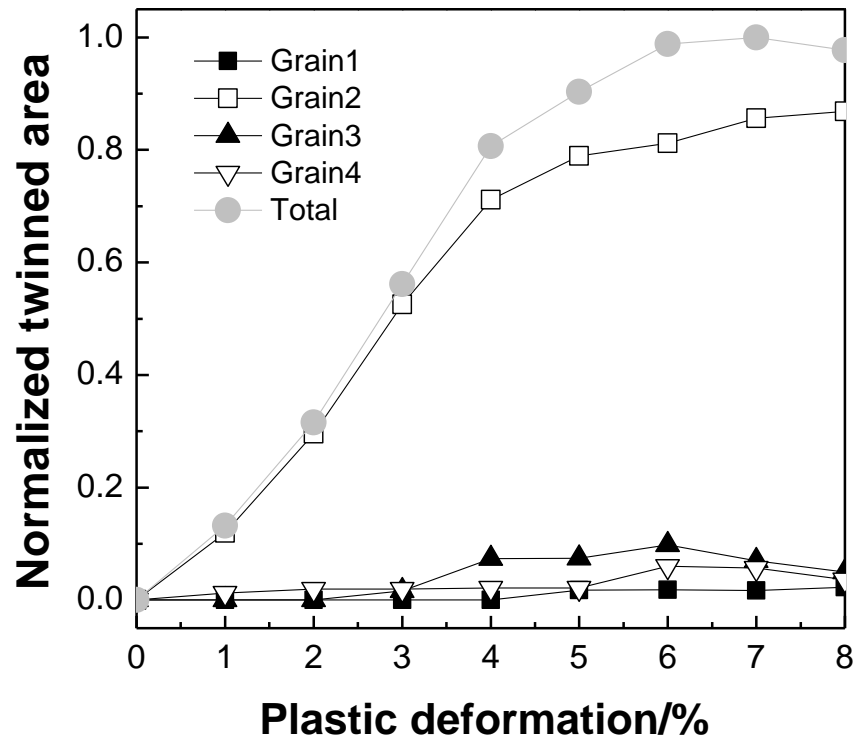


Figure 3-6. Activity of  $\{10\bar{1}2\} < 10\bar{1}1 >$  tensile twinning in each grain of 18nm  $[11\bar{2}0]$ -textured structure at 1.18 GPa.

Dislocation processes in a larger grain size sample are shown in Fig. 3-7. A tensile stress of 1.3GPa was applied to the same initial structure with 60nm grain size.

Basically, the deformation behavior is similar to that of the 18nm grain structure shown in Fig. 3-6. As exhibited in Fig. 3-7(a), deformation process took place by  $\{10\bar{1}2\} < 10\bar{1}1 >$

tensile twinning, basal  $\langle a \rangle$  and pyramidal  $\langle c+a \rangle$  partial slip. Basal extended dislocations (marked as 'A' in Fig. 3-7(a)) initiated from a GB were also produced.

Moreover, the number of extended dislocations increased markedly at larger strain, as shown in Fig. 3-7(b). A pyramidal  $\langle c+a \rangle$  dislocation was also generated in grain 2, Fig. 3-7 (a). Cores of full dislocations were observed, marked as 'B' in Fig. 3-7(b).

Comparing Figs. 3-6 and 3-7, we can identify a grain-size effect on the dislocation mode

for this  $[11\bar{2}0]$ -textured structure. During deformation tests of structures with grain size ranging from 6nm to 60nm, the fraction of the total number of dislocations that were extended or full dislocations consistently increased as the grain size increased. This tendency is consistent with a transition from partial to the extended slip with increasing a grain size in nanocrystalline Al [73].

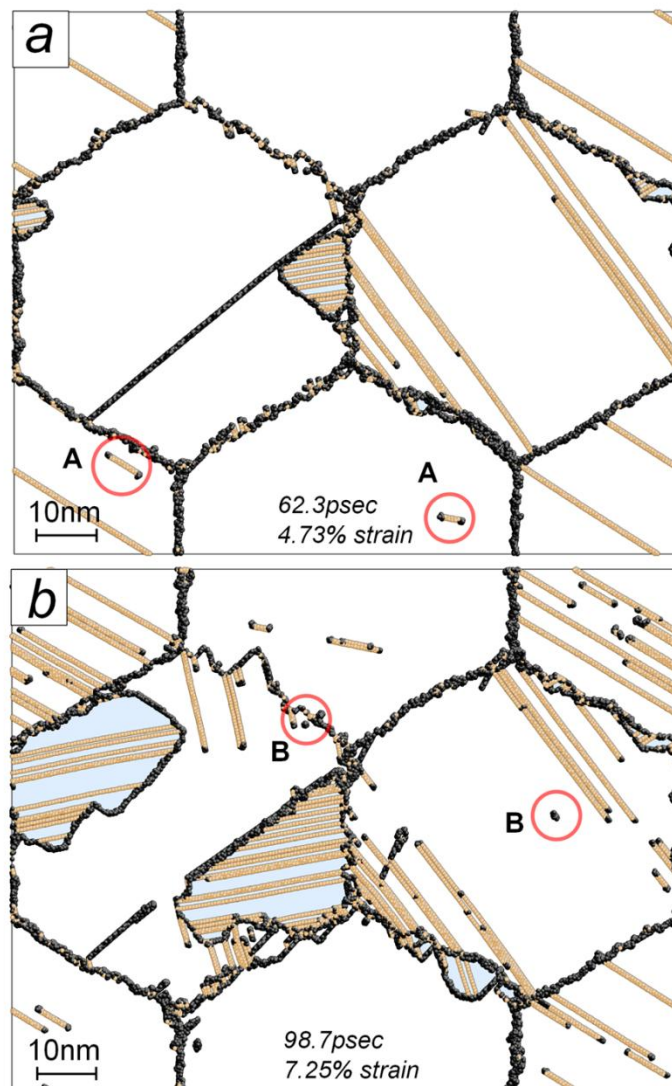


Figure 3.7. Snapshots of strained  $[11\bar{2}0]$ -textured structures with grain size of 60nm at 1.3GPa. (a) and (b): total strains are 4.73 and 7.25% at 1.3GPa, including elastic strain of  $\sim 3\%$ . Note microstructural features: A - extended dislocation, B - full dislocation.

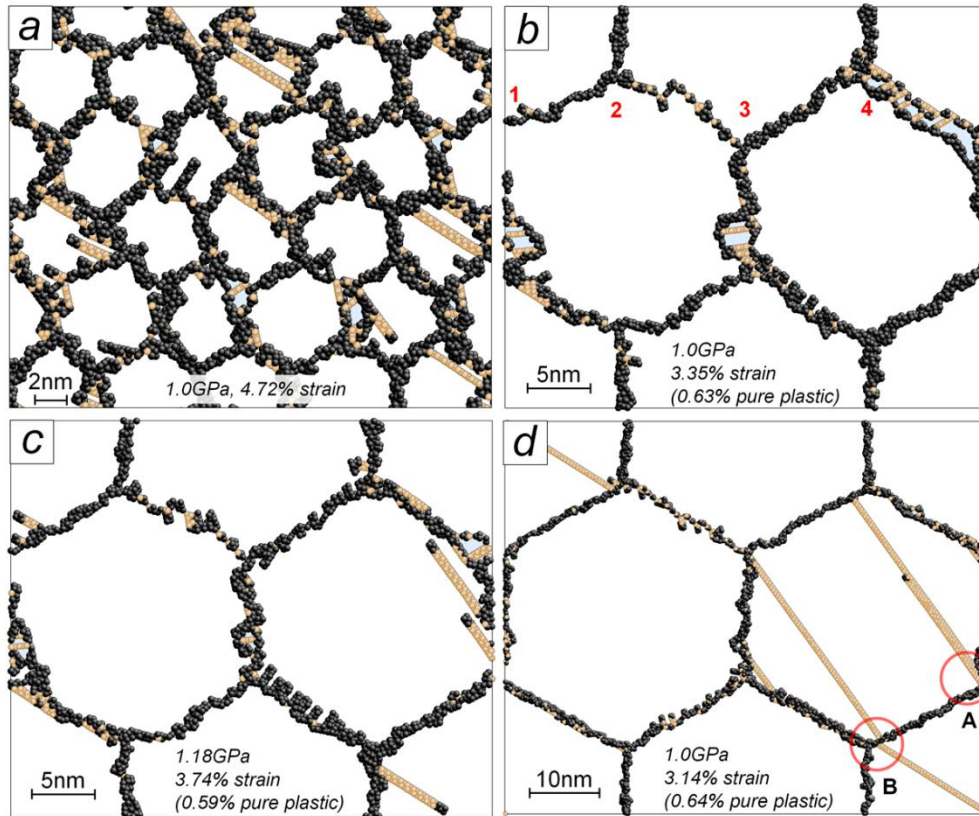


Figure 3-8. Snapshots of strained  $[11\bar{2}0]$ -textured structures with grain sizes from 6 to 40nm at 1.0 or 1.18GPa. (a): structure with 6nm grain shows both basal  $\langle a \rangle$  slip and  $\{10\bar{1}2\} \langle 10\bar{1}1 \rangle$  tensile twinning at 1.0GPa. Comparing this structure to ones with larger grains ( $>18$ nm), the twinning process is however less active than slip through whole plastic deformation. There is also no completed twinned grain over 10% plastic strain. (b) and (c): the crossover of initiation process from twinning to slip using the same initial structure of 18nm grain size by increasing an external stress from 1.0GPa to 1.18Gpa. (d): Plastic behaviors of 40nm grain structure at 1.0GPa. Circled A and B indicate two different basal slip sources, twinning dislocation and GBs (including a triple point). Cyan, brown and black mean a twinned region, stacking fault (FCC), disordered (non- HCP or FCC), respectively.

It is well-known that in nanocrystalline FCC metals, GB-mediated processes dominate the deformation mechanism as the grain size decreases, and that a maximum strength exists at a critical size (typically 10 ~ 20nm) above which conventional slip processes dominate [42, 44, 50]. As shown in Fig. 3-8, the grain size dependence (6,

18, and 40nm) of the deformation processes were investigated for loads of 1.0 and 1.18GPa. As shown in Fig. 3-8(a), at small grain size (6nm)  $\{10\bar{1}2\} < 10\bar{1}1 >$  twins and basal  $\langle a \rangle$  partial dislocations were produced. This indicates that plastic deformation at extremely small grain size can be promoted by both slip and twinning processes, not only by GB-mediated processes. In Figs. 3-8(b), (c), and (d), we compare the initiation process of slip and twinning at an early stage of deformation. First, two structures with grain size of 18nm were deformed from the same initial structure as in Figs. 3-8(b) and (c) to the same plastic stain, but under different stresses. For the case given in Fig. 3-8(b), twinning developed prior to activation of slip process. This result is in apparent conflict with experimental findings that some dislocations are introduced in polycrystalline Mg before twins are observed [95, 96, 103, 104]. Most importantly, Koike [95] reported that the  $\{10\bar{1}2\} < 10\bar{1}1 >$  twins are formed in the early stage of deformation in order to accommodate concentrated stresses due to dislocation slip. To investigate the origin of this discrepancy, the initiation processes of twinning and slip were also examined at larger grain sizes. Consistent with the experimental trend, for 40nm grain size system shown in Fig. 3-8(d) slip was activated prior to twinning. Comparing Figs. 3-8(b) and (d) for a similar strain and similar degree of twin growth, it is clear that the strained cell with 40nm grain size follows the known defect activation sequence better than the 18nm system. Analogously, the effect of stress on activation of slip and twinning can be seen by comparing in Figs. 3-8(b) and (c). Even though the tensile loads of 1.0 and 1.18GPa are not much different, the higher stress also promotes slip over twinning.

In order to understand the dependence of defect activation on stress more clearly, deformation under even higher external stress was investigated, as shown in Fig. 3-9. The same initial structures having a grain size of 40nm were strained at 1.25, 1.32, 1.4, and 1.5GPa. Figures 3-9(a) to (d) show their structures for essentially the same values of strain: these total strains of 9.63 ~ 9.83%, corresponding to plastic strains of 5.52 ~ 6.63%. Figure 3-9(a) shows that grain 2 is nearly completely twinned. The pyramidal  $\langle\mathbf{c+a}\rangle$  dislocations, indicated as 'A' in Fig. 4-9(a), cannot propagate at 1.25GPa because they are blocked by the twinning in grain 2 and the basal  $\langle\mathbf{a}\rangle$  slip in grain 4. As Fig. 3-9(b) shows, these pyramidal  $\langle\mathbf{c+a}\rangle$  dislocations do however propagate at higher stress (1.32GPa); this has the effect of preventing the progress of the twin across all of grain 2. The activity of pyramidal  $\langle\mathbf{c+a}\rangle$  slip increases continuously with increasing external stress; at 1.32GPa extended  $\langle\mathbf{c+a}\rangle$  dislocations first appear. As shown in Fig. 3-9(d), a high density of pyramidal  $\langle\mathbf{c+a}\rangle$  dislocations is observed at 1.5GPa, almost completely suppressing the twinning of grain 2. In addition, grain 4 now manifests basal  $\langle\mathbf{a}\rangle$  slip as a dominant deformation mode. Considering the series of twinned regions in Figs. 3-9(a) - (d), we can conclude that the size of the twinned regions decreases with increasing external stress. This competition between twinning and pyramidal  $\langle\mathbf{c+a}\rangle$  slip has been observed experimentally: Lou et al. [98] suggested that in the AZ31B Mg alloy the pyramidal  $\langle\mathbf{c+a}\rangle$  dislocations act as barriers to twin nucleation and propagation. Proust et al. [96] also reported that the more  $\langle\mathbf{c+a}\rangle$  dislocations there are in AZ31 magnesium alloys, the more difficult it becomes to produce tensile twinning.

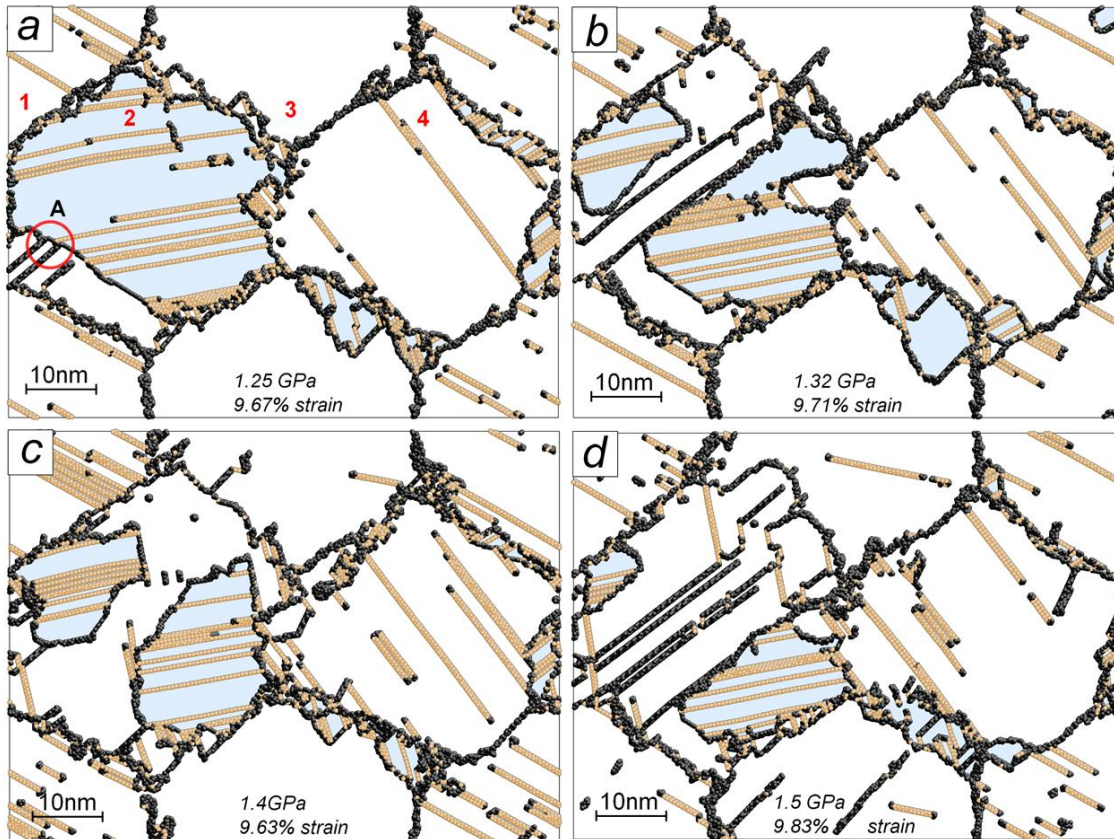


Figure 3-9. Snapshots of strained  $[11\bar{2}0]$ -textured structures with 40nm grain size under various external stresses from 1.25 to 1.5GPa. (a): total strain 9.67% (plastic 6.63%) at 1.25GPa, (b): total strain 9.71% (plastic 6.45%) at 1.32GPa, (c): total strain 9.63% (plastic 5.92%) at 1.4GPa, and (d): total strain 9.83% (plastic 5.52%) at 1.5GPa. Cyan, brown and black mean a twinned region, stacking fault (FCC), disordered (non- HCP or FCC), respectively.

### 3-4. Stress Analysis of Dislocation Activation

The activation of dislocations depends on stress. A stress map can give information about sites where slip occurs. Figure 3-10 shows a shear stress map of 18nm  $[11\bar{2}0]$ -textured Mg under constant  $\gamma$ -stress of 1.1GPa. To observe activation of basal  $\langle a \rangle$  slip, basal plane and  $[\bar{1}100]$  of grain 4 are chosen as a shear plane and direction, respectively. Force of each atom on the shear plane to the shear direction is plotted on the 2D plane of Fig. 3-10. The snapshot was captured during basal  $\langle a \rangle$  slip is activating

at grain 4: The dislocation size is  $\sim 0.5\text{nm}$ . The partial basal  $\langle a \rangle$  dislocation is marked with a blue circle in Fig. 3-10 (a). High shear stress ( $> -0.7\text{GPa}$ ) of a large area (more than 2~3 atoms) is mainly found at GB. This is consistent with classical dislocation theory that a critical concentration of shear stress at GB results in activating slip process.

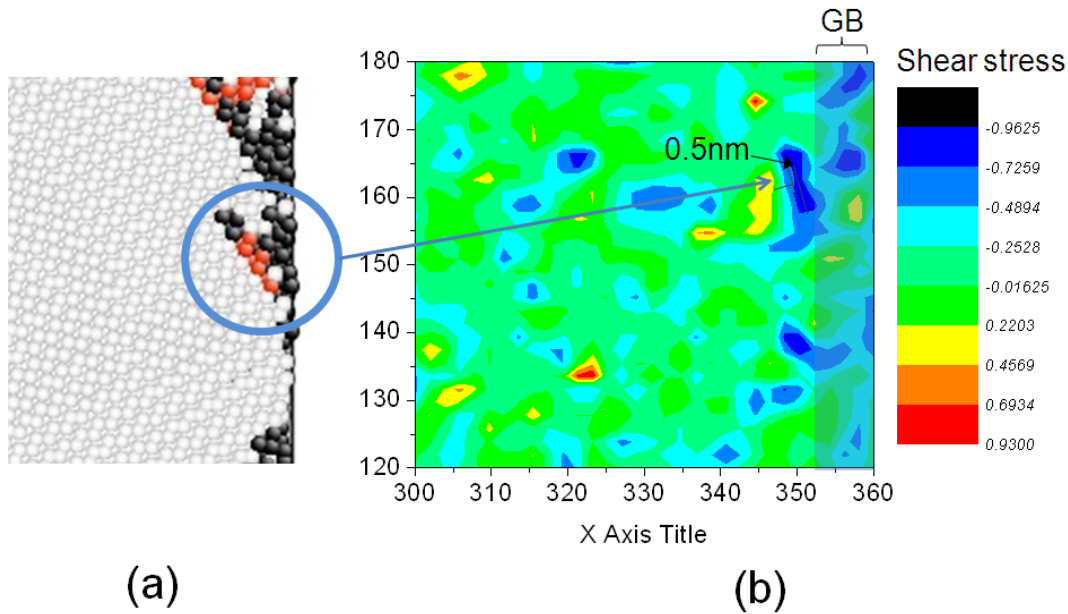


Figure 3-10. CNA image and shear stress map of strained  $[11\bar{2}0]$ -textured structures with 18nm grain size under 1.1GPa.

### 3-5. Transitions in Dislocation Mode

Typically, slip process in FCC metals involve partial dislocations for grain sizes below  $\sim 20\text{nm}$  [42, 73], with a transition to extended or full dislocations at larger grain sizes [73, 105]. The cores of the extended dislocations are split into two Shockley partials connected by stacking faults. The splitting distance of two partial cores (the stacking fault distance,  $r$ ) is a function of the resolved shear stress ( $\sigma$ ) [73]. Whether a dislocation is partial or extended depends on the splitting distance relative to the grain size. For large enough grain sizes, extended dislocations are normally stable, though

partial dislocations are present at very high stresses. However, this behavior is not seen in the present simulations. Dislocations in the  $[1\bar{1}20]$ -textured structure consist of basal  $\langle\mathbf{a}\rangle$  and pyramidal  $\langle\mathbf{c}+\mathbf{a}\rangle$  types. Considering the basal  $\langle\mathbf{a}\rangle$  dislocation, a partial dislocation process is frequently seen even for the large grain size of 60nm. By contrast, extended dislocations appear in 10nm grain structures when strained over 10%. As the grain size or the external stress increase in the  $[1\bar{1}20]$ -textured structure, extended dislocations become more prevalent than partial dislocations. A similar tendency is seen for the pyramidal  $\langle\mathbf{c}+\mathbf{a}\rangle$  slip in the  $[1\bar{1}20]$ -textured structure. Because various slip modes - basal, prismatic and pyramidal – can be manifested, the transition of slip mode in the polycrystalline HCP metals cannot be explained by a simple equation as it was for the case of FCC metals [73].

### 3-6. Competition between Slip and Twinning

The interactions between slip and twinning can be viewed as processes of competition and cooperation. The first competition takes place between pyramidal  $\langle\mathbf{c}+\mathbf{a}\rangle$  slip and  $\{10\bar{1}2\} \langle 10\bar{1}1 \rangle$  twinning. As already exhibited in Fig. 3-9(b), the growth of the twinning region can be physically blocked by the pyramidal  $\langle\mathbf{c}+\mathbf{a}\rangle$  dislocation. Moreover, increasing the stress accelerates this phenomenon by promoting slip rather than twinning. The same trend is also found between basal  $\langle\mathbf{a}\rangle$  slip and  $\{10\bar{1}2\} \langle 10\bar{1}1 \rangle$  twinning. At low stress, the twinning process is more dominant than the basal slip. However, twinning activity decreases compared to the basal slip as the stress increases.

By contrast, there are also several cooperative processes between slip and twinning, with one deformation mechanism helping the activation of the other. For example, as discussed later, a  $\{10\bar{1}2\} \langle 10\bar{1}1 \rangle$  tensile twin originating at GBs can initiate a basal  $\langle \mathbf{a} \rangle$  slip through dislocation emission. Conversely, a high density of dislocations leads to compressive twinning. A second cooperative process is observed in the slip behavior in a twinned area. When an I1-type SF in  $\{10\bar{1}2\} \langle 10\bar{1}1 \rangle$  twinned area accommodates the propagation of twinning, the Schmid factor for slip increases, promoting a new slip process.

### 3-7. Summary

This chapter has attempted to probe the plastic behavior of a nanocrystalline HCP metal using MD simulation of  $[1\bar{1}20]$ -textured Mg. We observed typical creep curves for a nanocrystalline metal in which GB-mediated process are dominant. Further, there was a transition in the nature of the dislocations and a crossover in the initiation process of twinning and slip at the nanoscale. In addition, other deformation mechanisms typical of coarse grained HCP metal were observed. Although twinning behaviors are normally suppressed at small grain sizes, high twinning activity in this structure enabled us to examine various interactions between twinning and slip. The twinning process in this simulation was found to be prevalent for  $\sim 6\%$  plastic strain, as has previously been seen for coarse grained HCP metal.

Most of the experimentally known slip and twinning systems were reproduced in our simulations, despite the limitations of a textured microstructure. The GBs of the nanocrystalline structure acted as a source of twinning as well as dislocations for slip. The transition from partial to extended dislocation were found for both basal  $\langle \mathbf{a} \rangle$  and

pyramidal  $\langle \mathbf{c+a} \rangle$  slip. The extended basal  $\langle \mathbf{a} \rangle$  dislocation is similar to the corresponding dislocation in FCC metals. However its transition from partial to extended cannot be as easily explained due to the complex slip modes available to HCP crystals. In the columnar structure, three types of twinning are formed by GB and dislocation assisted processes.  $\{10\bar{1}2\} \langle 10\bar{1}1 \rangle$  tensile twinning is initiated from GBs at low stress, while compressive  $\{10\bar{1}1\}$  and  $\{10\bar{1}3\}$  twinning are nucleated from an interaction of dislocations at high stress. A crossover in initiation process from slip to twinning at nanoscale was found with decreasing a grain size. It was also found that the transition of deformation mechanism from  $\{10\bar{1}2\} \langle 10\bar{1}1 \rangle$  tensile twinning to pyramidal  $\langle \mathbf{c+a} \rangle$  slip occurs with increasing stress. Thus, the plastic behavior is embodied by competing and cooperating processes between slip and twinning.

CHAPTER 4  
OVERALL MECHANICAL RESPONSE OF 2D NANOCRYSTALLINE-TI METALS

Although both Ti and Mg have the HCP crystal structure, they show quite different mechanical properties, as previously shown in Table 2-2. Although the  $c/a$  ratio is usually considered as a factor to explain different deformation properties in each HCP metals, it is not enough. In Table 4-1, Zn and Cd having similar  $c/a$  ratio show the same slip modes. This is similarly applied to Ti and Zr. However, if we see principle slip system according to deviation change from Cd to Be, Be violates the trend. There has been an attempt to understand the dependence of deformation modes in HCP metals in terms of the d-electrons [106].

Table 4-1.  $c/a$  ratio and slip modes of various HCP metals [8].

Element	$c/a$	Deviation from the Ideal $c/a = 1.633$	Principal Slip System	Secondary Slip System	Other Slip Systems
Cd	1.886	+15.5 pct	basal (0001) $\langle 11\bar{2}0 \rangle$	pyramidal {11 $\bar{2}2$ } $\langle 11\bar{2}3 \rangle$	prismatic {10 $\bar{1}0$ } $\langle 11\bar{2}0 \rangle$ pyramidal {10 $\bar{1}1$ } $\langle 11\bar{2}0 \rangle$
Zn	1.856	+13.6 pct	basal (0001) $\langle 11\bar{2}0 \rangle$	pyramidal {11 $\bar{2}2$ } $\langle 11\bar{2}3 \rangle$	prismatic {10 $\bar{1}0$ } $\langle 11\bar{2}0 \rangle$
Mg	1.624	-0.5 pct	basal (0001) $\langle 11\bar{2}0 \rangle$	prismatic {10 $\bar{1}0$ } $\langle 11\bar{2}0 \rangle$	pyramidal {10 $\bar{1}1$ } $\langle 11\bar{2}0 \rangle$ {11 $\bar{2}2$ } $\langle 11\bar{2}3 \rangle$
Co	1.623	-0.6 pct	basal (0001) $\langle 11\bar{2}0 \rangle$	none	none
Zr	1.593	-2.4 pct	prismatic {10 $\bar{1}0$ } $\langle 11\bar{2}0 \rangle$	basal (0001) $\langle 11\bar{2}0 \rangle$	pyramidal {10 $\bar{1}1$ } $\langle 11\bar{2}0 \rangle$ {11 $\bar{2}2$ } $\langle 11\bar{2}3 \rangle$
Ti	1.588	-2.8 pct	prismatic {10 $\bar{1}0$ } $\langle 11\bar{2}0 \rangle$	basal (0001) $\langle 11\bar{2}0 \rangle$	pyramidal {10 $\bar{1}1$ } $\langle 11\bar{2}0 \rangle$ {11 $\bar{2}2$ } $\langle 11\bar{2}3 \rangle$ {10 $\bar{1}1$ } $\langle 11\bar{2}3 \rangle$
Hf	1.581	-3.2 pct	prismatic {10 $\bar{1}0$ } $\langle 11\bar{2}0 \rangle$	basal (0001) $\langle 11\bar{2}0 \rangle$	—
Be	1.568	-4.0 pct	basal (0001) $\langle 11\bar{2}0 \rangle$	prismatic {10 $\bar{1}0$ } $\langle 11\bar{2}0 \rangle$	pyramidal {10 $\bar{1}1$ } $\langle 11\bar{2}0 \rangle$ {11 $\bar{2}2$ } $\langle 11\bar{2}3 \rangle$

The Stacking fault energy (SFE) is an important factor in determining the behavior of dislocations and on twinning. The SFEs are shown in Table 4-2. A low SFE easily activates partial slip. It is well known that the twinning behavior of fcc metals is strongly affected by the stacking fault energy (SFE). Deformation twinning is easier in FCC

crystals with very low SFE value, but becomes more difficult in the fcc crystals with medium to high SFEs. As a twin boundary (TB) appears as a SF in FCC metals, low SFE can make the TB more stable. In Table 4-2, the SFEs are obtained from SFs occurring parallel to the basal plane. Hence, behaviors of the basal slip are explained with the SFEs in Table 4-2. To relate the SFEs with twinning in HCP metals, the SFEs of TBs should be considered, as will be discussed later.

Table 4-2. Lattice constants and stacking fault energies of various HCP metals obtained by First principle calculation.[107].

Parameters	Zr	Be	Ti	Mg	Zn
SFE(mJ/m <sup>2</sup> ) *	223	557	287	21	102

\*stable SFEs on the (0001) plane.

#### 4-1. Potentials and Mechanical Response

For simulations of the mechanical properties of Ti, empirical potentials of the EAM and MEAM types are considered in this study.

The EAM potential for Ti is known to give a wrong c/a ratio, close to the ideal value of 1.633 instead of 1.58; this is due to lack of anisotropy in the EAM formalism. Hence, using the EAM potential a dominant slip mode appears as a basal <a> slip, not prismatic slip as has been experimentally reported [83-85]. The first MEAM potential reported by Baskes does not reproduce the experimental lattice parameter or HCP as the lowest energy structure [108, 109]. The MEAM potential fitted by Kim et al.[26] is chosen for our first MD simulation of Ti. As shown in Fig. 4-1, the creep tests of 18nm [0001]-textured Ti indicates that plasticity of the nc-Ti texture occurs at stresses in excess of 3GPa. The structure of the strained samples is analyzed in Fig. 4-2 to determine the deformation mechanisms. After an external stress of 10GPa is applied to the y-direction, the texture is cooling down at 0.01K. A snapshot of potential energy of

Fig. 4-2 (a) exhibits high and low energy boundaries (A and B) inside the grains; these boundaries are produced by the deformation process. It is found that the each region in the deformed texture has different lattice constants, as summarized in Table 4-3. Moreover, a change of CN in the intermediate region appears in Fig.4-2(b). While normal atoms show the 12 neighbors' characteristic of an HCP metal, the atoms between A and B have the CN of 14. After examining the atomic structure, this region is identified as having the BCC structure. Although BCC has 8 nearest neighbors (at  $0.866a$ ), it also has 6 second neighbors (at  $1.0a$ ), which is within the cutoff used in the CN analysis. Under the external stress a phase transition to BCC, instead of dislocations or SFs of FCC, results from higher energy difference between BCC and HCP than that between BCC and HCP[26] for this potential. This potential is thus not suitable for deformation simulations.

As seen in Fig. 4-3, two textures near a formed boundary have the same phase and lattice parameter ( $\sim 2.94 \text{ \AA}$ ) at 0.01K. The boundary is created by twinning, not a phase transition. Hence, the present research of Ti uses the Ti MEAM potential of Hennig et al. [82] does not have such a problem. Further simulation of Ti is performed with the Hennig potential.

Table 4-3. Lattice constants of strained 18nm [0001]-textured Ti at 0.1K.

Normal atoms	Region A	Intermediate region (between A and B)	Region B
$\sim 2.94\text{\AA}$	$2.72\sim 2.81\text{\AA}$	$\sim 2.80\text{\AA}$	$2.86\sim 2.92\text{\AA}$

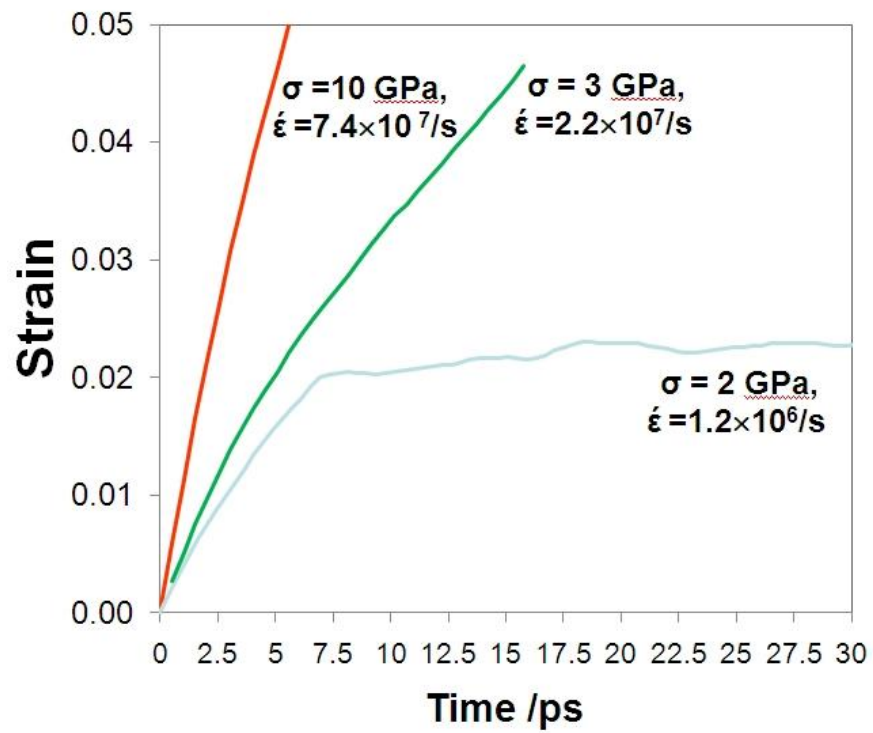


Figure 4-1. Strain-Time curves of 18nm [0001]-textured Ti as a function of external stress.

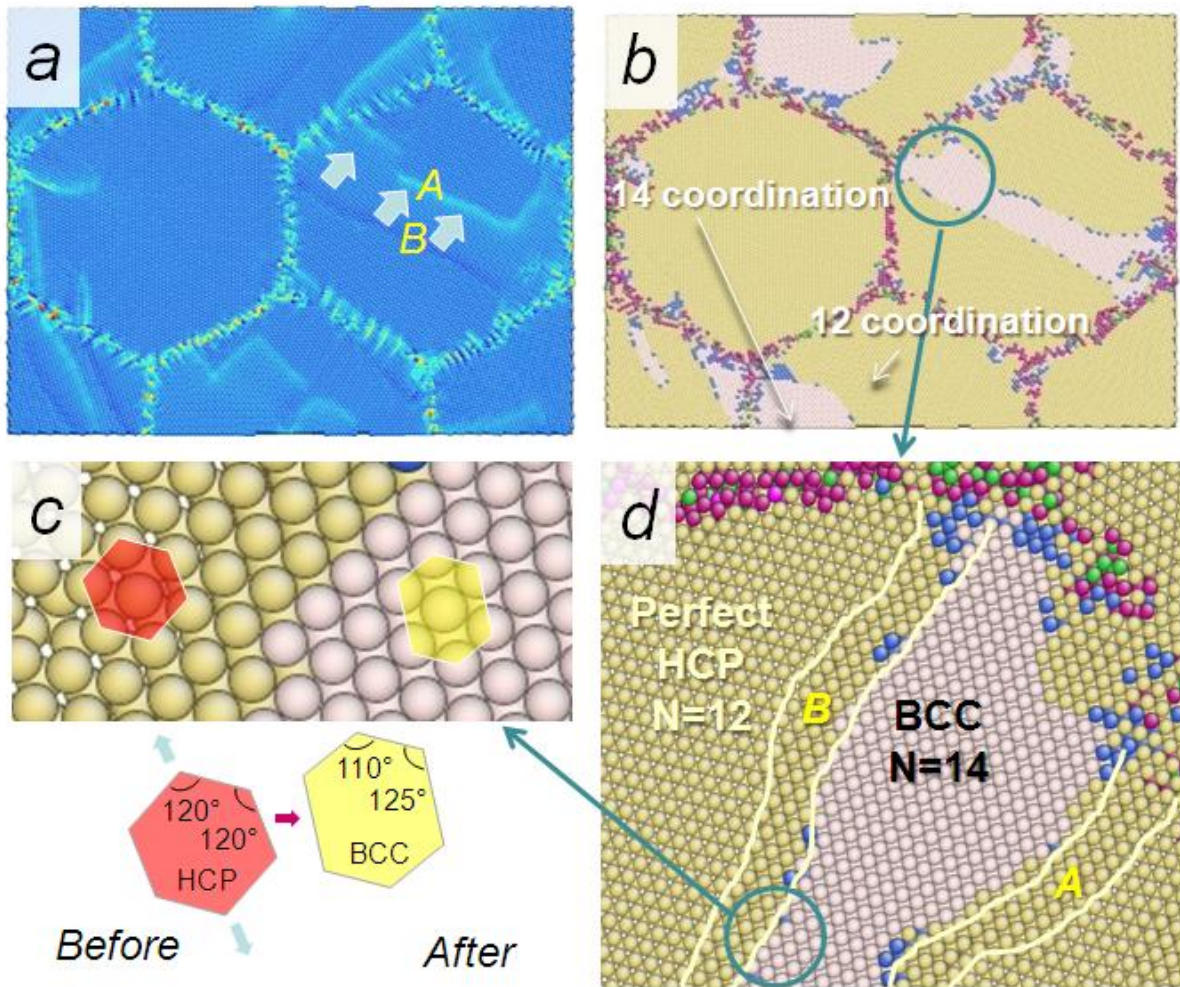


Figure 4-2. PE and CN image of strained  $[11\bar{2}0]$ -textured structures with 18nm grain size under 3.0GPa. Kim et. al.'s MEAM potential was used. a.Cyan region A: boundary with higher energy : lattice constant decreased, and atoms were compressed. Deep blue region B: boundary with lower energy: lattice constant increased, and atoms were pulled out. In the region between A and B, a BCC phase is found.

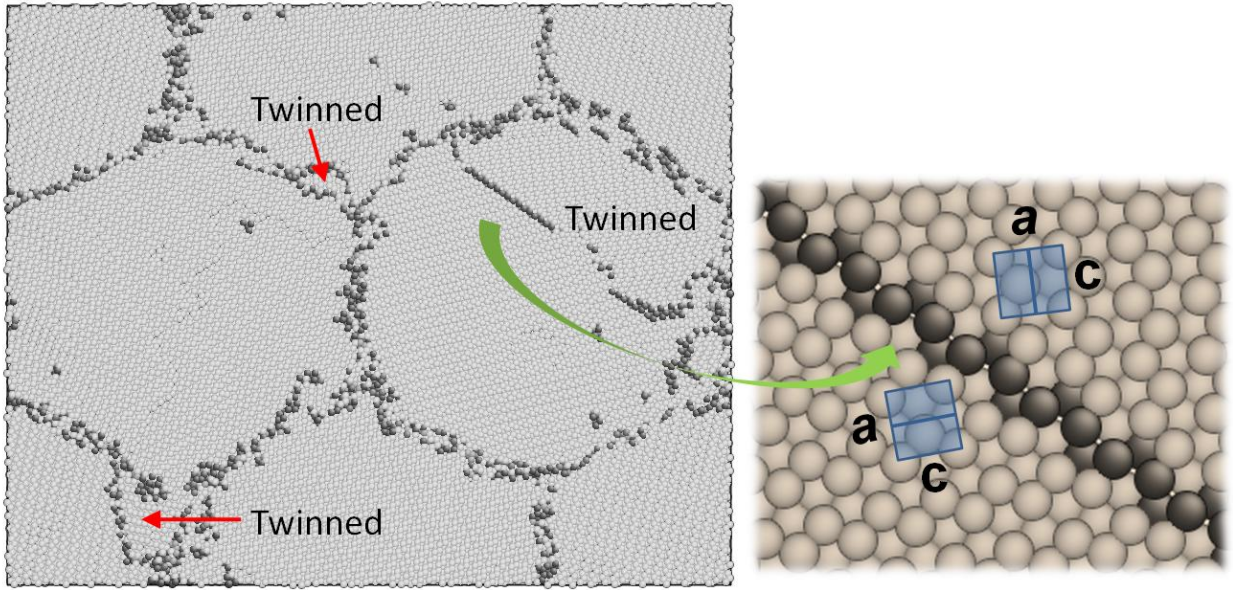


Figure 4-3. Snapshots of strained  $[11\bar{2}0]$ -textured structures with 18nm grain size under 2.75GPa. There is no change in CN. Two textures have the same phase.

#### 4-2. Stress-dependence of Mechanical Response in Ti

As Fig. 4-4 showed, the yield stress for Ti, described with the Hennig potential, lies between 2.50 and 2.75GPa, at which tertiary creep appears. We recall that our earlier simulations showed that tertiary creep of Mg of the same grain size occurs at 0.9GPa; the stress in Ti is three times larger. This is similar to a ratio of the cohesive energies of Mg and Ti ( $E_{\text{coh Mg}}: -1.6\text{eV}$ ,  $E_{\text{coh Ti}}: -4.7\text{eV}$ ); thus the occurrence of this creep curve at 2.75GPa seems physically quite reasonable. At  $\sigma < 2.5\text{GPa}$ , strain rates are in a range of  $\sim 10^7 \text{ s}^{-1}$ , noted as a typical strain rate by GB Process. As external stress increases over 2.75GPa, the strain rate jumps from  $\sim 10^7$  to  $\sim 10^9 \text{ s}^{-1}$ . In strain-stress curves of Mg and Al [73] displaying a tertiary creep from 50 and 100 ps, the strain rates are less than  $7 \times 10^8 \text{ s}^{-1}$ . The comparative high strain indicates that slip and twinning actively takes place at the tertiary creep. The strained texture of Ti is discussed in the following section.

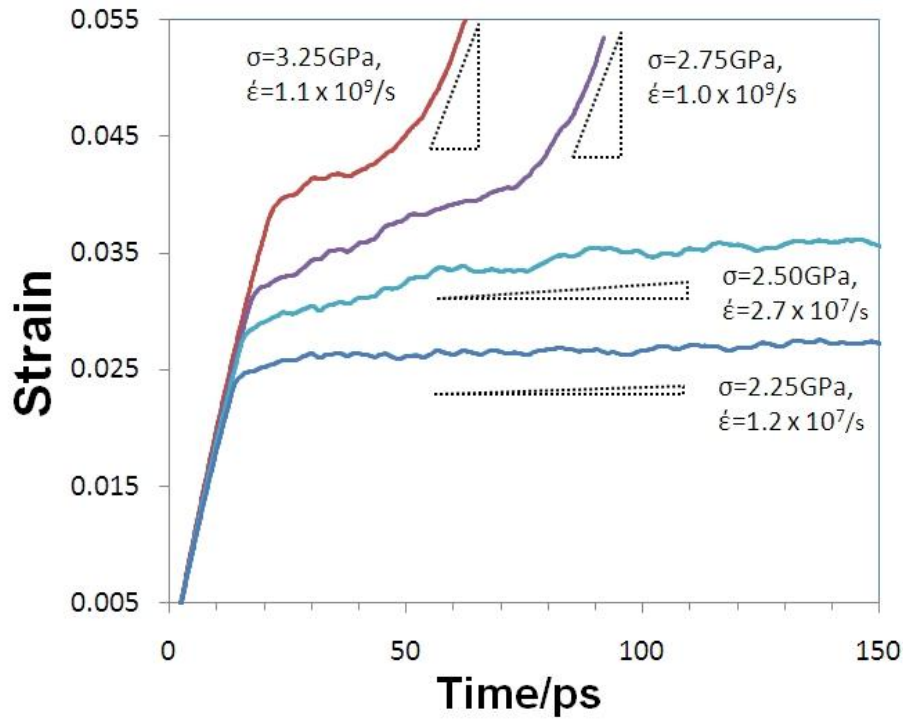


Figure 4-4. Creep curves of  $[1\bar{1}20]$ -textured Ti having a grain size of 18nm.

### 4-3. Comparison of Mg and Ti

Figure 4-5 (a) and (b) shows snapshots of 10%-strained Ti and Mg samples with 18nm grain size under 3.25GPa and 1.2GPa stresses. In our previous results, flow stresses of  $[1\bar{1}20]$ -textured Ti and Mg were 2.75 and 1.0GPa. Thus these specific external stresses were homologous in the sense of being 120% of the flow stress for each material. The deformation strain rates were  $1.4 \times 10^9$  and  $1.0 \times 10^9 \text{ s}^{-1}$ , for Ti and Mg respectively. As shown in Fig.4-5 (a) and (b), various slip and twinning processes are observed in these deformed textures.

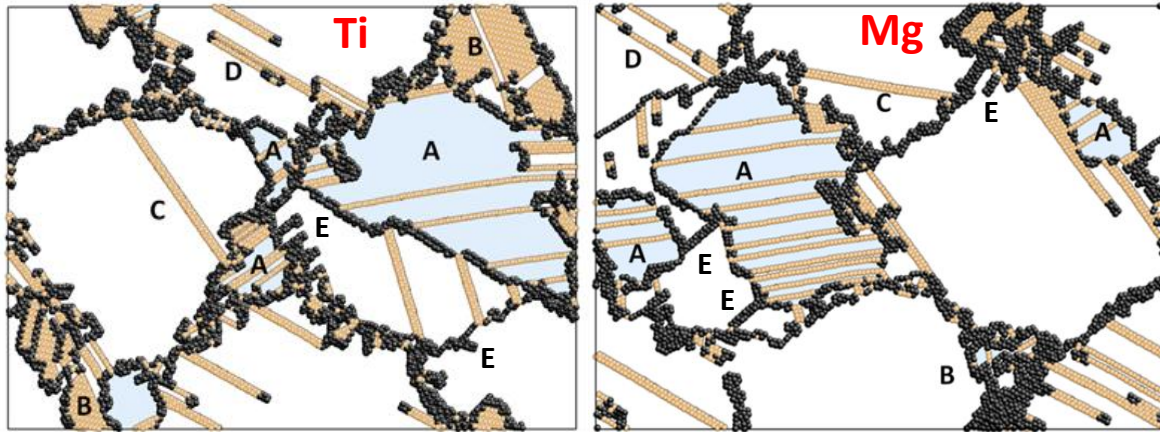


Figure 4-5. Snapshots of nano-structured Ti (left) and Mg (right) plastically deformed at 3.25 and 1.2GPa, respectively. Their samples have the same grain size (18nm) and crystallographic texture ( $[1\bar{1}\bar{2}0]$ ). Cyan, brown and black mean a twinned region, stacking fault (FCC), disordered (non- HCP or FCC), respectively.

In the untwined region, slip process are actively in Mg (left) than in Ti (right). The dislocation density of Mg is also larger than that of Ti in Fig. 4.5. This is explained by the ten times higher SFE of Ti, as shown in Table 4-2. Due to the small grain size, both Ti and Mg textures exhibit mostly partial basal slip (C) having two FCC lines. The different basal SFs (D) having one SF line are also found in the deformed textures. The first-order pyramidal  $\langle c+a \rangle$  slip (E) on the  $\{10\bar{1}1\}$  plane is often found in the Mg-texture, but rarely occurs in our  $[1\bar{1}\bar{2}0]$ -textured Ti: E doesn't glide in Ti image.

The  $\{10\bar{1}2\} \langle 10\bar{1}1 \rangle$  twinning mode (A) is manifested in both Ti and Mg of Fig. 4-5. In our  $[1\bar{1}\bar{2}0]$ -textured Mg, the most common three twinning modes, as already shown in Fig. 3-5, are observed. The stress condition and texture to activate those modes in Mg can be satisfied in the  $[1\bar{1}\bar{2}0]$ -texture. However, the two specific modes,  $\{10\bar{2}1\} \langle 10\bar{1}2 \rangle$  and  $\{10\bar{2}2\} \langle 1\bar{1}\bar{2}3 \rangle$ , of Ti are difficult to nucleate because in the  $[1\bar{1}\bar{2}0]$ -texture. Thus, the next probable twinning mode (B),  $\{10\bar{1}1\} \langle 10\bar{1}2 \rangle$ , is found in Ti. In Fig. 4-4

(a), the  $\{10\bar{1}1\} < 10\bar{1}2 >$  twinning, noted as 'B', apparently looks like FCC stacking. The FCC region is, however, believed to be creation of continuous intrinsic stacking fault (D) in twinned area.

During preparing the  $[10\bar{1}0]$ -textured Ti, twin nuclei were found near GBs and inside grains. The twins in the strained cell are noted by a circle in Fig. 4-5(a). A texture of pyramidal direction, noted by B'C in the HCP unit cell of Fig. 3-3, appears on the  $(10\bar{1}0)$  plane surrounded with dark atoms of twin boundary in Fig. 4-5(b). Cross section of Fig. 4-5(b) is seen in Fig. 4-5(c). Untwined and twinned lattices display basal and  $(10\bar{1}0)$  planes, respectively. A red dash dot line on hexagon representing the basal plane is rotation axis, normal to  $< 10\bar{1}1 >$  in Fig. 2-6(a), for  $\{10\bar{1}2\}$  tensile twinning in Fig. 4-5(c). The angle is identified to be  $\sim 86^\circ$  of  $\{10\bar{1}2\} < 10\bar{1}1 >$  tensile twinning. Thus, the twins which occurs during cooling the  $[10\bar{1}0]$ -textured Ti are the  $\{10\bar{1}2\} < 10\bar{1}1 >$  mode.

This texture was designed for  $\{11\bar{2}2\} < 11\bar{2}\bar{3} >$  and  $\{11\bar{2}1\} < 11\bar{2}\bar{6} >$  because those twins choose the  $[10\bar{1}0]$ -direction, thickness of the texture as a twin rotation axis [20]. However,  $\{10\bar{1}2\} < 10\bar{1}1 >$  tensile twins forms just by thermal stress ( $< 1$  GPa in Fig. 4-6). Moreover, some twins are homogeneously nucleated inside grains. The homogeneous nucleation without any external stress is normally very difficult to occur: it is similar with creation of dislocations without the Frank-Read source inside grains, not at GBs. The Hennig potential particularly describes martensitic phase transformations between titanium phases of  $\alpha$ ,  $\beta$ , and  $\omega$  [82]. Such a martensitic phase transformation may be related with the homogeneous twin nucleation in this simulation.

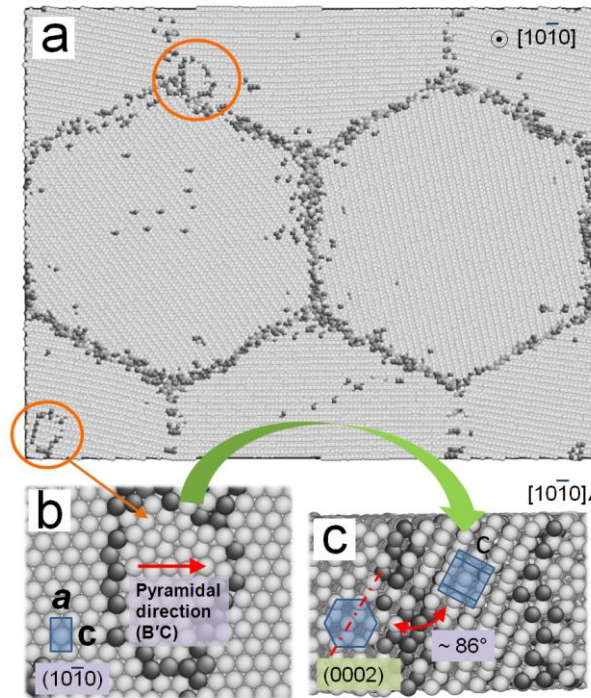


Figure 4-6. Formation of  $\{10\bar{1}2\} \langle 10\bar{1}1 \rangle$  tensile twins during cooling the  $[10\bar{1}0]$ -textured Ti from 700 to 100K. (a) Light and dark grays denote 12 CN and non 12 CN atoms, respectively. (b) Blue square indicates  $(10\bar{1}0)$  plane.  $B'C$ ,  $a$ , and  $c$  denote pyramidal direction and lattice constants in the HCP unit cell, respectively. (c) Blue hexagon and squares are HCP unit cell. Dash dot line denotes rotation axis for twinning.

After obtaining twin-free initial  $[10\bar{1}0]$ -textured Ti, a creep test was carried out under 3GPa. The 6%-strained sample is seen in Fig. 4-7(a) and (b). Each snapshot of displays shear strain (a) and central symmetry (b) parameters  $[110]$ . Figure 4-7(a) clearly shows two twins,  $\{10\bar{1}2\} \langle 10\bar{1}1 \rangle$  ( $\alpha$ ) and  $\{11\bar{2}2\} \langle 11\bar{2}3 \rangle$  ( $\beta$ ). Bright dots at grain interiors are cores of prismatic  $\langle a \rangle$  dislocations. In this deformed texture, motion ( $\gamma$ ) and reorganization to twin boundary ( $\gamma'$ ) of GBs are also observed. SFs of partial dislocations are seen as dark blue in Fig. 4-7(b). A small central symmetry parameter means a more symmetrical and ordered structure. Grains I and III, having enough slip

or twinning process, are low symmetry states due to their high elastic energy. We indeed find that prismatic  $\langle a \rangle$  slip and  $\{11\bar{2}2\}\langle 11\bar{2}3 \rangle$  twinning known as a dominant mode in titanium appear in this simulation.

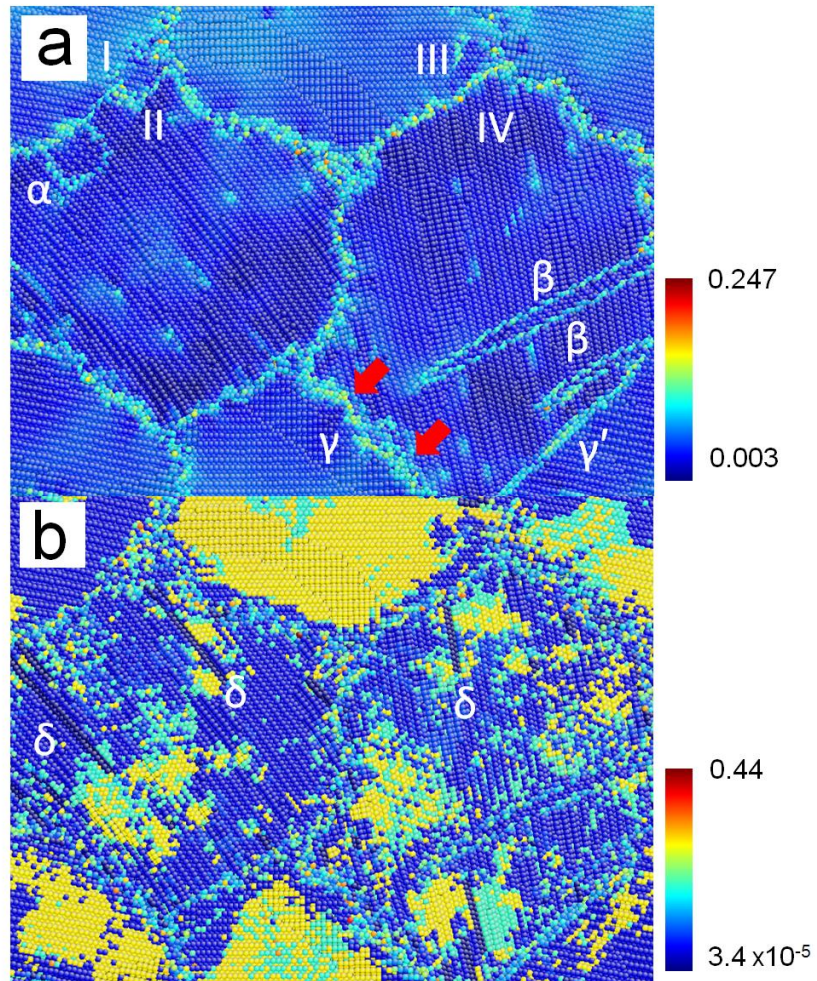


Figure 4-7. Snapshots of shear strain and central symmetry of the 6%-strained  $[10\bar{1}0]$ -textured Ti at 3GPa.  $\alpha$ ,  $\beta$ ,  $\gamma$ ,  $\gamma'$ , and  $\delta$  denote  $\{10\bar{1}2\}\langle 10\bar{1}1 \rangle$  twin,  $\{11\bar{2}2\}\langle 11\bar{2}3 \rangle$  twin, GB moving, reorganizing of GB, and SF on the prismatic  $\langle a \rangle$  plane, respectively. I ~ IV correspond to each grain.

#### 4-4. Summary

Most EAM and MEAM potentials are unable to capture the large anisotropy of Ti; they thus fail to capture the fundamental deformation processes. However, the Ti MEAM potential reported by Hennig et al. has the properties most consistent with experiment, correctly reproducing plasticity of Ti by deformation modes of slip and twinning identified experimentally. The Hennig potential designed to reproduce phase transitions of Ti seems to result in some distortion of nucleation process of the  $\{10\bar{1}2\} < 10\bar{1}1 >$  twin.

From time-strain curves, an acceleration of plastic deformation by successive slip and twinning occurs at 2.7GPa. Yielding behaviors in nc-Ti is achieved by only GB process for stresses less than 2.7GPa. In the present work, observed slip modes are prismatic and basal  $<a>$ .  $\{10\bar{1}2\} < 10\bar{1}1 >$ ,  $\{11\bar{2}2\} < 11\bar{2}\bar{3} >$  and  $\{10\bar{1}1\} < 10\bar{1}2 >$  twinning also appear at strained textures.

## CHAPTER 5 PYRAMIDAL <C+A> SLIP IN COLUMNAR NC-MG

As discussed in Chapter 2 , hexagonal close-packed (HCP) metals manifest either prismatic <a> or basal <a> slip as their principal slip mode [21]. While the primary <a> slip mode is prismatic in Ti, Zr, and Hf, basal slip dominates in Co, Zn, Be and Mg [111, 112]. Usually, if the primary slip is basal, then the secondary slip mode is prismatic, and vice versa. These two slip modes can, however, only produce strain along the <a> directions. Hence, these two <a> slip systems alone are not enough for homogeneous plastic deformation [111]. Activation of pyramidal <c+a> slip enhances the homogeneity in plastic deformation of HCP metals by providing a strain component along the <c> direction. The pyramidal <c+a> slip in HCP crystals has two modes: a first-order  $\{10\bar{1}1\}\{11\bar{2}\bar{3}\}$  mode and a second-order  $\{11\bar{2}2\}\{11\bar{2}\bar{3}\}$  mode. Such pyramidal <c+a> slip plays a key role in the ductility of polycrystalline HCP metals [113].

The <c+a> dislocations have been studied in experiment [113-115] and by theory and simulation [112, 116-124]. In the experiments, deformed polycrystalline samples were examined using an optical microscope (OM), or transmission electron microscope (TEM), in order to identify the <c+a> dislocations. It was found in Mg that  $\{11\bar{2}2\}\{11\bar{2}\bar{3}\}$  pyramidal dislocations are strongly bound on the basal planes[113]. Tonda and Ando [115] reported that <c+a> edge dislocations are immobilized by their dissociation into a sessile <c> and a glissile <a> dislocation in Cd, Zn and Mg. Simulation studies have focused on the structures and stability of the <c+a> dislocation. A  $\{11\bar{2}2\}\{11\bar{2}\bar{3}\}$  second-order pyramidal edge dislocation was shown by Minonishi et al.[120, 121] and Liang and Bacon [118] to have two types of cores; undissociated and dissociated. Yoo et al. [112] found the  $\{11\bar{2}2\}\{11\bar{2}\bar{3}\}$  edge

dislocation core with a Shockley partial connected by a basal-plane stacking fault to a sessile partial. They also suggested from a calculation using anisotropic elasticity that  $\langle c+a \rangle$  screw dislocations can cross slip from a prismatic plane into a pyramidal plane [112]. Analysis [116] of simulations using a Lennard-Jones potential revealed a temperature dependence of the core structure in  $\langle c+a \rangle$  edge and screw dislocations, and double cross-slip of  $\langle c+a \rangle$  screw dislocation on  $\{10\bar{1}1\}$  and  $\{11\bar{2}2\}$ . In contrast to studies focusing on second-order pyramidal slip of  $\{11\bar{2}2\}\langle 11\bar{2}\bar{3} \rangle$ , first-order pyramidal slip has been addressed in Ti [114] and Mg [117]. In particular, Numakura et al. [123, 124] suggested three different core structures for  $\{10\bar{1}1\}\langle 11\bar{2}\bar{3} \rangle$  dislocations, one planar and two non-planar. Li and Ma [117] reported first-order pyramidal slip,  $\{10\bar{1}1\}\langle 11\bar{2}\bar{3} \rangle$  in Mg.

In simulation studies, pyramidal dislocations have been created in single crystals either by manually moving some atoms [118-124] or by applying external stress to an artificial cavity [117]. It is not possible to investigate the initiation of  $\langle c+a \rangle$  dislocations when they are constructed by hand. In creating a  $\langle c+a \rangle$  dislocation from a cavity, the only source of the pyramidal dislocation is the cavity itself. It is thus hard to see the various activation processes of  $\langle c+a \rangle$  slip that might be active in polycrystalline materials, in which grain boundaries (GBs) can be a source of dislocations [125].

This study focuses on the heterogeneous nucleation of  $\langle c+a \rangle$  dislocations from GBs in polycrystalline Mg. In particular, the structure and properties of both first- and second-order pyramidal  $\langle c+a \rangle$  dislocations in Mg are compared.

### 5-1. Occurrence of $\langle \mathbf{c+a} \rangle$ Slip

As reported in an earlier paper, pyramidal  $\langle \mathbf{c+a} \rangle$  slip processes are common in the  $[1\bar{1}20]$  Mg columnar texture. To activate pyramidal slip in this work, the  $[1\bar{1}20]$ -texture is strained under uniaxial stress of 1.18 GPa. After activation of pyramidal dislocations, the structure is quenched at 0.01K. The structure is characterized with CNA to distinguish FCC from HCP environments. Gray, brown and black denote atoms in HCP environments, FCC environments (in stacking faults) and non-twelve fold coordinated atoms, i.e., non- HCP or FCC (in dislocations and grain boundaries) atoms. In the  $[1\bar{1}20]$ -textured structure, only partial dislocations are generated from GBs under low applied stresses. As discussed previously [5, 126], the structure labeled  $\alpha$  in Fig. 5-1(a) is a  $1/6\langle 20\bar{2}3 \rangle$  pyramidal  $\langle \mathbf{c+a} \rangle$  dislocation. At higher applied stresses, a transition of the partial  $\langle \mathbf{c+a} \rangle$  dislocation into two different structures takes place. Figures 5-1 (b) and (c) show the structures for a stress of 1.45 GPa. One of the regions of the  $\langle \mathbf{c+a} \rangle$  partials is of the extended type, as seen in Fig. 5-1 (b). The extended  $\langle \mathbf{c+a} \rangle$  pyramidal dislocations are denoted  $\alpha'$ . The other high stress region is denoted  $\alpha''$  in Fig. 5-1 (c). It seems not to be an extended dislocation, but rather the result of the connection of long and short partial pyramidal dislocations. In these simulations, the  $\alpha''$  structure is generally produced at higher stress than the  $\alpha'$ . Pyramidal  $\langle \mathbf{c+a} \rangle$  slip is also found in a simulation of the  $[10\bar{1}0]$ -textured microstructure at an applied stress of 1.24GPa. In Fig. 5-1 (d),  $\beta$  and  $\beta'$  indicate partial and extended pyramidal  $\langle \mathbf{c+a} \rangle$  dislocations, respectively. However,  $\langle \mathbf{c+a} \rangle$  slip nucleation appears to be less frequent in the  $[10\bar{1}0]$ -texture than in the  $[1\bar{1}20]$ -texture. Moreover, there is a difference between

$\langle c+a \rangle$  partials in the  $[1\bar{1}20]$ - and  $[10\bar{1}0]$ -textured polycrystals. The  $\langle c+a \rangle$  partials can glide through a grain in the  $[1\bar{1}20]$  texture, via a stacking fault mechanism. However, after being activated in the  $[10\bar{1}0]$ -texture, the partial denoted as  $\beta$  in Fig. 5-2(d) is unstable, and hence immediately transforms into an extended  $\langle c+a \rangle$  dislocation.

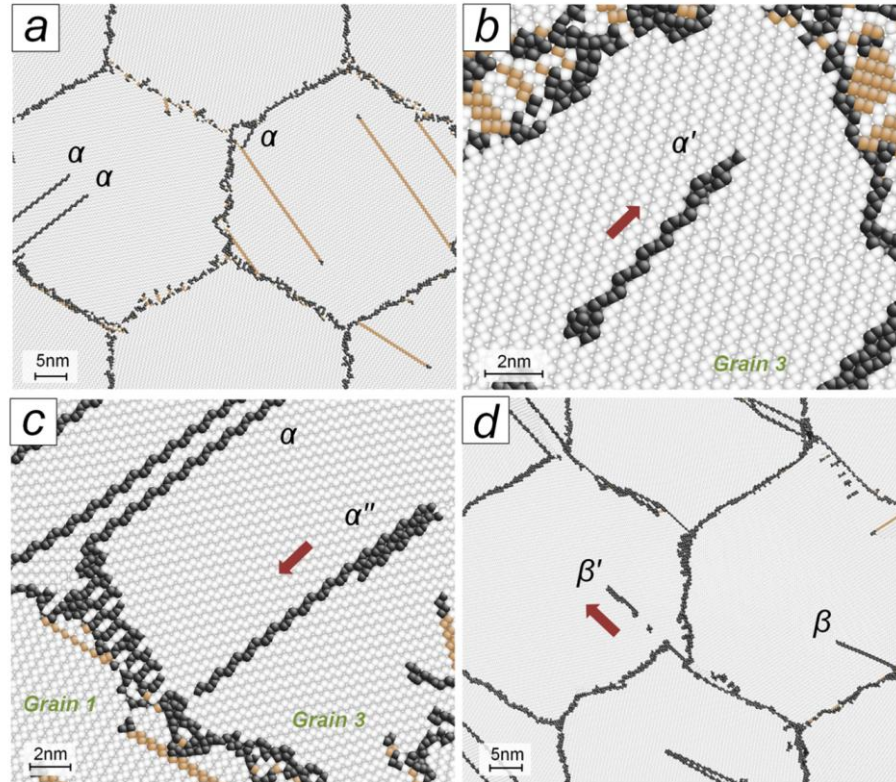


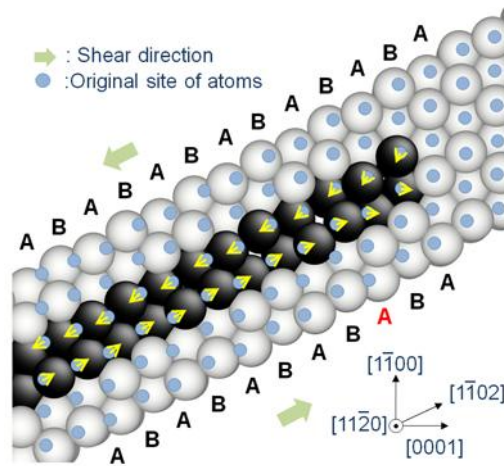
Figure 5-1. Snapshots of pyramidal  $\langle c+a \rangle$  slip activated in  $[1\bar{1}20]$ - and  $[10\bar{1}0]$ - textured structures. Gray, black and brown denote normal (HCP), disordered (non-HCP or FCC), and stacking fault (FCC) atoms respectively. Arrows denote the directions in which the  $\langle c+a \rangle$  dislocations move. (a) The partial  $\langle c+a \rangle$  pyramidal ( $\alpha$ ) and basal dislocations, shown as brown lines, are nucleated at 1.18GPa. (b) Extended pyramidal dislocation,  $\alpha'$ , is activated at 1.45GPa. Its shape changes during glide. (c) Two connected partial dislocations,  $\alpha''$ , appear at 1.45GPa. (d) Pyramidal  $\langle c+a \rangle$  dislocations with partial ( $\beta$ ) and extended types ( $\beta'$ ) are found during deformation in  $[10\bar{1}0]$ - textured Mg.

## 5-2. Structures of $\langle c+a \rangle$ Dislocations

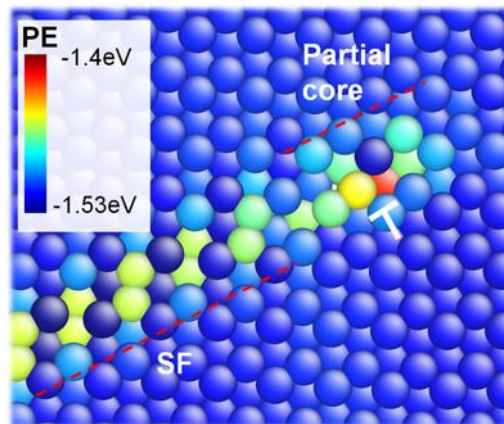
We first examine the partial and extended dislocations appearing in the  $[1\bar{1}\bar{2}0]$ -textured structure. To understand the mechanism of partial slip, the structure of the leading core connected to a stacking fault is illustrated in Fig. 5-2; the  $\langle c+a \rangle$  dislocation is seen as black atoms among the atoms in HCP environments (gray). Blue dots denote the positions of the atoms before slip. The HCP stacking sequence in a basal direction is represented as alternating 'A' and 'B' layers. Green arrows denote directions of the shear stress that causes the slip. In the non-basal SF, the atomic displacement, indicated by the yellow arrows is parallel to  $[1\bar{1}02]$  and normal to  $[1\bar{1}\bar{2}0]$ . These two directions are on the  $\{10\bar{1}\}$  plane between two  $\langle c+a \rangle$  pyramidal slip planes previously illustrated in Fig. 2-1 (a); hence, the depicted dislocation is a first-order pyramidal partial. The observed dislocation has a partial core and stacking fault (SF), as shown in Fig. 5-2(b). The pyramidal  $\langle c+a \rangle$  dislocation line exists in the  $[1\bar{1}\bar{2}0]$  direction, indicated as ' $\perp$ ' in Fig. 5-2(b). The potential energy (PE) of atoms in dislocation structure is also shown in Fig. 5-2(b). Although the atom positions show some disorder at the core of the partial dislocation, a stacking fault is formed by coordinated atomic motion. The two layers of the stacking fault colored in black move in opposite directions: one along  $1/12[20\bar{2}\bar{3}]$ , the other along  $1/12[\bar{2}0\bar{2}\bar{3}]$ . These opposite atomic displacements combine to produce  $1/6[20\bar{2}\bar{3}]$  partial slip, as shown previously in [23].

An extended pyramidal dislocation in the  $[1\bar{1}\bar{2}0]$ -texture is more complicated than the partial dislocation. CNA results and PEs of the extended dislocation are shown in Figs. 5-3(a) and (b), respectively. The extended dislocation can be divided into leading

and trailing partials connected with a SF, see Fig. 5-3(a). The regions with high PE in Fig. 5-3(b) correspond to the leading and trailing partial cores. Extra half planes are found near the cores. There is a boundary of layers, denoted by the dotted (blue) line, at the upper side of the extended dislocation. The nature of this boundary will be discussed below in connection with sequential slip that leads to the formation of an extended dislocation.



(a)



(b)

Figure 5-2. Common neighbor analysis (CNA) and potential energy (PE) map of the partial pyramidal dislocation in the  $[11\bar{2}0]$ -textured structure. The white '⊥' denote the cores of the edge dislocations in (b).

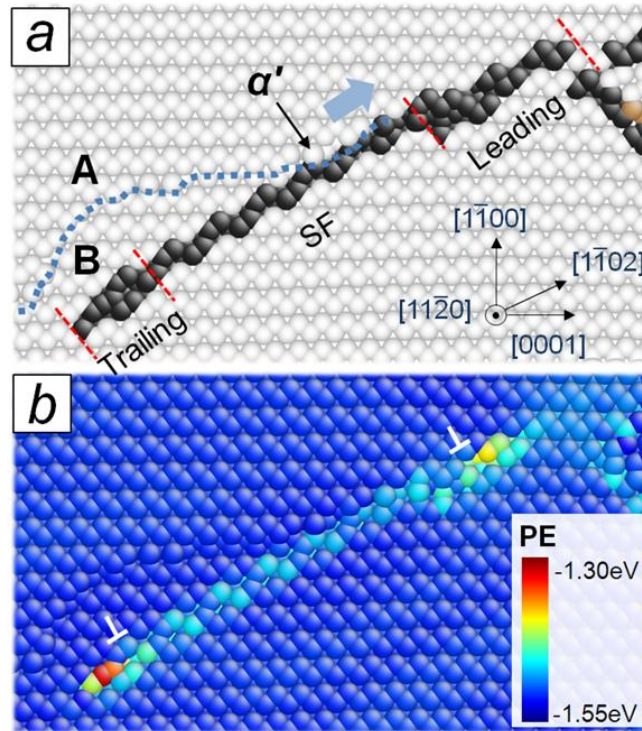


Figure. 5-3. CNA and PE map of the extended pyramidal dislocation observed in the  $[1\bar{1}20]$ -textured structure. (a)  $\alpha'$  denotes the extended  $\langle c+a \rangle$  dislocation. Blue dots indicate a boundary of different layers: A and B denote different layer in the direction of  $[1\bar{1}20]$ . (b) The white 'L' represent the cores of the edge dislocations.

The structures of the leading and trailing partials are characterized in detail in Fig. 5-4. Among the three stacking fault lines (layers I, II, and III) of the trailing core, layers II and III move in opposite directions, as indicated by the yellow arrows in Fig. 5-4(a). To quantitatively determine their displacements, the atomic structure of layers I, II, and III are illustrated in Fig. 5-4(c). The slip of layers II and III is  $1/12[2\bar{0}23]$  and  $1/12[\bar{2}0\bar{2}3]$ . They thus form a total of  $1/6[2\bar{0}23]$  partial slip, in the same manner as shown earlier in Fig. 5-2. The atomic structure of the dislocation core in the leading partial is also exhibited in Fig. 5-4(b). Each atom moves in the direction denoted by the yellow

arrows. Some atomic displacements are not parallel to the glide direction of the extended pyramidal dislocation in the leading core of Fig. 5-4(d). In the leading core, all the atomic displacements collectively make two components of partial slip:  $1/18[4\bar{2}\bar{6}3]$  and  $1/9[1\bar{1}03]$ . Figure 5-5 shows the Burgers vectors of the extended pyramidal dislocation in the HCP unit cell. The three partials observed in the leading and trailing parts produce perfect pyramidal slip:

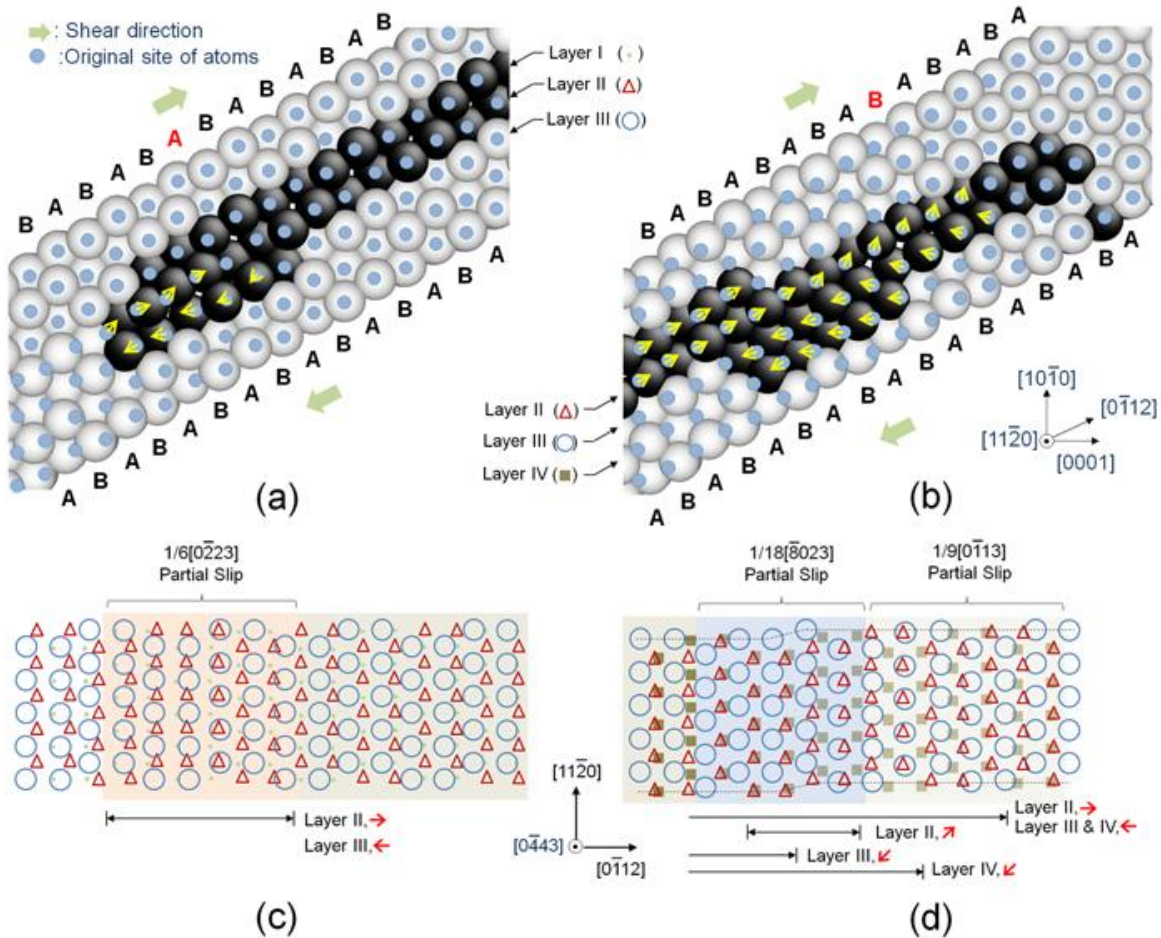


Figure 5-4. Atomic structures of a (a) leading and (b) trailing of the extended  $\langle c+a \rangle$  dislocation including CNA. (c) and (d): corresponding atomic displacement on the 1<sup>st</sup> order pyramidal slip plane,  $(10\bar{1}1)$ .



$$1/9[0\bar{1}13] + 1/18[\bar{6}243] + 1/6[0\bar{2}23] \rightarrow 1/3[\bar{1}123] \quad (5-1)$$

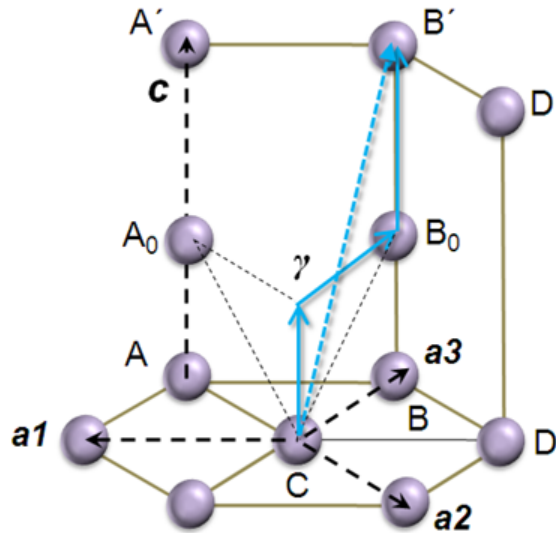


Figure 5-5. Burgers vectors of the 1<sup>st</sup> order pyramidal extended dislocation shown in the HCP unit cell.

In the above, it has been demonstrated that the  $\langle \mathbf{c} + \mathbf{a} \rangle$  dislocations in the  $[1\bar{1}20]$ -textured structure lie on the first-order pyramidal plane, appearing either as partials or as fully extended dislocations. Now we focus on the pyramidal dislocations found in the  $[10\bar{1}0]$ -texture. In order to characterize their structure, the atomic-level details of the  $\langle \mathbf{c} + \mathbf{a} \rangle$  dislocation found in the  $[10\bar{1}0]$  texture of Fig. 5-1 are shown in Fig. 5-6. The CNA analysis in Fig. 5-6(a) shows that the dislocation has an extra half-plane parallel to the basal direction. The dislocation seems to be divided into two different parts, as seen in the potential energy map of Fig. 5-6(b). The head partial, which contains a series of high-energy atoms, lies parallel to the z-direction,  $[10\bar{1}0]$ . The left image of Fig. 5-6(b)

shows that the head core extends to the basal plane. This extended plane connects to the tail part, seen as an angular plane. This shape is quite different from the extended pyramidal dislocation formed in the  $[1\bar{1}20]$ -textured structure. Because the structures of the head and tail partials are keys to understanding a formation mechanism of the extended  $\langle\mathbf{c}+\mathbf{a}\rangle$  dislocation, they are displayed in further detail in Fig. 5-7.

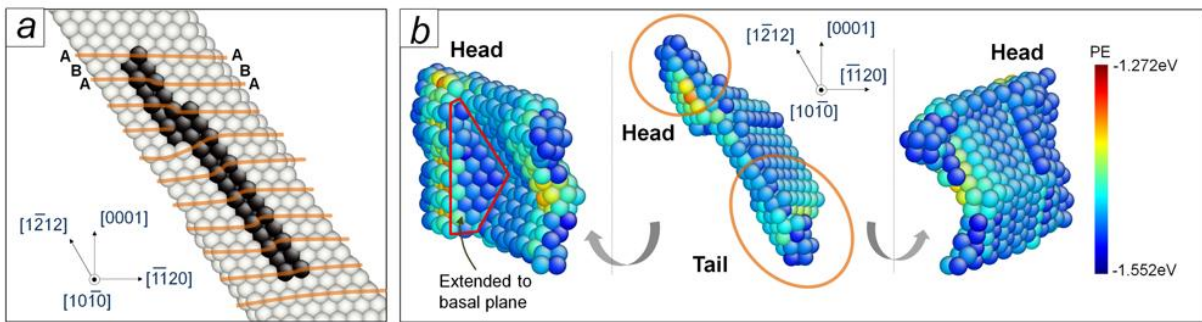


Figure 5-6. (a) CNA and (b) PE map of the pyramidal  $\langle\mathbf{c}+\mathbf{a}\rangle$  dislocation activated in the  $[10\bar{1}0]$ -textured structure.

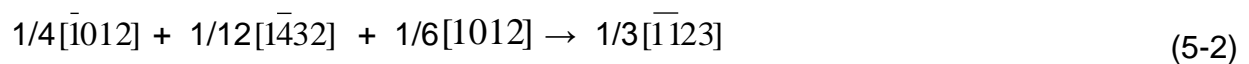
Figure 5-7 shows CNA images projected on both the  $(10\bar{1}0)$  and  $(0001)$  planes in the two left columns, while the potential energy (PE) on  $(0001)$  is mapped in the right column. The first- and second-order pyramidal  $\langle\mathbf{c}+\mathbf{a}\rangle$  slip planes are seen as semi-transparent red and blue. Blue dots and yellow arrows denote the sites of atoms before slip and the atomic displacement, respectively. The stacking sequence of HCP in the basal direction is also seen as 'A' and 'B'. Slip on the secondary  $\langle\mathbf{c}+\mathbf{a}\rangle$  plane can be seen in the CNA results of Fig. 5-7(a). Referring to the  $(0001)$  oriented CNA figure, the yellow arrows indicate that the atoms do not displace in the same direction as in secondary pyramidal slip. The difference in the slip behavior at each atomic layer

parallel to the slip plane is due to the motion of zonal dislocations known to typically occur in pyramidal slip [21]. The zonal dislocations appear as zigzag 'shuffling' displacements. They are also known to make displacement of  $\sim 1/4b^*c$  ( $[1\bar{1}2\bar{3}]$ ), see Fig. 5-5 [21]. Most of the atomic displacements shown in the vicinity of secondary pyramidal slip plane,  $\{1\bar{1}2\bar{2}\}$ , of Fig. 5-7 are also  $\sim 1/4b^*c$ . In addition, the PEs of atoms on the slip plane are higher than those of bulk HCP atoms. The next basal layer of the cross section of Fig. 5-7 (a) along is shown in Fig. 5-7 (b). The secondary pyramidal slip has progressed more in Fig. 5-7 (b), as evidenced by atomic displacements and PEs on the slip plane of Fig. 5-7 (b). As shown in the (0001)-oriented CNA result of Fig. 5-7(a), the atomic displacement takes place on one layer parallel to the secondary  $\langle c+a \rangle$  slip plane of  $(1\bar{1}2\bar{2})$ ; yellow arrows form a monolayer in the  $[1\bar{1}2\bar{0}]$  microstructure. Two layers move, however, by individual displacement of atoms adjacent to the slip plane, as shown by the two yellow arrows in the (0001)-oriented CNA result of Fig. 5-7(b). As the secondary pyramidal slip progress, a region of atoms with high PEs appears between the secondary pyramidal slip plane and an angular boundary in the (0001)-oriented PE map of Fig. 5-7(b). This implies that additional displacements occur on a basal plane by the motions of zonal dislocations on a second pyramidal plane. The stress on the basal plane thus activates slip on the first-order pyramidal plane of  $(10\bar{1}1)$ , as exhibited in Fig. 5-7(c). The extended pyramidal dislocation is thus revealed to contain both first- and second-order pyramidal slip. As already observed in Fig. 5-6(a), the secondary pyramidal slip is edge type, as evidenced by an extra half plane of

atoms. However, because the first-order  $\langle \mathbf{c+a} \rangle$  partial slip doesn't show an extra-half plane, it appears to be a screw dislocation.

Figure 5-8 exhibits the tail partials of the extended  $\langle \mathbf{c+a} \rangle$  dislocation structure in the  $[10\bar{1}0]$  texture. The semi-transparent red and blue sheets denote the first- and second-order pyramidal slip planes, respectively. The atomic displacements associated with slip are represented by green arrows. The edge dislocation line of the secondary  $\langle \mathbf{c+a} \rangle$  slip is denoted  $\vec{t}_e$  in Figs. 5-8(a) and (b). The first-order pyramidal slip is initiated in Fig. 5-8(b). As shown in the  $(0001)$ -oriented CNA result of Fig. 5-7(c), the atomic motions occur along  $\langle 11\bar{2}0 \rangle$ . However, as Fig. 5-8(c) shows, the atomic motions change to the pyramidal  $\langle \mathbf{c+a} \rangle$  direction. The presence of a screw dislocation can be seen in Figs. 5-8(g) and (h). Although the same plane is seen in both, in Fig. 5-8(g) line  $\alpha$  is disconnected, and line  $\beta$  is continued, while in Fig. 5-8(h) the line  $\alpha$  is continued, and line  $\beta$  is disconnected. This feature is typical of screw dislocations. Hence, the pyramidal dislocation at the trail partial is screw type, having a dislocation line,  $\vec{t}_s$ .

In the above analyses, both first-order [114, 117, 118, 123, 124] and second-order [113, 115, 116, 119-122] pyramidal dislocation structures have been considered. For the first-order pyramidal plane, Liang and Bacon [118] studied the pyramidal slip on the  $\{10\bar{1}1\}$  plane using a Lennard-Jones potential. They identified a dissociation reaction:



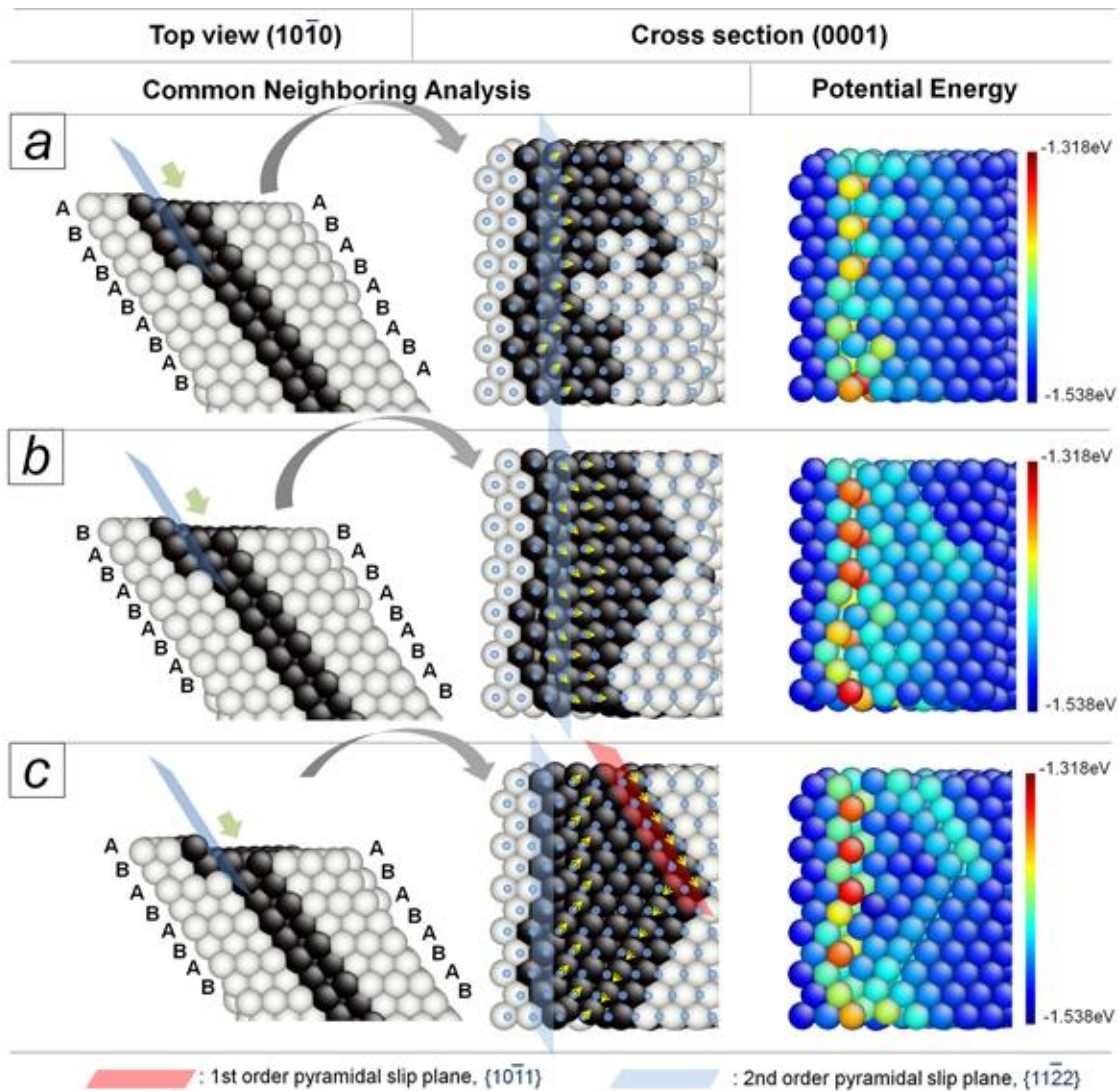


Figure 5-7. CNA visualization and PE mapping of the extended  $\langle c+a \rangle$  pyramidal dislocation projected onto the  $(10\bar{1}0)$  and  $(0001)$  planes. Atomic structures where one and two layers of top basal surface are removed at (a) are shown at (b) and (c), respectively. 'A' and 'B' represent the stacking sequence of HCP in the basal direction. The shear direction is marked by the green arrow.

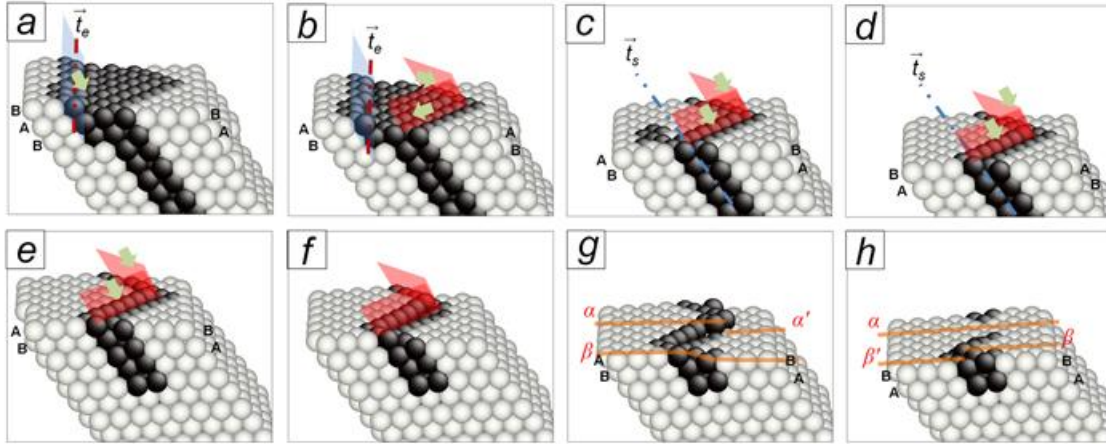
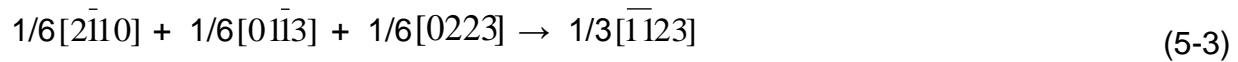


Figure 5-8. Layer structures of the extended pyramidal  $\langle \mathbf{c+a} \rangle$  dislocation in the  $[1\bar{0}\bar{1}0]$ -texture by CNA. The semi-transparent red and blue sheets denote the first- and second-order pyramidal slip planes, respectively. 'A' and 'B' represent the stacking sequence of HCP in the basal direction. The direction of local slip is seen as a green arrow.  $\vec{t}_e$  and  $\vec{t}_s$  indicate a dislocation line of screw and edge, respectively.  $\alpha\alpha'$  and  $\beta\beta'$  denote discontinuous atomic layers in the basal direction. However, each atom has less level difference than atomic radius ( $1.6\text{\AA}$ ) in continuous lines of  $\alpha$  or  $\beta$ .

Li and Ma suggested a dissociation process of the first-order  $\langle \mathbf{c+a} \rangle$  dislocation in

Mg:



Although their Mg EAM potential [127] is the same as that used in this work, the reaction in Eq. 5-3 is quite different from that seen in our simulations:



This mechanism was previously reported by Jones and Hutchinson [114]. Using a hard sphere model for a titanium alloy (Ti-6Al-4V), they characterized the first-order pyramidal slip as dissociated. Thus, at this point, there is a question as to why the same dissociation process takes place in both Mg and Ti. While Mg has an essentially

spatially isotropic electronic structure of s and p orbitals [126], the  $3d^2$  orbitals of Ti make it strongly anisotropic [126]. Such an anisotropy is responsible for the non-ideality in the  $c/a$  ratio and differences in the dominant slip mode: Mg and Ti have basal and prismatic slip as a dominant slip mode, respectively [128]. It is important to note that the work by Jones and Hutchinson [114] was performed using an intrinsically isotropic hard-sphere model. Hence, it is not surprising that the partial dissociations they observed are the same as those we see in Mg.

The secondary  $\langle \mathbf{c+a} \rangle$  edge dislocation is known to display three variants [120, 122]. Type I is a perfect dislocation, while Type II consists of two  $1/2 \langle \mathbf{c+a} \rangle$  partials. The Type I transforms to the Type II on heating from 0K to 293K [116]. The dissociation reaction of Type II is:



Morris et al. [122] suggested a Type III variant, in which the dissociation is different:



Partial edge cores of Type II are found in the  $[10\bar{1}0]$ -textured structure in our simulations. In contrast to these reactions, pyramidal dislocations in the  $[10\bar{1}0]$ -textured structure have both edge and screw components. Considering a screw dislocation, there are two issues to be compared to previous studies. First, the screw dislocation is likely to cross-slip: it has been reported that a  $\langle \mathbf{c+a} \rangle$  screw dislocation spreads on two  $\{10\bar{1}0\}$  first-order pyramidal planes at 0K [116]. Yoo et al. [112] concluded that a  $\langle \mathbf{c+a} \rangle$  screw dislocation may split on multiple slip planes, e.g.  $\{10\bar{1}0\}$  and  $\{1\bar{1}2\bar{2}\}$ . In the  $[10\bar{1}0]$ -

textured structure the pyramidal  $\langle \mathbf{c+a} \rangle$  dislocation takes place by cross-slip on the first- and second-order slip planes mediating a basal plane (see Figs. 5-7 and -8). The screw core also appears as a junction of two  $\{10\bar{1}0\}$  planes in this simulation. Second, the secondary  $\langle \mathbf{c+a} \rangle$  edge dislocation becomes immobilized: the secondary pyramidal edge dislocations of Type II is known to be sessile at  $> 30\text{K}$  because of the extended core along the (0001) [116]. Type III is also sessile with a basal stacking fault, as seen in Eq. 5-6 [122]. This spreading of the second-order pyramidal dislocation on the basal plane was already observed in Figs. 5-6, -7 and -8. This non-planar core spreading in HCP causes dislocations to be sessile [128]. The immobilization of secondary  $\langle \mathbf{c+a} \rangle$  edge dislocations may be one of the reasons why it is difficult to form long partial  $\langle \mathbf{c+a} \rangle$  dislocations in the  $[10\bar{1}0]$ -texture, as previously mentioned in Section 5-1.

### 5-3. Activation Process of $\langle \mathbf{c+a} \rangle$ Dislocations

The simulations described above show that  $\langle \mathbf{c+a} \rangle$  pyramidal slip processes are more easily observed in the  $[1\bar{1}20]$ -texture than in the  $[10\bar{1}0]$ -texture. Hence, first-order pyramidal slip in the  $[1\bar{1}20]$ -texture takes place more easily than second-order pyramidal slip in the  $[10\bar{1}0]$ -texture. This is in disagreement with the experimental findings that secondary pyramidal slip on  $1/3\{1\bar{1}22\} \langle \bar{1}\bar{1}23 \rangle$  dominates in Mg. To address this discrepancy, we compare the atomic motion, potential energies, and stacking fault energies of pyramidal edge dislocations in the two textures.

In the  $[1\bar{1}20]$ -texture the first-order partial pyramidal dislocation,  $1/6[20\bar{2}3]$ , arises from partial motion of two adjacent layers,  $\sim 1/12[20\bar{2}3]$  and  $1/12[\bar{2}023]$ , as previously shown in Fig. 5-2. By contrast, the core of secondary pyramidal slip with edge type is

obtained by full motion of only one layer with zonal behavior in Fig. 5-7. For the purposes of an energy analysis of the 1<sup>st</sup> and 2<sup>nd</sup> order pyramidal dislocations, the distributions of total strain energy per Burgers vector are represented in Fig. 5-9 as a function of distance from the centers of dislocation cores. The total strain energy ( $E_{\text{total}}$ ), expressed by adding core and elastic strain energy ( $E_{\text{core}} + E_{\text{elastic}}$ ) [129], is useful for analyzing the size and energy of a dislocation core. Pyramidal dislocations are partial or extended types in this work: the 1<sup>st</sup> and 2<sup>nd</sup> pyramidal dislocations are connected with a  $\{10\bar{1}1\}$  SF and with screw dislocation consisting of two  $\{10\bar{1}1\}$  planes, respectively. In order to focus on the edge cores of pyramidal slip, we examine the total strain energy of core regions ( $E_{\text{core}}$ ) rather than that of the elastic region ( $E_{\text{elastic}}$ ). The magnitude of Burgers vector ( $\mathbf{b}$ ) for both partial pyramidal slip is 3.2Å; the total strain energy is plotted to  $3.75\mathbf{b}$ , as shown in Fig. 5-9. Taking the dislocation core size to be  $3\mathbf{b}$  [129-132], it is possible to estimate the core energy from Fig. 5-9. The second-order pyramidal dislocation core in the  $[10\bar{1}0]$ -texture is found to have much higher strain energy than the first-order pyramidal slip in the  $[1\bar{1}20]$ -texture.

In addition, analysis of stacking faults energies (SFEs) in Mg from various simulation and experimental methods are compared in Table 5-1. The SFEs in the present work were determined from SF regions > 5nm apart from a core, created in polycrystalline by partial slip. Since there has been little analysis of SFEs on the  $\langle \mathbf{c}+\mathbf{a} \rangle$  plane, we tried to obtain consistency of our results through comparing well-known SFEs on the basal plane. The calculated energies of basal intrinsic stacking fault-1 (ISF-1) and -2 (ISF-2) are less than those which were reported by Liu[127]. This discrepancy may be caused by imperfect relaxation of our polycrystalline structure due to the

presence of residual stress after partial slip process; by contrast single crystals having no other defects would allow complete stress relaxation. However, our SFEs are still in the range of values experimentally reported. As shown in Table 5-1, the SFE on the second order  $\langle \mathbf{c}+\mathbf{a} \rangle$  slip plane,  $253 \text{ mJ/m}^2$  is twice that of the SFE on the first order  $\langle \mathbf{c}+\mathbf{a} \rangle$  slip plane,  $122 \text{ mJ/m}^2$ . The second-order pyramidal  $\langle \mathbf{c}+\mathbf{a} \rangle$  dislocations did not show long SFs connecting their partial cores, whereas long SFs are easily produced in the first order  $\langle \mathbf{c}+\mathbf{a} \rangle$  dislocations. Presumably, this is a result of the differences in their SFEs.

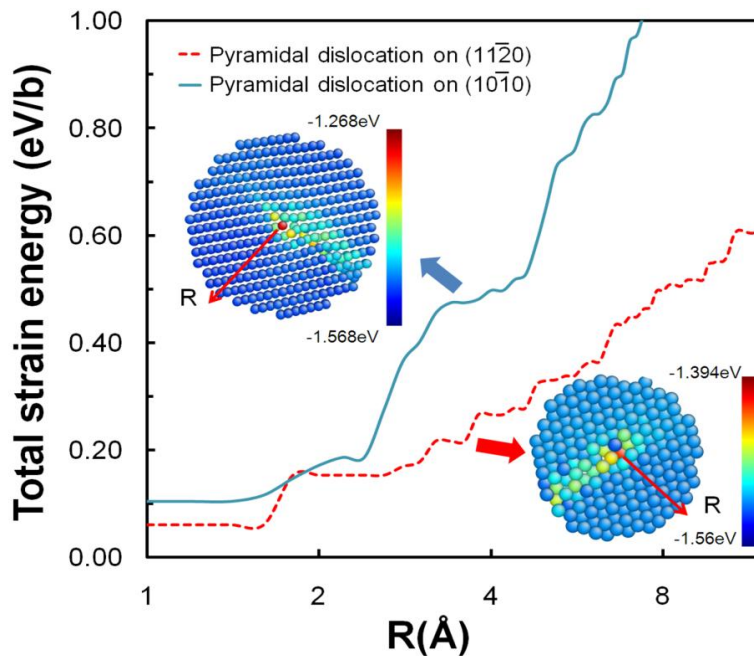


Figure 5-9. Potential energy distributions (snapshots) and strain energy curves within cylinders of radius  $R$  having a center of an edge pyramidal  $\langle \mathbf{c}+\mathbf{a} \rangle$  dislocation line.

In summary, the atomic motions and partial core energies explain the more frequent occurrence of the first-order pyramidal dislocation. Although the second-order  $\langle \mathbf{c}+\mathbf{a} \rangle$  edge dislocations nucleate GBs, their non-planar structure prevent them from

gliding inside a grain. As local stress is concentrated at these sessile dislocations, however, the nucleated partials become mobile. Due to their high SFEs, they normally appear as extended dislocations rather than partial cores separated by long SFs. Moreover, the high SFE of second pyramidal  $\langle c+a \rangle$  slip indicates that the second order  $\langle c+a \rangle$  slip are likely to be a screw type or dissociated ( $\langle c+a \rangle \rightarrow$  sessile  $\langle c \rangle +$  glissile  $\langle a \rangle$ ) processes rather than pure edge type, as reported in previous studies [113].

Table 5-1. Stacking fault energies in magnesium

	Stacking Fault Energy ( $E_{sf}$ , mJ/m <sup>2</sup> )				Method
	Basal $\langle a \rangle$ , (0001)		1 <sup>st</sup> order $\langle c+a \rangle$	2 <sup>nd</sup> order $\langle c+a \rangle$ slip	
	ISF-1	ISF-2	slip plane, $\{10\bar{1}1\}$	plane, $\{1\bar{1}2\bar{2}\}$	
This work	24 27	48 54	122 121, 225	253 198	MD (poly), Liu EAM MD (single), Liu EAM
Nogaret [133]	-	44	118, 240	x	MD (single), Sun EAM
	-	-	180	236	
Morris [134]	-	-	-	173	
Chetty [135]	-	44	-	-	Ab initio
Jelinek [136]	18	37	-	-	
Yasi [137]	-	34	-	-	
Wang [138]	-	21	-	-	
Sastry [139]	-	78	-	-	
Devlin [140]	-	60	-	-	
Fleischer [141]	-	>90	-	-	Experiment
Couret [142]	-	<50	-	-	

It is instructive to compare these simulation results with experimental findings. Tonda and Ando [115] reported a difference in yield shear stress between first- and second-order pyramidal slip of only ~ 20%. This difference is small comparable to the critical resolved shear stress (CRSS) ratio for non-basal to basal slip. This indicates that first-order pyramidal slip of  $1/3\{10\bar{1}1\} \langle \bar{1}12\bar{3} \rangle$  should also be manifested for appropriate textures and applied stresses; activation of deformation modes in HCP metals, such as Mg, strongly depends on texture and applied stress [143]. Indeed, Li and Ma [117] also

suggested that first-order pyramidal slip takes place in MD simulation of single crystalline Mg, and identified the associated stacking faults in TEM [4].

#### 5-4. Comparison of Different Potentials

The properties of a material as determined in a simulation can depend strongly on the description of the interatomic interactions. There are two literature EAM potentials for Mg: one developed by Liu et al. [127], the other developed by Sun et al. [144]. To this point, we have adopted the Liu potential to simulate plastic deformation of nanocrystalline Mg [5, 126]. The EAM potential fitted by Sun et al. has been found to manifest more active basal slip behavior than the Liu potential, a result of the lower Peierls stress [133]. We have compared the deformation behavior as given by the Sun potential with the results above for the Liu potential [126]. We find that there are far fewer nucleation events for twinning and  $\langle\mathbf{c}+\mathbf{a}\rangle$  slip for the Sun potential [126]. In addition, intergranular cracks are frequently seen even at small plastic strains ( $< 3\%$ ) during plastic deformation process of polycrystalline sample, as shown in Fig. 5-10(b), presumably a consequence of the reduced twinning and  $\langle\mathbf{c}+\mathbf{a}\rangle$  slip activity. Such cracks are common in simulation of 3D polycrystalline Mg using Sun potential.

As described by the Liu potential, the 1<sup>st</sup> order pyramidal  $\langle\mathbf{c}+\mathbf{a}\rangle$  partial slip in the  $[1\bar{1}20]$  texture shows partial dislocations joined by long SFs; moreover the extended  $\langle\mathbf{c}+\mathbf{a}\rangle$  dislocations glide easily. In contrast, Sun potential produces comparatively short non-basal SFs often connected with a SF of FCC on the basal plane, as exhibited in Fig. 5-10(a), and less mobile extended  $\langle\mathbf{c}+\mathbf{a}\rangle$  dislocations. Comparing the structure of  $\langle\mathbf{c}+\mathbf{a}\rangle$  dislocations using Liu and Sun potentials in  $[1\bar{1}20]$  and  $[10\bar{1}0]$  textures of Mg,

there was no significant difference (Fig. 5-10), consistent with the results of Nogaret et al.[133].

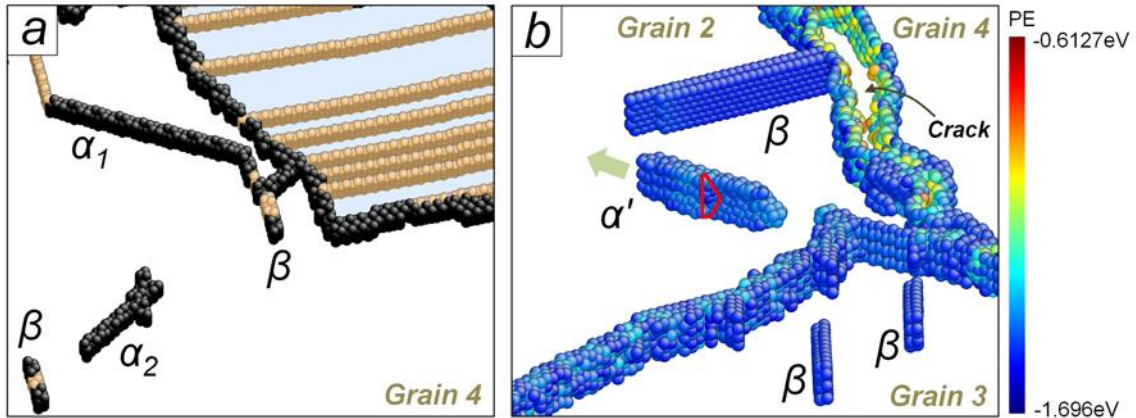


Figure 5-10. Pyramidal  $\langle \mathbf{c+a} \rangle$  dislocations simulated by Sun potential. (a) CNA image of  $[11\bar{2}0]$  texture at 1.45 GPa; black, brown and cyan denote disordered (non-HCP or FCC), stacking fault (FCC) atoms, and twinned area.  $\alpha_1$  is connected with FCC stacking faults, and  $\alpha_2$  shows two  $\langle \mathbf{c+a} \rangle$  dislocations joined on two different slip planes (b) Potential energy analysis of  $[10\bar{1}0]$  texture at 1.32 GPa in (a). Arrow indicates the directions in which the  $\langle \mathbf{c+a} \rangle$  dislocations move.  $\alpha$  and  $\beta$  denote pyramidal  $\langle \mathbf{c+a} \rangle$  and basal  $\langle \mathbf{a} \rangle$  dislocations.  $\alpha'$  has the same structure as the extended  $\langle \mathbf{c+a} \rangle$  dislocation illustrated in Fig. 5-6. An intergranular crack appears between grains 2 and 4.

### 5-5. Role of Pyramidal $\langle \mathbf{c+a} \rangle$ Dislocations in Plastic Deformation

The pyramidal  $\langle \mathbf{c+a} \rangle$  dislocations are found to play a number of roles. First, homogeneous plastic deformation requires pyramidal  $\langle \mathbf{c+a} \rangle$  slip [34, 35]. A basal or prismatic mode appears as dominant slip in HCP metals. However, if some grains require high CRSS to activate the basal or prismatic mode, the secondary slip mode, pyramidal  $\langle \mathbf{c+a} \rangle$ , should be activated for plastic deformation. Activation of this secondary mode has a direct effect on mechanical response of the material at meso- and macro levels. Single crystalline textures of Mg show noticeable differences in stress-strain curve according to the directions in which stress is applied [36]. The

activation of secondary  $\langle \mathbf{c+a} \rangle$  slip is one of the important reasons for these differing deformation responses.

Second, the interaction between  $\langle \mathbf{c+a} \rangle$  slip and twinning results in hardening. The twinning and  $\langle \mathbf{c+a} \rangle$  slip compete in grains in which basal slip is rare. Figure 5-11 shows hardening from the interaction between the  $\langle \mathbf{c+a} \rangle$  dislocation and the twinning boundary. Initially the simulated  $[1\bar{1}20]$  textures are defect-free, except for the GBs. The interaction can be thus examined between dislocations and twinning created under the external stress. To maintain the specific stress value needed for the  $\langle \mathbf{c+a} \rangle$  slip-twinning interaction, a creep test is more suitable than a tensile test. The initial textures are strained at 1.035 and 1.18GPa, showing a  $\langle \mathbf{c+a} \rangle$  dislocation-twinning interaction and only twinning in Fig. 5-11(b) and (c), respectively. While the 1.18GPa-curve shows the strain rate ( $\dot{\epsilon}_A$ ) of  $1.5 \times 10^9 \text{ s}^{-1}$ , a significant decrease ( $\dot{\epsilon}_B = 1.4 \times 10^8 \text{ s}^{-1}$ ) of strain rate appears in 1.035GPa-curve of Fig. 5-11(a). As shown in Fig. 5-11(b) and (c). We attribute this hardening to growth of the  $\{10\bar{1}2\} \langle 10\bar{1}1 \rangle$  tensile twinning blocked by the  $\langle \mathbf{c+a} \rangle$  dislocations of order  $\{10\bar{1}1\}\langle 11\bar{2}3 \rangle$ . In addition, it was experimentally reported that under compressive stress the  $\langle \mathbf{c+a} \rangle$  slip has a harmful effect on room temperature ductility of Mg: it produces severe strain hardening by dissociation to mobile  $\langle \mathbf{a} \rangle$  and immobile  $\langle \mathbf{c} \rangle$  dislocations [4, 37].

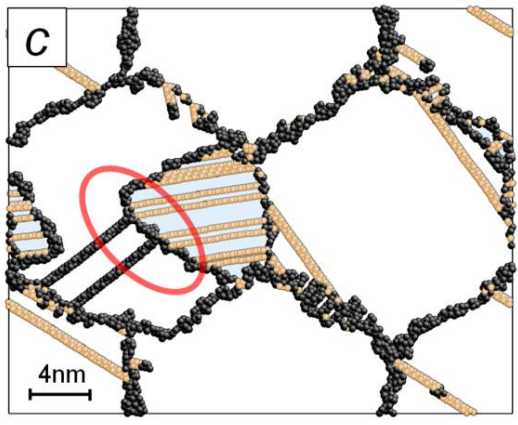
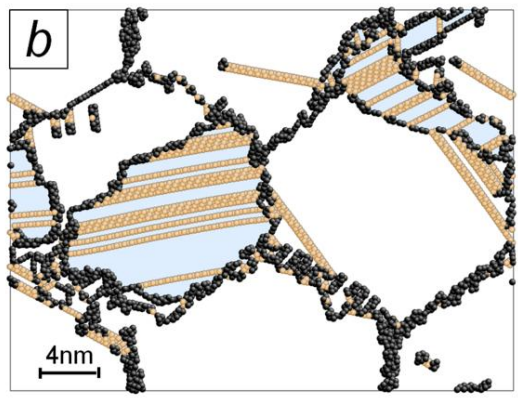
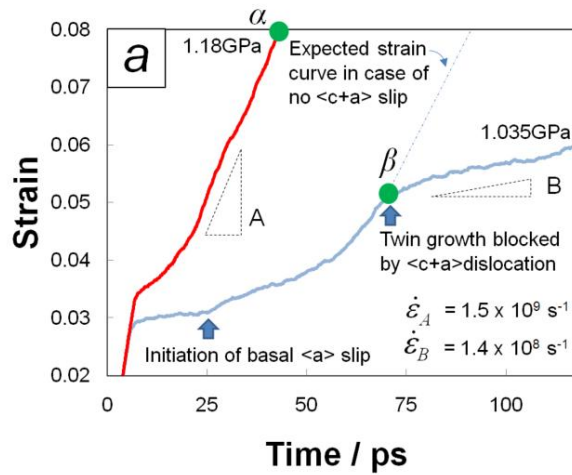


Figure 5-11. Creep curves and snapshots of strained columnar Mg with 18nm grain size. Cyan, brown and black in (b) and (c) mean a twinned region, stacking fault (FCC), disordered (non- HCP or FCC), respectively. (a) Time-strain curves at 1.035 and 1.18GPa. (b) Snapshot at  $\alpha$  of 1.18Gpa-curve. (c) Snapshot at  $\beta$  of 1.035Gpa-curve. A red circle indicates a region where an interaction between twinning and  $\langle c+a \rangle$  dislocations take place.

## 5-6. Summary

Pyramidal  $\langle \mathbf{c+a} \rangle$  dislocations were created at GBs in  $[1\bar{1}20]$ - and  $[10\bar{1}0]$ -textured Mg using MD simulation. It was found that both the first- and second-order pyramidal slip can be activated in Mg. The first-order  $\langle \mathbf{c+a} \rangle$  dislocations in the  $[1\bar{1}20]$ -texture manifested various forms, depending on the external stress. At low stress they are  $1/6 \langle \bar{2}023 \rangle$  partials. Two phases, extended dislocation and connected partials, appear at high stress. The extended type of the first-order pyramidal slip takes place through a dissociation reaction of  $1/9[0\bar{1}13] + 1/18[\bar{6}243] + 1/6[0\bar{2}23] \rightarrow 1/3[1\bar{1}23]$ . While all of the dislocations in the  $[1\bar{1}20]$  texture are of edge type, the extended secondary pyramidal dislocation in the  $[10\bar{1}0]$  texture exhibits both types of edge and screw. The edge partial appears as a leading core of the secondary  $\langle \mathbf{c+a} \rangle$  slip, formed by typical zonal dislocation in HCP metals. The partial core, due to spreading on the basal plane and high SFE, remain sessile. During deformation, stress concentration which occurs at the sessile dislocation finally causes an activation of screw dislocation on the basal plane connected with the edge core. Hence, the complex dislocation is possible to glide in the  $[10\bar{1}0]$  columnar textures without leaving SF having high energy.

Comparing the two different EAM potentials, the atomistic structures of pyramidal  $\langle \mathbf{c+a} \rangle$  dislocations are found to be very similar, though the Liu potential shows more active  $\langle \mathbf{c+a} \rangle$  slip than Sun potential.

The textured columnar nano-structures considered here are in many ways ideal for fundamental studies; however, they are optimized for edge dislocation. As a next step, large-scale randomly-oriented, non-textured Mg polycrystals will be simulated; these will

allow for a greater diversity of plastic process and allow more direct comparisons with experiment.

## CHAPTER 6 TWINNING IN 2D NANOCRYSTALLINE-MG

Three types of twinning were manifested in the deformed magnesium of 40nm grain size under a tensile load of 1.25GPa. Figure 6-1 shows  $\{10\bar{1}2\} \langle 10\bar{1}1 \rangle$  tensile twinning (A) identical to the ideal case shown in Fig. 2-6. This twin was the most prevalent. The other twins,  $\{10\bar{1}1\} \langle 10\bar{1}2 \rangle$  (B) and  $\{10\bar{1}3\} \langle 30\bar{3}2 \rangle$  (C) compressive twinning rarely appeared. The most probable twinning modes in Mg are  $\{10\bar{1}2\} \langle 10\bar{1}1 \rangle$ ,  $\{10\bar{1}1\} \langle 10\bar{1}2 \rangle$ , and  $\{10\bar{1}3\} \langle 30\bar{3}2 \rangle [145]$ , as our simulations indeed display. Having illustrated the signatures of all of the relevant microstructural features, in this chapter we address the issue of how they are created and how they evolve under applied stresses.

### 6-1. Nucleation of Twins

The deformation simulations of  $[1\bar{1}20]$ -textured Mg manifested all three expected types of twinning: tensile  $\{10\bar{1}2\} \langle 10\bar{1}1 \rangle$  twins, and compressive  $\{10\bar{1}1\} \langle 10\bar{1}2 \rangle$  and  $\{10\bar{1}3\} \langle 30\bar{3}2 \rangle$  twins. With regards to twinning nucleation, it is known that extended defect structures such as GBs and cross-slip can act a heterogeneous nucleation source of twinning [27]. The polycrystalline model used in this study provides various extended defect structures as potential nucleation sites for twinning that are not available in single crystals [76] or bicrystals [146]. In a single crystalline structure of pure Mg, the ratio  $CRSS_{twin}/CRSS_{basal}$  ranges from 2.4 to 4.4 [98], indicating that activation of slip is easier than activation of twinning. However, the simulations of the polycrystalline structure show that  $\{10\bar{1}2\} \langle 10\bar{1}1 \rangle$  tensile twinning takes place at the GBs in an early stage of a plastic deformation process. Moreover, this GB-mediated

process operates for all grain sizes studied at low stresses (0.6 to 0.9GPa) where there is no slip activity. The GBs in the polycrystalline structure thus appear to act as heterogeneous nucleation sources that decrease  $CRSS_{\text{twin}}$  for  $\{10\bar{1}2\} \langle 10\bar{1}1 \rangle$  tensile twinning. As the external stress gradually increases, the dislocation processes are activated in the grain interiors, with the high density of dislocations providing another nucleation site for the  $\{10\bar{1}1\} \langle 10\bar{1}2 \rangle$  and  $\{10\bar{1}3\} \langle 30\bar{3}2 \rangle$  compressive twins. An example of  $\{10\bar{1}1\} \langle 10\bar{1}2 \rangle$  twin formation is illustrated in Figs. 6-2(a) - (d). The nucleation of the  $\{10\bar{1}1\} \langle 10\bar{1}2 \rangle$  twin takes place at dislocation interactions, which are located in the center of a sequence of stacking faults. This nucleation of twinning by Shockley dislocations has been observed in simulation work of FCC Cu, where it occurred under the high local compressive stress arising from dislocations [147]. It is similarly noted that twinning may be nucleated from the partial dislocations that are on parallel and neighboring glide planes [148].

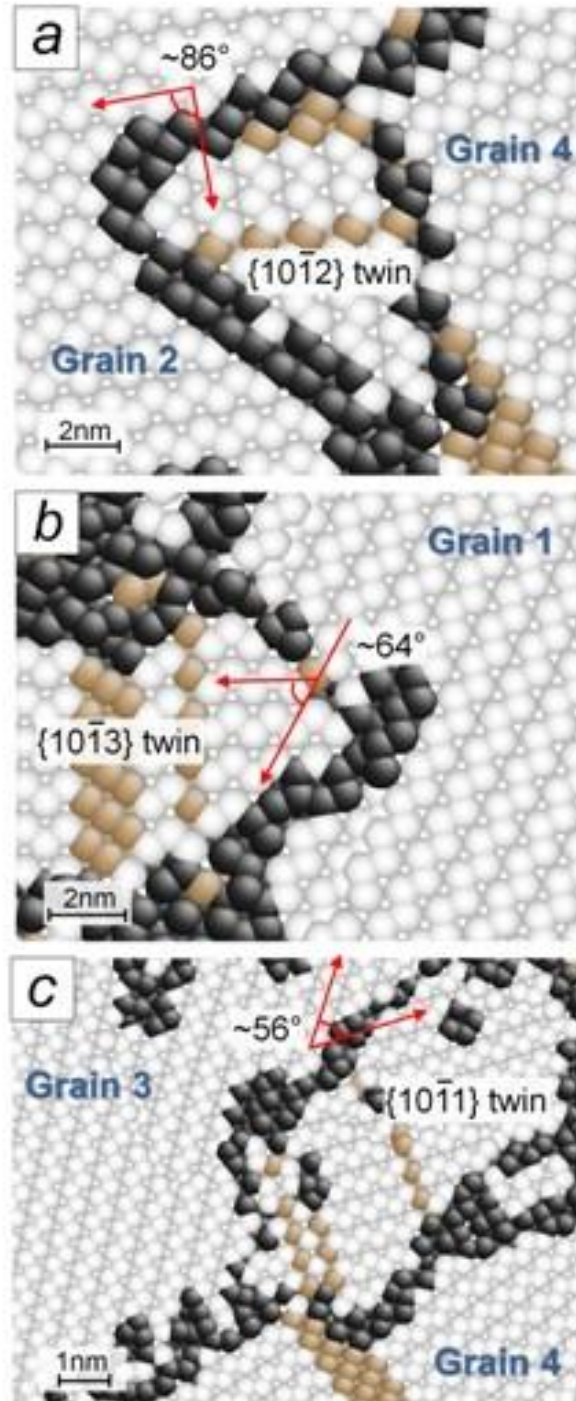


Figure 6-1. Three types of twins found during creep, from a simulation of a grain size of 40nm under 1.25GPa. (a)  $\{10\bar{1}2\} \langle 10\bar{1}1 \rangle$  tensile twinning at the boundary of grain 2 and 4, (b)  $\{10\bar{1}3\} \langle 30\bar{3}2 \rangle$  compressive twinning at the triple junction among grain 1,3, and 4. (c)  $\{10\bar{1}1\} \langle 10\bar{1}2 \rangle$  compressive twinning at the boundary of grain 3 and 4.

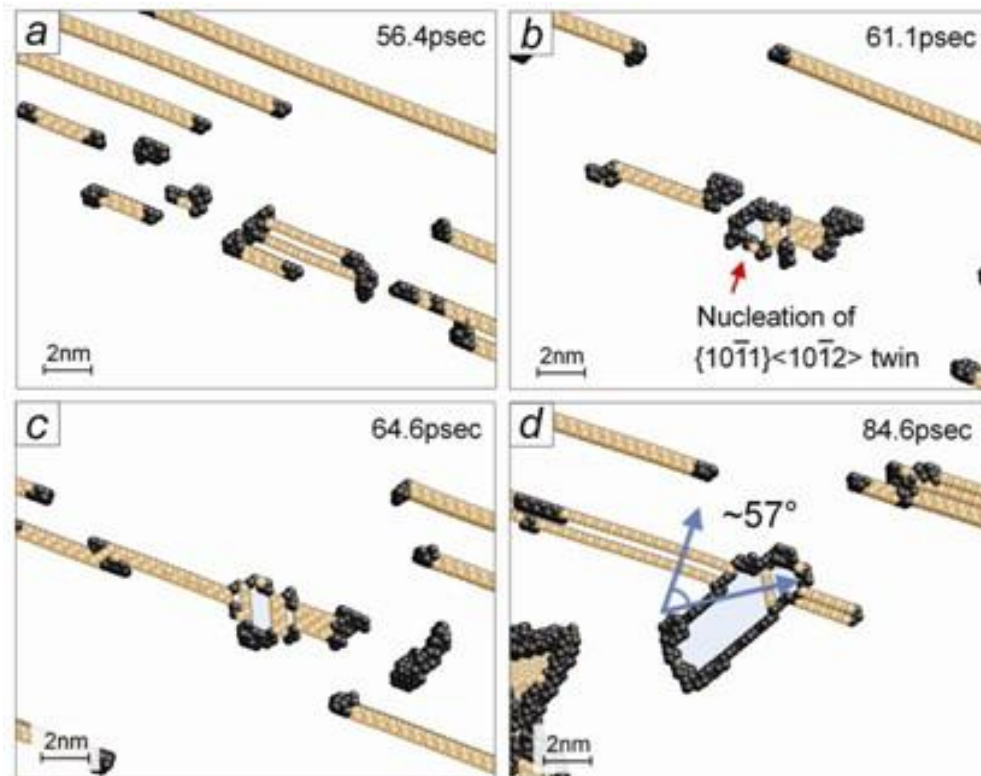


Figure 6-2. Snapshots of nucleation process of  $\{10\bar{1}1\} \langle 10\bar{1}2 \rangle$  primary twinning at the grain 1 of  $[1\bar{1}20]$ -textured structure with 40nm grain size deformed under 1.25GPa.

Here, in contrast to to the  $\{10\bar{1}2\} \langle 10\bar{1}1 \rangle$  tensile twin, the  $\{10\bar{1}1\} \langle 10\bar{1}2 \rangle$  and  $\{10\bar{1}3\} \langle 30\bar{3}2 \rangle$  compressive twins are formed by the interaction between dislocations, or between a GB and dislocations, possibly contributed by either a basal  $\langle a \rangle$  or a pyramidal  $\langle c+a \rangle$  dislocation. Thus, the compressive twins require higher stress for their nucleation. There is evidence to support our finding that the CRSS (76 to 153MPa) of the  $\{10\bar{1}1\} \langle 10\bar{1}2 \rangle$  twinning is much larger than the CRSS (2 to 3MPa) of  $\{10\bar{1}2\} \langle 10\bar{1}1 \rangle$  twinning in Mg alloys [95]. In the simulations, the  $\{10\bar{1}2\} \langle 10\bar{1}1 \rangle$  tensile twin

is nucleated only at GBs; however, the  $\{10\bar{1}1\} < 10\bar{1}2 >$  and  $\{10\bar{1}3\} < 30\bar{3}2 >$  compressive twins are nucleated both at GBs and in the interior of grains. The two compressive twins were not found for structures with grains smaller than  $\sim 18\text{nm}$ . As previously mentioned, due to the crossover of deformation mechanism from slip to GB-mediated processes, dislocation activity in nanocrystalline materials decreases at grain size below  $10 \sim 20\text{nm}$ . It can be deduced from the simulation results that the restriction of the compressive twin nucleation is caused by the decrease in slip involved in their nucleation at grain sizes below  $\sim 18\text{nm}$ . Twinning normally consists of primary and secondary (or double) types [27]. After primary twinning occurs, secondary twinning can take place within the reoriented primary twinned area [27, 149]. Although  $\{10\bar{1}1\} - \{10\bar{1}2\}$  and  $\{10\bar{1}3\} - \{10\bar{1}2\}$  double twins are frequently found experimentally [31, 149, 150], no such secondary twinning is seen here. Further study is required about the  $\{10\bar{1}3\} - \{10\bar{1}2\}$  double twin. The nucleation conditions of  $\{10\bar{1}1\} < 10\bar{1}2 >$ ,  $\{10\bar{1}2\} < 10\bar{1}1 >$ , and  $\{10\bar{1}3\} < 30\bar{3}2 >$  primary twins from 6 to 60nm grain size are summarized in Table 6-1.

Table 6-1 Nucleation conditions for  $\{10\bar{1}1\} < 10\bar{1}2 >$ ,  $\{10\bar{1}2\} < 10\bar{1}1 >$ , and  $\{10\bar{1}3\} < 30\bar{3}2 >$  primary twinning.

Twinning	Places	Mechanism	External Stress	Strain
$\{10\bar{1}2\} < 10\bar{1}1 >$	Only GB	Separation of twinning dislocation from GB	Low ( $< \sigma_f$ )	$< 0.5\%$ plastic
$\{10\bar{1}1\} < 10\bar{1}2 >$	GB or Grain interior	Interaction between dislocations or GB-	High ( $> \sigma_f$ )	$> \sim 3\%$ Plastic
$\{10\bar{1}3\} < 30\bar{3}2 >$	GB or Grain interior	Interaction between dislocations or GB-	High ( $> \sigma_f$ )	$> \sim 3\%$ Plastic

## 6-2. Nucleation Mechanism of Compressive Twinning from Grain Boundaries

The three twinning modes shown in Table 6-1 are found in  $[11\bar{2}0]$ -textured Mg. Another twin mode is found in a creep test of the  $[10\bar{1}0]$  texture, and displayed in Fig. 6-3.

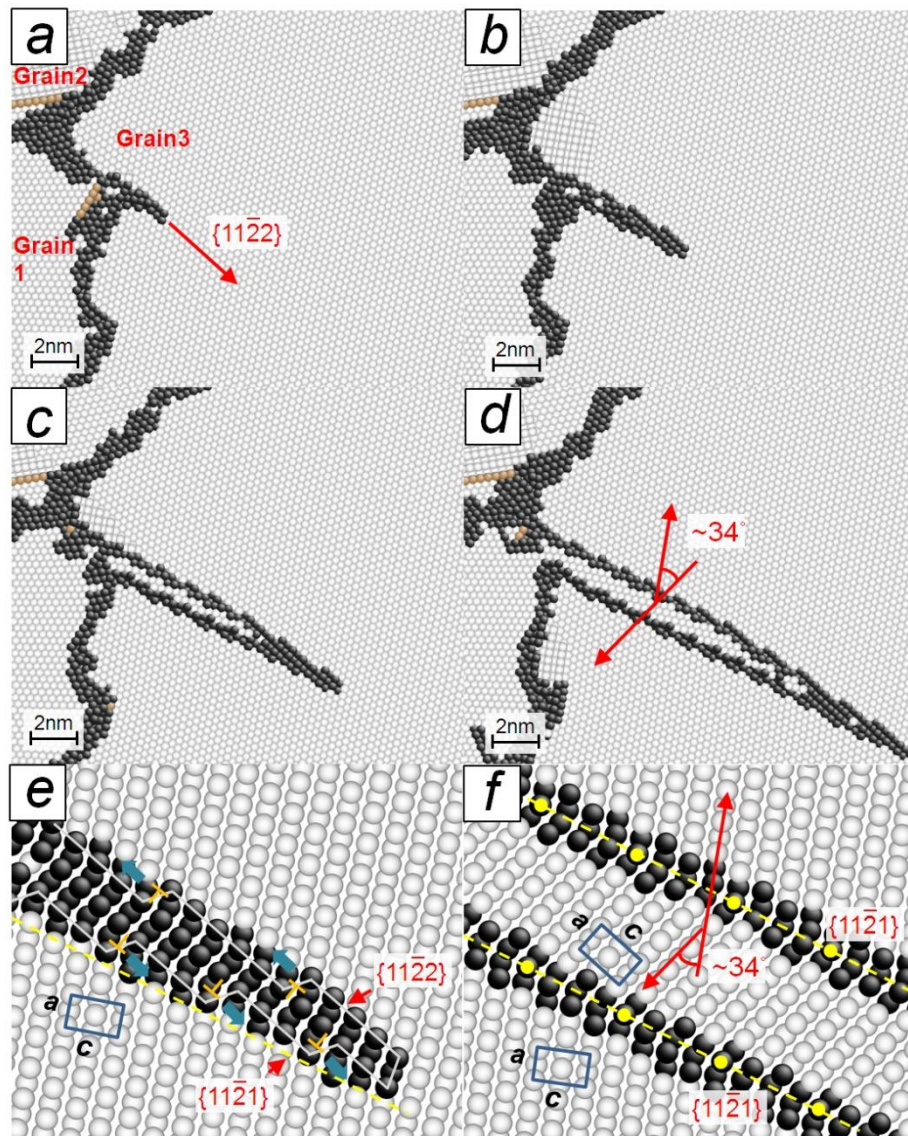


Figure 6-3.  $\{11\bar{2}2\} \langle 11\bar{2}\bar{3} \rangle$  twinning activated in the 18nm  $[10\bar{1}0]$ -textured Mg.  $a$  and  $c$  indicate lattice constants of Mg in (e) and (f).

First pyramidal  $\langle \mathbf{c+a} \rangle$  slip appears from the GB in the 18nm  $[10\bar{1}0]$ -textured Mg sample strained at 1.2 GPa. The  $\langle \mathbf{c+a} \rangle$  slip occurs on the second-order pyramidal plane,  $\{11\bar{2}2\} \langle 11\bar{2}3 \rangle$  in Fig. 6-3(a). After growing to  $\sim 5$ nm, the  $\langle \mathbf{c+a} \rangle$  edge dislocation is changed to  $\{11\bar{2}2\} \langle 11\bar{2}3 \rangle$  twinning (see Fig. 6-3(a) - (d)). In the previous chapter, we observed second-order  $\langle \mathbf{c+a} \rangle$  dislocation cross-slipping to first-order pyramidal plane in  $[11\bar{2}0]$ -textured Mg. Thus, the second-order pyramidal slip can choose either a transformation to the other  $\langle \mathbf{c+a} \rangle$  slip, or twinning. The  $\{11\bar{2}2\} \langle 11\bar{2}3 \rangle$  twin mode has not been experimentally found in Mg [27]. It indicates that the  $\{11\bar{2}2\} \langle 11\bar{2}3 \rangle$  twin can take place under particular conditions, e.g. in the columnar texture. Indeed, some MD simulations reported activation of the  $\{11\bar{2}2\} \langle 11\bar{2}3 \rangle$  twin[151, 152].

### 6-3. Nucleation Mechanism of Tensile Twinning from GB

#### 6-3-1. Nucleation Process in a Large Grain

The nucleation of the  $\{10\bar{1}2\} \langle 10\bar{1}1 \rangle$  twin is first manifested at a boundary of a grain (A in Fig. 6-4) with the c-axis almost parallel ( $11.15^\circ$ ) to the external stress, exhibited as a series of the nucleation process in panels a to e. The  $\{10\bar{1}2\} \langle 10\bar{1}1 \rangle$  twin is initiated from atoms in a disordered inter-grain region, marked as a red circle, gradually expanding with angle  $86^\circ$  to an original texture of grain A, along the GB. In Fig. 6-4(b), a twin nucleus, noted as a red area surrounded with a yellow solid line below the disordered atoms, is formed to thickness of a few (0001) layers. The atoms in the disordered region move to a neighboring lattice site on the next basal plane, thereby growing the twin texture to the c-axis of the grain A, as shown in Fig. 6-4(c). Such a process also causes thickening of the twin to  $86^\circ$ -tilted direction from an original texture

in Fig. 6-4(d). Figure 6-4(f) and (g) are reproduced from Fig. 6-4(a) and (e) to understand an original and twined texture separated by a twin boundary. Finally, a well developed  $\{10\bar{1}2\} \langle 10\bar{1}1 \rangle$  twin is observed in Fig. 6-4(g), having a width of  $\sim 2\text{nm}$ . In summary, the nucleation process of  $\{10\bar{1}2\} \langle 10\bar{1}1 \rangle$  twin is found to consist of stepping forward to the c-axis of an original texture,  $[0001]$  and thickening with an angle of  $86^\circ$  to the c-axis. The thickening of the twin is clearly conducted by a zonal twin dislocation, as discussed extensively in the literature.[153-156].

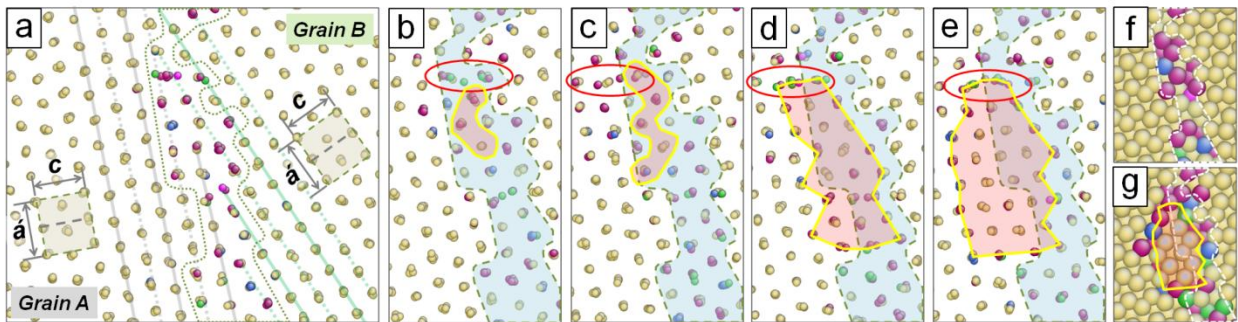


Figure 6-4. Nucleation process of  $\{10\bar{1}2\} \langle 10\bar{1}1 \rangle$  twinning from GB at 293K. Atoms having a coordination number of 9, 10, 11, 12 and 13 are shown as magenta, green, violet, yellow and blue, respectively. (a) initial GB structure. A crystallographic direction is indicated by a unit cell of HCP, having two different lattice constants of  $a$  ( $\acute{a}$  is seen due to z-direction of,  $\acute{a} = 2 a \cos 30^\circ [1\bar{1}20]$ ) and  $c$ , in grain A and B. Solid and dot straight lines note alternative stacking (ABAB) of two atomic layers in c-direction of grains A (gray) and B (green). Miscoordinated area, GB, between grains is surrounded by small black dot line. (b) ~ (e), during a tensile test, snapshots from b to e were captured at 18.8 (0.9), 21.2 (1.3), 22.3 (1.4), and 23.5psec (1.6% - removing an elastic strain in a total strain), respectively. Cyan area surrounded by a dot line indicates an initial GB. Red circle denote a cluster of disordered atoms. Transparent red inside yellow line indicates twinned atoms.(f) and (g), initial and twin-nucleated GB (23.5psec) are shown as larger atoms than in (a)~(e).

The most interesting points are the nucleation site and propagation of the twin achieved by the disordered atoms. The disordered atoms successively move through a

path of  $1/6\langle 2\bar{2}03 \rangle$  between the two closest lattice sites. On the basis of classical dislocation theory, that direction is sessile[21] with a low Schmid factor of  $< 0.1$ . Accordingly, the simulations strongly suggest that the propagation of the  $\{10\bar{1}2\} < 10\bar{1}1 \rangle$  twin occurs by migration of individual disordered atoms.

Figure 6-5 shows a proposed mechanism for the propagation of a twin in a 2-dimensional view. First, the GB structure shown in Fig. 6-4 is shown schematically in Fig. 6-5(a). If there is an atom at site III (atom-III), a very high repulsive would occur between two atoms (atom II and III) due to their small interatomic separation. This is essentially unlikely to occur in nature. Hence, site III should be vacant, as shown in Fig 6-5(a). Considering the atoms in Fig. 6-5(a), there is an overlap of the potential curves between the atom-II and vacancy-III in Fig. 6-5(b), defined as an intergrain PWO (Potential Well Overlap) site. In Fig. 6-5(c), the atomic energy should contain a contribution ( $\Delta E_T$ ) by thermal vibration at temperature T. The atom at site II, thus, has its increased energy to  $E_{RT, \text{ no stress}}$  from  $E_{0K, \text{ no stress}}$  at 0K. As soon as an external stress is applied to the x-direction, atom-II has elastic energy  $\Delta E_E$ . Atom-II has the position of  $\alpha_0$  at 0K in the absence of external stress, being affected by attractive force,  $F_B(\alpha_0)$ , arising from the potential field of vacancy shown as a blue dotted line. Because the potential is the interaction between atoms, vacancy doesn't have such an interaction. If, however, an atom approaches the vacancy, a force is generated between the atom and lattice atoms surrounding the vacancy. The effective potential field of vacancy thus indicates the interaction which the lattice atoms surrounding the vacancy act on.

The force at  $r = \alpha_0$  can be expressed in Eq. 6-1.

$$F_B(\alpha_0) = - \left. \frac{dU_B}{dr} \right|_{r = \alpha_0} \quad (6-1)$$

As discussed above, by thermal activation and applied stress, the energy of atom-II is increased from  $E_{0K, \text{ no stress}}$  to  $E_{RT, \text{ stress}}$ ; the atoms also move from  $\alpha_0$  to  $\alpha_2$ . The change of position from  $\alpha_0$  to  $\alpha_2$  increases the attractive force acting on the atom-II from the potential curve of grain B, from  $F_B(\alpha_0)$  to  $F_B(\alpha_2)$ . The total energy of the atom-II ( $\Delta E_{TOT}$ ) is thus expressed as a sum of thermal energy ( $\Delta E_T$ ), interatomic elastic energy ( $\Delta E_E$ ), and the energy ( $\Delta E_A$ ) arising from the attractive force ( $F_B$ ) of potential of grain B.

$$\Delta E_{TOT} = \Delta E_T + \Delta E_E + \Delta E_A \quad (6-2)$$

If the total energy is larger than  $\Delta E_{PWO}$ , the atom can move to III. The specific energy condition is

$$\frac{1}{2} k_b T + \int_{\alpha_1}^{\alpha_2} F_A(r) dr - \int_c^{\alpha_2} F_B(r) dr > \Delta E_{PWO} \quad (6-3)$$

where,  $k_b$  and  $T$  are the Boltzmann constant and temperature, and  $c$  is the intersection point between the blue dotted line and the  $r$ -axis.  $F_A$  and  $F_B$  are derived from  $dU_A(r)/dr$  and  $dU_B(r)/dr$ .

After that the atomic positions and potentials are changed in Fig. 6-5(d), there are two unoccupied sites, II and V: a vacancy caused by the atom which moved to III and an empty lattice point in a new potential produced by the moved atom,. Hence, atom motion is possible from I to V or from III to II.

A driving force for the successive migration can be identified by considering an applied stress acting on two textures of grain A and B. In Fig. 6-5(a), an external stress ( $\sigma = \sigma_x, \sigma_y = \sigma_z = 0$ ) is resolved to  $\sigma_{Ax}$  ( $= \sigma_x \cdot \cos \theta_A$ ) and  $\sigma_{Bx}$  ( $= \sigma_x \cdot \cos \theta_B$ ) at the  $c$ -axis of two different grains. Since  $\theta_A < \theta_B$ ,  $\sigma_{Ax} > \sigma_{Bx}$ . Each interatomic strain produced by the resolved stresses,  $\sigma_{Ax}$  and  $\sigma_{Bx}$ , at sites of I and III can be expressed as:

$$\sigma_{Ax} \propto |\beta_2 - \beta_1| \quad (6-4)$$

$$\sigma_{Bx} \propto |\gamma_2 - \gamma_1| \quad (6-5)$$

Because  $\sigma_{Ax} > \sigma_{Bx}$ , Eqs. 7.4 and 5 can be combined to give:

$$|\beta_2 - \beta_1| > |\gamma_2 - \gamma_1| \quad (6-6)$$

This result, due to  $|\beta_1 - \beta_0| = |\gamma_1 - \gamma_0|$ , means  $\beta_2$  is closer to a vacancy site than  $\gamma_2$ .

The total energy of atoms-I and -III are then given by:

$$E_{TOT, I} = \frac{1}{2}k_bT + \int_{\beta_1}^{\beta_2} F_A(r)dr - \int_c^{\beta_2} F_B(r)dr \quad (6-7)$$

$$E_{TOT, III} = \frac{1}{2}k_bT + \int_{\gamma_1}^{\gamma_2} F_B(r)dr - \int_c^{\gamma_2} F_A(r)dr \quad (6-8)$$

The energy difference ( $E_{TOT, I} - E_{TOT, III}$ ), obtained from Eqs. 7.7 and 7.8, of atoms-I and -III may indicate which process between  $I \rightarrow V$  and  $III \rightarrow II$  takes place. Considering

$U_A(\beta_1) = U_B(\gamma_1) = \frac{1}{2}k_bT$ ,  $U_A(c) = U_B(c)=0$ , the energy difference can be summarized as:

$$E_{TOT, I} - E_{TOT, III} = [U_A(\beta_2) - U_B(\beta_2)] + [U_A(\gamma_2) - U_B(\gamma_2)] \quad (6-9)$$

Because  $\beta_2$  is closer to a vacancy site than  $\gamma_2$ , the following conditions are obtained from Fig. 6-5(d).

$$U_A(\beta_2) - U_B(\beta_2) < 0 \quad (6-10)$$

$$U_A(\gamma_2) - U_B(\gamma_2) > 0 \quad (6-11)$$

$$|[U_A(\beta_2) - U_B(\beta_2)]| < |[U_A(\gamma_2) - U_B(\gamma_2)]| \quad (6-12)$$

Therefore,

$$E_{TOT, I} - E_{TOT, III} = |[U_A(\beta_2) - U_B(\beta_2)] + [U_A(\gamma_2) - U_B(\gamma_2)]| > 0 \quad (6-13)$$

$$E_{TOT, I} > E_{TOT, III} \quad (6-14)$$

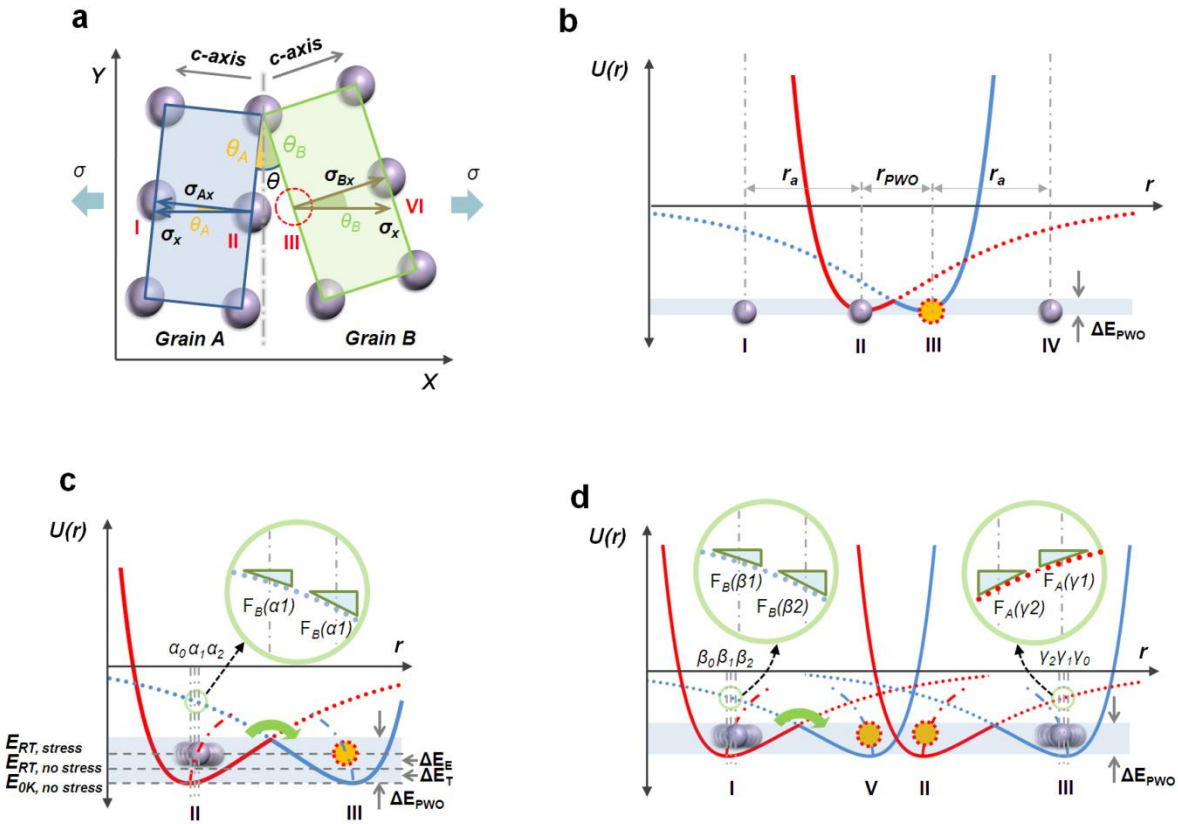


Figure 6-5. Potential Well Overlap (PWO) model of twin nucleation at GB. (a) Simplified 2D GB structure having a twin nucleation site from Fig. 6-2. Circles of violet and red dots denote Mg atoms and vacancy. In real HCP stacking, each basal plane is stacked in a manner of ABAB to the c-axis. A GB between grain A and B appears as a gray dash line.  $\sigma$  and  $\sigma_x$  denote a tensile stress.  $\sigma_{Ax}$ , and  $\sigma_{Bx}$  are resolved atomistic stresses at each texture of grain A and B, respectively. (b) Overlap of potential curves at I - IV sites of the GB.  $U(r)$  is a potential energy as a function of atomic position,  $r$ . Circles of violet and orange surrounded by red dots denote atom and vacancy.  $r_a$  and  $r_{PWO}$  indicate the atomic distances at lattice and PWO sites.  $\Delta E_{PWO}$  is the energy barrier for atom moving from site II to III. (c) and (d) the first and second atom moving at PWO site.  $\Delta E_T$  and  $\Delta E_E$  indicate thermal and interatomic elastic energy.  $E_{0K, no stress}$ ,  $E_{RT, no stress}$ , and  $E_{RT, stress}$  indicate atomic energy of unstrained sample at 0 and 293K, and of strained one at 293K, respectively.  $\alpha_0$ ,  $\alpha_1$ , and  $\alpha_2$  ( $\beta_0$ - $\beta_2$  and  $\gamma_0$ - $\gamma_2$ ) denote atom position at  $E_{0K, no stress}$ ,  $E_{293K, no stress}$ , and  $E_{293K, stress}$ , respectively. Red and blue dash curves show pathways of an atom with changing an energy state of atom.

Equation 6-14 indicates the atom at site I, having a higher energy state than the one at site II, can more easily jump over  $\Delta E_{PWO}$ . The atom moving from I to V is thus

favored. This indicates that successive atom motion is possible in this model, having selectivity and consistency of its direction. Furthermore, this model explains why the  $\{10\bar{1}2\} \langle 10\bar{1}1 \rangle$  twin experimentally nucleates and propagates into one grain with the c-axis more parallel to an external stress direction at two neighboring grains.

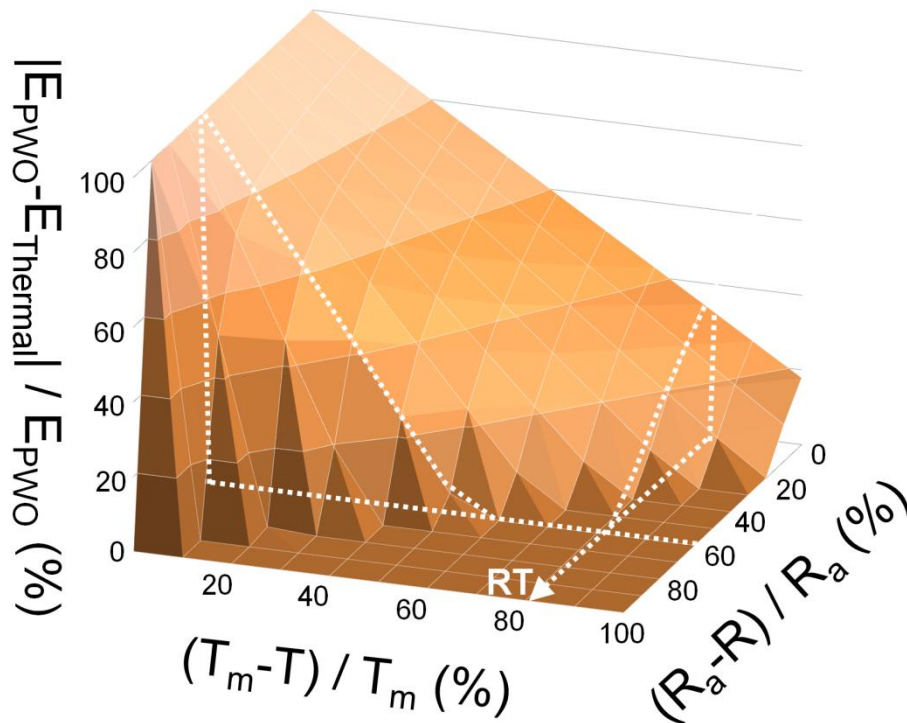


Figure 6-6. a difference between  $E_{PWO}$  and  $E_{Thermal}$  at scales of temperature ( $T$ ) and length ( $R$ ) from Mg potentials.  $RT$ ,  $T_m$ , and  $R_a$  denote room temperature ( $=293K$ ), melting temperature and normal atomic distance at  $0K$ . The calculation is conducted using Mg EAM potential [24].

In our 2D simulation, the density of PWO sites in a GB having misorientation angle of  $20 \sim 30^\circ$  is a few sites per 10nm; this is for twin nucleation in coarse grained metals. Although the discussion above was in terms of a PWO site consisting of only single

atom and vacancy, twin nucleation at PWO sites with multi-atoms and vacancy is also observed in this simulation.

In the PWO model, temperature is one of the important factors. Figure 6-6 shows the difference between  $E_{PWO}$  and  $E_{Thermal}$  as a function of temperature and length. If  $R$  is  $0.4Ra$  at RT,  $E_{PWO}$  is of the same magnitude as  $E_{Thermal}$ . This means atom motion can occur at intergrain PWO sites of Mg having a separation of  $< 0.4Ra$  by thermal energy alone, even without any external stress. In addition, a high temperature is not necessary for such a migration. The case of low temperature will be discussed later.

We now extend the discussion of the nucleation mechanism of  $\{10\bar{1}2\}$  twinning obtained in Mg to all HCP metals by addressing the critical issues, and validating the results against experimental findings.

First, twinning shear doesn't fully explain the occurrence of the  $\{10\bar{1}2\}$  twinning. There is a relation between twinning shear (TS) and nucleation of  $\{10\bar{1}2\}$  twinning that has been established for a long time[157]. In spite of its important physical meaning, the theory has raised two key questions:

- why don't Ti, Zr and Re (rhenium) show the other dominant twin modes, not the  $\{10\bar{1}2\}$  mode having low TS?
- why does  $\{10\bar{1}2\}$  twinning occur dominantly in Be although the  $\{10\bar{1}3\}$  or  $\{10\bar{1}1\}$  mode has a lower TS?

$\Delta E_{PWO}$  depends on a potential well depth and thus strongly influences the bonding strength, cohesive energy, melting temperature, etc. The  $c/a$  ratios and melting points of HCP metals are illustrated in Fig. 6-7 as a function of their cohesive energies (CE). Interestingly, their CEs appear to be related to the  $c/a$  ratio. The nucleation of  $\{10\bar{1}2\}$

twinning depends systematically on the CEs and MPs of various HCP metals. Since the CEs increase with  $\Delta E_{PWO}$  for a twin nucleation, regimes I, II, and III indicate groups of elements for which  $\{10\bar{1}2\}$  twinning is dominant, subordinate, and rare, respectively. Filled circles indicate elements in which twinning modes have been reported from experiments.

The boundaries of each regime are assigned by the twinning modes reported from experiments. All filled circles (Cd [158], Zn [158], Mg [158], Be [158, 159], and Co [160]) denote elements showing the  $\{10\bar{1}2\}$  mode as a dominant twin in the regime I. The crossover of the dominant twin mode from  $\{10\bar{1}2\}$  to the other twinning mode (e.g.  $\{11\bar{2}4\}$  twinning at Ti [161] and  $\{11\bar{2}1\}$  at Zr [162] and Hf [162, 163]) first occurs at Ti. Hence, Ti is identified as the boundary between regimes I and II. In regime II, the  $\{10\bar{1}2\}$  twins are still active enough to have an effect on plasticity of each element although the other twin mode is dominant. This is noted by some papers which found both  $\{10\bar{1}2\}$  and the other twin modes frequently take place at those metals. In contrast to Ti, Zr, and Hf, the  $\{10\bar{1}2\}$  twin is very inactive in Re [164]. Hence, Re needs to be separated from the regime II, and regime III includes Re and Os having similar CE with Re.

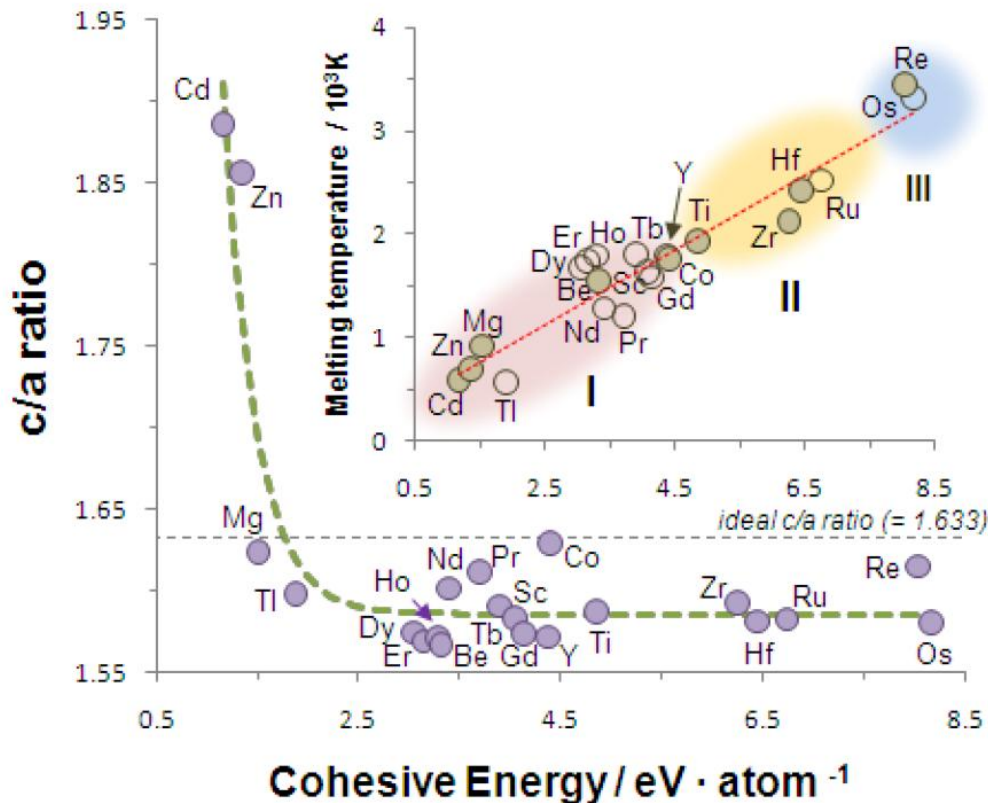


Figure 6-7.  $c/a$  ratios and melting temperatures as functions of cohesive energies of various HCP metals. For the  $c/a$  ratio,  $[c/a \text{ ratio}] = 12.985 \cdot \exp(-[CE] / 0.315) + 1.586$ ,  $R^2=0.871$ . For CE and MP, filled and unfilled circles denote elements whose twin mode is known and those where it is not, respectively. In regime I, II, and II, each element shows the  $\{10\bar{1}2\} <10\bar{1}1>$  twin dominantly, subordinately, and rarely, respectively.

Second, there is also a sensitive dependence of twin nucleation activity on grain size. Twinning becomes more inactive than slip with decreasing grain size, thus leading to a crossover in the dominant deformation mode from twinning to slip in coarse grained metals. It is found that the areal density of the PWO sites depends on the intergrain misorientation angle ( $\theta$ ), not the grain size ( $r$ ). Since there are more PWOs in larger areas of GB, assuming the same distribution of  $\theta$  at various  $r$  values, the only factor to control the rate of twin nucleation is the area of GB per grain. Assuming a spherical

grain with a surface area of  $4\pi r^2$ , the decrease of  $r$  causes a rapid drop, proportional to  $r^2$ , of twin nucleation activity [165].

For over a half century, twinning shear theory and classical dislocation theory have been applied to understand the  $\{10\bar{1}2\}$  twinning in HCP metals [27]. It is, however, been argued here that the  $\{10\bar{1}2\}$  twinning of polycrystalline HCP metals occurs by directional migration at intergrain PWO sites. Surprisingly, nucleation sites for the  $\{10\bar{1}2\}$  twin already exist at GBs, in contrast to slip which can take place at any place of high stress concentration. Moreover, the external stress field, not shear stress, to cause enough interatomic strain is required to nucleate the  $\{10\bar{1}2\}$  twin at PWO sites. Furthermore, our theory may be a key to explaining GB phenomena such as stress-induced grain growth[166].

### **6-3-2. Nucleation process in Small Grains**

In Chapter 4, the crossover of initiation deformation mechanisms between basal  $\langle a \rangle$  slip and  $\{10\bar{1}2\} \langle 10\bar{1}1 \rangle$  twinning was observed in  $[11\bar{2}0]$ -textured Mg. As discussed above, the twin nucleation mechanism by interatomic strain at PWO sites is explained for grain sizes of  $> 40\text{nm}$ . To examine whether the crossover is caused by a different twinning mechanism of  $\{10\bar{1}2\} \langle 10\bar{1}1 \rangle$  at small grain size, the twin nucleation in  $18\text{nm}$   $[11\bar{2}0]$ -textured Mg is analyzed in Fig. 6-8. An initial GB structure is seen in Fig. 6-8(a). The white zigzag lines indicate the same  $z$ -position along the thickness direction of  $[11\bar{2}0]$ . After the tensile stress is applied to the texture, disordering of atomic structure having coordination number (CN) of 11 is found on the right side of the GB in Fig. 6-8(b). The white zigzag lines show the initial atomic positions mismatch with the lattice of grain 2. A displacement vector between from the initial positions at grain 2

indicates shear parallel to the GB. Such a shear component is not found at the  $\{10\bar{1}2\} < 10\bar{1}1 >$  twin nucleation at large grain sizes ( $>20\text{nm}$ ). We thus need to consider the possibility that GB processes, such as GB sliding or diffusion, are enhanced in nano-size grains. GB sliding may lead to twin nucleation for grain sizes of  $< 18\text{nm}$ . As already shown in the time-strain curves, the GB processes begin before the slip process in dislocation-free nanocrystalline metals. The change into the twin nucleation mode mediated by the GB sliding is a reason for the crossover of initiation deformation modes from slip to twinning in the  $[11\bar{2}0]$  texture.

#### 6-4. Summary

The deformation simulations of  $[11\bar{2}0]$ -textured Mg reproduce all three expected types of twinning: tensile  $\{10\bar{1}2\} < 10\bar{1}1 >$  twins, and compressive  $\{10\bar{1}1\} < 10\bar{1}2 >$  and  $\{10\bar{1}3\} < 30\bar{3}2 >$  twins. The  $\{10\bar{1}1\} < 10\bar{1}2 >$  and  $\{10\bar{1}3\} < 30\bar{3}2 >$  compressive twins are formed by the interaction between dislocations, or by the interaction between a GB and dislocations. The  $\{11\bar{2}2\} < 11\bar{2}3 >$  twinning is created from a first-order  $\langle \mathbf{c+a} \rangle$  edge dislocation. It is revealed that the  $\{10\bar{1}2\} < 10\bar{1}1 >$  twinning of polycrystalline HCP metals occurs by directional migration at intergrain PWO sites.  $\{10\bar{1}2\} < 10\bar{1}1 >$  twin sites already exist at GBs in contrast to slip which can take place at any places of high stress concentration.

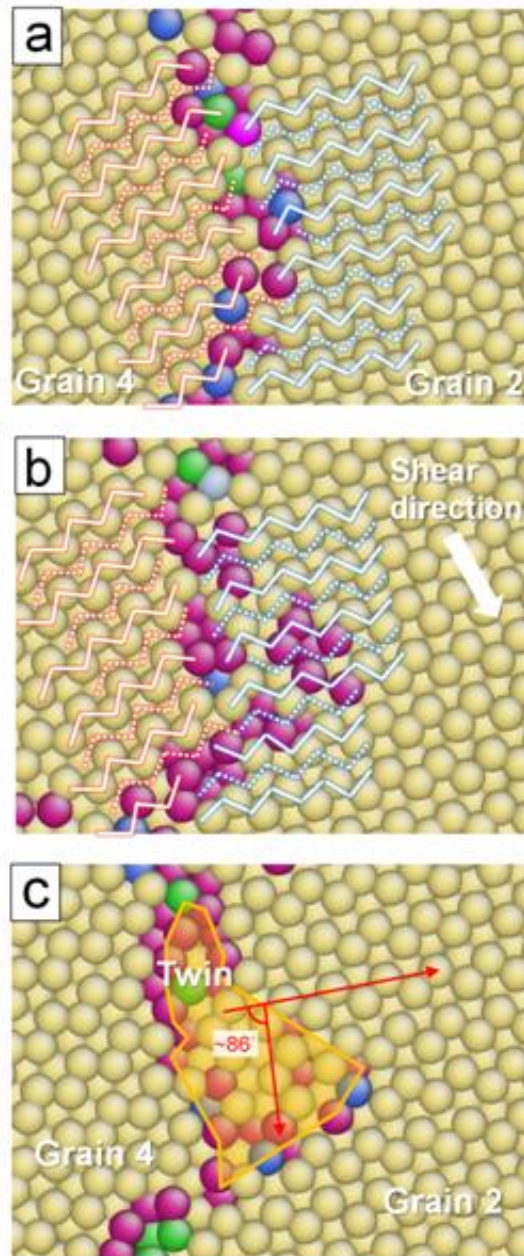


Figure 6-8. Nucleation of  $\{10\bar{1}2\} \langle 10\bar{1}1 \rangle$  twin in 18nm  $[11\bar{2}0]$ -textured Mg. (a) An initial GB structure. White zigzag lines indicate atoms on the same atomic plane normal to the thickness direction. (b) A plastically strained GB structure at 27.8psec. (c) An obvious twin nuclei of  $\{10\bar{1}2\} \langle 10\bar{1}1 \rangle$  is found at 29.8psec.

## CHAPTER 8 OVERALL MECHANICAL RESPONSE OF RANDOMLY ORIENTED HCP METALS

In previous chapters, the plasticity of HCP metals was studied in 2D textured materials. As is known from studies of FCC metals, the 2D textures successfully reproduce the fundamental processes of GB process, slip and twinning [49, 73, 86]. However, the activations and interactions of deformation modes occur somewhat independently in the 2D system. For example, although basal  $\langle a \rangle$  slip can appear in  $[11\bar{2}0]$ -textured Mg, prismatic  $\langle a \rangle$  slip is not observed at any value of external stress in the same texture. This is because a GB in the 2D columnar texture does not produce a shear stress in the thickness direction. To examine interactions between basal and prismatic, 3D structures having a realistic grain shape, not a columnar texture, are thus required. This chapter examines the comparative ease of activation of slip and twinning processes. Furthermore, not only the Hall-Petch behavior but also GB processes are addressed here.

### 7-1. Strain-Stress Response

Strain-stress curves of fully dense 3D Mg are shown in Fig.7-1. Grain sizes range from 36nm to 6nm. The polycrystalline structure already shown in Fig. 2-10 was strained at constant rate of  $1.5 \times 10^9 \text{s}^{-1}$ . Young's modulus and a tensile strength decrease with decreasing the grain size in Fig.7-1(a). Such behavior in a nanocrystalline metal is already well known [44, 87]. One of the important phenomena in nanocrystalline is an inverse Hall-Petch response. Strength is normally enhanced, as the grain size decreases. However, when the grain size becomes less than a critical value, the strength begins to decrease due to GB processes [42, 43]. To find such a critical grain size in nanocrystalline Mg, a Hall-Petch plot is constructed in terms of the

flow stress (average stress at strain range from 8 % to 10%) of Fig. 7-1(b), as shown in Fig. 7-2.

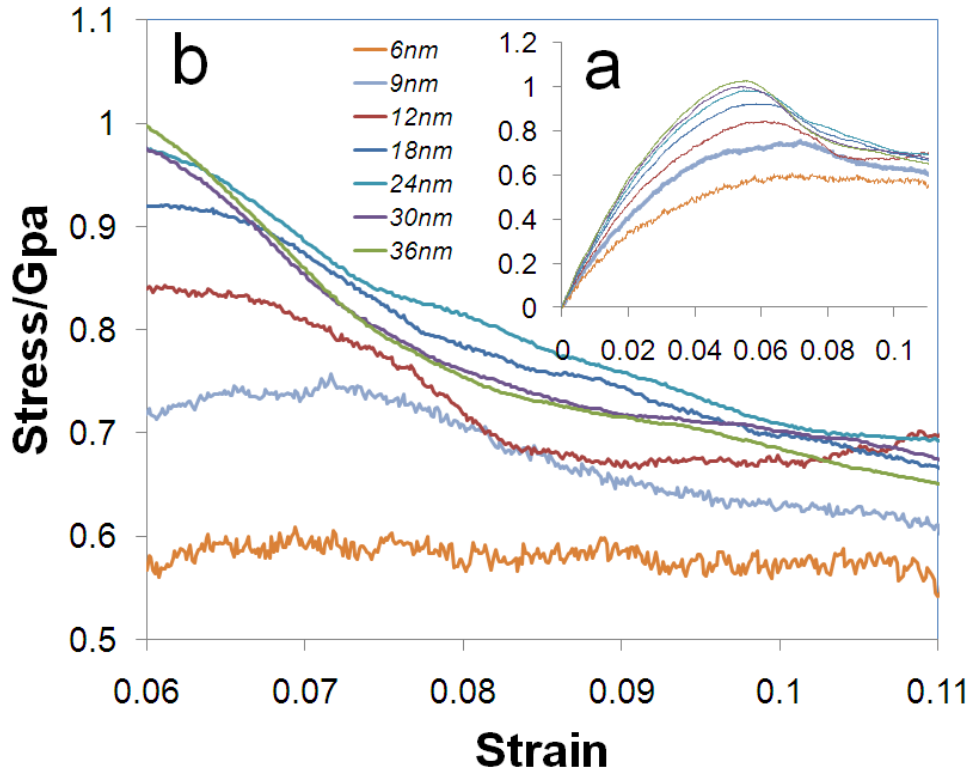


Figure 7-1. Strain-stress curves of nanocrystalline Mg with fully dense 3D structure. Each simulation of tensile test was conducted at 293K under uniaxial stress. A strain rate was  $1.5 \times 10^9 \text{s}^{-1}$  during tensile test. a. stress-strain curves of full scale. x and y-axis indicate strain and stress. b. stresses at strain between 0.06 and 0.11.

## 7-2. Hall-Petch Relation

As expressed in Eq. 7-1, the strength of materials normally increases with decreasing grain size according to ‘Hall-Petch behavior’ [3]; however, the trend becomes the opposite (i.e., decreasing with decreasing grain size) below a critical grain size. This phenomenon is well known as inverse Hall-Petch (H-P) behavior.

$$\sigma_y = \sigma_0 + K_y d^{-0.5} \quad (7-1)$$

The crossover from “normal” to “inverse” H-P behavior at a critical grain size of typically 20 ~ 30 nm is thought to be due to a change in the dominant deformation mode, from one based on dislocations to one mediated by GB processes [167].

Figure 7-2 shows the flow stress calculated from 8 -11% strain of Fig. 7-1 as a function of grain size in nc-3D Mg. The polycrystalline structure already shown in Fig. 2-10 was strained. The H-P relation is obtained from the relation between the yield strength and the grain size. However, the flow stress is often adopted for the H-P graph because it is hard to identify the yield strength in nc-metals[42, 43]. The crossover in the H-P slope in Mg appears at grain size of 24nm, which is similar to previous MD results for FCC metals such as Cu (~15nm) [42, 43] and Al (~20nm) [36]. The normal and inverse H-P slopes are 1.2 and 0.9 MPa mm<sup>0.5</sup>, respectively.

In general, the normal H-P slope obtained in MD simulation of nc-metals, as previously shown in the general H-P graph of Fig. 2-7, is smaller than that in coarse-grained metals due to reduced activity of slip and twinning [43, 87]. Nevertheless, it is instructive to compare simulations and experiments, as this can help to understand the difference of plasticity in HCP and FCC metals. Table 7-1 represents the normal H-P slopes of pure Mg and Cu as determined from MD simulations and experiments. The slope of simulated nc-Mg is much smaller than that of simulated nc-Cu or experimental Mg. By contrast, the simulated nc-Cu shows a similar value of H-P slope with experimental one. The small slope in the simulated nc-Mg is due to the restrained twinning activity at this small length scale. As the grain size  $r$  decreases, the twin activity rapidly decrease proportionally to  $r^{-2}$  [165]. If grain size is not small enough (~ a few ten nanometers) to yield significant GB processes in HCP metals, then only basal slip is

active, and this cannot properly produce plasticity without a help of twinning. However, slip processes in nc-Cu are still dominant at grain size of 20 ~ 100 nm because slip activity decrease proportionally to  $r^{-0.5}$  in coarse grains and  $r^{-1}$  for nano-grains [50].

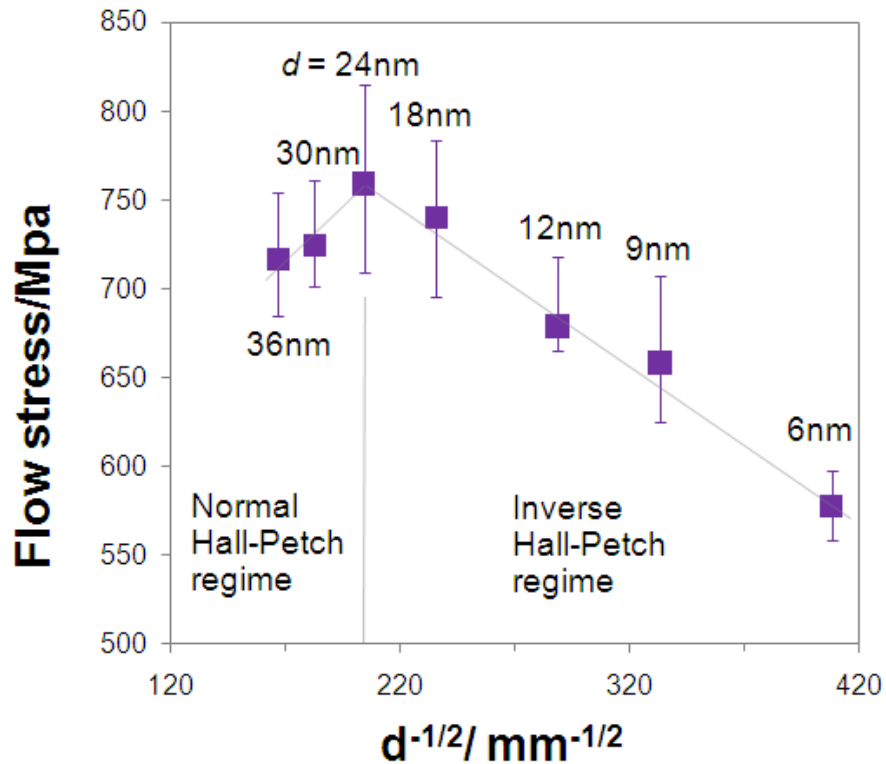


Figure 7-2. the Hall-Petch graph in nc-Mg. The flow stress is calculated by averaging strain values between 8 and 11% in strain-stress curves of Fig. 7-1.

Table 7-1. Hall-Petch slopes of pure Cu and Mg from MD simulations and experiments.

	Mg		Cu	
	$K_y / \text{MPamm}^{0.5}$	Grain size	$K_y / \text{MPamm}^{0.5}$	Grain size
MD simulation	1.2*	24~36 nm	5.9 [43]	24~49 nm
Experiment	10 [168]	43~172 $\mu\text{m}$	4.7 [169, 170]	15~120 $\mu\text{m}$

\* From the present simulation

### 7-3. Microstructure Evolution

In this section, the deformation mechanism in nc-Mg is characterized by analyzing the strained structure and the deformation modes. From Fig. 7-2, we find that the critical grain size in the Hall-Petch graph of Mg is 24nm. The normal and inverse Hall-Petch behaviors separated at the critical size need to be related to the deformation processes. To examine the relation between the Hall-Petch behavior and microstructure evolution, the comparative prevalence of individual deformation mechanisms (slip, twinning and GB process) is examined in samples of three different grain sizes (9, 18, and 36nm).

Figure 7-3 shows an 18nm grain size polycrystal strained by 11% at 293K at a constant strain rate of  $1.5 \times 10^9 \text{s}^{-1}$ . Initial and deformed structures are seen in Fig. 7-3 (a) and (b), respectively. After cooling down to 0.01K, the sample was analyzed with CNA. FCC SFs, pyramidal dislocations and twins appear as deformation structures. The deformation modes are very similar to those manifested in the 2D columnar microstructure. Slip and twinning processes occur in different grains. This means that, as previously revealed in columnar textures, there is complementarity between slip and twinning in order to promote plasticity under the external stress.

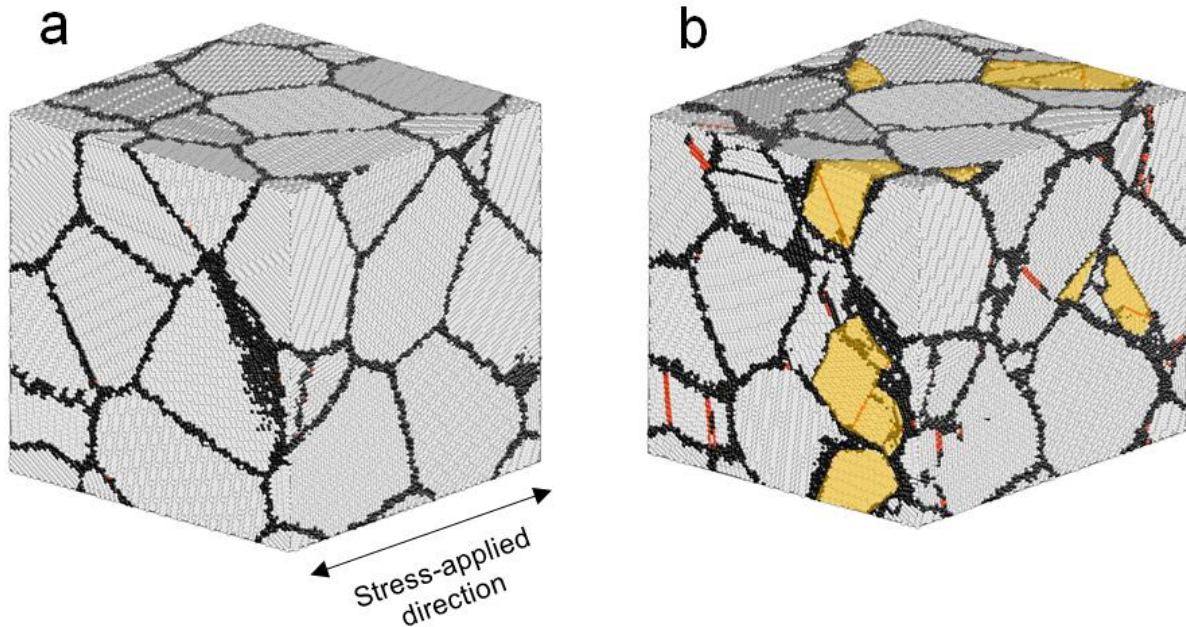


Figure 7-3. Snapshot of 11%-strained structure of 18nm grain size at 293K with constant strain rate of  $1.5 \times 10^9 \text{ s}^{-1}$ . a and b represent structures before and after straining, respectively. Gray, black and red denote normal (HCP), disordered (non- HCP or FCC), and stacking fault (FCC), respectively. Twinned area is shown transparent orange.

Figures 7-4 and 5 show a plastic deformation process during a tensile test of the 36nm Mg structure. Basal  $\langle a \rangle$  slip first occurs, as denoted by  $\alpha$  in Fig. 7-4(b), at a total strain of 4.81%. Twinning is not observed for this relatively low strain. From the yield point to the beginning point of slip, GB processes may thus contribute to the plasticity of nc-Mg. The strain range ( $\epsilon_{\text{GB}}$ ) of almost 3% is large when compared to  $\epsilon_{\text{GB}}$  of  $< \sim 0.25\%$  in the columnar structures. This obvious difference in  $\epsilon_{\text{GB}}$  can be explained by less active GB processes caused from smaller GB area and the columnar textures with a hexagonal grain shape. In Fig. 7-4(c), the activated  $\langle a \rangle$  dislocation glides with an extended type, and new  $\langle a \rangle$  slip is activated at another grain. The basal  $\langle a \rangle$  dislocations normally have a low shear strain, shown as a uniform blue color; however it

is possible for the stress to locally have a high value, shown in orange, near the GB. The prismatic dislocation and twinning appear for the first time in Fig 7-4(d). The  $\langle 10\bar{1}0 \rangle$  directions with which the prismatic dislocation propagates does not have any stable sites for partial slip. Therefore, in contrast to basal  $\langle \mathbf{a} \rangle$  slip, the prismatic  $\langle \mathbf{a} \rangle$  slip is not manifested with a wide SF. The twin boundaries are normally seen as parallel orange SFs owing to their high shear strain. The tensile strength (TS) point of Mg with 36nm grain size appears at  $\sim 5.5\%$  strain in the Fig. 7.4. Full-scale plasticity achieved by twinning and slip leads to softening after the TS point. As the strain to the loading direction keeps increasing, the density of dislocations, SFs, and twins rapidly increase in Fig 7-4(d) to -5. The stress drop after the TS point is closely related with the activation of slip and twinning, as will be discussed later. In the following section the specific deformation mechanisms and their properties are addressed.

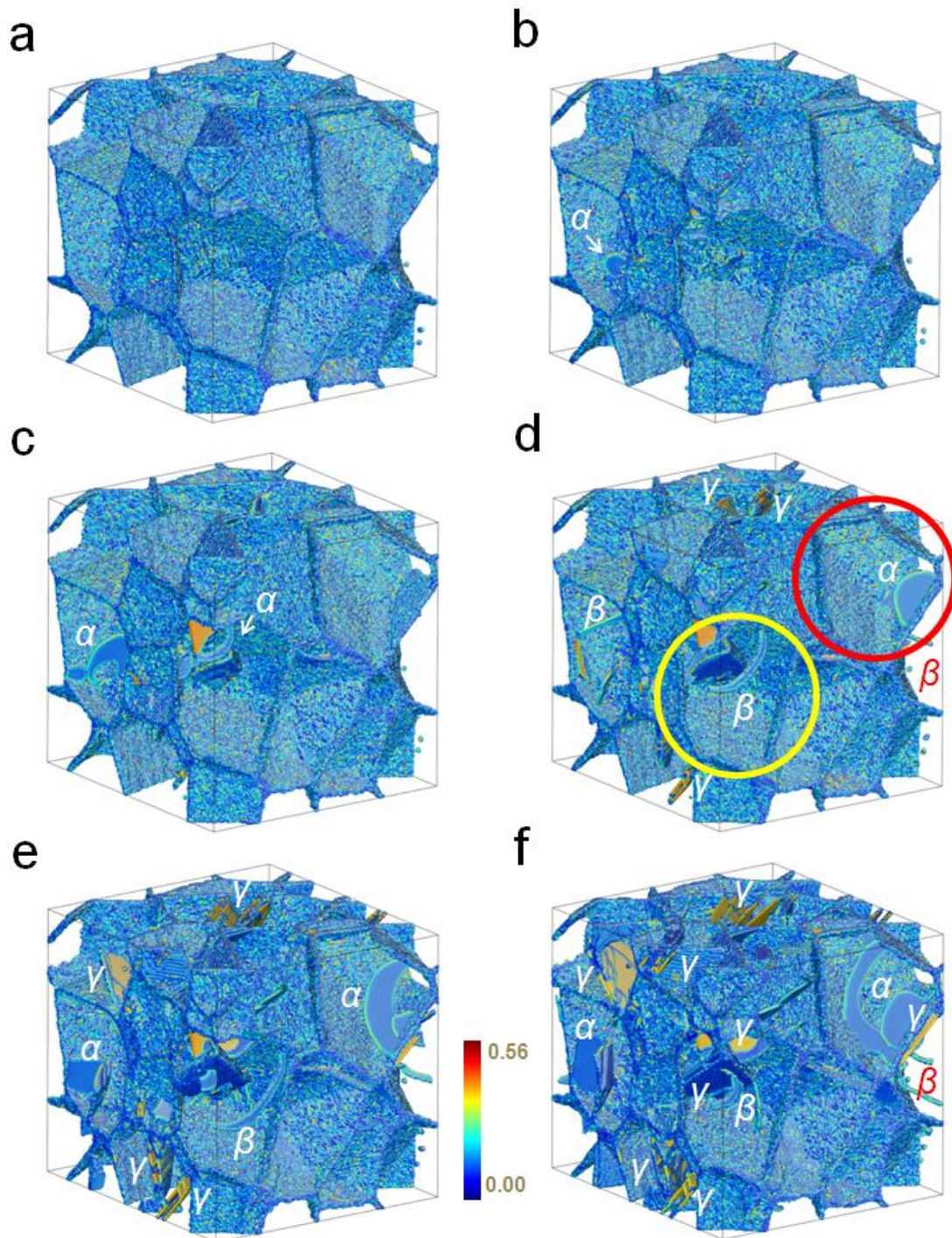


Figure 7-4. Shear strain map of nc-Mg with 36nm grain size. Normal HCP atoms are not shown.  $\alpha$ ,  $\beta$ , and  $\gamma$  denote a basal  $\langle a \rangle$  dislocation, pyramidal  $\langle c+a \rangle$  dislocation, and twin, respectively. (a) 27.4psec, 4.19% strain, (b) 31.3psec, 4.81%, (c) 35.2psec, 5.43%, (d) 39.2psec, 6.05%, (e) 43.1psec, 6.68%, and (f) 47.0psec, 7.3%.

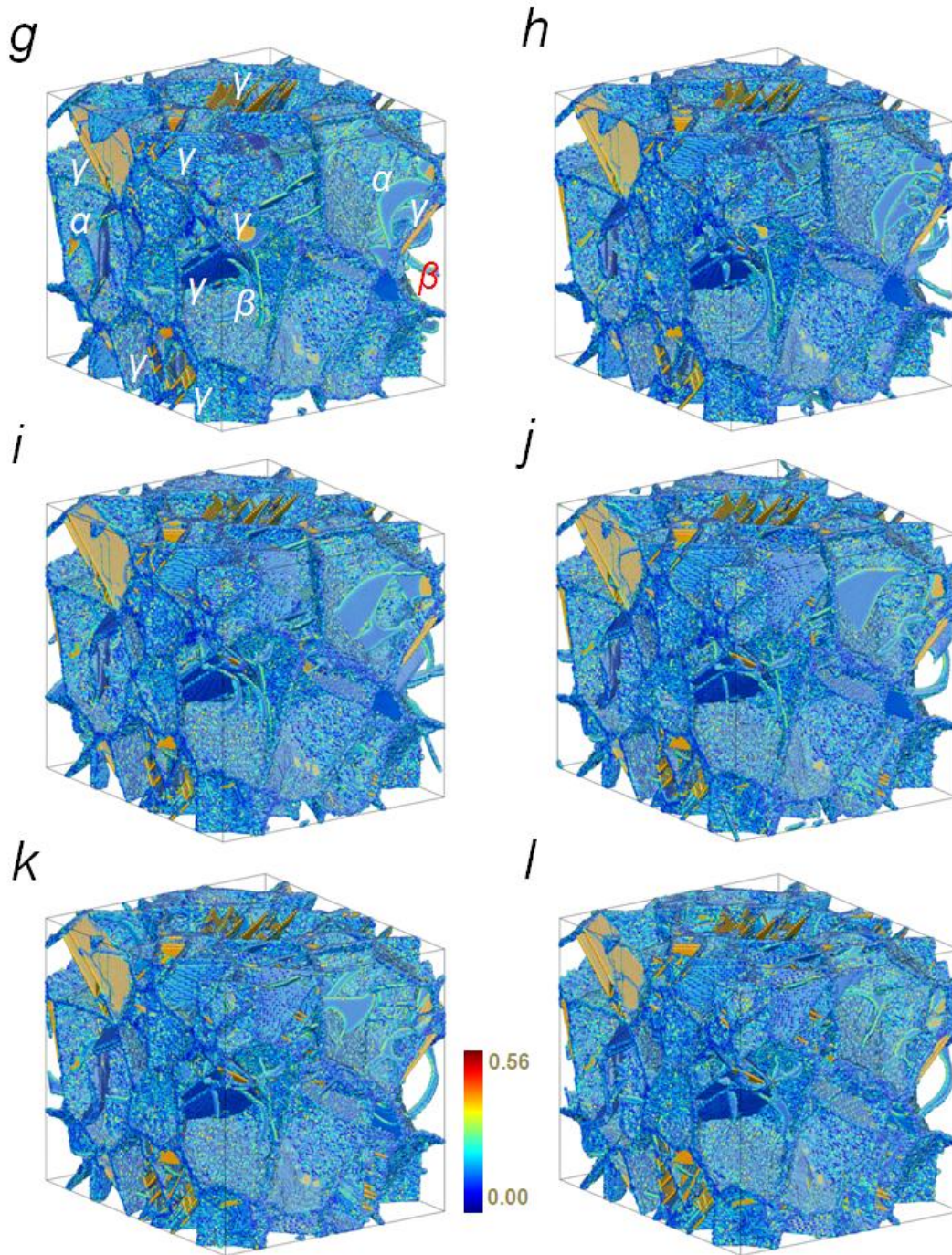


Figure 7-5. Shear strain map of nc-Mg with 36nm grain size. Normal HCP atoms are not shown.  $\alpha$ ,  $\beta$ , and  $\gamma$  denote a basal  $\langle a \rangle$  dislocation, pyramidal  $\langle c+a \rangle$  dislocation, and twin, respectively. (g) 50.9psec, 7.94% strain, (h) 54.8psec, 8.57%, (i) 58.7psec, 9.21%, (j) 62.6psec, 9.86%, (k) 66.6psec, 10.5%, and (l) 70.5psec, 11.1%

## 7-4. Individual Defect Process

### 7-4-1. $\langle a \rangle$ slip

The  $\langle a \rangle$  slip mode is the dominant deformation process in Mg. As illustrated in Fig. 7-6, various types of  $\langle a \rangle$  slip can take place during plastic deformation. In nc-Mg, due to the absence of Frank-Read sources, each  $\langle a \rangle$  slip mode can only be produced by direct activation from GBs and from cross-slip from the other  $\langle a \rangle$  slip.

In grains in which  $\langle a \rangle$  slip is the first process, it is almost always the sole process, e.g., the grain noted by a red circle in Figs. 7-4 and -5. Because the basal  $\langle a \rangle$  slip mode is easier to generate than the prismatic or pyramidal modes, the basal  $\langle a \rangle$  mode does not cross-slip to the other higher-energy modes. The basal  $\langle a \rangle$  slip mode has a tendency to appear as a full, a partial, or an extended dislocation.

The prismatic  $\langle a \rangle$  slip mode is shown in Fig. 7-6(b). Initially two prismatic  $\langle a \rangle$  edge dislocations are activated from one and the other side of a GB, as noted by A and B. The prismatic  $\langle a \rangle$  dislocation, denoted by 'A', is changed into screw type at both ends of the edge type, and one of the screw dislocation cross-slips to a basal  $\langle a \rangle$  dislocation. The other prismatic  $\langle a \rangle$  edge dislocation, denoted by 'B', is similarly altered to screw and extended basal  $\langle a \rangle$  dislocations. In conclusion, even if the prismatic  $\langle a \rangle$  slip is initiated with an edge-type, it is energetically favored to become screw-type and to cross-slip to the basal  $\langle a \rangle$  slip.

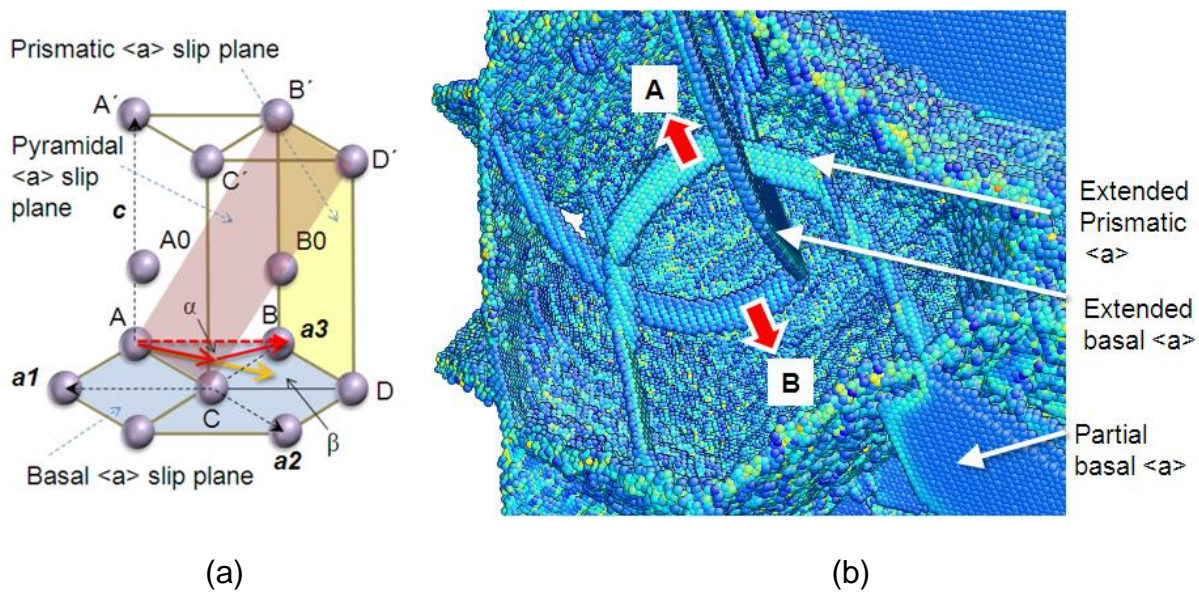


Figure 7-6.  $\langle a \rangle$  slip process in a 3D Mg structure with 24nm grain size. (a) Various  $\langle a \rangle$  slip vectors and planes in a HCP unit cell: Basal, prismatic, and pyramidal slip plane are  $\{0002\}$ ,  $\{10\bar{1}0\}$ , and  $\{10\bar{1}1\}$ .  $A\alpha$  (or  $\alpha B$ ), and  $A\beta$  are  $1/3\langle\bar{1}100\rangle$  and  $2/3\langle\bar{1}100\rangle$  partial dislocations, respectively. (b) Potential energy map of dislocations and GBs.

#### 7-4-2. $\langle c+a \rangle$ and $\langle c \rangle$ slip

In contrast to active  $\langle a \rangle$  slip in a deformed sample, no independent  $\langle c+a \rangle$  process is found. However, some prismatic  $\langle a \rangle$  dislocations are identified as creating  $\langle c+a \rangle$  and  $\langle c \rangle$  dislocations. Activation processes of  $\langle c \rangle$  and  $\langle c+a \rangle$  from prismatic  $\langle a \rangle$  dislocations are exhibited in Fig. 7-7. The snapshots show a grain being compressed in the  $c$ -direction. Normal HCP atoms are not shown, and each color denotes the boundaries between different grains. In Fig. 7-7(a), two prismatic  $\langle a \rangle$  dislocations (I and II) activated from a right corner of the grain are gliding on the  $(10\bar{1}0)$  plane in the  $[11\bar{2}0]$  direction. The dislocation (I) keeps gliding with curvature by bowing in Fig 7-7(b). The curvatures are different at the upper and lower parts of the pure edge component. Simply considering the relation between stress and radius of the curvature by tension,  $\tau = Gb/r$ , [4] bowing stresses ( $\tau_A, \tau_B$ ) resulting in bowing of the dislocation

are  $\tau_A > \tau_B$  due to  $r_A < r_B$ . The gliding behavior of prismatic  $\langle \mathbf{a} \rangle$  dislocations, II and V, is a little different from that with I. III and V which denote compressive twinning have a role in preventing one of end of II and V from moving, respectively. Significant changes appear in the ends of dislocations I, as seen in Fig. 7-7(c) and (d). The prismatic  $\langle \mathbf{a} \rangle$  dislocation terminated as a screw-type is comparatively easy to move up or down on the prismatic plane. The upper end of I cross-slips to a basal  $\langle \mathbf{a} \rangle$  extended edge dislocation. Hence, the edge part of basal  $\langle \mathbf{a} \rangle$  cannot follow the vertical movement of I to the c-axis, finally separated from I. The separated edge basal  $\langle \mathbf{a} \rangle$  is seen as I' in Fig. 7-7(d). At the lower end of I, the curvature ( $r_A$ ) becomes smaller in Fig. 7-7(c). The dislocation I is transformed into the 'hook' in Fig. 7-7(d). The tail of the hook ( $\alpha_1$ ) is separated in Fig. 7-7(e). As dislocation I glides, dislocation segments of  $\alpha_2$  and  $\alpha_3$  are left in Fig. 7-7(f). On the other hand, two prismatic  $\langle \mathbf{a} \rangle$  dislocations, II and V, gliding to the opposing directions exhibit two reactions. After two dislocations encounters, the upper parts keep moving while the lower parts dissociate to  $\beta_1$  and  $\beta_1$ , as shown in Fig. 7-7(d).

Formation of  $\langle \mathbf{c} \rangle$  and  $\langle \mathbf{c} + \mathbf{a} \rangle$  dislocations from prismatic  $\langle \mathbf{a} \rangle$  slip process is described in Fig. 7-8. Three prismatic  $\langle \mathbf{a} \rangle$  dislocations activated from a GB are captured in Fig. 7-8(a). In contrast to the pure prismatic  $\langle \mathbf{a} \rangle$  dislocation of I, dislocation II consists of pyramidal as well as prismatic and basal  $\langle \mathbf{a} \rangle$  components on planes of  $\alpha$ , (0001), and  $\beta$ , ( $10\bar{1}0$ ). While I includes many jogs, II has one jog at its middle. The jog is normally known to move on a non-slip plane with the help of a vacancy [21]. Although a few vacancies, denoted by O, are found, they are not enough to explain the motion of the jogs. In this simulation, a ledge on the prismatic  $\langle \mathbf{a} \rangle$  dislocations is called as a jog due to its protrusion out of ( $10\bar{1}0$ ) slip plane. It is, however, necessary to understand

the jog on the other slip plane, (0001). Non vacancy-assisted process may be possible to move the jog. The jog at II is the direct reason for the complex processes observed between II and V. II and V glide away without any collision above the jog due to some distance between their slip planes in Fig. 7-8(a). But, below the jog, the II and V dislocations collide on the exact same slip plane. After the collision, the upper parts of the dislocation II and V are connected at the jog, the other ends at the GB keep gliding to the opposite directions. The lower parts become dissociated, leaving some dislocation segments denoted  $\beta_1$  and  $\beta_2$  in Fig. 7-7(d).

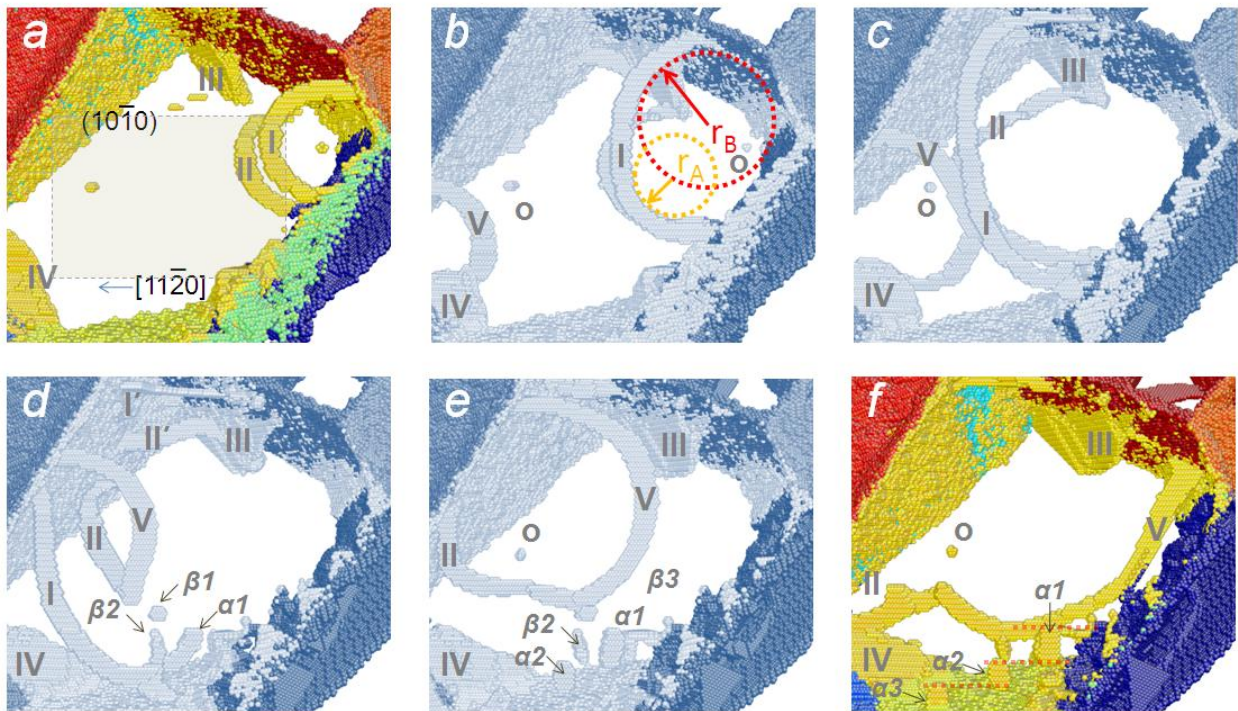


Figure 7-7. Prismatic  $\langle a \rangle$  slip process in a 3D Mg structure with 36nm grain size. I and II, and V denote prismatic  $\langle a \rangle$  dislocations. II and IV denote  $\{10\bar{1}1\} \langle 10\bar{1}2 \rangle$  compressive twins. O indicates a vacancy. I' and II' are dislocation segments separated from I and II.  $\beta_1$  and  $\beta_2$  are segments produced by interaction between II and V.  $\alpha_1$ ,  $\alpha_2$ , and  $\alpha_3$  indicates  $\langle a \rangle$  dislocations. (a), (b), (c), (d), (e), and (f) are captured at 43.1psec (total strain: 6.68%), 47.0psec (7.3%), 50.9psec (7.94%), 54.8psec (8.57%), 58.7psec (9.21%), and 62.6psec (9.86%), respectively.

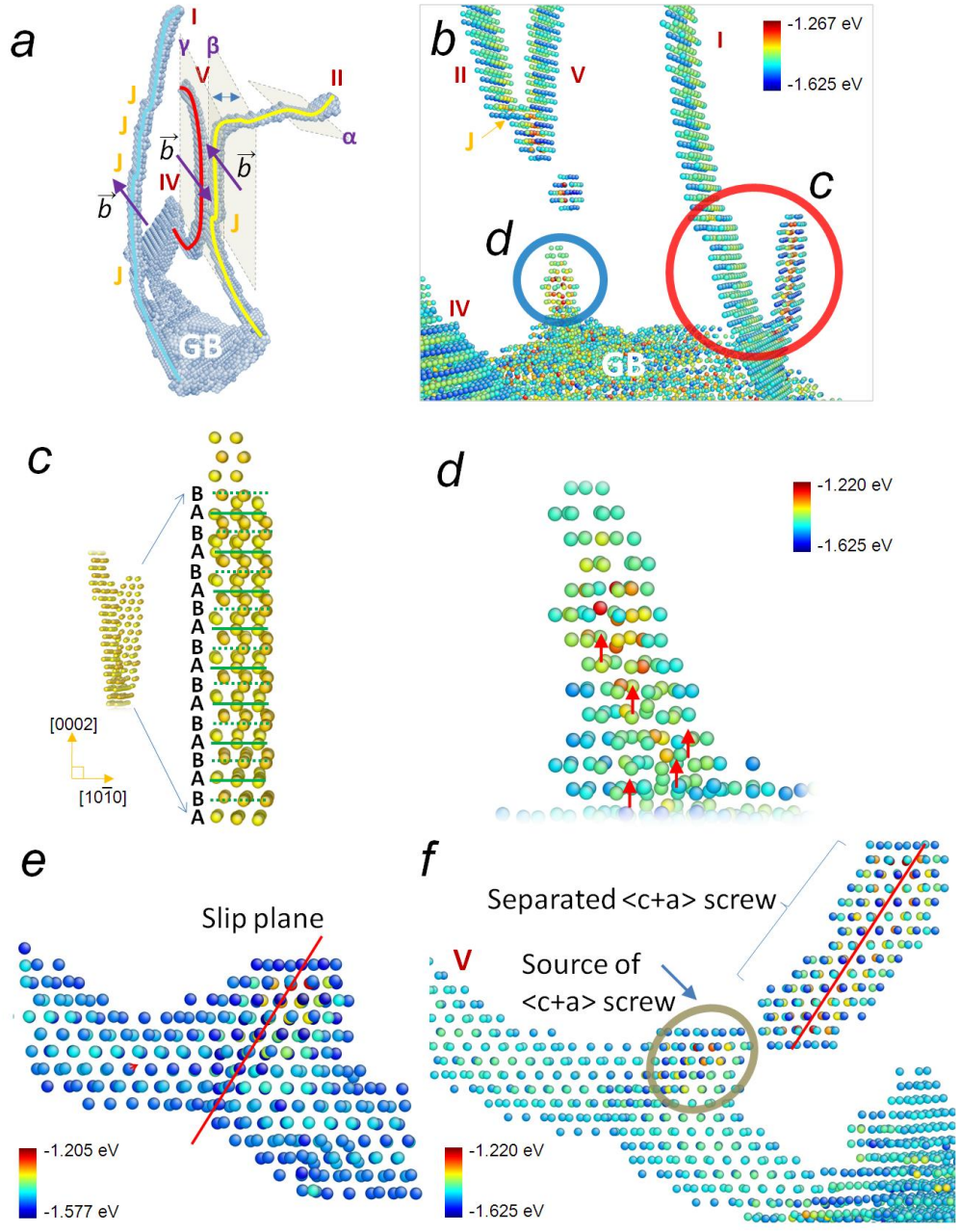


Figure 7-8. Dislocation processes which occur from prismatic  $\langle a \rangle$  slip. (a)  $\langle a \rangle$  dislocations shown in Fig. 7-7c are gliding.  $\alpha$  and  $\beta$  denote slip planes of basal and prismatic  $\langle a \rangle$ . J denotes jog. (b) Creation of dislocation segments in Fig. 7-7(d). (c) A screw  $\langle c+a \rangle$  dislocation cross-slipped from V. (d)  $\langle c \rangle$  dislocation segment produced from interaction between V and II. (e) Initial stage of  $\langle c+a \rangle$  slip. Red line denotes second-order pyramidal slip plane,  $\{11\bar{2}\}$ . (f) Separation of the  $\langle c+a \rangle$  dislocation .

Figure 7-8(b) shows a potential energy map for the dislocations in Fig. 7-7(d). Different energy structures with normal prismatic  $\langle \mathbf{a} \rangle$  dislocation are seen at (c) and (d): analysis of the energies of the structures shows that the energy of the dislocation cores is  $\sim 0.2\text{eV}$  higher than that of normal prismatic  $\langle \mathbf{a} \rangle$ . It is evident that the segments with the high energy are not typical prismatic  $\langle \mathbf{a} \rangle$  dislocations. In order to identify the dislocations, they are magnified in Fig. 7-8(c) and (d). Leading prismatic  $\langle \mathbf{a} \rangle$  and the trailing part with high energy are aligned along the c-axis in Fig. 7-8(c). The basal planes in the trailing part are lifted, thereby being between the original A and B layers. It means that the slip vector of the trailing segment contains the  $\langle \mathbf{c} \rangle$ -component. The dislocation segment is revealed to have pure  $\langle \mathbf{c} \rangle$ -component, as atomic displacements to the  $[0001]$  are denoted by red arrows in Fig 7-8(d). The formation of the slip vector component to the c-axis from prismatic  $\langle \mathbf{a} \rangle$  slip is further investigated in Fig 7-8(e) and (f). Initiation of slip process is observed from screw  $\langle \mathbf{a} \rangle$  on the second-order pyramidal  $\langle \mathbf{c}+\mathbf{a} \rangle$  slip plane in Fig 7-8(e). Even though the  $\langle \mathbf{c}+\mathbf{a} \rangle$  slip develops a screw dislocation, the  $\langle \mathbf{c}+\mathbf{a} \rangle$  screw is separated due to the different direction and magnitude of slip vector with the prismatic  $\langle \mathbf{a} \rangle$  dislocation body, as shown in Fig 7-8(f). The separation of the screw  $\langle \mathbf{c}+\mathbf{a} \rangle$  dislocation is imperfect, thus a part of it is left. The left part on the screw  $\langle \mathbf{a} \rangle$  dislocation acts as a source for new screw  $\langle \mathbf{c}+\mathbf{a} \rangle$  dislocations.  $\alpha_1$ ,  $\alpha_2$  and  $\alpha_3$  were  $\langle \mathbf{c}+\mathbf{a} \rangle$  screws, generated from the source in Fig. 7-7(e) and (f). However, because they are not independently stable, the  $\langle \mathbf{c}+\mathbf{a} \rangle$  dislocations are rapidly changed into pure  $\langle \mathbf{a} \rangle$  dislocation after separated. The slip vector of  $\langle \mathbf{c}+\mathbf{a} \rangle$  in Fig. 7-8(c) corresponds to  $1/18 \bar{[6243]}$  shown as  $\gamma B_0$  in Fig. 6-5, and a pure  $\langle \mathbf{c} \rangle$  component is very small. How the

$\langle \mathbf{c+a} \rangle$  can be changed to the  $\langle \mathbf{a} \rangle$  without any other interaction may be due to such a small  $\langle \mathbf{c} \rangle$  component in the slip vector of the  $\langle \mathbf{c+a} \rangle$ .

In the present simulation, the  $\langle \mathbf{c+a} \rangle$  slip is directly activated from one prismatic  $\langle \mathbf{a} \rangle$  dislocation without the help of  $\langle \mathbf{c} \rangle$  dislocations. This is in contradiction to an earlier model, reported by Yoo et al. [23], of  $\langle \mathbf{c} \rangle$  dislocation-assisted activation for  $\langle \mathbf{c+a} \rangle$  dislocation in Fig. 7-9. The activation process of  $\langle \mathbf{c+a} \rangle$  and  $\langle \mathbf{c} \rangle$  dislocations in this study are summarized in Fig. 7-10 and 11.

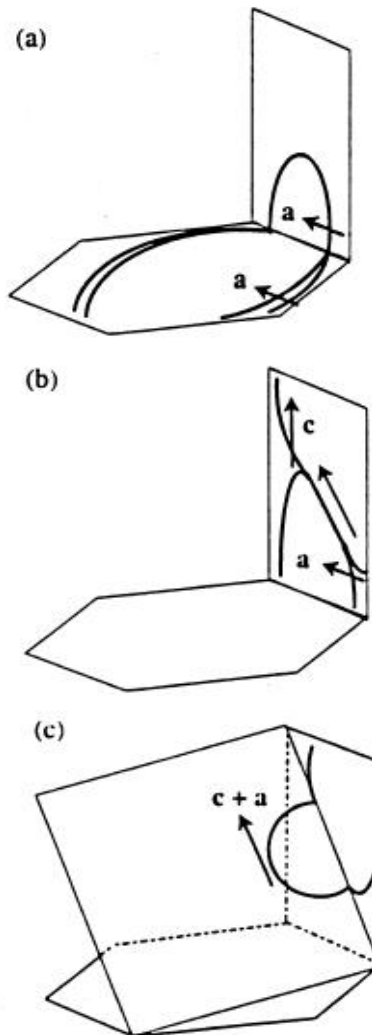


Figure 7-9. Evolution of the dislocation source in a  $\langle \mathbf{c+a} \rangle$  pyramidal slip [23]. (a) cross slip of a dislocation (b) formation of junction for  $\langle \mathbf{c+a} \rangle$  dislocation, and (c) cross slip of  $\langle \mathbf{c+a} \rangle$  dislocation.

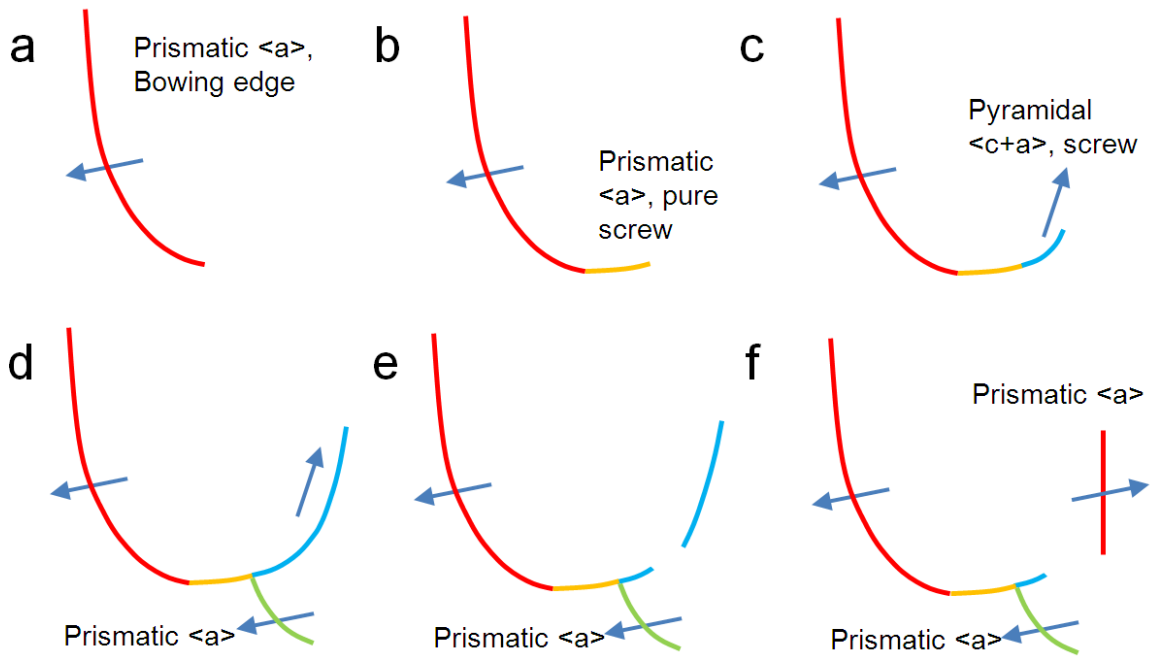


Figure 7-10. Activation process of pyramidal  $\langle c+a \rangle$  slip from a single prismatic  $\langle a \rangle$  dislocation.

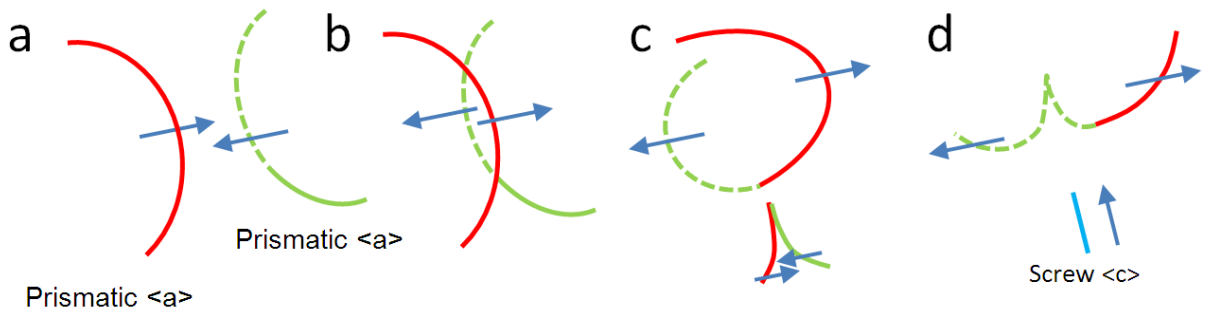


Figure 7-11. Activation process of  $\langle c \rangle$  dislocation between two approaching prismatic  $\langle a \rangle$  dislocations. Green dot line denote a part of the prismatic  $\langle a \rangle$  dislocation gliding on a different plane.

The competition between activation of the  $\langle \mathbf{c+a} \rangle$  slip and bowing is now examined. Figure 7-12(a) shows the prismatic  $\langle \mathbf{a} \rangle$  dislocation in the shape of a hook before the  $\langle \mathbf{c+a} \rangle$  dislocation is separated. First, the bowing of pure edge part (II) is required to make screw  $\langle \mathbf{a} \rangle$  component. After fully bowing, a screw  $\langle \mathbf{a} \rangle$  component forms. Although  $\langle \mathbf{c+a} \rangle$  slip is observed in the present simulation, there appear to be two competing processes depending on direction of shear stress. The two cases are illustrated in Fig. 7-12(b) and (c). If the shear stress in a grain is less than the CRSS for second-order pyramidal  $\langle \mathbf{c+a} \rangle$ , the screw  $\langle \mathbf{a} \rangle$  dislocation would bow, as shown in Fig. 7-12(b). For the purposes of analysis of bowing of II and IV, the bowing is treated as arising from bending. According to the elastic theory of dislocations, the bending energy depends on the type of dislocation (e.g. edge or screw) and the bending length and angle [21].

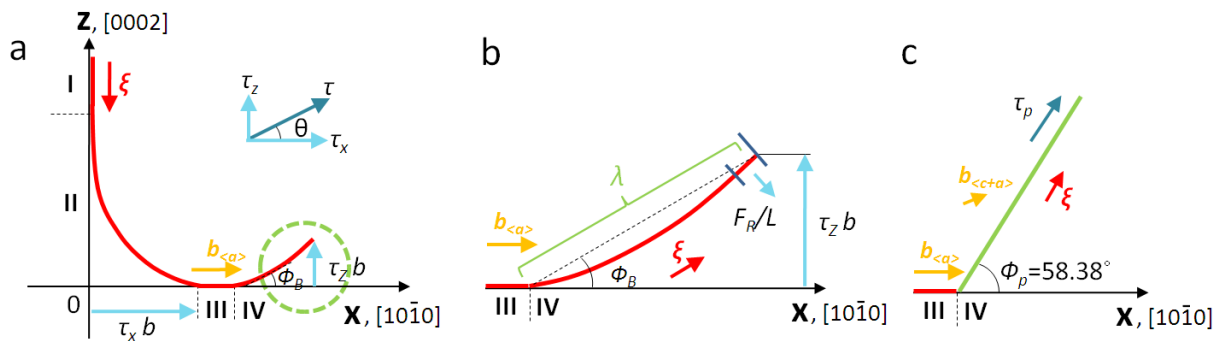


Figure 7-12. Bowing of a prismatic  $\langle \mathbf{a} \rangle$  dislocation and activating of second-order pyramidal  $\langle \mathbf{c+a} \rangle$  slip. I, II, III and IV denote dislocations of pure edge prismatic  $\langle \mathbf{a} \rangle$ , bowed (mixed)  $\langle \mathbf{a} \rangle$ , pure screw  $\langle \mathbf{a} \rangle$ , and bowed (mixed)  $\langle \mathbf{a} \rangle$ , respectively.  $\xi$  indicates dislocation line.  $\Phi_B$  and  $\Phi_p$  denote the bowing angle of screw  $\langle \mathbf{a} \rangle$  dislocation and the angle between basal and second-order pyramidal slip planes, respectively.  $\tau$ ,  $\tau_x$ ,  $\tau_z$ , and  $\tau_p$  indicates shear stress causing the  $\langle \mathbf{a} \rangle$  dislocation to glide on the prismatic plane, resolved shear stresses to the directions of  $x$ ,  $z$ , and the second-order pyramidal slip.

Figure 7-13 is obtained the standard equations for the energies of edge and screw types [21]:

$$\frac{E_e}{L} = \frac{\mu}{4\pi} \left[ b_e^2 \left( \frac{\cos \phi_B - 1 + \gamma \sin^2 \phi_B \cos \phi_B}{(1-\gamma) \sin \phi_B} \right) \right] \ln \lambda \quad (7-2)$$

$$\frac{E_s}{L} = \frac{\mu}{4\pi} \left[ b_s^2 \left( \frac{\cos \phi_B - 1}{\sin \phi_B} - \frac{\gamma \sin \phi_B \cos \phi_B}{1-\gamma} \right) \right] \ln \lambda \quad (7-3)$$

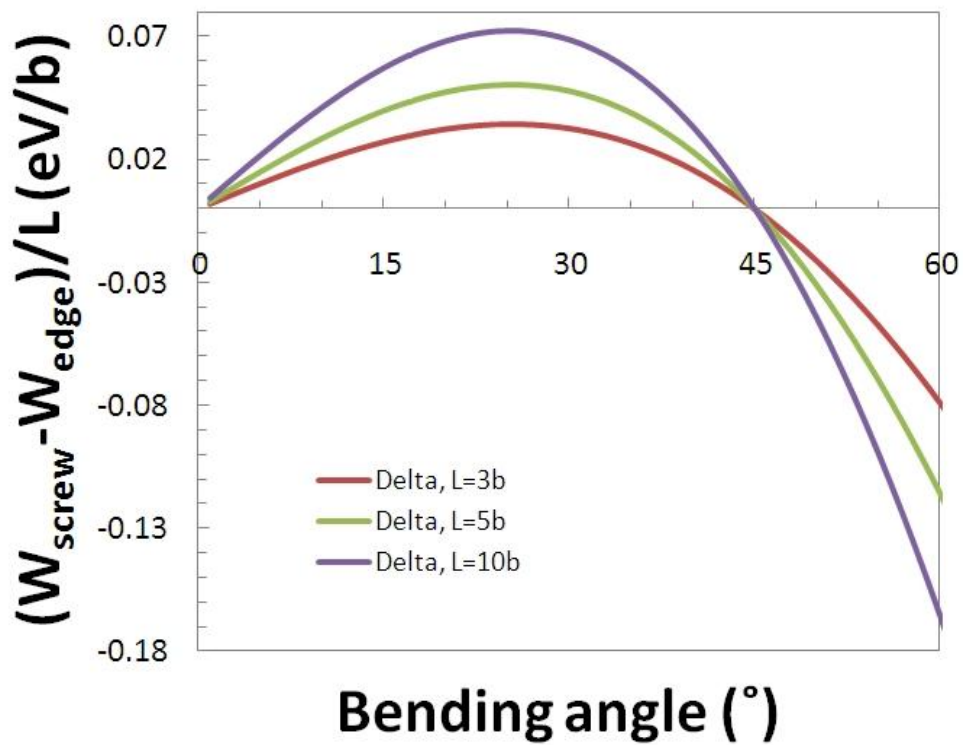


Figure 7-13. Energy difference  $(W_{\text{screw}} - W_{\text{edge}}/L)$  as a function of bending angle.  $L$  denotes bending length of a straight dislocation.

Bowing may be considered as a series of bending processes at very small distances. In Fig. 7-13, the difference of bending energy between screw and edge

dislocations per unit length,  $(W_{\text{screw}} - W_{\text{edge}})/L$ , is always positive number at small angles ( $<15^\circ$ ). Thus, the screw dislocation is harder to bend than the edge dislocation. This tendency increases with increasing bending length,  $L$ . Compared to the prismatic edge  $\langle a \rangle$  dislocations, the bending or bowing of the screw dislocations, IV, would be rare. This is consistent with the present simulation results and general theory of elasticity [21].

The bending energy mentioned above can be expressed as the total energy by combining with the strain energy:

$$E_{\text{Total, screw}} = E_{\text{Strain Energy, screw}} + E_{\text{Bending Energy, screw}} \quad (7-4)$$

where,  $E_{\text{Total, screw}}$ ,  $E_{\text{Strain Energy, screw}}$ , and  $E_{\text{Bending Energy, screw}}$  denotes total, strain, and bending energy of screw dislocation, respectively.

The strain energy is normally noted:

$$\frac{E_{\text{Strain, screw}}}{L} = \frac{\mu b_s^2}{4\pi} \ln \frac{R}{r_0} \quad (7-5)$$

where,  $\mu$ ,  $b$ ,  $R$ , and  $r_0$  denotes bulk modulus, Burgers vector, the range of the strain field, and dislocation core size, respectively.

In real materials,  $R$  is considered as a half of the distance between neighboring dislocations.  $R$  can be replaced by dislocation density,  $\rho$  by:

$$R = 2/\sqrt{\rho} \quad (7-6)$$

In addition,  $r_0$  is normally taken to be  $\sim 3b$  [129, 171, 172]. Thus, substituting  $r_0$  and  $R$  in Eq. 7-5 by  $3b$  and Eq. 7-6, yields

$$\frac{E_{\text{Strain,screw}}}{L} = \frac{\mu b_s^2}{4\pi} \ln \frac{2/\sqrt{\rho}}{3b} \quad (7-7)$$

The total energy of  $\langle a \rangle$  and  $\langle c+a \rangle$  screw dislocations in Fig. 7-12(b) and (c) can be determined by combining Eqs. 7-3 and 7:

$$\frac{E_{\text{Totalscrew}}}{L} = \frac{\mu b_s^2}{4\pi} \ln \frac{2/\sqrt{\rho}}{3b} + \frac{\mu}{4\pi} \left[ b_s^2 \left( \frac{\cos \phi_B - 1}{\sin \phi_B} - \frac{\gamma \sin \phi_B \cos \phi_B}{1 - \gamma} \right) \right] \ln \lambda \quad (7-8)$$

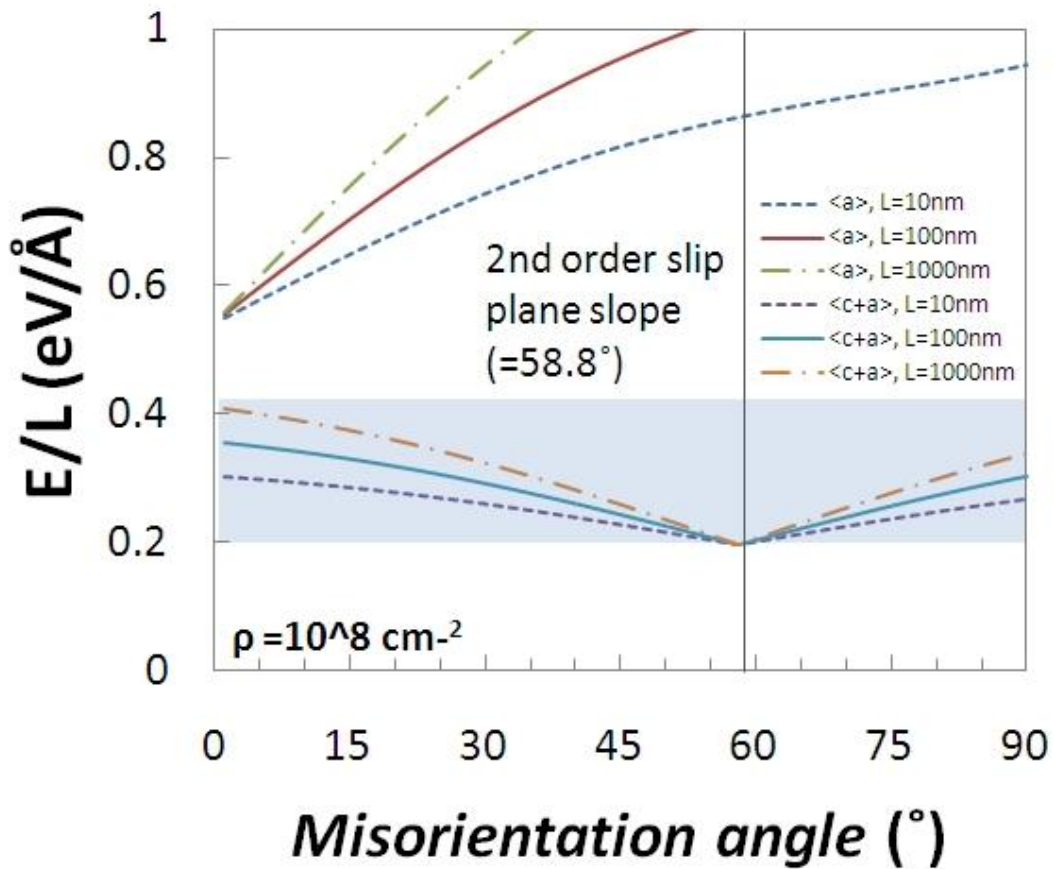


Figure 7-14. Relation between misorientation angle and dislocation energy per unit length ( $E/L$ ) of screw  $\langle a \rangle$  and pyramidal  $\langle c+a \rangle$  dislocations at dislocation density ( $\rho$ ) of  $10^8 \text{ cm}^{-2}$ .  $L$  denotes bending length.

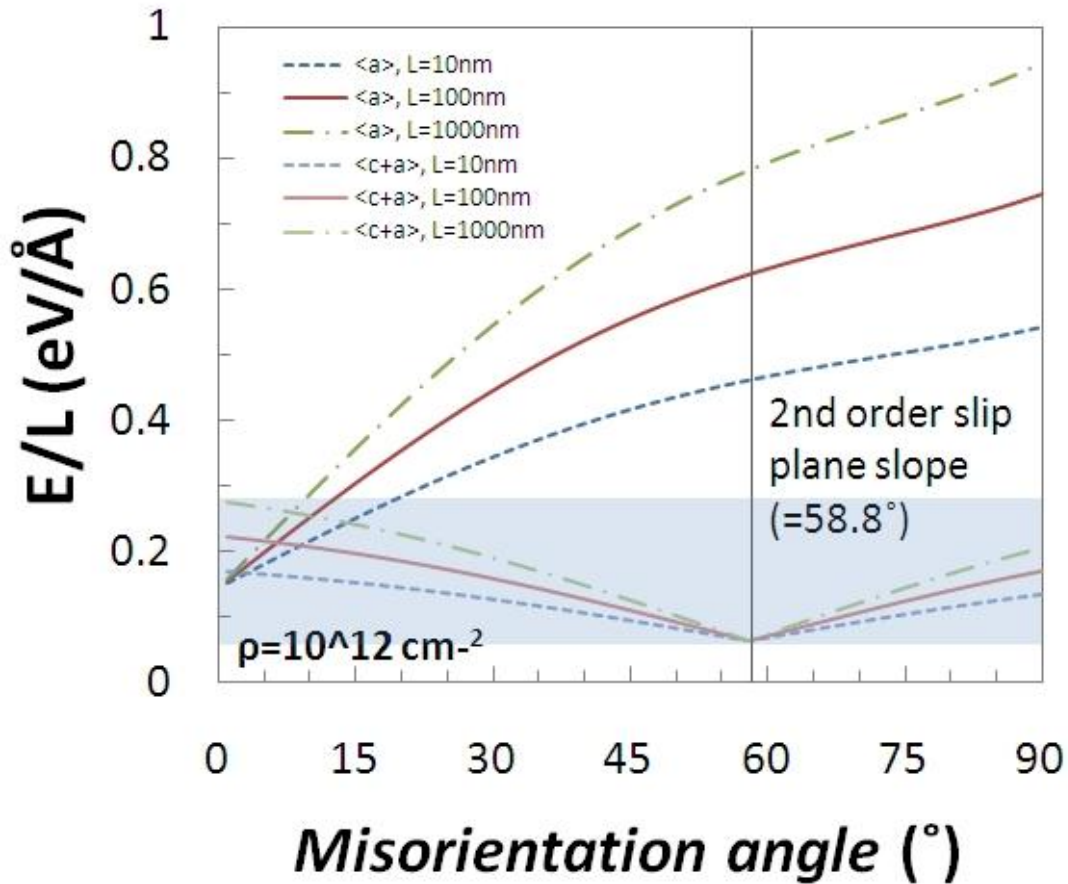


Figure 7-15. Relation between misorientation angle and dislocation energy per unit length ( $E/L$ ) of screw  $\langle a \rangle$  and pyramidal  $\langle c+a \rangle$  dislocations at dislocation density ( $\rho$ ) of  $10^{12} \text{ cm}^{-2}$ .  $L$  denotes bending length.

According to Eq. 7-8, screw  $\langle a \rangle$  and  $\langle c+a \rangle$  dislocations are energetically compared in Figs. 7-14 and 15. It is here necessary to understand the meaning of misorientation angle,  $\theta$ . First,  $\theta$  determines the bowing of  $\langle a \rangle$  and activation of  $\langle c+a \rangle$ . As the direction of the shear stress ( $\tau$ ) is close to the second-pyramidal slip plane,  $\{11\bar{2}2\}$  in Fig. 7-12(a) and (c), the  $\langle c+a \rangle$  slip occurs more easily due to the higher RSS to the  $\{11\bar{2}2\}$  direction. Low  $\theta$  may allow only bowing of  $\langle a \rangle$ , not activation of  $\langle c+a \rangle$ , to take place. If the  $\langle c+a \rangle$  slip once occurs, Figs. 7-14 and 15 are obtained.

$\theta=0^\circ$  and  $\theta=90^\circ$  indicating the  $\langle \mathbf{a} \rangle$ -axis of  $[10\bar{1}0]$  and the  $\langle \mathbf{c} \rangle$ -axis, respectively. If the screw  $\langle \mathbf{a} \rangle$  dislocation glides along  $[10\bar{1}0]$ ,  $\theta$  is zero, and there is no bending energy. If the dislocation bends to some angle  $\theta$ , the total energy increases by contributing to its bending energy. On the other hand, the  $\langle \mathbf{c}+\mathbf{a} \rangle$  screw dislocation is most stable on the pyramidal plane tilted  $58.8^\circ$  from the  $[10\bar{1}0]$  direction in the basal plane. The  $\langle \mathbf{c}+\mathbf{a} \rangle$  dislocation can also bend like the  $\langle \mathbf{a} \rangle$  dislocation. But, bending of the  $\langle \mathbf{a} \rangle$  and  $\langle \mathbf{c}+\mathbf{a} \rangle$  dislocation occurs on different planes: the  $\{10\bar{1}0\}$  and  $\{11\bar{2}2\}$ , respectively. As displayed in Fig. 7-14, at low dislocation density ( $\rho = 10^8 \text{ cm}^{-2}$ ) the  $\langle \mathbf{c}+\mathbf{a} \rangle$  dislocation always has a lower energy than the  $\langle \mathbf{a} \rangle$  dislocation, regardless of the bending length. The reason of this result is much smaller burgers vector of  $\langle \mathbf{c}+\mathbf{a} \rangle$  dislocation: the magnitude of  $\mathbf{b}_{\langle \mathbf{c}+\mathbf{a} \rangle}$  is equal to that of  $\sim 1/3 \mathbf{b}_{\langle \mathbf{a} \rangle}$ . However, in Fig. 7-15 the energy difference becomes small at the high dislocation densities ( $\rho = 10^{12} \text{ cm}^{-2}$ ) which appear in severely deformed metals. As the dislocation density increases, bending of the  $\langle \mathbf{a} \rangle$  dislocations may be thus more frequent. In addition, the energy of the  $\langle \mathbf{a} \rangle$  dislocation increases more rapidly than that of  $\langle \mathbf{c}+\mathbf{a} \rangle$  dislocation with increasing bending length.

### 7-4-3. Twinning

As observed in columnar structures,  $\{10\bar{1}2\} \langle 10\bar{1}1 \rangle$  tensile twins and  $\{10\bar{1}1\} \langle 10\bar{1}2 \rangle$  or  $\{10\bar{1}3\} \langle 30\bar{3}2 \rangle$  compressive twins are nucleated with very different mechanism and conditions. A similar trend is also seen in 3D structures. Figure 7-15 shows nucleation processes of  $\{10\bar{1}1\} \langle 10\bar{1}2 \rangle$  and  $\{10\bar{1}2\} \langle 10\bar{1}1 \rangle$ . The  $\{10\bar{1}1\} \langle 10\bar{1}2 \rangle$  compressive twin is initiated from a triple junction in Fig. 7-15(a), propagating with a sharp shape normal to GB in Fig. 7-15(b). After fully penetrating the grain, the twin begins to thicken. As shown in Fig. 7-15(d), new twins sometimes occur inside the

twin which has sufficiently grown. On the other hand, the boundary of the  $\{10\bar{1}2\} < 10\bar{1}1 >$  twin slowly expands parallel to the GB in the initial stage of nucleation. The  $\{10\bar{1}2\} < 10\bar{1}1 >$  tensile twin is verified to follow the mechanism revealed in a 2D columnar texture (see chapter 7). Hence, the compressive twin is further examined.

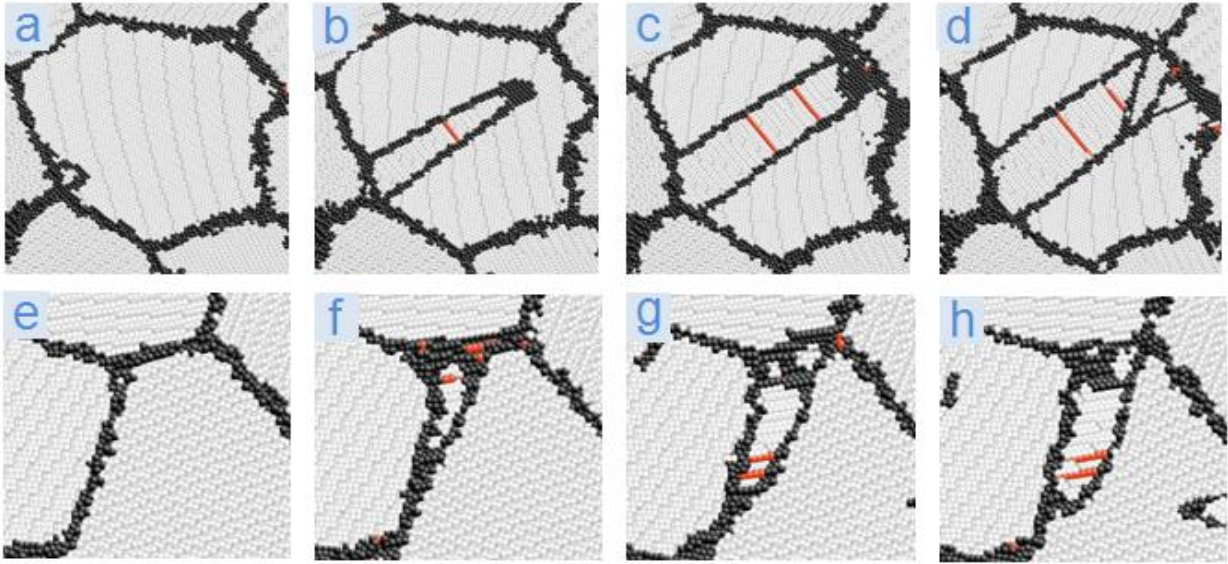


Figure 7-15. Twin nucleation process of the compressive  $\{10\bar{1}1\} < 10\bar{1}2 >$  mode (a ~ d) and tensile  $\{10\bar{1}2\} < 10\bar{1}1 >$  mode (e ~ h). Gray, black and red denote normal (HCP), disordered (non- HCP or FCC), and stacking fault (FCC), respectively. The  $\{10\bar{1}1\} < 10\bar{1}2 >$  twin propagates much faster than the  $\{10\bar{1}2\} < 10\bar{1}1 >$  twin.

The  $\{10\bar{1}1\} < 10\bar{1}2 >$  twin is seen through its potential energy in Fig. 7-16. The blue plane ( $\sim -1.51\text{eV}$ ) indicates an FCC SF shown as the red line in the 2D snapshot of Fig. 7-15. The energy structure of compressive twin boundary (TB) is quite different with that of the FCC SF.

The twin boundary (TB) has alternating lines of atoms with high ( $\sim -1.45\text{ eV}$ ) and low ( $\sim -1.55\text{eV}$ ) energy. This energy and structure are the same as those of the non-basal SF found in partial first-order pyramidal  $\langle \mathbf{c}+\mathbf{a} \rangle$  dislocation previously shown in

Fig. 6-2(b). Hence, the TB is a non-basal SF, and it is highly probable that the compressive twin propagates by dislocation process. The mechanism of twin nucleation by slip has been frequently reported in FCC metals [49, 147, 173]. In addition, it is the reason why the  $\{10\bar{1}1\} < 10\bar{1}2 >$  twin propagates much faster than the  $\{10\bar{1}2\} < 10\bar{1}1 >$  twin, mentioned in Fig. 7-15: both twins have different propagation mechanisms.

### 7-5. Grain Size Effect on Plasticity

The maximum strength of polycrystalline Mg was noted to occur at a grain size of 24nm from Fig. 7-2. The reason for the maximum strength is the crossover of deformation mechanisms from slip and twinning to GB processes with decreasing grain size [36, 42, 43]. Basal  $\langle a \rangle$  slip, pyramidal  $\langle c+a \rangle$  slip, and compressive twin boundaries were successively identified as SFs in Fig. 7-16. Removing the GBs from the images enables us to clearly see a series of deformation processes. Figure 7-16 was obtained using CNA twice. First CNA identifies HCP, FCC, and disordered atoms. After removing HCP atoms from the list of total atoms, the coordination numbers (CNs) of FCC SFs become 6 or 9, and CN of non-Basal SFs appears to be 5. A second CNA process is carried out to distinguish pure SFs. Both GBs and non-basal SF are identified as disordered structure after the first CNA. However, since one atom has the same coordination as neighboring atoms in the SF, the atoms in the SF can be distinguished from those in GBs. Some clusters consisting of a few atoms exist because some atoms can sometimes have the same CN. The clusters are removed using a filtering condition that atoms having CN of smaller than 3 or larger than 11 are not processed.

Now the crossover of deformation mechanisms at nc-Mg is examined, coupling a strain-stress curve and evolution of the SFs. Initiation point of slip and twinning is examined at three grain sizes in Fig. 7-17.

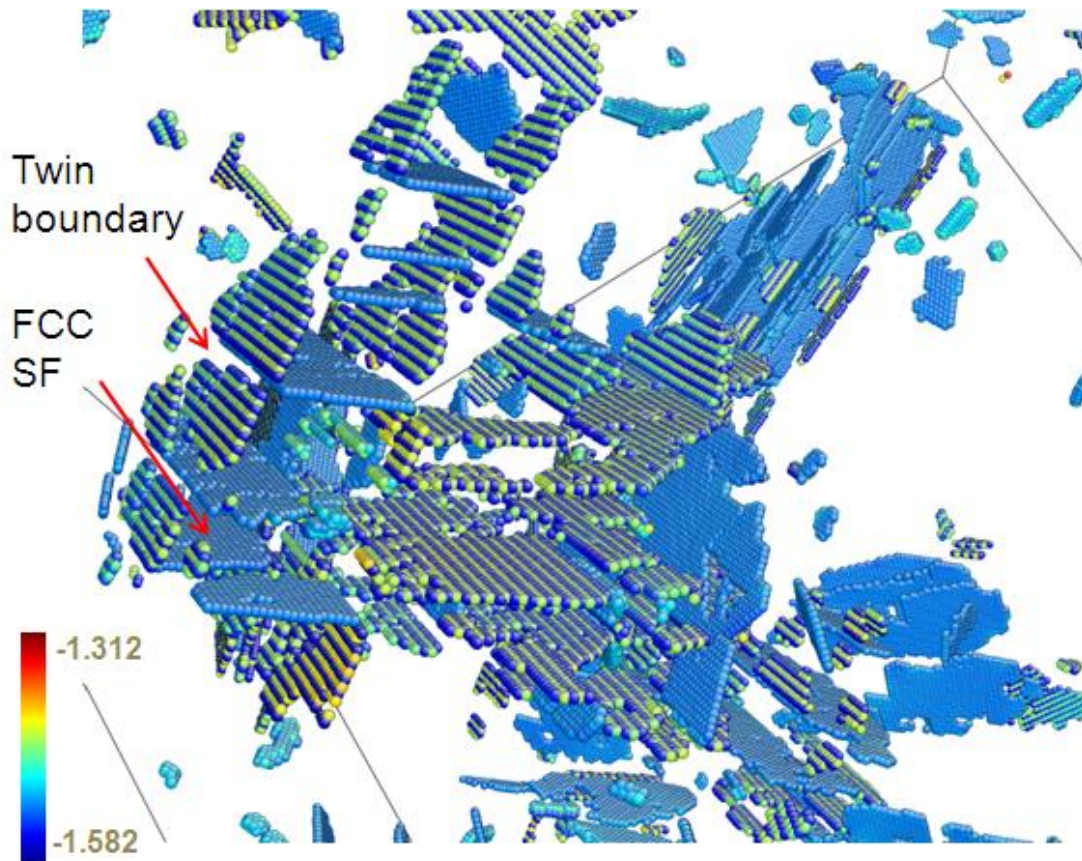


Figure 7-16. Potential energy map of SFs in 11.1%-strained Mg with 36nm grain size. Normal HCP and disordered atoms like GB are not shown here. Removing method of GB is explained at next page.

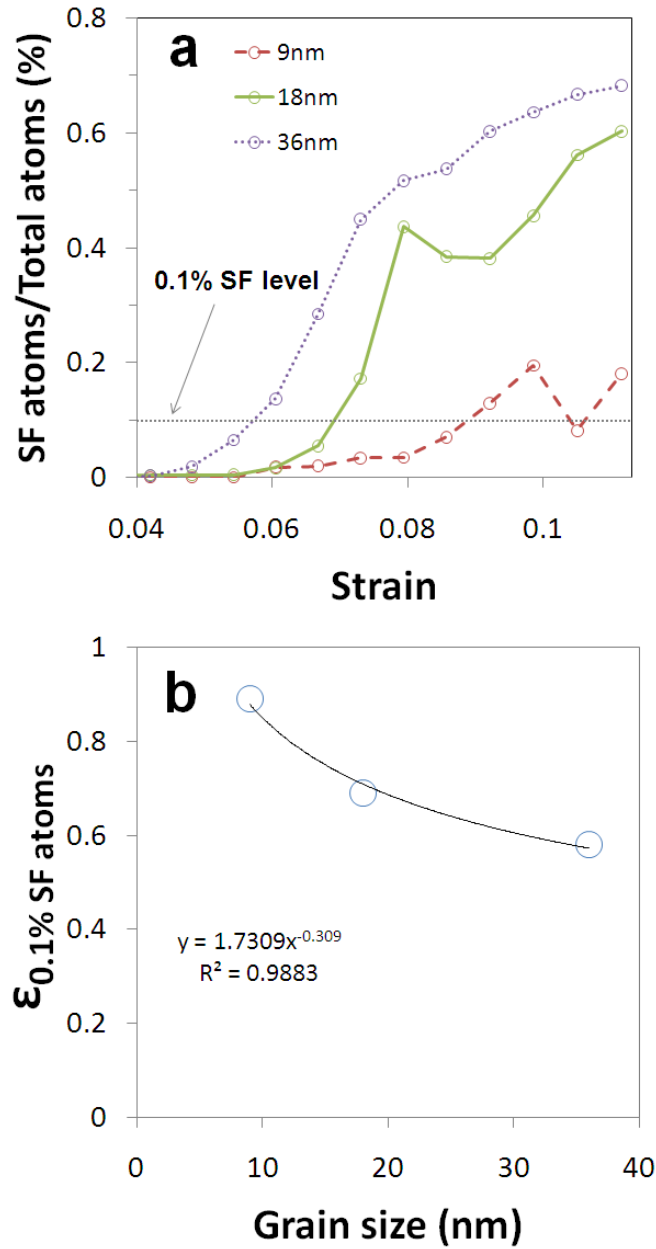


Figure 7-17. Strain and evolution of SFs with increasing strain at different grain sizes (9, 18, and 36nm). The strains of 0.1% SF atoms per total atoms in a increases with decreasing grain size.

In a strained structure, the large number of SF atoms means high activity of conventional deformation process: slip and twinning. Evolution of SFs in Fig. 7-17(a) begins more lately with decreasing grain size. Comparing SF atoms of three grain sizes

at same strain, small grain size shows a small number of SFs. Hence, at small grain sizes, GB processes support insufficient slip and twinning. The SF atom ratio of 0.1% is chosen to remove noise and to accelerate slip and twinning processes in Fig. 7-17(a). The strains at SF atom ratio of 0.1% ( $\epsilon_{0.1\% \text{ SF atoms}}$ ) are shown as a function of grain size in Fig. 7-18(b). The strain point which slip and twinning begins in nc-Mg has the following relation with grain size,  $r$ .

$$\epsilon_{0.1\% \text{ SF atoms}} \sim r^{0.3} \quad (7-9)$$

Graphs of SF evolution and stress-strain at each grain size are seen in Fig. 7-19. In the strain-stress curve of coarse-grained material, the elastic limit depends on how much stress is needed to make a dislocation. This process occurs by pre-existing dislocations inside the material. In Fig. 7-19, SFs are not observed at the yield point. This indicates that the yielding process begins by GB processes in nc-Mg. Normally, the tensile limit at which stress decreases first in the strain–stress curve appears by acceleration of slip or twinning process in coarse-grain materials. Initiation of the SFs before the tensile strength (TS) point in Fig. 7-19 is consistent with that in the coarse-grain materials. Thus, the SFs don't initiate yielding, but are involved with the TS. To deal with a tensile point and initiation of SFs, a strain offset is defined in Eq. 7-10.

$$\text{Strain offset} = \epsilon_{\text{TS}} - \epsilon_{0.1\% \text{ SF atom ratio}} \quad (7-10)$$

The strain offset,  $\sigma_{\text{TS}}$ , and  $\sigma_{0.1\% \text{ SF atom ratio}}$  are summarized in Table 7-2.

Table. 7-2.  $\epsilon_{\text{TS}} - \epsilon_{0.1\% \text{ SF atom ratio}}$ ,  $\sigma_{\text{TS}}$  and  $\sigma_{0.1\% \text{ SF atom ratio}}$  of nc-Mg at grain sizes of 9, 18, and 36nm

Grain size	$\epsilon_{\text{TS}} - \epsilon_{0.1\% \text{ SF atom ratio}}$	$\sigma_{\text{TS}} / \text{GPa}$	$\sigma_{0.1\% \text{ SF atom ratio}} / \text{GPa}$
9nm	0.02375	0.732	0.601
18nm	0.01025	0.918	0.898
36nm	0.00375	1.022	1.021

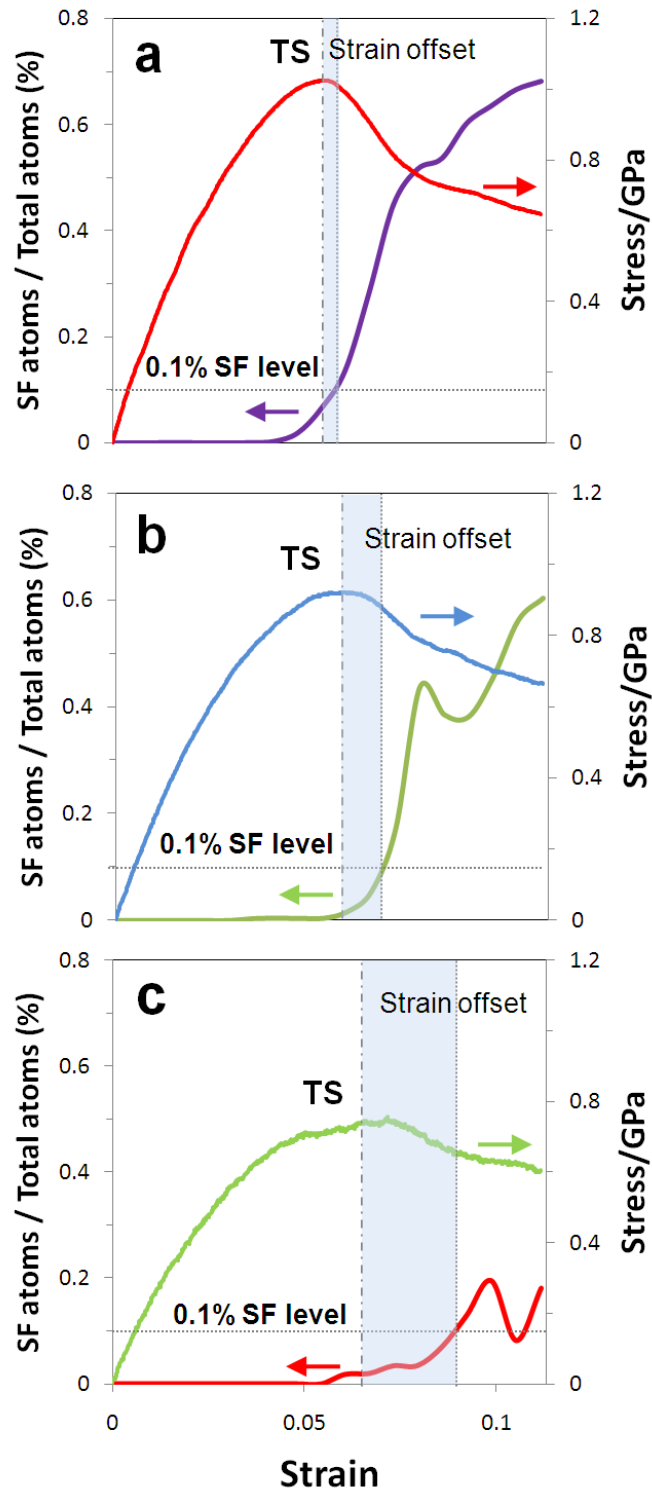


Figure 7-18. Stress and evolution of SFs with increasing strain at different grain sizes. (a) 36nm, (b) 18nm, and (c) 9nm

Snapshots of 11.1%-strained Mg with 9, 18, and 36nm are displayed in Fig. 7-19. The maximum strength of Mg appears at grain size of 24nm. There are fewer SFs at grain sizes smaller than 24nm than that at the 36nm grain size. The larger number of SFs is observed at 36nm grain size, thereby causing strength hardening in nc-Mg. The much lower density of SFs would be insufficient for such hardening. This explains the inverse Hall-Petch behavior at small grain size. The increase in the nucleation stress for dislocations at small grain sizes reduces the evolution of SFs [50]. In nanocrystalline materials, large GB area per unit volume and the high nucleation stress of dislocation allows a GB process to significantly contribute to plasticity.

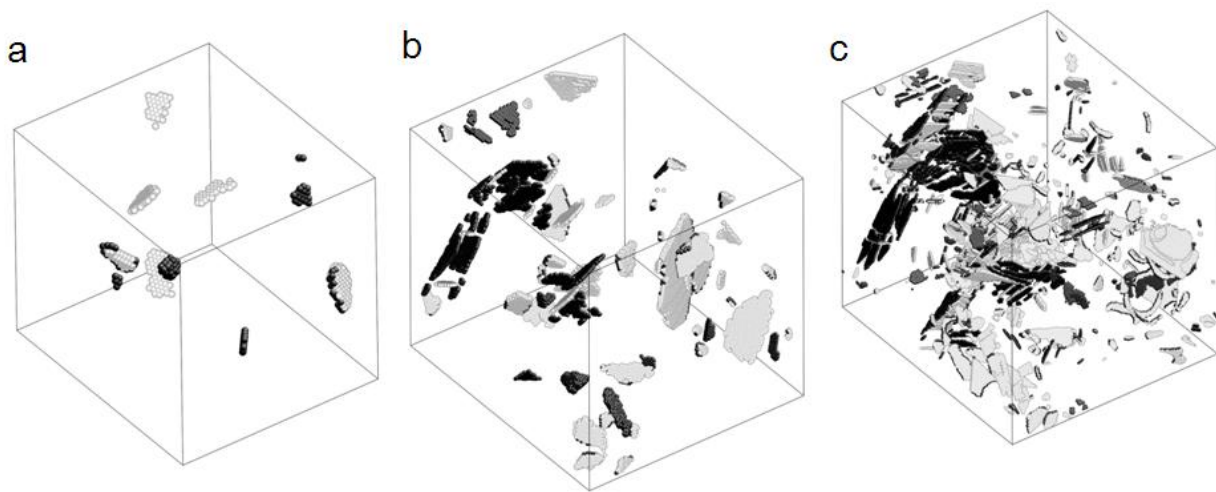


Figure 7-19. SF evolutions of 11.1%-strained samples with three different grain sizes. a. 9nm, b. 18nm, and c. 36nm. GB is not shown in these snapshots. Gray and black denotes twin boundary or dislocation cores and FCC SFs, respectively.

## 7-6. Summary

Using molecular dynamics simulations, physical phenomena in nc-3D Mg were reproduced and analyzed in this chapter. The crossover of the Hall-Petch slope in Mg

appears at grain size of 24nm.  $\langle a \rangle$  slip including basal, prismatic, and pyramidal modes is the dominant deformation process in Mg. There is some direct activation of  $\langle c+a \rangle$  and  $\langle c \rangle$  dislocations from the GBs. The  $\langle c+a \rangle$  and  $\langle c \rangle$  dislocations are nucleated from the prismatic  $\langle a \rangle$  slip process. While the  $\langle c \rangle$  dislocation appears by the interaction between two prismatic  $\langle a \rangle$  dislocations gliding in opposite directions, the  $\langle c+a \rangle$  slip is directly activated from one prismatic  $\langle a \rangle$  dislocation without the help of  $\langle c \rangle$  dislocations. The activation of  $\langle c+a \rangle$  slip can be considered as competing with the bending of a screw  $\langle a \rangle$  dislocation according to the shear stress direction. As the dislocation density increases, bending of the  $\langle a \rangle$  dislocations may be more frequent than the activation of  $\langle c+a \rangle$  dislocations. In addition, the energy of an  $\langle a \rangle$  dislocation increases more rapidly than that of a  $\langle c+a \rangle$  dislocation with increasing bending length. In contrast to boundary of  $\{10\bar{1}2\} \langle 10\bar{1}1 \rangle$  tensile twin, compressive TB is mainly a non-basal SF formed by dislocation processes. Considering the evolution of SFs, slip and twinning are main deformation mechanisms in normal Hall-Petch regime (grain size:  $> 24\text{nm}$ ). The increase in the nucleation stress for dislocations at small grain size reduces the evolution of SFs. Hence, the overall conclusion is that GB processes enhanced at small grain size produce plasticity in nc-Mg.

## CHAPTER 8 CATION ORDERING IN SODIUM BISMUTH TITANATE

Piezoelectric behavior in  $\text{Na}_{0.5}\text{Bi}_{0.5}\text{TiO}_3$  (NBT), an A-site complex perovskite compound, was first identified by Smolenskii et al. in 1960[174]. NBT displays three different phases as the temperature increases: a rhombohedral phase (< 533K), a tetragonal phase (from 533K to 783-813K), and a cubic phase (>~ 800K) phases [175]. The crystallographic structure of NBT at room temperature has R3c symmetry, as Figure 8-1 shows. Four R3c rhombohedral unit cells (in a 2X2 configuration) distinguished by yellow lines are combined in the a-b plane of Fig. 8-1(a). The R3c structure has one unit-cell length in the z-direction of Fig. 8-1(b). The R3c structure can also be viewed as a hexagonal structure, as delineated by black line on the xy-plane. The Ti and the other cations (Na and Bi) are alternatively arranged along the c-axis. Six oxygens surrounding a titanium atom form an octahedron, as noted by transparent blue structure in Fig. 8-1(b). Two vertices of the octahedra are corner connected with other octahedra in diagonal direction of R3c cell seen in Fig. 8-1(b). Figure 8-1(c) the R3c structure in pseudo-cubic axis ( $x_p, y_p,$  and  $z_p$ )

The R3c phase of NBT can be expressed with a  $\bar{a}\bar{a}\bar{a}$  tilt system which appears in rhombohedral perovskites arising from oxygen octahedra along each axis. This results in cell doubling of all three pseudo-cubic axes [175]. In this case, the cH setting of hexagonal R3c structure corresponds to  $[111]_p$  of pseudo-cubic axis. In the rhombohedral system, a rhombohedrally centered hexagonal lattice projected down the threefold axis be considered as hexagonal axes, whose lattice parameters  $a_H$  and  $c_H$

are specified in relation to the double pseudo-cubic cell ( $2a_p \times 2b_p \times 2c_p$ ) by the following matrix [175].

$$\begin{pmatrix} 0.5 & 0 & -0.5 \\ -0.5 & 0.5 & 0 \\ 1 & 1 & 1 \end{pmatrix} \quad (9.1)$$

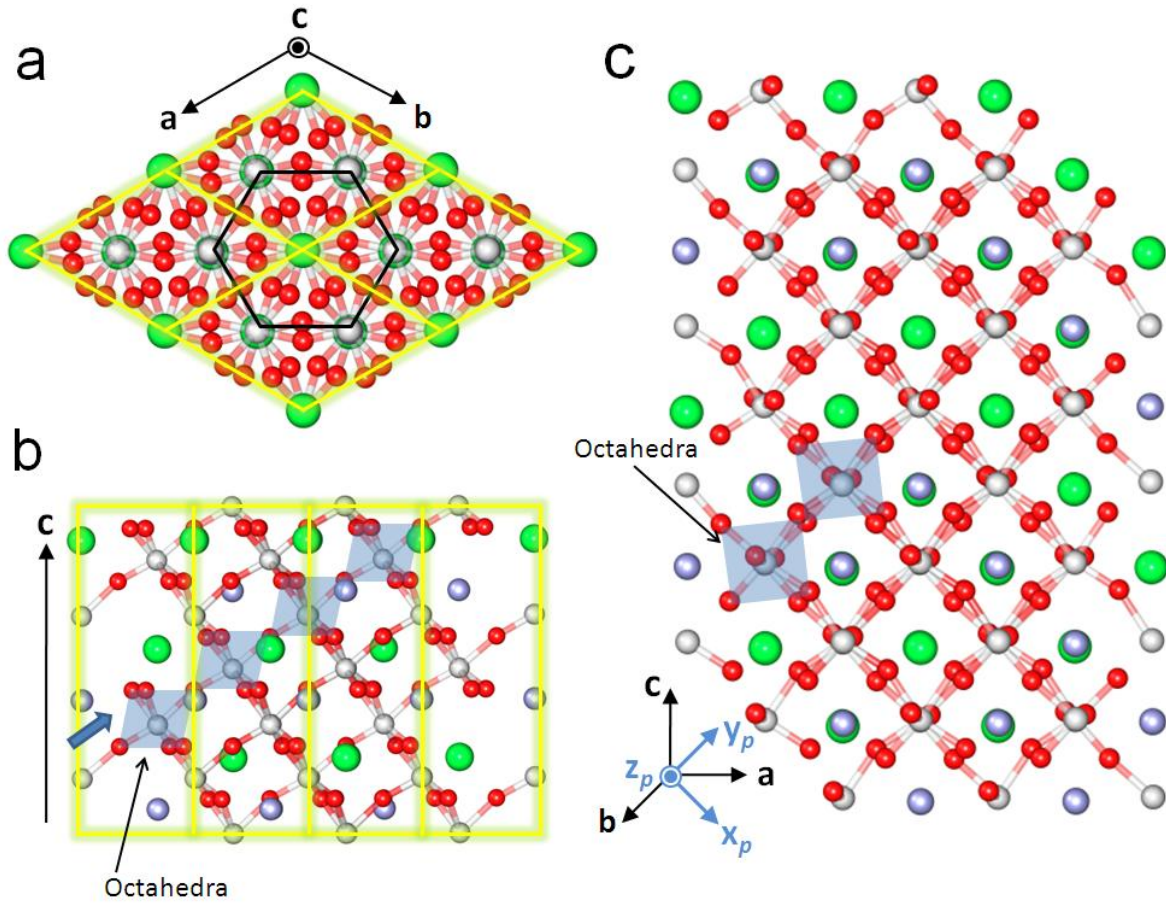


Figure 8-1. R3c structure of 2 X 2 X 1 unit cell sizes. White, green, and red indicate titanium, Na or Bi, and oxygen, respectively.  $a$ ,  $b$ , and  $c$  denotes hexagonal axis, and  $x_p$ ,  $y_p$ , and  $z_p$  represents pseudo-cubic axis.

Table 8-1. Three different phases and crystallographic data of NBT[175]

Crystal system	Rhombohedral**	Tetragonal	Cubic
Temperature (K)	< 673	> 673, < 873	> 873
Space group	R3c	P4bm	Pm $\bar{3}$ m
$a_H$ (Å)	5.4887	-	-
$c_H$ (Å)	13.5048	-	-
$a_p$ (Å)	-	5.5179	3.91368
$c_p$ (Å)	-	3.9073	-
$\alpha, \beta, \gamma$ (°)	90, 90, 120	90, 90, 90	90, 90, 90
$\alpha_p$ (°)	89.83		
Tilt system	$a^-a^-a^-$ (three tilt system, antiphase)	$a^0a^0c^+$ (one tilt system, in-phase)	$a^0a^0a^0$ (zero-tilt system)
Displacements	Parallel along $[111]_p$	Antiparallel along $[001]$	None
$\omega$ (°)	8.24	3.06	-

\* Some parameters are updated.

\*\* Monoclinic phases are being reported instead of the rhombohedral phase with R3c.

The pseudo-cubic cells are shown in Fig. 8.2. The left of Fig. 8.2 represents a view of the rhombohedral structure of double pseudo-cubic cell down  $[001]$  showing the tilt system.  $\omega$  and circle denote a tilting angle of octahedra and Na/Bi atoms, respectively. Single pseudo-cubic cell with a shape of  $ABX_3$  (A, B=cation, X=anion) perovskite structure is seen in right of Fig. 8.2. Hatched and black circles indicate A and B atoms, respectively.

$PbZr_{0.5}Ti_{0.5}O_3$  (PZT) having a perovskite structure of  $ABO_3$  (A=Pb, B=Zr and Ti) has numerous applications, due to its superior ferroelectric and piezoelectric properties. However, as previously mentioned in Chapter 1, since PZT contains lead, there have been various attempts to find identify alternative compositions [176-178].  $Na_{0.5}Bi_{0.5}TiO_3$

(NBT) is one potential alternative for PZT. The ferroelectric and piezoelectric properties of NBT are similar to those of PZT. A high coercive field and a relative high conductivity are however obstacles to overcome for applications [179].

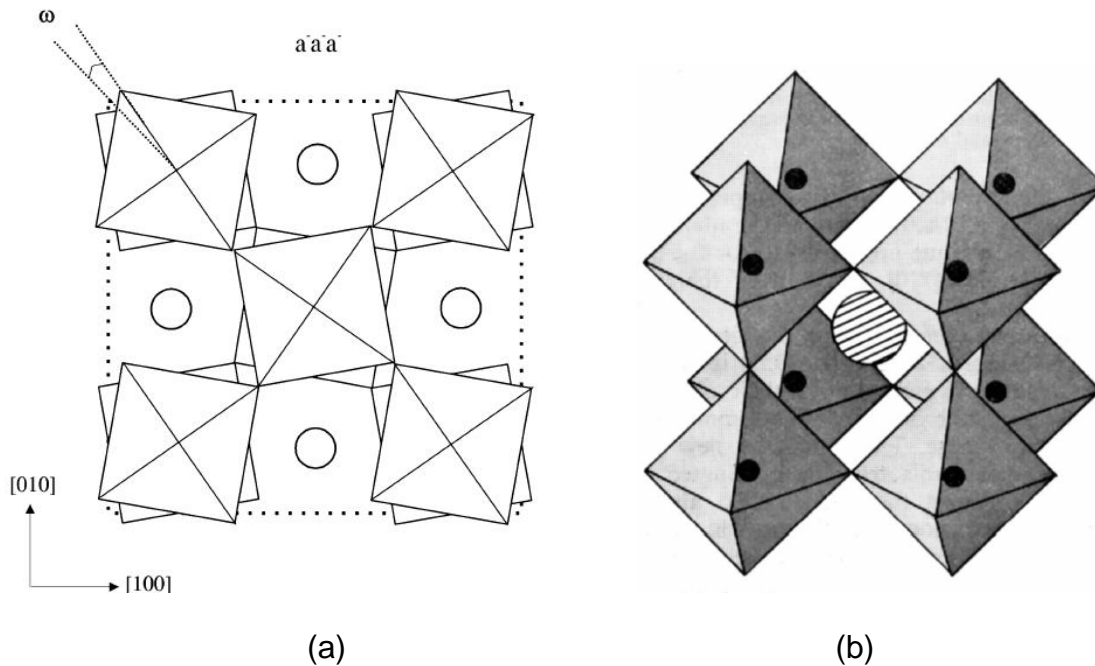


Figure 8-2. Pseudo-cubic cells of perovskite. (a) The projection of the rhombohedral cell down [001]. open circles denotes Na/Bi sites [175]. (b) The ideal cubic perovskite of  $ABX_3$  (A, B = cation, X = anion). The anions are at the vertices of the octahedra. Hatched and black circles denotes A and B cations [180].

To improve the properties of NBT, we need to understand its structure at the atomic level. In the structure of NBT, sodium and bismuth occupy the A in the  $ABO_x$  perovskite structure. There have been only a few studies of the arrangement of the Na and Bi cations. Moreover, the results are contradictory. Short-range cation ordering of Na and Bi was found in neutron scattering by Vakhrushev et. al [181]. However, long-range ordering between  $Na^+$  and  $Bi^{3+}$  cations was observed in XRD analysis using a single crystal rotation camera [182].

As previously mentioned in Fig.-2-2, *ab-initio*, or first principles, calculation are useful for characterization of the atomic and electronic structures at small scales. Since the cation ordering is presumed to involve a relatively small number (less than a few hundred) of Na and Bi atoms, first principles calculations can be used.

Table 8-2. Comparison of ferroelectric properties of PZT[9] and NBT[179].

Properties	PZT	NBT
Remnant polarization (Pr)	35 $\mu$ C/cm <sub>2</sub>	38 $\mu$ C/cm <sub>2</sub>
Coercive field (Ec)	20KV/cm	73KV/cm

## 8-1. Background

### 8-1-1. First Principles Calculations

First principles calculations are based on the interactions of the electrons and nuclei in a system. These interactions are described by quantum mechanics through the Schrödinger Equation. The time-independent, non-relativistic Schrödinger Equation [183] is written as:

$$H\Psi = E\Psi \quad (9-3)$$

where H is the Hamiltonian operator,  $\Psi$  is the eigenstate wave function and E is the eigenvalue (energy). Eq. 9-3 can be solved exactly for only a very few specific cases, such as the hydrogen atom. The Hamiltonian in Eq. 9-3 can be expanded with Born-Openheimer approximation to:

$$\left[ \frac{-\hbar^2}{2m} \sum_{i=1}^N \nabla_i^2 + \sum_{i=1}^N V(r_i) + \sum_{i=1}^N \sum_{j<i}^N U(r_i, r_j) \right] \Psi = E\Psi \quad (9-4)$$

Where, m is the mass of the electron and N is the total number of electrons in the system [184]. The individual terms in the Hamiltonian in Eq. 9-4 are, from left to right,

the kinetic energy of each electron, the electron-nuclei interactions, and the electronic-electron interactions, respectively.

The total wave function  $\Psi$  is a function of the spatial coordinates of the N electrons, or

$$\Psi = \Psi(r_1, r_2, \dots, r_N) \quad (9-5)$$

This full wave function can be approximated as a product of individual wave functions, known as the Hartree product, and expressed as:

$$\Psi = \Psi(r_1) \Psi(r_2) \dots \Psi(r_N) \quad (9-6)$$

In the Copenhagen interpretation of quantum mechanics, the electron density at a particular position,  $r$ , can be written in terms of the wave function as:

$$n(r) = 2 \sum_i \Psi_i(r) \Psi_i^*(r) \quad (9-7)$$

where, the asterisk indicates the complex conjugate of the wave function. The prefactor of 2 in Eq.9-7 takes into account the Pauli exclusion principle that each individual electron wave function can be occupied by two electrons with opposite spin.

Considering N electrons in the system, this density approach reduces Eq.9-4 to be a function of 3N coordinates. This electron density is the main motivation towards the development of density functional theory (DFT).

### 8-1-2. Density Functional Theory (DFT)

The Kohn-Sham theorem [185] states that *“the electron density that minimizes the energy of the overall functional is the true electron density corresponding to the full solution of the Schrödinger’s Equation.”* According to this theorem, the properties of a many-electron system are determined by using functionals which are the spatially

dependent electron density. The name of density functional theory thus comes from the use of functionals of the electron density.

Based on the Hohenberg-Kohn theorem [184], the simplified energy functional can be written as :

$$E[\{\Psi_i\}] = E_{\text{known}}[\{\Psi_i\}] + E_{\text{XC}}[\{\Psi_i\}] \quad (9-8)$$

where,

$$E_{\text{known}}[\{\Psi_i\}] = \frac{-\hbar^2}{m} \sum_i \int \Psi_i^* \nabla^2 \Psi_i d^3r + \int V(r)n(r) d^3r + \frac{e^2}{2} \iint \frac{n(r)n(r')}{|r-r'|} d^3r d^3r' \quad (9-9)$$

$$+ E_{\text{ion}}$$

and  $E_{\text{XC}}[\{\Psi_i\}]$  is the exchange-correlation functional which defines all the other interactions not included by Eq.9-9. The terms in Eq.9-9 are, from left to right, the kinetic energy of electrons, the Coulomb interaction between the electrons and nuclei, the Coulomb interactions between electrons, and the Coulomb interactions between nuclei. In order to solve for  $E_{\text{XC}}[\{\Psi_i\}]$ , Kohn-Sham showed that the correct electron density can be expressed as solving a set of Equations involving single electrons only. Therefore, Eq.9-4 can be written in terms of the Kohn-Sham Equation as:

$$\left[ \frac{-\hbar^2}{2m} \nabla_i^2 + V_{\text{ion}}(r) + V_H(r) + V_{\text{XC}}(r) \right] \Psi_i(r) = \varepsilon_i \Psi_i(r) \quad (9-10)$$

Where  $V_{\text{ion}}(r)$  is the electron-ion potential,  $V_H(r)$  is the Hartree potential,  $V_{\text{XC}}(r)$  is the exchange-correlation potential,  $\varepsilon_i$  is the Kohn-Sham eigenvalue, and  $\Psi_i$  is the wave function of state  $i$ . The Hartree potential is given by:

$$V_H(r) = e^2 \iint \frac{n(r')}{|r-r'|} d^3r' \quad (9-11)$$

The exchange-correlation potential is given as:

$$V_{XC}(r) = \frac{\delta E_{XC}(r)}{\delta n(r)} \quad (9-12)$$

where,  $E_{XC}(r)$  is the exchange –correlation energy.

Even though Eq.9-10 looks very similar to Eq.2-32, there is one very distinct difference: Eq.9-10 does not contain any of the summations that are present in Eq.9-4. This makes replacement of the electron wave function by the electron density much more useful from a computational standpoint.

The solution of Eq.9-10 proceeds as follows [184]:

- a) An initial guess of the electron density,  $n(r)$  is made.
- b) The Kohn-Sham equation is solved to find the single particle wave functions,  $\Psi_i(r)$ .
- c) The electron density is calculated from the single particle wave functions obtained from step b) using  $n_{KS}(r) = 2 \sum_i \Psi_i(r) \Psi_i^*(r)$ .
- d) The previous value of  $n(r)$  and the calculated  $n_{KS}(r)$  are compared. If the two densities are the same then the ground-state electron density has been identified. If not, then steps b) - d) are repeated to convergence

### 8-1-3. Exchange-Correlation Functional

The key idea behind the Kohn-Sham theory was to make the unknown contribution ( $E_{XC}[n(r)]$ ) as small as possible. Nevertheless, it is important to choose a good exchange –correlation approximation for the system under consideration.

One common approximation is the local density approximation (LDA) [184]. In this approximation the exchange –correlation potential at any position,  $r$ , is assumed to be describable as a homogeneous electron gas having the same density. Since a homogeneous gas approximation is not always physically appropriate in real systems, a

more sophisticated description of the functional is given by the generalized gradient approximation (GGA) [186]. The GGA functional includes both the local electron density and the local gradient in the electron density.

One would expect that GGA with a more elaborate description of the exchange-correlation functional for individual calculations would match experiment better. However, this is not always the case [184]. Hence, care must be taken in choosing the exchange-correlation functional for individual calculations.

## 8-2. Computational Details

To investigate the comparative stability of various arrangements of the Na and Bi cations around the Ti and O octahedra, the Vienna *ab initio* Simulation Package (VASP) based on the DFT is used in the present work. For these calculations, the electron exchange-correlation energy is described in the generalized gradient approximation (GGA) with pseudopotentials of projector augmented wave (PAW). The GGA is chosen because GGA generally gives substantially better materials properties than the LDA, particularly for the cohesive properties, bonding length and atomization energies.

The cutoff energy for the plane wave basis set is chosen to be 450e. The criteria for considering the calculations as fully converges is that the total force on all of the atoms atoms is  $<0.02$  eV/Å. The 2 X 2 X 2 NBT supercell is treated with a 2 X 2 X 1 Monkhorst-Pack *k*-point mesh to sample the Brillouin zone.

The simulation structure has symmetry of R3c which is the room temperature phase of NBT shown in Table 8-1. In the R3c hexagonal unit cell of NBT, the A sites are occupied by 3 Na and 3 Bi atoms. Both short and long range ordering of Na and Bi are considered in the present work. For charge neutrality, the number of Na and Bi in the supercell are set to be equal. If the hexagonal structure is considered as being formed

from three identical rhombohedral unit cells, then the six inequivalent cation sites can be occupied by three Na and Bi, resulting in four different arrangements of Types I - IV as shown in Table 8-3 and Figure 8-3. Type IV appears not to have any long range ordering in the pseudo-cubic perovskite structure, in contrast to Types I, II, and III (see Fig. 8-4). By contrast, if all of the cations in a 2X2X2 supercell of hexagonal unit cell are treated as being independent, then there are many more possible cation arrangements. Types VI - IX have twenty four Na and twenty four Bi atoms which occupy the forty eight cation sites in the 2X2X2 cell in various different ways. In particular, Type V is obtained by expanding the Type I cation ordering of 1X1X1 supercell to the 2X2X2 supercell. When a unit cell of Type I is connected with the other one, of the A cation changes identity. Thus the structure becomes NaNaNa|BiBiBi or BiBiBi|NaNaNa (see [100] and [010] in Table 8-3). However, there is no such change in cation ordering in Type V. When viewed as a pseudo-cubic perovskite structure, the layers of Type V consist of cations of the same species along the [100] and [010] directions and alternating cations along the orthogonal [001] direction.

Table 8-3. Arrangements of Na and Bi in 2 X 2 X 2 super cell.

Types	Method of cation arrangement	Cation arrangements				Ordering of Na and Bi
		Hexagonal unitcell A B C D E F	Perovskite axis			
			[100] <sub>p</sub>	[010] <sub>p</sub>	[001] <sub>p</sub>	
I		N B B B N N	N N N B B B	N N N B B B	N B B N B B	
II	Duplicating a hexagonal unit cell	N B N B N B	N B N B N B	N B N B N B	N B N B N B	long range
III		B B B N N N	N N N B B B	N N N B B B	N N N B B B	
IV		B N N B N B	Not fixed			
V	Arranging Na and Bi in a	-	All N (or B)	All N (or B)	N B N B N B	long range
VI - IX	2X2X2 frame of Ti-O	Not fixed				Short range

\* N and B denote Na and Bi, respectively

\* 'A' ~ 'F' in 'Hexagonal unit cell' represent available sites for Na and Bi in Fig. 8-3.

\* [100]<sub>p</sub>, [010]<sub>p</sub>, and [001]<sub>p</sub> in 'Perovskite axis' indicate x, y, and z axis of pseudo-cubic.

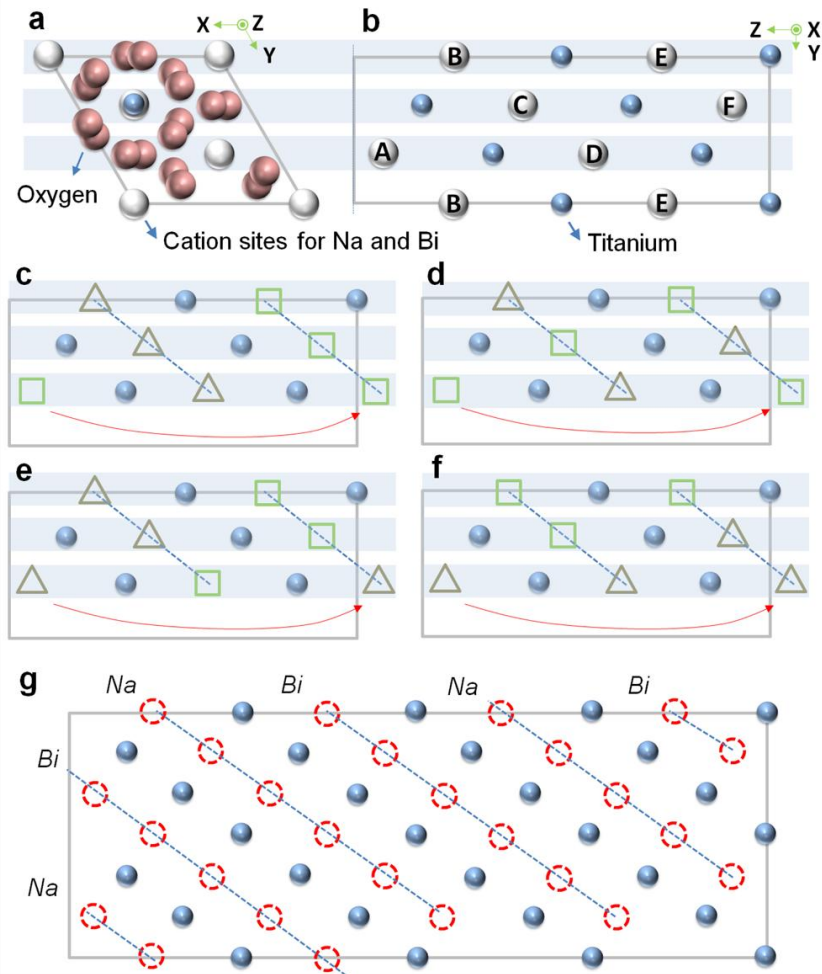


Figure 8-3. Cation arrangements adopted in the present work. (a) a unit cell of NBT on the x-y plane (basal) (b) a unit cell of NBT in the z-axis (c ,d, e, and f ) Type 1, 2, 3, and 4 (T1,T2,T3,T4) (g) a 2X2X2 frame of NBT for Type 5, 6, 7, 8, and 9 (T5, T6, T7, T8, and T9). Red dot circle denotes cation sites for Na and Bi. Each blue dot line, indicating one of the perovskite axes, has alternating cations in Type 5, as denoted with a chemical element of Na or Bi. From T6 to T9, the red dots are occupied by Na and Bi.

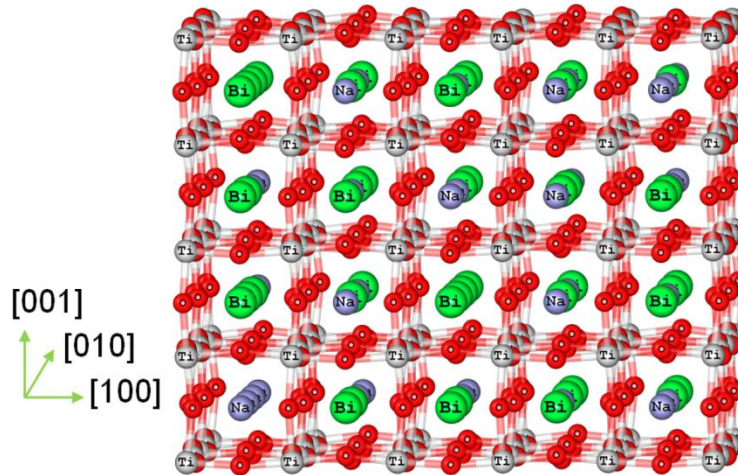


Figure 8-4. Cation ordering in T4 with 5 X 4 X 4 psuedo-cubic size.

### 8-3. Analysis of Structure Change

Structural information and energies of samples from T1 to T9 optimized using the GGA calculations are shown in Table 8-4. Among the various types, the R3C symmetry of  $a=b \neq c$ ,  $\alpha=\beta=90^\circ$  and  $\gamma=120^\circ$  is closely satisfied by the T1, T2, and T3 structures. To compare each type effectively, the lattice constants and angles are plotted in Fig. 8-5.

Table 8-4. Structural parameters and energies of each ordering type.

Type	T1	T2	T3	T4	T5	T6	T7	T8	T9
E/eV	-1803.33	-1803.65	-1803.37	-1803.77	-1807.27	-1804.41	-1804.65	-1804.61	-1804.36
a/Å	10.98919	10.9908	10.98999	10.99561	10.88887	10.99918	10.99815	10.99954	10.99877
b/Å	10.98917	10.9908	10.99023	11.00228	11.02058	10.99924	10.99961	10.99736	11.0081
c/Å	26.98994	27.42721	26.99251	27.29441	27.14211	27.36157	27.37067	27.34045	27.2759
$\alpha/^\circ$	90.0005	90.0001	89.9993	89.818	90.1559	89.9733	89.9725	89.9253	89.9579
$\beta/^\circ$	89.9996	90.0000	89.9993	90.1202	89.9998	89.9917	89.9739	90.0723	89.9291
$\gamma/^\circ$	120.0003	120.0001	119.9999	119.9271	119.6057	119.9762	119.9931	119.9716	120.0415
V/Å <sup>3</sup>	2822.677	2869.261	2823.437	2861.688	2831.856	2867.467	2867.759	2864.989	2858.797

T5 sample doesn't satisfy the R3c symmetry due to anisotropy in its lattice constants (a and b) and angles ( $\alpha$  and  $\beta$ ), as shown in Table 8-4 and in Fig. 8-5(a). In all

samples except T5, the lattice parameters,  $a$  and  $b$ , are essentially identical,  $a=b$ . Interestingly, the energy of the T5 (-1807.27eV) having the distorted structure from R3c is clearly lower than that of the other samples (-1803.33 - 1804.65eV) in the  $2 \times 2 \times 2$  supercell containing 240 atoms in Fig. 8-5(b). The T5 sample will be discussed later. Except T5, samples from T6 to T9 with random arrangements of cations have lower energy than cation ordering manipulated with some rules from T1 to T4. This indicates that if NBT is identified from R3c by XRD(X-ray Diffraction) or ND (Neutron Diffraction) in experiments, random ordering of Na and Bi would be prevalent. This is also coincident with Vakhrushev et. al.[181]'s ND results and Park et. al.[182]'s XRD results of NBT sample prepared by the flux method. On the other hand, non-R3c NBT at room temperature has been reported. Park et al.[182] identified NBT grown by the Czochralski method as pseudo-cubic with a small deviation from ideal cubic. Aksel et al. [187] also found a monoclinic phase of NBT instead of R3c symmetry using XRD analysis. Assuming that the T5 structure could be the low symmetry structure found experimentally, structure analysis and formation mechanism of T5 would be important. Hence, in the next section, the T5 sample having the lowest energy is compared with T2 sample satisfying R3c symmetry. In addition, a symmetrical analysis and probable reason for the distortion of T5 structure are dealt with in detail.

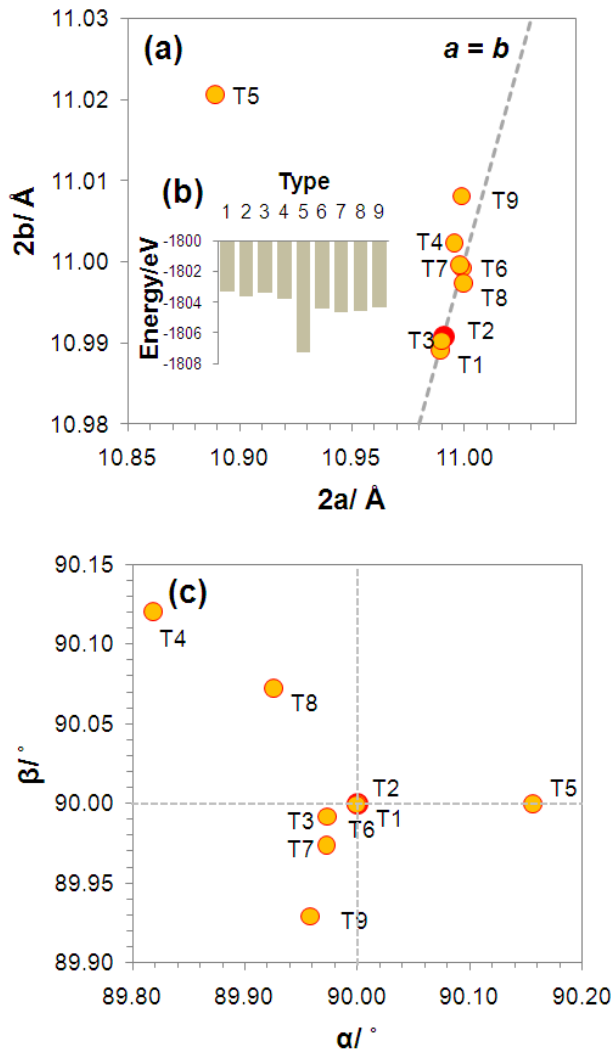


Figure 8-5. Energy and correlation between structural parameters. (a)  $2a$ - $2b$ . (b) Energy. (c)  $\alpha$ - $\beta$ .

#### 8-4. Analysis of Layered NBT

The final optimized structures of T2 (left) and T5 (right) are exhibited in the pseudo-cubic perovskite axes ( $a_p$ ,  $b_p$ , and  $c_p$ ) in Fig. 8-6. T2 is a reference structure of R3c symmetry. T5 displays the largest deviation between the initial and final structures, as discussed above. While T2 appears as the pseudo cubic cells of Fig. 8-2, cells of zigzag by distorted oxygen (pink dots) structure are seen in T5. In contrast to sodium (green dots), bismuth (blue dots) is off-center in cells of Ti (white dots) and O in T5 of

Fig. 8-6. Hence, it is revealed that there is a big structural change in T5, resulting in a large difference in lattice parameters shown in Table 8-4 and Figure 8-5.

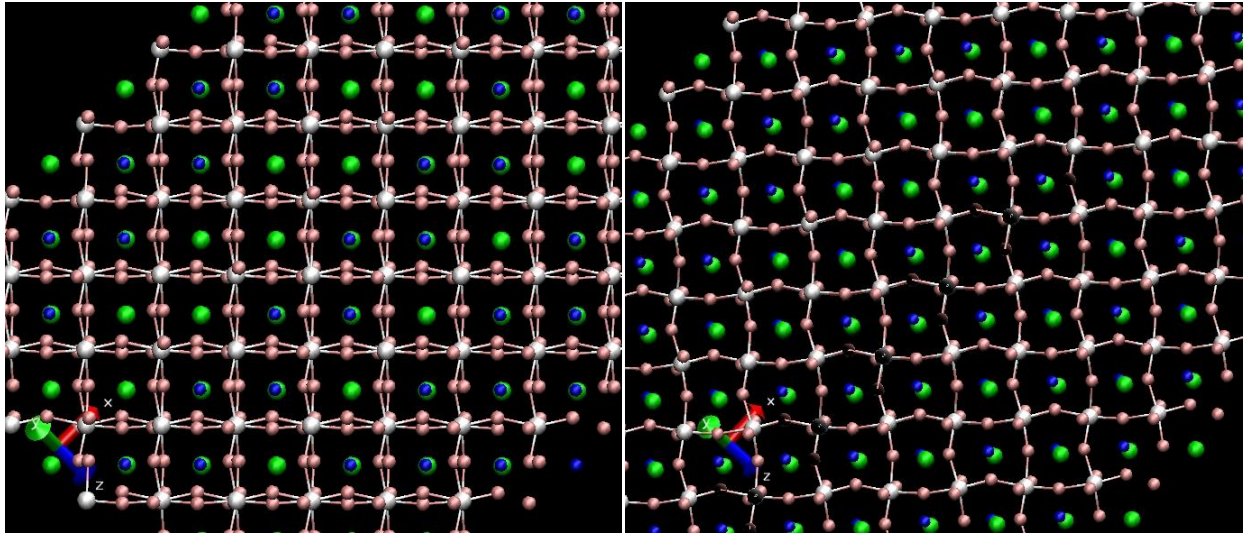


Figure 8-6. Final optimized structures of T2 (left) and T5 (right) in the perovskite axis ( $a_p$ ,  $b_p$ , and  $c_p$ ). Blue, green, pink, white dots denote bismuth, sodium, titanium, and oxygen, respectively. Blue, red, and green arrows indicate three perovskite axis,  $a_p$ ,  $b_p$ , and  $c_p$ , respectively.

Variations of energy and force are compared between T2 and T5 in Fig.9-7. As shown in Fig. 8-7(a), the final structure of T2 having the lowest energy (-1803.6 eV) is obtained at 38 ionic iteration steps (ITS). The final optimized structure of T2 is R3c. On the other hand, T5 shows similar trend of energy and force with T2 for the first 55 ionic iteration steps. For the next ~15 iteration steps, the force actually increases even though the energy decreases from -1806.2 to -1807.2 eV after 60 ITS. Such changes of force and energy indicate that there is a significant change in the structure of T5. Analyzing the final optimized structure of T5, a new phase is found, which does not satisfy the R3C symmetry of the initial structure.

Figure 8-8 shows the optimized T5 structure. As shown in the two schematics, it has lower symmetry than R3C. Along the c-axis, the layers of Na and Bi are alternatively stacked, with the Na and Bi columns offset from each other. Such a distorted structure can be attributed to the charge balance in and between layers of Na and Bi having a charge of +1 and +3, respectively. The structural characterization of the layered structure is shown in Table 8-5.

Table 8-5. Structural information of the layered structure, T5.

Symmetry	Lattice constants			Lattice angles		
	a	b	c	$\alpha$	$\beta$	$\gamma$
P1	7.77322	7.77768	7.82025	90.0030	89.9993	88.8383

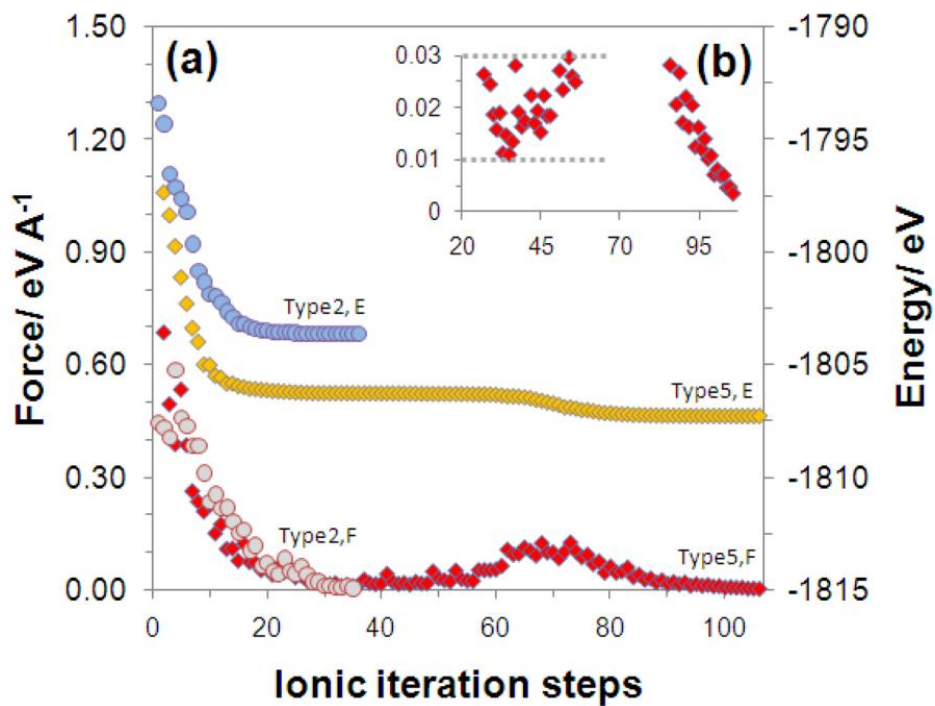


Figure 8-7. Change of force and energy in T2 and T5 as a function of an ionic iteration step. E and F denote energy and force.

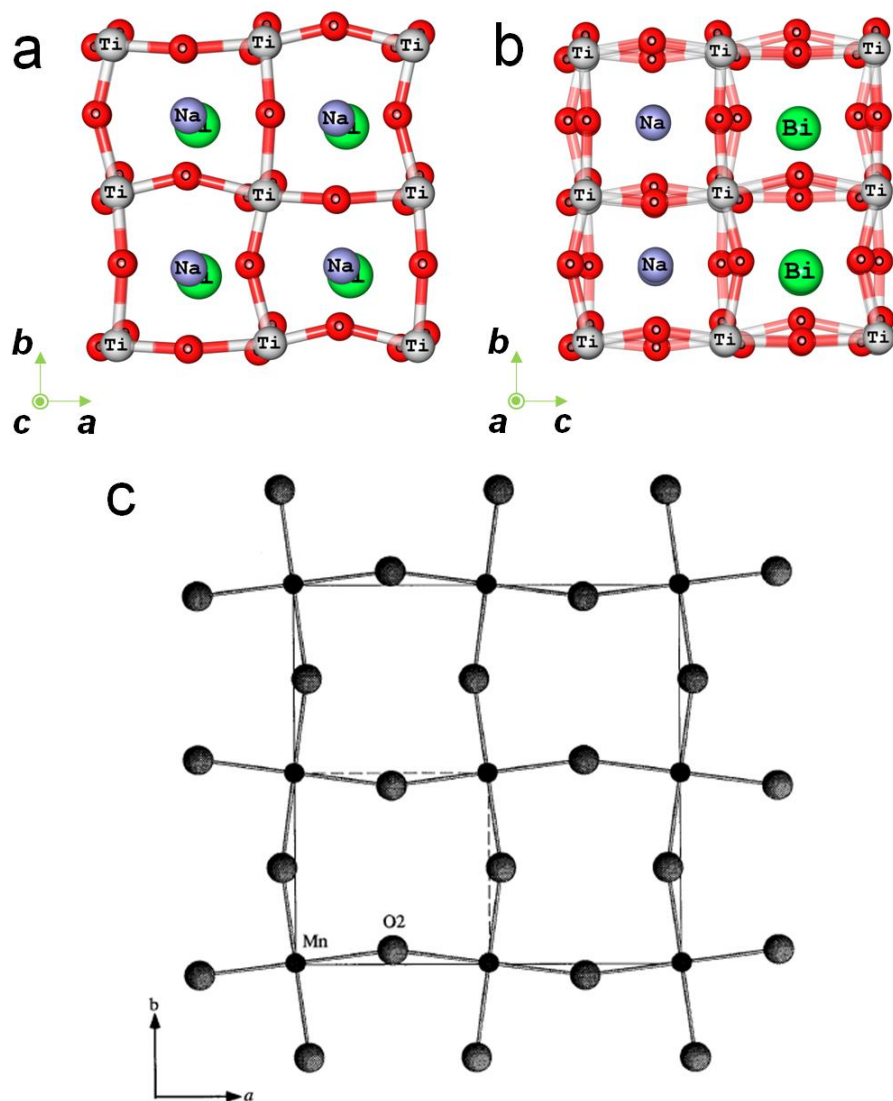


Figure 8-8. A unit cell of optimized T5 after structural optimization (a and b) and projections of simplified Pr<sub>0.5</sub>Sr<sub>0.5</sub>MnO<sub>3</sub> perovskite structure with symmetry of F4/mmc [188] (c). Only manganese (small dot) and oxygen (large dot) are shown.

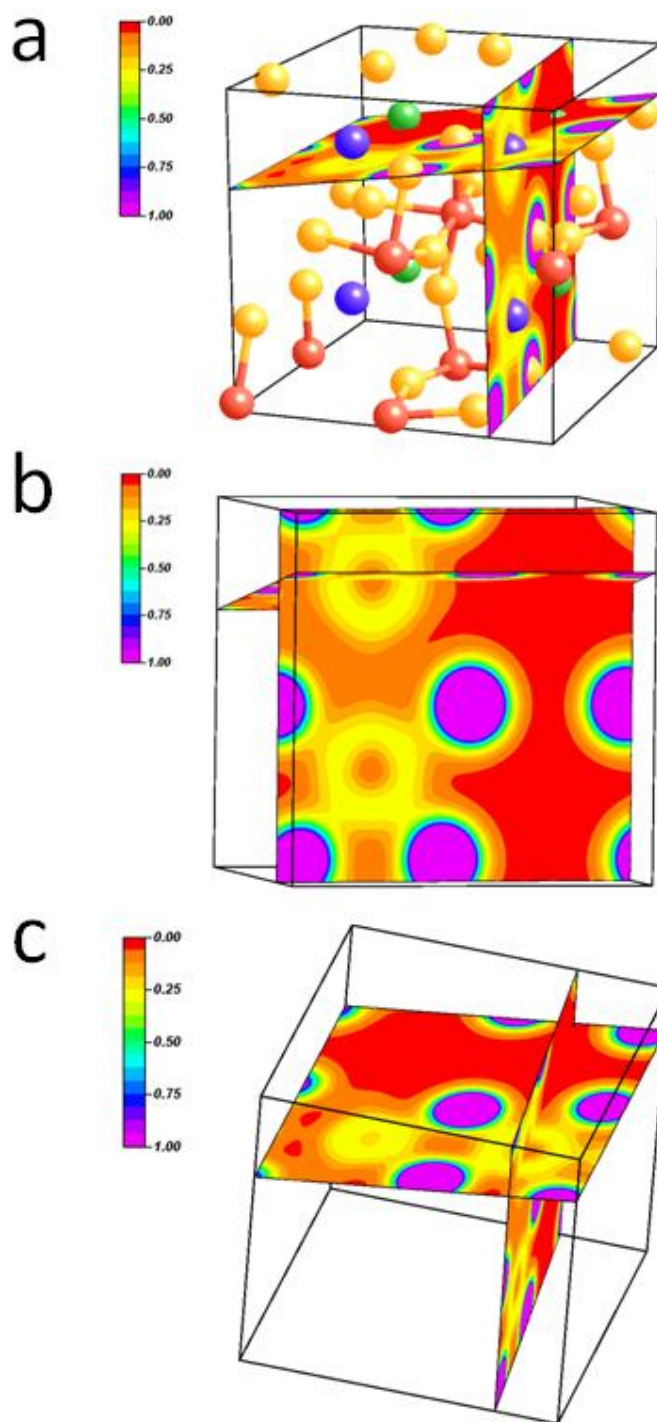


Figure 8-9. Charge density images of P1 phase. a. blue, orange, red, and green denote bismuth, oxygen, titanium, and sodium, respectively. Pink indicates interior of oxygen atom and bismuth is seen yellow in b and c.

In Fig. 8-8(a), the network of oxygen and titanium is similar to that of the F4/mmc structure shown in Fig. 8-8(c) [188]. To display F4/mmc symmetry, a structure has to be tetragonal with  $a=b$  and  $\alpha=\beta=\gamma=90^\circ$ . However, T5 having alternative layers of Na and Bi is monoclinic with symmetry of P1 due to the deviations in the positions of Na and Bi sites in the c-direction (see Fig. 8-8(a)). As a result, the lattice parameters of T5 are not consistent with those of a tetragonal system (see Table 8-5).

The displacement of the oxygen atoms is much larger than that of titanium in the P1 phase of T5. In order to characterize the bonding of the Na and Bi atoms with neighboring oxygen atoms, an analysis of charge density is carried out.

Figure 9-9 exhibits charge density images for the P1 phase of T5. Neighboring oxygen atoms strongly bond with bismuth atoms, but no obvious bonding is observed between Na and neighboring oxygen atoms. Therefore, the bonding of Bi-O is highlighted in Fig. 8-11(a) and (b). The charge density is captured on two planes to show all oxygen atoms neighboring a Bi in Fig. 8-9(a). There are two kinds of Bi. One is coordinated with four oxygen atoms, and the other with two oxygen atoms in Fig. 8-11(a). On the other plane the Bi atom with two neighboring oxygen atoms in Fig. 8-11(a) is coordinated with four oxygen atoms in Fig. 8-11(b). Similarly, the Bi atom with four neighboring oxygen atoms is surrounded with other two oxygen atoms in Fig. 8-11(b). This is consistent with the Bi atom being 6-fold-coordinated, and forming  $[\text{BiO}_6]^{-9}$  units [189].

### 8-5. Distortion of Octahedra

The structure change from R3c to P1 phase results from the distortion of octahedra consisting of oxygen atoms. There are three main reasons why the structure of lattice may be distorted [190]:

- The bonds valence and length may not be topologically equivalent.
- Atoms may have an intrinsically anisotropy in their electronic structure.
- Steric strains may be caused by stretching or compressing of bonds.

The first and second reasons are applied for new systems or external stress. In this study, two different phases, R3c and P1, of NBT takes place by change of cation ordering in the same perovskite frame consisting of Ti-O bonding. Therefore, the electronic structure is focused on to elucidate the relation between cation ordering and structure change.

According to the Jahn–Teller theorem [191], a system with a degenerate electronic structure in the ground-state will distort if such a distortion can remove the degeneracy. The distortion in ceramic materials normally results from the followings [190]:

- The stereoactive lone pairs associated with main group cations in lower valence states (e.g.  $S^{4+}$  and  $As^{3+}$ )
- The octahedrally coordinated transition metals with a  $d^0$  or  $d^1$  configuration (e.g.  $V^{5+}$ )
- The crystal field effect, commonly referred to as the ‘Jahn–Teller distortion’, found around octahedrally coordinated  $Cu^{2+}$  and  $Mn^{3+}$ .

The first and second mechanisms are called ‘second-order Jahn–Teller effect (SOJT) [192, 193].  $Ti^{4+}$  in NBT is considered as a  $d^0$  transition metal owing to its electronic structure of  $[Ar] 4s^2 3d^2$  [194]. The second mechanism can be applied to

explain the structure distortion. As mentioned in the analysis of the charge density results of NBT, Bi has an important role in the P1 structure by bonding neighboring oxygen atoms. Bi has 10 d-electrons in Table 8-6. In octahedral complexes, the Jahn–Teller effect is most commonly observed when an odd number of electrons occupy the  $e_g$  orbitals; *i.e.*, in  $d^0$ , low-spin  $d^7$  or high-spin  $d^4$  complexes [195]. The only factor to cause the distortion is a lone pair ( $3d^2$ ) in Bi. Hence,  $Ti^{4+}$  and  $Bi^{+3}$  can produce the distortion in NBT. The primary distortive cause (intra-octahedral displacement[196]) can be attributed to SOJT effects with both the  $d^0$  transition metals and lone-pair cations [194, 197]. In this case, the primary distortion (intra-octahedral displacement) of the  $d_0$  transition metal occurs by the secondary distortion (interactions between the polyhedra having lone pairs and the  $MO_6$  octahedra) [194]. Combination of two mechanisms and distortion of a pseudo-cubic structure are related to examine  $Na_{0.5}Bi_{0.5}TiO_3$  and  $Na_{0.5}La_{0.5}TiO_3$

- $Na_{0.5}Bi_{0.5}TiO_3$  (NBT): lone pairs ( $Bi^{+3}$ ) +  $d^0$  transition metal ( $Ti^{+4}$ )
- $Na_{0.5}La_{0.5}TiO_3$  (NLT):  $d^0$  transition metal ( $La^{+3}$ ) +  $d^0$  transition metal ( $Ti^{+4}$ )

As shown in Table 9-6, La is chosen to compare to Bi owing to its charge, electronic structure, and ionic radius.

Table 8-6. Radius and electronic structures of Bi and La [198-200].

Element	Charge	Radius/nm			Electronic structure	After ionization
		Ionic	Covalent	Atomic		
Bi	+3	103	148	156	$[Xe] 4f^{14} 5d^{10} 6s^2 6p^3$	$6s^2$ is left: <b>lone pair</b>
La	+3	103	207	187	$[Xe] 5d^1 6s^2$	$[Xe]$ is left

All the Bi atoms are substituted with La in the P1 phase; the lowest energy structure of  $Na_{0.5}La_{0.5}TiO_3$  (NLT) is then determined using the GGA approximation, see

Fig. 9-10. The system still has P1 symmetry. However, the cell is more symmetrical than that of NBT, as characterized by small displacements of the oxygen atoms, and the near colinearity of the Na and Bi cations. Hence, the combination of lone pairs and the  $d^0$  transition metal can deform octahedra of a perovskite cell more severely than that of  $d^0$  transition metals. Excessive Bi is reported to increase the SOJT effect in  $\text{Bi}_4\text{Ti}_3\text{O}_{12}$  [201]

The distortion results in making cations and octahedra asymmetric [194] or off-center [196]. Figure 8-11 represents this. We cannot see Na atoms in Fig. 8-11 (a) and (b). As shown in Fig. 8-8, the Na and Bi atoms do not sit on the same plane. The La and Na are, however, on the same plane in Fig. 8-11 (c) and (d). Moreover, some Na atoms in Fig. 9-11(d) form weak bonding with oxygen atoms. Na atoms contribute to determining the structure NLT structure, in contrast to their small effect in NBT.

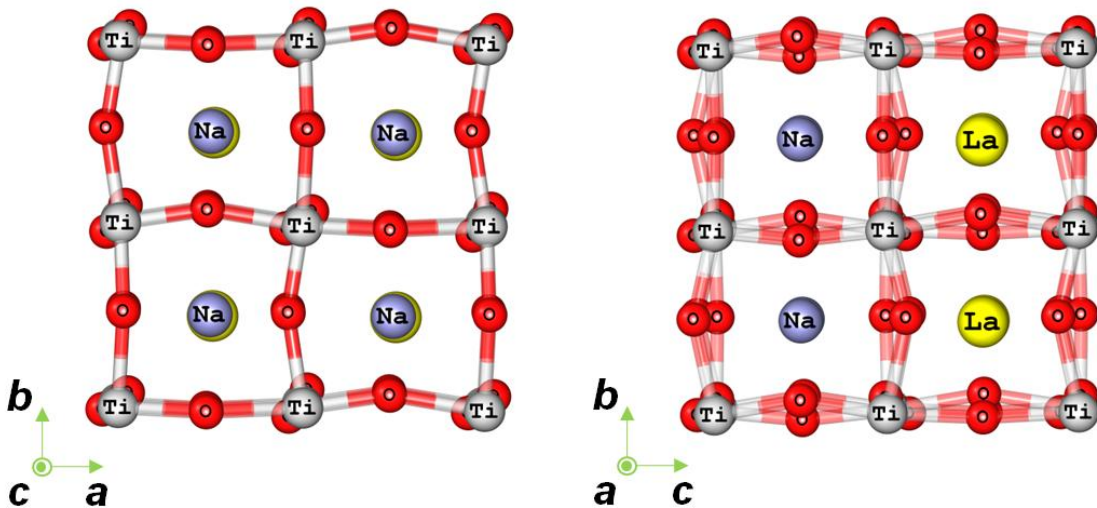


Figure 8-10. Optimized unit cell of  $\text{Na}_{0.5}\text{La}_{0.5}\text{TiO}_3$ . Compare with Fig. 8-8(a) and (b) for NBT.

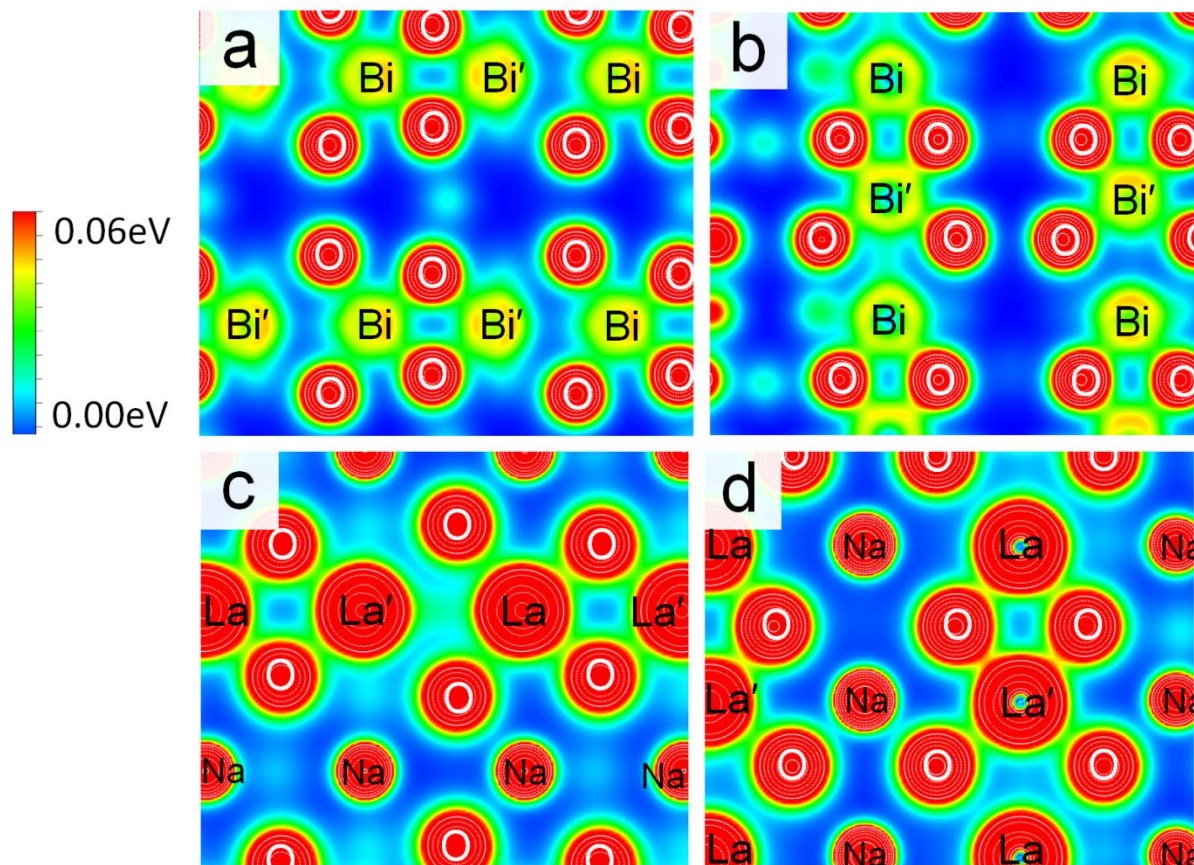


Figure 8-11. Contour map of charge density of  $\text{Na}_{0.5}\text{Bi}_{0.5}\text{TiO}_3$  and  $\text{Na}_{0.5}\text{La}_{0.5}\text{TiO}_3$  on different planes of pseudo cubic type cell.

### 8-6. Summary

Understanding the cation structure of NBT is important for engineering the properties of NBT as a replacement for PZT for ferroelectric and piezoelectric applications. Density functional theory calculations at the level of the GGA were used to determine the relative energies of various arrangements of Na and Bi cations.

The T2 structure, having alternative arrangement of Na and Bi in the perovskite axis, has the lowest energy of the cation arrangements that have R3c structure. However, the R3c structures with ordered cations have higher energies than structures with random cation arrangements. This indicates that the random arrangement of cation

can be expected to be favored. The T5 with layers of Na and Bi shows the lowest energy among all of the structures analyzed, and revealed to have a P1 phase by distortion of octahedra in its perovskite. To analyze the structure distortion, elements (Ti-Bi and Ti-La) causing the second-order Jahn–Teller effect are chosen and, compared in structure and charge density. The combination of lone pairs and the  $d^0$  transition metal can deform octahedra of a perovskite cell more severely than that of  $d^0$  transition metals. The cation-layered structure of  $\text{Na}_{0.5} \text{Bi}_{0.5} \text{TiO}_3$  may be influenced by the Jahn-Teller effect, thereby having the lowest energy.

## REFERENCE LIST

- [1] Levy RA, North Atlantic Treaty Organization. Microelectronic materials and processes : [proceedings of the NATO Advanced Study Institute on Microelectronic Materials and Processes, Il Ciocco, Castelvechio Pascoli, Italy, June 30-July 11, 1986]. Dordrecht ; Boston, 1989.
- [2] Widmann D, Mader H, Friedrich H. Technology of integrated circuits. Berlin ; New York, 2000.
- [3] Callister WD. Materials science and engineering : an introduction. New York, 2007.
- [4] Barrett CR, Nix WD, Tetelman AS. The principles of engineering materials. [Englewood Cliffs, N.J., 1973.
- [5] Czerwinski F. Magnesium injection molding. New York, 2007.
- [6] Ye HZ, Liu XY. J. Mater. Sci. 2004;39:6153.
- [7] Wei Q. J. Mater. Sci. 2007;42:1709.
- [8] Bacon DJ, Vitek V. Metall. Mater. Trans. A 2002;33:721.
- [9] Barrow DA, Petroff TE, Tandon RP, Sayer M. J. Appl. Phys. 1997;81:876.
- [10] Guo R, Cross LE, Park SE, Noheda B, Cox DE, et al. Phys. Rev. Lett. 2000;84:5423.
- [11] Noheda B, Gonzalo JA, Cross LE, Guo R, Park SE, et al. Phys. Rev. B 2000;61:8687.
- [12] Scott JF, Araujo CA, Melnick BM, McMillan LD, Zuleeg R. J. Appl. Phys. 1991;70:382.
- [13] Park SE, Chung SJ, Kim IT. J. Am. Ceram. Soc. 1996;79:1290.
- [14] Zhao SC, Li GR, Ding AL, Wang TB, Yin QR. J. Phys. D 2006;39:2277.
- [15] Zhou ZH, Xue JM, Li WZ, Wang J, Zhu H, et al. Appl. Phys. Lett. 2004;85:804.
- [16] Balasubramanian S, Anand L. Acta Mater. 2002;50:133.
- [17] Roberts CS. Magnesium and its alloys. New York,, 1960.
- [18] Zheng-Johansson JX, Eriksson O, Johansson B. Phys. Rev. B 1999;59:6131.

- [19] Bacon DJ, Vitek V. Metall. Mater. Trans. A 2002;33:721.
- [20] Lütjering G, Williams JC. Titanium. Berlin ; New York, 2003.
- [21] Hirth JP, Lothe J. Theory of dislocations. New York, 1982.
- [22] Agnew SR, Yoo MH, Tome CN. Acta Mater. 2001;49:4277.
- [23] Yoo MH, Agnew SR, Morris JR, Ho KM. Mater. Sci. Eng. A 2001;319:87.
- [24] Liu XY, Adams JB, Ercolessi F, Moriarty JA. Modelling and Simul. in Mater. Sci. Eng. 1996;4:293.
- [25] Friedrich HE, Mordike BL, SpringerLink. Magnesium technology metallurgy, design data, automotive applications. Berlin: Springer, 2004. p1.
- [26] Kim YM, Lee BJ, Baskes MI. Phys. Rev. B 2006;74.
- [27] Christian JW, Mahajan S. Progr. Mater. Sci. 1995;39:1.
- [28] Reed-Hill RE, Hirth JP, Rogers HC, Metallurgical Society of AIME. Institute of Metals Division. Deformation twinning; proceedings. New York, 1965.
- [29] Yoo MH. Metall. Mater. Trans. A 1981;12:409.
- [30] Wu L, Jain A, Brown DW, Stoica GM, Agnew SR, et al. Acta Mater. 2008;56:688.
- [31] Barnett MR. Mater. Sci. Eng. A 2007;464:1.
- [32] Dieter GE. Mechanical metallurgy. New York, 1986.
- [33] Courtney TH. Mechanical behavior of materials. New York, 1990.
- [34] Gleiter H. Progr. Mater. Sci. 1989;33:223.
- [35] Gleiter H. Zeitschrift Fur Metallkunde 1995;86:78.
- [36] Wolf D, Yamakov V, Phillpot SR, Mukherjee A, Gleiter H. Acta Mater. 2005;53:1.
- [37] Meyers MA, Mishra A, Benson DJ. Progr. Mater. Sci. 2006;51:427.
- [38] Yamakov V, Wolf D, Phillpot SR, Gleiter H. Acta Mater. 2003;51:4135.
- [39] Van Swygenhoven H, Derlet PM, Froseth AG. Nat. Mater. 2004;3:399.
- [40] Caro A, Van Swygenhoven H. Phys. Rev. B 2001;63.

- [41] Farkas D, Van Petegem S, Derlet PM, Van Swygenhoven H. *Acta Mater.* 2005;53:3115.
- [42] Schiotz J, Di Tolla FD, Jacobsen KW. *Nature* 1998;391:561.
- [43] Schiotz J, Jacobsen KW. *Science* 2003;301:1357.
- [44] Van Swygenhoven H, Spaczer M, Caro A, Farkas D. *Phys. Rev. B* 1999;60:22.
- [45] Phillpot SR, Wang J, Wolf D, Gleiter H. *Mater. Sci. Eng. A* 1995;204:76.
- [46] Phillpot SR, Wolf D, Gleiter H. *J. Appl. Phys.* 1995;78:847.
- [47] Zhu HL, Averback RS. *Mater. Sci. Eng. A* 1995;204:96.
- [48] Yamakov V, Wolf D, Phillpot SR, Gleiter H. *Acta Mater.* 2002;50:61.
- [49] Yamakov V, Wolf D, Phillpot SR, Mukherjee AK, Gleiter H. *Nat. Mater.* 2002;1:45.
- [50] Yamakov V, Wolf D, Phillpot SR, Mukherjee AK, Gleiter H. *Nat. Mater.* 2004;3:43.
- [51] Chen MW, Ma E, Hemker KJ, Sheng HW, Wang YM, et al. *Science* 2003;300:1275.
- [52] Zheng GP, Wang YM, Li M. *Acta Mater.* 2005;53:3893.
- [53] Kumar KS, Van Swygenhoven H, Suresh S. *Acta Mater.* 2003;51:5743.
- [54] Allen MP, Tildesley DJ. *Computer simulation of liquids.* Oxford New York, 1987.
- [55] Andersen HC. *J. of Chem. Phys.* 1980;72:2384.
- [56] Parrinello M, Rahman A. *Phys. Rev. Lett.* 1980;45:1196.
- [57] Parrinello M, Rahman A. *J. Appl. Phys.* 1981;52:7182.
- [58] Green DJ. *An introduction to the mechanical properties of ceramics.* Cambridge ; New York, 1998.
- [59] Berendsen HJC, Postma JPM, Vangunsteren WF, Dinola A, Haak JR. *J. of Chem. Phys.* 1984;81:3684.
- [60] Adelman SA, Doll JD. *J. of Chem. Phys.* 1974;61:4242.
- [61] Doll JD, Myers LE, Adelman SA. *J. of Chem. Phys.* 1975;63:4908.

- [62] Adelman SA, Doll JD. *J. of Chem. Phys.* 1976;64:2375.
- [63] Nose S. *J. of Chem. Phys.* 1984;81:511.
- [64] Hoover WG. *Phys. Rev. A* 1985;31:1695.
- [65] Phillpot SR, Sinnott SB. *Science* 2009;325:1634.
- [66] Shan TR, Devine BD, Hawkins JM, Asthagiri A, Phillpot SR, et al. *Phys. Rev. B*;82.
- [67] Lewis GV, Catlow CRA. *J. Phys. C* 1985;18:1149.
- [68] Daw MS, Foiles SM, Baskes MI. *Mater. Sci. Rep.* 1993;9:251.
- [69] Baskes MI. *Mater. Chem. Phys.* 1997;50:152.
- [70] Rose JH, Smith JR, Guinea F, Ferrante J. *Phys. Rev. B* 1984;29:2963.
- [71] Ebrahimi F, Bourne GR, Kelly MS, Matthews TE. *Nanostructured Materials* 1999;11:343.
- [72] Ebrahimi F, Liscano AJ, Kong D, Krishnamoorthy V. *Phil. Mag.* 2003;83:457.
- [73] Yamakov V, Wolf D, Salazar M, Phillpot SR, Gleiter H. *Acta Mater.* 2001;49:2713.
- [74] Hu WY, Zhang BW, Huang BY, Gao F, Bacon DJ. *J. Phys.: Condens. Matter.* 2001;13:1193.
- [75] Baskes MI, Johnson RA. *Modelling and Simul. in Mater. Sci. Eng.* 1994;2:147.
- [76] Li B, Ma E. *Acta Mater.* 2009;57:1734.
- [77] Olmsted DL, Hector LG, Curtin WA, Clifton RJ. *Modelling and Simul. in Mater. Sci. Eng.* 2005;13:371.
- [78] Xia ZG, Sun DY, Asta M, Hoyt JJ. *Phys. Rev. B* 2007;75.
- [79] Couret A, Caillard D. *Acta Metall.* 1985;33:1455.
- [80] Devlin JF. *J. Phys. F: Met. Phys* 1974;4:1865.
- [81] Sastry DH, Prasad YVR, Vasu KI. *Scripta Metall.* 1969;3:927.
- [82] Hennig RG, Lenosky TJ, Trinkle DR, Rudin SP, Wilkins JW. *Phys. Rev. B* 2008;78.

- [83] Johnson RA, Oh DJ. *J. Mater. Res.* 1989;4:1195.
- [84] Oh DJ, Johnson RA. *J. Mater. Res.* 1988;3:471.
- [85] Oh DJ, Johnson RA. *J. Nuc. Mater.* 1989;169:5.
- [86] Haslam AJ, Phillpot SR, Wolf H, Moldovan D, Gleiter H. *Mater. Sci. Eng. A* 2001;318:293.
- [87] Schiotz J, Vegge T, Di Tolla FD, Jacobsen KW. *Phys. Rev. B* 1999;60:11971.
- [88] Jonsson H, Andersen HC. *Phys. Rev. Lett.* 1988;60:2295.
- [89] Clarke AS, Jonsson H. *Phys. Rev. E* 1993;47:3975.
- [90] Li J. *Modelling and Simul. in Mater. Sci. Eng.* 2003;11:173.
- [91] Bacon DJ, Martin JW. *Phil. Mag. A* 1981;43:883.
- [92] Ando S, Gotoh T, Tonda H. *Metall. Mater. Trans. A* 2002;33:823.
- [93] Stohr JF, Poirier JP. *Phil. Mag.* 1972;25:1313.
- [94] Li B, Ma E. *Phil. Mag.* 2009;89:1223.
- [95] Koike J. *Metall. Mater. Trans. A* 2005;36A:1689.
- [96] Proust G, Tome CN, Jain A, Agnew SR. *Int. J. Plasticity* 2009;25:861.
- [97] Brown DW, Agnew SR, Bourke MAM, Holden TM, Vogel SC, et al. *Mater. Sci. Eng. A* 2005;399:1.
- [98] Lou XY, Li M, Boger RK, Agnew SR, Wagoner RH. *Int. J. Plasticity* 2007;23:44.
- [99] Song SG, Gray GT. *Metall. Mater. Trans. A* 1995;26:2665.
- [100] Tomsett DI, Bevis M. *Phil. Mag.* 1969;19:129.
- [101] Dickson JI, Robin C. *Mater. Sci. Eng.* 1973;11:299.
- [102] Song SG, Gray GT. *Acta Metall. Mater.* 1995;43:2325.
- [103] Agnew SR, Tome CN, Brown DW, Holden TM, Vogel SC. *Scripta Mater.* 2003;48:1003.

- [104] Clausen B, Tome CN, Brown DW, Agnew SR. *Acta Mater.* 2008;56:2456.
- [105] Van Swygenhoven H. *Science* 2002;296:66.
- [106] Legrand B. *Phil. Mag. B* 1984;49:171.
- [107] Wu XZ, Wang R, Wang SF. *Appl. Surf. Sci.*;256:3409.
- [108] Mae K, Nobata T, Ishida H, Motoyama S, Hiwatari Y. *Modelling and Simul. in Mater. Sci. Eng.* 2002;10:205.
- [109] Kim D -H, Manuel M V, Ebrahimi F, Tulenko J S, Phillpot S R. Unpublished work 2009.
- [110] Kelchner CL, Plimpton SJ, Hamilton JC. *Phys. Rev. B* 1998;58:11085.
- [111] Balasubramanian S, Anand L. *Acta Mater* 2002;50:133.
- [112] Yoo MH, Morris JR, Ho KM, Agnew SR. *Metall Mater Trans A* 2002;33:813.
- [113] Obara T, Yoshinga H, Morozumi S. *Acta Metall* 1973;21:845.
- [114] Jones IP, Hutchinson WB. *Acta Metall* 1981;29:951.
- [115] Tonda H, Ando S. *Metall Mater Trans A* 2002;33:831.
- [116] Ando S, Gotoh T, Tonda H. *Metall Mater Trans A* 2002;33:823.
- [117] Li B, Ma E. *Phil Mag* 2009;89:1223.
- [118] Liang MH, Bacon DJ. *Phil Mag A* 1986;53:181.
- [119] Minonishi Y, Ishioka S, Koiwa M, Morozumi S. *Phil Mag A* 1982;46:761.
- [120] Minonishi Y, Ishioka S, Koiwa M, Morozumi S, Yamaguchi M. *Phil Mag A* 1981;43:1017.
- [121] Minonishi Y, Ishioka S, Koiwa M, Morozumi S, Yamaguchi M. *Phil Mag A* 1982;45:835.
- [122] Morris JR, Ho KM, Chen KY, Rengarajan G, Yoo MH. *Modelling and Simul in Mater Sci Eng* 2000;8:25.
- [123] Numakura H, Minonishi Y, Koiwa M. *Phil Mag A* 1990;62:525.

- [124] Numakura H, Minonishi Y, Koiwa M. *Phil Mag A* 1990;62:545.
- [125] Jain A, Agnew SR. *Mater Sci Eng A* 2007;462:29.
- [126] Kim D -H, Manuel M V, Ebrahimi F, Tulenko J S, Phillpot S R. *Acta Mater* 2010;58:6217.
- [127] Liu XY, Adams JB, Ercolessi F, Moriarty JA. *Modelling and Simul in Mater Sci Eng* 1996;4:293.
- [128] Bacon DJ, Vitek V. *Metall Mater Trans A* 2002;33:721.
- [129] Hull D, Bacon DJ. *Introduction to dislocations*. Oxford [Oxfordshire] ; Boston, 2001.
- [130] Osetsky YN, Bacon DJ. *Modelling and Simul in Mater Sci Eng* 2003;11:427.
- [131] Voskoboinikov RE, Osetsky YN, Bacon DJ. *Mater Sci Eng A* 2005;400:45.
- [132] Wang GF, Strachan A, Cagin T, Goddard WA. *Modelling and Simul in Mater Sci Eng* 2004;12:S371.
- [133] Nogaret T, Curtin WA, Yasi JA, Hector LG, Trinkle DR. *Acta Mater*;58:4332.
- [134] Morris JR, Scharff J, Ho KM, Turner DE, Ye YY, et al. *Phil Mag A* 1997;76:1065.
- [135] Chetty N, Weinert M. *Phys Rev B* 1997;56:10844.
- [136] Jelinek B, Houze J, Kim S, Horstemeyer MF, Baskes MI, et al. *Phys Rev B* 2007;75.
- [137] Yasi JA, Nogaret T, Trinkle DR, Qi Y, Hector LG, et al. *Modelling and Simul in Mater Sci Eng* 2009;17.
- [138] Medlin DL, McCarty KF, Hwang RQ, Guthrie SE, Baskes MI. *Thin Solid Films* 1997;299:110.
- [139] Sastry DH, Prasad YVR, Vasu KI. *Scripta Metall* 1969;3:927.
- [140] Devlin JF. *J Phys F* 1974;4:1865.
- [141] Fleischer RL. *Scripta Metall* 1986;20:223.
- [142] Couret A, Caillard D. *Acta Metall* 1985;33:1455.

- [143] Kelly EW, Hosford WF. Transactions of the Metallurgical Society of Aime 1968;242:654.
- [144] Sun DY, Mendeleev MI, Becker CA, Kudin K, Haxhimali T, et al. Phys Rev B 2006;73.
- [145] Koike J. Metall. Mater. Trans. A 2005;36A:1689.
- [146] Serra A, Bacon DJ. Mater. Sci. Eng. A 2005;400:496.
- [147] Wang J, Huang HC. Appl. Phys. Lett. 2004;85:5983.
- [148] Zhang L, Han Y. Mater. Sci. Eng. A 2009;523:130.
- [149] Jiang L, Jonas JJ, Luo AA, Sachdev AK, Godet S. Scripta Mater. 2006;54:771.
- [150] Jiang L, Jonas JJ, Boyle K, Martin R. Mater. Sci. Eng. A 2008;492:68.
- [151] Nogaret T, Curtin WA, Yasi JA, Hector LG, Trinkle DR. Acta Mater.;58:4332.
- [152] Tang TA, Kim S, Horstemeyer MF, Wang P. Eng. Frac. Mech.;78:191.
- [153] Serra A, Bacon DJ. Philosophical Magazine a-Physics of Condensed Matter Structure Defects and Mechanical Properties 1986;54:793.
- [154] Serra A, Bacon DJ. Philosophical Magazine a-Physics of Condensed Matter Structure Defects and Mechanical Properties 1996;73:333.
- [155] Serra A, Bacon DJ, Pond RC. Acta Metallurgica 1988;36:3183.
- [156] Serra A, Pond RC, Bacon DJ. Acta Metallurgica Et Materialia 1991;39:1469.
- [157] Yoo MH. Metallurgical Transactions a-Physical Metallurgy and Materials Science 1981;12:409.
- [158] Mathewson CH, Phillips AJ. Transactions of the American Institute of Mining and Metallurgical Engineers 1928;78:445.
- [159] Sisneros TA, Brown DW, Clausen B, Donati DC, Kabra S, et al. Mater. Sci. Eng. A;527:5181.
- [160] Zhang XY, Zhu YT, Liu Q. Scr. Mater. 2010;63:387.
- [161] Battaini M, Pereloma EV, Davies CHJ. Metall. Mater. Trans. A 2007;38A:276.
- [162] Adressio LB, Cerreta EK, Gray GT. Metall. Mater. Trans. A 2005;36A:2893.

- [163] Subhash G, Ravichandran G, Pletka BJ. Metall. Mater. Trans. A 1997;28:1479.
- [164] Churchman AT. Transactions of the American Institute of Mining and Metallurgical Engineers 1960;218:262.
- [165] Barnett MR. Scripta Materialia 2008;59:696.
- [166] Rupert TJ, Gianola DS, Gan Y, Hemker KJ. Science 2009;326:1686.
- [167] Wolf D, Yamakov V, Phillpot SR, Mukherjee AK. Zeitschrift Fur Metallkunde 2003;94:1091.
- [168] Ono N, Nowak R, Miura S. Materials Letters 2004;58:39.
- [169] Hansen N, Ralph B. Acta Metall. 1982;30:411.
- [170] Nagarjuna S, Srinivas M, Sharma KK. Acta Mater. 2000;48:1807.
- [171] Voskoboinikov RE, Osetsky YN, Bacon DJ. Mater. Sci. Eng. A 2005;400:45.
- [172] Osetsky YN, Bacon DJ. Modelling and Simul. in Mater. Sci. Eng. 2003;11:427.
- [173] Yamakov V, Wolf D, Phillpot SR, Gleiter H. Acta Mater. 2002;50:5005.
- [174] Smolenskii GA, Isupov VA, Agranovskaya AI. Soviet Physics-Solid State 1960;1:1438.
- [175] Jones GO, Thomas PA. Acta Crystallogr. Sect. B 2002;58:168.
- [176] Nagata H, Takenaka T. Jap. J. of Appl. Phys. 1997;36:6055.
- [177] Prasad K, Kumari K, Lily, Chandra KP, Yadav KL, et al. Solid State Communications 2007;144:42.
- [178] Zhang HB, Jiang SL, Kajiyoshi K. J. Am. Ceram. Soc. 2009;92:2147.
- [179] Marchet P, Boucher E, Dorcet V, Mercurio JP. J. Euro. Ceram. Soc. 2006;26:3037.
- [180] Glazer AM. Acta Crystallogr. Sect. A 1975;31:756.
- [181] Vakhrushev SB, Ivanitskii BG, Kvyatkovskii BE, Maistrenko AN, Malysheva RS, et al. Fizika Tverdogo Tela 1983;25:2613.
- [182] Park SE, Chung SJ, Kim IT, Hong KS. J. Am. Ceram. Soc. 1994;77:2641.

- [183] Martin RM. Electronic structure : basic theory and practical methods. Cambridge, UK ; New York, 2004.
- [184] Sholl DS, Steckel JA. Density functional theory : a practical introduction. Hoboken, N.J., 2009.
- [185] Kohn W, Sham LJ. Physical Review 1965;140:1133.
- [186] Perdew JP. Phys. Rev. Lett. 1985;55:1665.
- [187] Aksel E, Forrester JS, Jones JL, Thomas PA, Page K, et al. Appl. Phys. Lett. 2011;98.
- [188] Argyriou DN, Hinks DG, Mitchell JF, Potter CD, Schultz AJ, et al. J. Solid State Chem. 1996;124:381.
- [189] Yang J, Dolg M. J. Phy. Chem. B 2006;110:19254.
- [190] Brown ID. Chemical Reviews 2009;109:6858.
- [191] Jahn HA, Teller E. Proceedings of the Royal Society of London Series a-Mathematical and Physical Sciences 1937;161:220.
- [192] Burdett JK, Eisenstein O. Inorg. Chem. 1992;31:1758.
- [193] Chang HY, Kim SH, Halasyamani PS, Ok KM. J. Am. Chem. Soc. 2009;131:2426.
- [194] Halasyamani PS. Chem. Mater. 2004;16:3586.
- [195] Janes R, Moore E, Royal Society of Chemistry (Great Britain), Open University. Metal-ligand bonding. Cambridge, 2004.
- [196] Kunz M, Brown ID. J. Solid State Chem. 1995;115:395.
- [197] Pearson RG. J. Am. Chem. Soc. 1969;91:4947.
- [198] Mantina M, Chamberlin AC, Valero R, Cramer CJ, Truhlar DG. J. Phy. Chem. A 2009;113:5806.
- [199] Shannon RD. Acta Crystallogr. Sect. A 1976;32:751.
- [200] Cordero B, Gomez V, Platero-Prats AE, Reves M, Echeverria J, et al. Dalton Transactions 2008:2832.
- [201] Yau CY, Palan R, Tran K, Buchanan RC. Appl. Phys. Lett. 2004;85:4714.

## BIOGRAPHICAL SKETCH

Dong-Hyun Kim was born in January 1976 at Masan, Republic of Korea. He graduated dept. Inorganic Materials Engineering of Pusan National University in 2008. He finished his master course at the same department under the supervision of Prof. Kwangho Kim in 2000. He studied chemical sensors and thin film processes. He has joined the research center of Daeyang Electrics Co., Ltd. as a researcher of the sensor device team in 2001. He worked at the Plasma Display Panel division of Samsung SDI as an assistant manager form 2004 to 2007. He has begun Ph. D course under the supervision of Prof. Simon R. Phillpot in Dept. Materials Science and Engineering of University of Florida in Aug 2007. His research is oriented towards atomistic simulation of metals and ceramics. Aug 2011, Dong-Hyun earned his Doctor of Philosophy in material science and engineering.